ISSN 1811-1165 (Print)
ISSN 2413-2179 (Online)

EURASIAN PHYSICAL TECHNICAL JOURNAL

VOLUME 22, NO. 2(52), 2025

phtj.buketov.edu.kz

EURASIAN PHYSICAL TECHNICAL JOURNAL

p - ISSN 1811-1165
e - ISSN 2413-2179

Volume 22, No. 2(52), 2025

1st issue – June, 2004

Journal Founder:

NLC "KARAGANDY UNIVERSITY OF THE NAME OF ACADEMICIAN E.A. BUKETOV

https://phtj.buketov.edu.kz

www.facebook.com/groups/1103109540750967

Registration Certificate No.4382-Zh, November 7, 2003.

Re-registration Certificate No.KZ50VPY00027647, October 6, 2020 issued by Information Committee of the Ministry of Information and Public Development of the Republic of Kazakhstan

Contact information:

Editorial board of EAPhTJ
(Build. 2, room 216)
Karaganda Buketov University
Universitetskaya Str.28, Karaganda,
Kazakhstan, 100024
Subscription index: 75240

Tel: +7(7212) 77-04-03
Fax: +7(7212) 35-63-98
E-mail: ephtj@mail.ru,
ephtj2021@gmail.com

Signed to print 25.06.2025.
Format 60x84 1/8. Offset paper.
Volume 21.5 p.sh. Circulation 300 copies.
Order No. 79.

Printed in the Publishing House of
Karagandy University of the name
of academician E.A. Buketov

Tel. +7 (7212) 35-63-16.
E-mail: izd_karu@buketov.edu.kz

Eurasian Physical Technical Journal, 2025, Vol. 22, No. 2(52)

CONTENTS

Dear authors and readers!

Dear colleagues!

In the preface, we traditionally inform the authors and readers about the most important achievements of the Eurasian Physical Technical Journal at the moment. Thanks to our authors and the qualified work of the editorial board members, the journal continues to be indexed in the Scopus database in all four scientific areas with a maximum percentile 26% on the Engineering direction. In all other directions, the percentile has also increased slightly. According to the Scimago Journal & Country Rank (SJR) website our Journal's Hirsch index is 8. These indicators were achieved thanks to the objective and highly qualified examination of materials by our reviewers, which guarantees the quality of the articles published in the Eurasian Physical Technical Journal.

Dr. Aybaba Hançerliögullari, Professor, Doctor, Department of Physics, Kastamonu Üniversitesi, Kastamonu, Turkey, has been invited to serve as a member of the Editorial Board. Dr. Aybaba Hançerliögullari's (H-index 12) scientific areas are environmental science and ecology, science and technology, etc. We hope that his work in the Editorial Board will attract new authors, which will also contribute to strengthening the rating of the journal.

Let us move on to a description of the contents of this issue.

The Materials Science section presents new original results on the study of material properties under various external influences. The Institute of Molecular Nanophotonics, Buketov University (Karaganda) researchers have studied the effect of a heavy atom on the generation of singlet oxygen in the plasmon field of silver nanoparticles. The authors found that the presence of a bromine atom in a dye molecule increases the efficiency of singlet oxygen production.

Scientists from the Orenburg State University (Russia) based on the results, a model was developed that describes "the kinetics of oxygen-dependent photoreactions in the film and the formation of luminescent response signals during its multi-pulse laser activation, taking into account the diffusion replenishment of oxygen molecules in the intervals between activating pulses."

In the next article, the authors investigated the optical properties and the distribution of the electric field strength around silver nanoparticles with a TiO_2 or SiO_2 shell. It was found that "the maximum electric field strength around plasmonic nanoparticles is concentrated radially and predominantly on their surface."

Astana and Almaty researchers used phenomenological and semi-microscopic analysis to determine the optimal optical potential. Detailed calculations yielded values of "spectroscopic amplitudes for configurations for different interactions at different energies of 15N incident ions."

The first two articles in the Energy section are devoted to environmental aspects of energy related to the possibilities of bioenergy. In particular, the authors from Indonesia used "a Cu-doped ZnO sample fabricated using a green synthesis method with bioreduction from pineapple peel extract" in their study. It was shown that "the 5% Cu-doped ZnO sample as a photoanode showed the highest efficiency of 1.67% with an electron lifetime of 12 ms compared to the undoped photoanode." In second article Buketov University employees together with a Tomsk scientist experimentally studied the optimal values of electrical parameters, "allowing to increase the degree of extraction of valuable components from organic raw materials with a simultaneous reduction in the time of electro-hydro-pulse processing."

The Almaty scientists' article presents the results of computer modeling of thermophysical processes occurring "during spraying and turbulent combustion of biofuel (biodiesel) droplets in the combustion chamber of an engine with direct injection." The results made it possible to obtain a visualization of the reacting flow with temperature and concentration characteristics of harmful emissions during the combustion of biodiesel.

The article by the Institute of Technical Thermophysics (NASU, Kyiv) author is devoted to the development of measures to improve the thermal efficiency of working surfaces and the coolant supply system. The results of complex studies of transfer processes in complex conditions of interaction of external and internal turbulent effects characteristic of thermal power equipment are considered.

Paper of our university employees and Russian scientist (Tomsk) is devoted to the study of the aerodynamic characteristics of a wind power plant, "equipped with two combined blades combining fixed profiles and rotating cylinders." The results of numerical modeling in the Ansys Fluent package and

laboratory tests showed that the use of combined blades allows increasing the aerodynamic efficiency of wind turbines by 8–10% compared to traditional designs.

The Engineering section articles examine practically important technical developments and solutions to current problems in the automation of modern technologies and monitoring systems. The Almaty authors article presents "the technology of Fourier-IR spectroscopy of hydrocarbon materials at low temperatures and atmospheric pressure", which allows studying the optical properties of various substances in a certain temperature range without using a vacuum.

The article by our university authors “the factors affecting the strength and corrosion rate of aluminum-magnesium alloys in sea water” is examined. It is shown that "the more aluminum cells contain the Mg2Al4 group as a rhombic subsystem, the higher the strength of these alloys".

Scientists from the Karaganda Industrial University (Temirtau) present the results of "finite element modeling of a new technology of combined deformation of radial-shear drawing and traditional drawing" in their article. Using the DEFORM program, it was established that the optimal conditions are the 30-25-20 scheme at a temperature of 900 °C”.

In the paper, researchers from Al-Farabi Kazakh National University (Almaty) and the School of Electronics and Information Engineering, Northwestern Polytechnical University (Xi'an, China) evaluated "the performance of YOLOv8n/v8s, YOLOv11n/v11s, and YOLOv12n/v12s models in extracting features from terrestrial thermal infrared images and videos captured by long-range infrared cameras."

The Physics and Astronomy section in the article by the authors from Fesenkov Astrophysical Institute (Almaty), Institute of Astronomy (RAS) and Sternberg Astronomical Institute, Moscow State University (Russia) the results of an analysis of “reflectance spectra of asteroids based on observations made at the Assy-Turgen Observatory (code 217) at an altitude of 2658 meters above sea level (77°.87114 E, 43°.225527 N) are shown. These results were obtained using “a long-slit spectrograph based on volume-phase holographic gratings installed at the main focus of the AZT-20 telescope with an aperture of 1.5 meters.”

The next article by scientists from Jordan universities developed a description of “a nonlinear equation that controls the oscillations of charged particles under the influence of an electric field using the homotopic perturbation method.”

An article by Almaty researchers devoted to the problems of astrophysics, the results of the analysis of the light curve of the star IRAS07080+0605, belonging to the FS CMa class, are presented using data from the ASAS SN survey in the period from 2014 to 2025. It is assumed that "the appearance of asymmetries in the phase curves indicates a possible change in the orbit, which may be associated with the dynamics of the system, including a change in the separation between objects."

We hope that the presented articles will be of interest to scientists, teachers and doctoral students.

In order to increase the international recognition and citation of your scientific articles published in the journal "Eurasian Physical Technical Journal", the editors recommend that authors register on the scientific platform ResearchGate (www.researchgate.net). Posting articles on ResearchGate will help expand the scientific audience of readers; increase the citation index of the author and the journal; establish new professional contacts; increase interest in your publications.

We will be glad to see you among our readers and authors of the following issues, in which it is planned to publish articles by leading scientists on the most relevant and priority areas of modern physics and technology.

We also invite authors and readers to visit our Facebook (https://www.facebook.com/groups/1103109540750967/members), where announcements and news about the Eurasian Physical Technical Journal are posted, and write your opinions and wishes.

With respect and best wishes for health and well-being to our authors and readers,

Editor-in-Chief, Professor Sakipova S.E.
June, 2025

EURASIAN PHYSICAL TECHNICAL JOURNAL

2025, Volume 22, No. 2 (52)

https://doi.org/10.31489/2025N2/5-12

Received: 26/02/2025 Revised: 11/06/2025 Accepted: 23/06/2025 Published online: 30/06/2025

Research Article

UDC 535.015, 535.2, 538.975

THE EFFECT OF THE INTERNAL HEAVY ATOM ON SINGLET OXYGEN GENERATION IN THE PRESENCE OF PLASMONIC NANOPARTICLES

Ibrayev N.Kh.*, Menshova E.P.

Institute of Molecular Nanophotonics, Buketov University, Karaganda, Kazakhstan
*Corresponding author: niazibrayev@mail.ru

Abstract. *The heavy atom effect on singlet oxygen generation in the plasmon field of silver nanoparticles was investigated. The dyes rhodamine 123 and dibromrhodamine 123 in polyvinyl butyral films were used as sensibilisers. The dye films were deposited by spin-coating onto silver island films synthesised on the quartz surface. The results showed that the presence of bromine atom in the dye molecules increased the singlet oxygen generation efficiency. The calculated Stern-Follmer constants demonstrate the enhancement of molecular oxygen quenching of triplet states of dibromorhodamine 123 dye molecules in the presence of Ag nanoparticles.*

Keywords: heavy atom effect, intersystem crossing, singlet oxygen, nanoplasmonics, photosensitiser.

1. Introduction

Singlet oxygen $O_2(^1\Delta_g)$ is the most stable excited state of molecular oxygen $O_2(^3\Sigma_g)$ which plays an important role in biological, chemical and industrial processes, acting as the main oxidant. It is highly sought after for photodynamic therapy, which is used in the therapeutic and/or palliative treatment of various cancers and benign diseases. The mechanism of cell destruction underlying photodynamic therapy combines the activation of sensitising molecules by light irradiation and the formation of singlet oxygen and cytotoxic reactive oxygen species (ROS). In addition, $O_2(^1\Delta_g)$ and ROS can act as oxidants in biological objects [1,2] and in organic synthesis [3,4], be used for light inactivation of proteins using chromophores [5] and photodegradation of organic contaminants [5,6], disinfection of drinking water [7], sterilisation of gases and solids, and self-cleaning of filter membranes [8].

To study the processes of molecular oxygen $O_2(^3\Sigma_g^-)$ activation, photosensitizers (PSs) based on organic dyes with high quantum yield to the triplet state and the ability to transfer energy to $O_2(^3\Sigma_g^-)$ oxygen are used [9]. One of the factors that increase the probability of intersystem crossing (ISC) and, consequently, the transition of sensitising molecules to the triplet state [10], is the adding of heavy atoms to the structure of dye molecules. This approach found wide application in the development of new PSs for photodynamic therapy and other fields requiring efficient generation of reactive oxygen species [11].

Much attention is also paid to the study of the interaction of organic photosensitisers with plasmonic nanoparticles (NPs), which can significantly enhance the luminescence intensity and shorten the phosphorescence lifetime due to the Purcell effect [12]. In the presence of silver or gold NPs, the local electromagnetic field is enhanced, that increases the probability of radiative transitions and accelerates the deactivation of excited states of the sensitiser [13]. Plasmon NPs can also increase the sensitivity and selectivity of sensitisers to oxygen due to more efficient energy transfer from the triplet state of the sensitiser

to the oxygen molecule [14]. In particular, the use of silver island films (SIFs) allows achieving enhanced luminescence due to the generation of localised surface plasmons and increasing the overall signal intensity [15]. In [16,17] a correlation between the effect of the heavy atom in the dye molecule and the degree of influence of the plasmon effect of silver NPs on the phosphorescence properties of a series of halogen-substituted xanthene and fluorescein dyes was carried out. A theoretical model is proposed to estimate the quantum yield of phosphorescence of dye molecules in the vicinity of plasmonic NPs. To this end, the rate constants of radiative and non-radiative intramolecular transitions of dyes were calculated.

This study is an extension of [16] using brominated rhodamine derivatives and silver plasmonic structures to improve the efficiency of singlet oxygen generation. The use of heavy atoms together with plasmonic NPs opens up the prospect of creating more efficient and precise photosensitisers for the targeted generation of reactive oxygen species [18].

2. Experimental part

The dyes rhodamine 123 (Rh123) and dibromhodamine 123 (Rh 123-2Br), which were purchased from Sigma-Aldrich, were chosen to study the effect of spin-orbit interaction on $O_2(^1\Delta_g)$ generation. The molecular structure of the dye molecules studied is shown in Figure 1. The dye films in polyvinyl butyral (PVB) were deposited by spin-coating at 1,500 rpm for 30 sec. The concentration of dyes in 7 wt% polymer was $5 \cdot 10^{-4}$ mol/L. Micro-weighing was used to control the thickness of films deposited on different substrates. The mass of the dye films on the surface was almost the same. The oxygen permeability of PVB is 0.95×10^{-10} $cm^3 \cdot cm/(cm^2 \cdot s \cdot atm)$ [19].

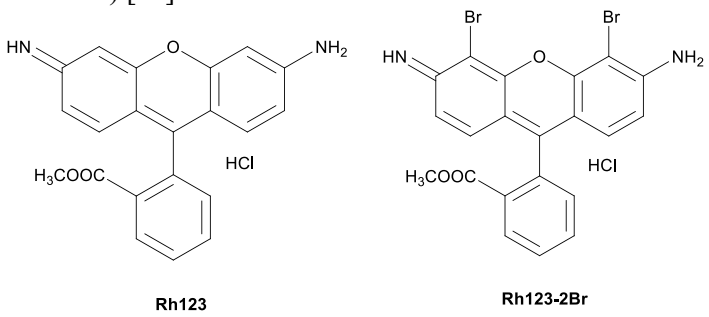

Fig. 1. Molecular structure of the investigated dye molecules

To study the effect of plasmonic NPs on $O_2(^1\Delta_g)$ generation in the presence of heavy atom, substrates of SIFs were prepared by chemical deposition [20]. Analytical grade purity chemicals from Sigma Aldrich and ultrapure water obtained using a Smart S15 UVF system (Drawell) were used to SIFs synthesise. SIFs were annealed at 240^0C for 30 min. This in turn helps to stabilise and improve the structural and functional properties of the silver films. According to scanning electron microscope (Mira 3LMU, Tescan) data, spherical islands of size 105 – 375 nm were uniformly distributed on the film's surface of the (Fig. 2a).

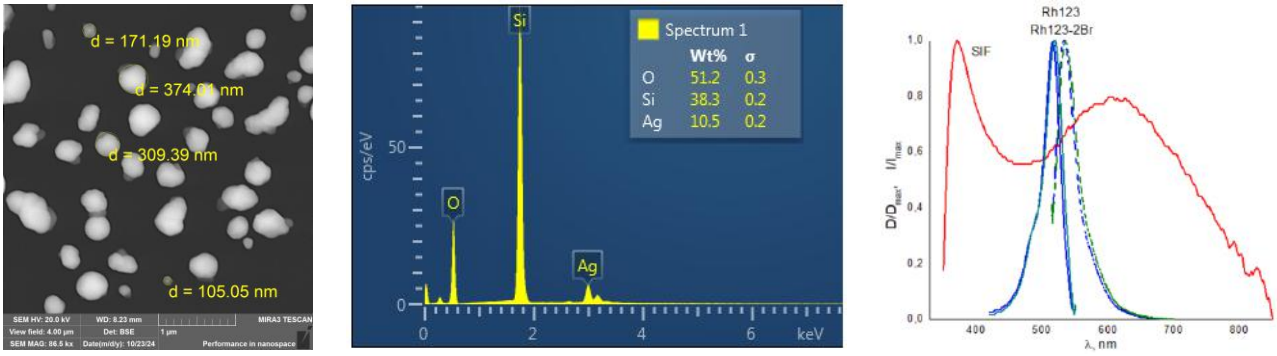

a b c

Fig. 2. (a) SEM image of SIFs obtained by chemical deposition on quartz glass, (b) XPS spectra of SIFs and (c) Absorption spectra of SIFs (red line), Rh123 (blue solid), Rh123-2Br (green solid) and fluorescence spectra of Rh123 (blue dashed), Rh123-2Br (green dashed) in PVB film on quartz glass (λ_{exc} = 510 nm, λ_{reg} = 540 nm)

Energy dispersive X-ray spectroscopy analysis of the SIFs surface showed the presence of silver, silicon and oxygen, where silicon and oxygen are related to the composition of quartz glass (Fig. 2b). The absorption spectrum of SIFs is broadened and has two peaks at 365 nm and 605 nm (Fig. 2c). The broadening is due to the large variation in the size of the islands.

Cary 300 and Eclipse spectrometers (Agilent Technologies) were used to record absorption, fast and delayed fluorescence spectra. Delayed fluorescence (DF) and phosphorescence (Phos) measurements of Rh123 and Rh123-2Br films were carried out under varying pressure conditions using an Optistat DN vacuum cryostat (Oxford Instruments).

A FLS1000 spectrometer (Edinburgh Instruments) with UV, Vis-PMT and NIR-PMT photomultipliers (Hamamatsu) was used to record the attenuation kinetics of long-lived luminescence of dyes and singlet oxygen phosphorescence. Photoexcitation of samples at λ_{exc}=510 nm was carried out by a laser system based on Nd:YAG laser LQ529 with OPO LP604 and second harmonic generator LG305 (SolarLS).

3. Results and Discussion

From the normalised absorption and fluorescence spectra of Rh123 and Rh123-2Br in the polymer films, it can be seen that the spectra of Rh123-2Br are bathochromically shifted, due to the presence of two bromine atoms (Fig. 2c). The maximum of the absorption spectrum (λ_{abs}^{max}) of Rh123 falls at 516 nm, Rh123-2Br – at 520 nm. The maximum of fluorescence spectrum (λ_{fl}^{max}) is at 535 nm for Rh123 and at 540 nm for Rh123-2Br. Figure 3 shows the long-lived luminescence spectra of the dye films, where two luminescence maxima are expressed. The first maximum at 540 nm coincides with the fast fluorescence and refers to DF. Whereas the maximum at around 670 nm is Phos of the dyes (Fig. 3).

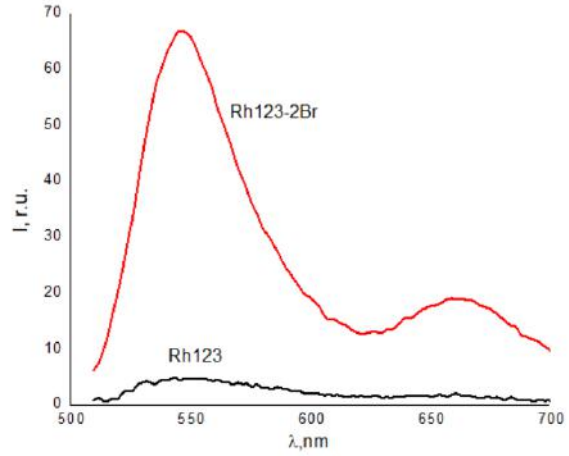

Fig. 3. Long-lived luminescence spectra of Rh123 and Rh123-2Br ($5*10^{-4}$ mol/L) in PVB film (7 wt%) (λ_{exc} = 510 nm) at cryostat air pressure of 10^{-3} mB and T = 293 K

From the I_{DF}/I_{Phos}, intensities ratio, which is 2.5 for the first dye and 3.2 for the second dye, it can be stated that Rh123-2Br has more pronounced phosphorescence than Rh123. DF and Phos intensities of the Br-substituted dye are an order of magnitude higher than those of Rh123. The shorter lifetime of DF and Phos of Rh123-2Br (Table 1) is due to the faster decay of the S_1 state not only to the ground state, but also to the nearby triplet state T_1 due to the increase in the probability of ISC due to the effect of the internal heavy atom [17].

The effect of oxygen concentration on the DF and Phos of Rh123-2Br was studied (Fig. 4). Dibromorhodamine molecules have a high probability of transition from the excited singlet state (S_1) в to the triplet state (T_1) due to ISC, which is characteristic of molecules containing heavy atoms.

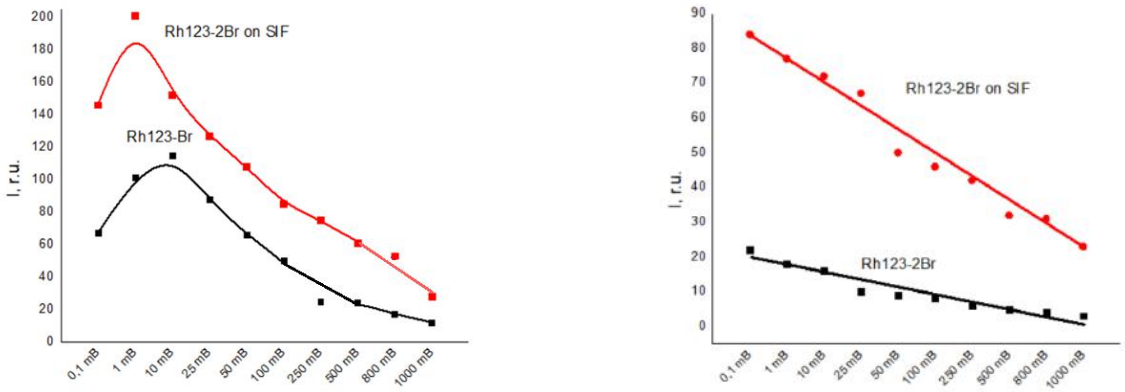

a b

Fig. 4. The dependence of the intensity of DF (a) and Phos (b) of Rh123-2Br in PVB films on the cryostat pressure (λ_{exc} = 510 nm, λ_{reg} = 540 nm for DF and λ_{reg} = 670 nm for Phos) at T = 293K

According to [21], the following processes can occur in the collision complexes of molecular oxygen and triplets of the sensitiser:

$$T + {}^3\Sigma_g^- \rightarrow \left[T\ldots{}^3\Sigma_g^-\right]^{1,3,5} \rightarrow S_0 + {}^1\Delta_g \quad (1)$$

$$T + {}^1\Delta_g \rightarrow \left[T\ldots{}^1\Delta_g\right]^3 \rightarrow S_1 + {}^3\Sigma_g^- \rightarrow S_0 + {}^3\Sigma_g^- + h\nu_{DF} \quad (2)$$

$${}^1\Delta_g \rightarrow {}^3\Sigma_g^- + h\nu_{Phos} \quad (3)$$

where S_0, S_1, T – ground, excited singlet and triplet states, ${}^3\Sigma_g^-$, ${}^1\Delta_g$ – molecular and singlet oxygen, $\left[T\ldots{}^3\Sigma_g^-\right]^{1,3,5}$ – intermediate complex between the sensitiser and oxygen, where the total spin multiplicity can be 1 (singlet), 3 (triplet), or 5 (quintet), $\left[T\ldots{}^1\Delta_g\right]^3$ – excited complex of the sensitiser with singlet oxygen, forming a triplet state, $h\nu_{DF}$ – photon emitted as DF of sensitiser, $h\nu_{Phos}$ – photon emitted during phosphorescence of singlet oxygen.

Process 1 is singlet oxygen sensitisation reaction; process 2 – singlet-triplet annihilation reaction; process 3 – generation of singlet oxygen phosphorescence.

Under the influence of an enhanced plasmon field, the intensity of all types of luminescence increases, as the probability of transition between energy levels increases and more dye molecules return to the ground state with the emission of light photons [22]. The intensity of fast fluorescence increased 2.6 times for Rh123 and 2.18 times for Rh123-2Br. Also, in the presence of plasmon, there is an increase in DF intensity by 2.4 and 2.18 times and Phos intensity by 3.5 and 3.81 times for Rh123 and Rh123-2Br, respectively (Table 1). While the luminescence lifetime decreases (Table 1).

This phenomenon is described by the Purcell effect, according to which near metallic nanostructures possessing plasmons, the lifetime of excited states decreases as rates of radiative transitions are amplified due to the local plasmon field. As a result, the long-lived luminescence becomes more intense, but its lifetime decreases [14, 23, 24].

Figure 4 shows the dependences of the intensity of DF and Phos of Br-substituted dye without the influence of plasmons and in its presence on the air pressure in the cryostat. For DF (Fig. 4a) on quartz glass and on SIFs, an increase of the luminescence intensity with pressure changes from 0.1 to 10 mB, and then a decrease is observed, that is a confirmation of singlet-triplet annihilation. While the Phos intensity (Fig. 4b) decreases monotonically. It is worth noting that the deactivation process of triplet states is more pronounced for Rh123-2Br in the presence of plasmon. The Phos quenching constants by oxygen molecules were calculated on the basis of the Stern-Folmer equation [25]:

$$\frac{I^0_{Phos}}{I_{Phos}} = 1 + k_q \tau_0 \cdot [Q], \quad (4)$$

where I^0_{Phos} – Phos intensity in the absence of O_2, I_{Phos} – Phos intensity in the presence of O_2, k_q – extinction coefficient, τ_0 – Phos lifetime in the absence of O_2, a $[Q]$ – O_2 concentration.

Table 1. Spectral-luminescence parameters of Rh123 and Rh123-2Br in PVB films

	λ^{max}_{abs} (nm)	D	λ^{max}_{fl} (nm)	I_{fl} (r.u.)	I_{DF} (r.u.)	τ_{DF} (ms)	I_{Phos} (r.u.)	τ_{Phos} (ms)	D/D_0	$I_{fl}/I_{fl\,0}$	$I_{DF}/I_{DF\,0}$	$\tau_{DF}/\tau_{DF\,0}$	I_{Phos}/I_{Phos0}	τ_{Phos}/τ_{Phos0}
Rh123														
Quartz	516	0.12	535	163	5	8.7±0.2	2	7.4±0.3	-	-	-	-	-	-
SIFs		0.16		423	12	8.5±0.1	7	5.7±0.7	1.33	2.60	2.4	0.97	3.5	0.77
Rh123-2Br														
Quartz	520	0.13	540	93	67	5.0±0.4	22	5.9±0.1	-	-	-		-	
SIFs		0.15		204	146	4.8±0.2	84	3.6±0.2	1.13	2.18	2.18	0.96	3.81	0.61

Figure 5 shows that a stronger quenching of the triplet state of the dye by oxygen molecules is observed in the plasmon field. For Rh123-2 films on glass k_q =6,2 • 10^2 $M^{-1}s^{-1}$, and on Ag island films k_q =9,1 • 10^2 $M^{-1}s^{-1}$.

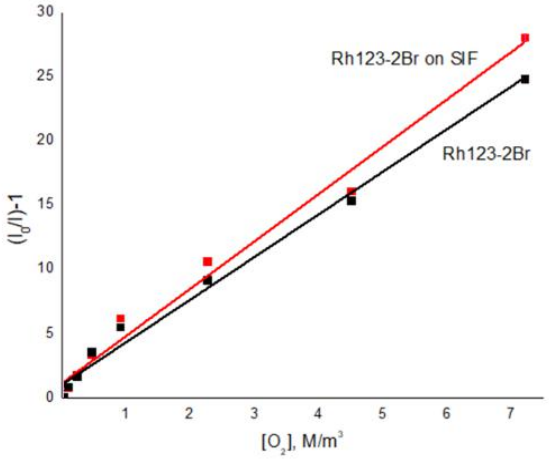

Fig. 5. Stern-Follmer quenching constants of R123-2Br phosphorescence by O_2 molecules on quartz (red line) and on SIFs (black line)

The value of the quenching constant (k_q) can be used as an indicator of the efficiency of singlet oxygen generation. Since k_q reflects how efficiently oxygen quenches the triplet state of the dye-sensitiser. Its value can be indirectly related to the singlet oxygen yield. The higher k_q, the more triplet states of the sensitiser transfer their energy to oxygen molecules as a result of heteroannihilation, that leads to an increase in the singlet oxygen yield $^1\Delta_g$.

Upon photoexcitation, phosphorescence of singlet oxygen was observed in the absorption band of Rh123-2Br, while Rh123 does not contribute to its effective generation. Under the influence of plasmonic field of SIFs the singlet oxygen generation sensitised by Rh123-2Br increased by 2.49 times (Fig. 6).

The kinetic of singlet oxygen phosphorescence is represented by two phases: rise and decay (Fig. 6) and can be approximated according to a two-exponential equation:

$$I(t) = I_0 \left[\exp\left(-\frac{t}{\tau_{decay}} \right) - \exp\left(-\frac{t}{\tau_{rise}} \right) \right] \quad (5)$$

where $I(t)$ – phosphorescence intensity of $O_2(^1\Delta_g)$ per second, I_0 – pre-exponential multiplier, τ_{decay} and τ_{rise} – time constants of the decay and rise phases [26].

The rise phase is determined by the rate of singlet oxygen formation as a result of energy transfer from the triplets of Rh123-2Br to $O_2\left({}^3\Sigma_g^-\right)$, the decay phase – by the process of singlet oxygen deactivation.

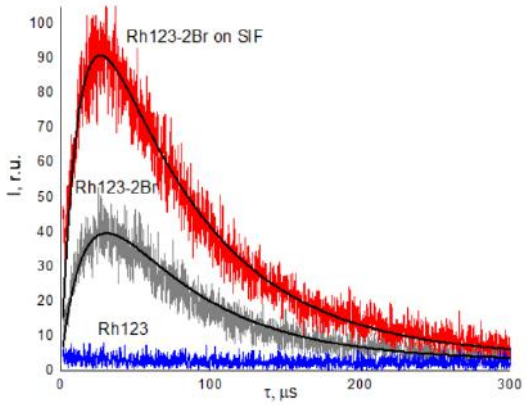

Fig. 6. Kinetics of singlet oxygen phosphorescence (λ_{reg} = 1270 nm) sensitised by R123 and R123-2Br dyes on quartz and SIFs at atmospheric pressure (λ_{exc} = 510 nm)

According to the fitting results, the duration of the rising phase was 16.13 μs and the duration of the decay phase was 75.60 μs. Under the action of plasmon, the duration of these phases decreased by 14% and 3%, respectively. (Table 2). The decrease of the lifetime of $O_2(^1\Delta_g)$ phosphorescence is associated with the enhancement of the radiation transition ${}^1\Delta_g \rightarrow {}^3\Sigma_g^-$.

Table 2. Plasmon effects on the intensity and lifetime of singlet oxygen phosphorescence (λ_{reg} = 1270 nm at atmospheric pressure (λ_{exc} = 510 nm)

	I, r.u.	τ_{rise}, μs	τ_{decay}, μs	I/I_0	$\tau_{rise}/\tau_{rise\ 0}$	$\tau_{decay}/\tau_{decay\ 0}$
$O_2(^1\Delta_g)$ on quartz	60	16.13±0.77	75.60±0.91	-	-	-
$O_2(^1\Delta_g)$ on SIFs	112	12.25±1.61	71.89±0.61	2.49	0.76	0.95

4. Conclusions

In this study, a comparative analysis of the singlet oxygen $O_2(^1\Delta_g)$ generation efficiency by Rh123 and Rh123-2Br dyes in polymer films in the presence of plasmonic silver NPs was carried out. The addition of a heavy bromine atom into Rh 123 molecules leads to a significant increase of the probability of ISC and singlet oxygen generation, as evidenced by an increase of the intensity and decrease in the phosphorescence lifetime. The presence of silver plasmonic NPs further enhances the luminescence processes due to the Purcell effect, reducing the lifetime of excited states and increasing the luminescence intensity. The Stern-Volmer constants for Rh123-2Br on SIFs substrates show a higher quenching coefficient, indicating an increase of the energy transfer efficiency of oxygen molecules and singlet oxygen generation in the plasmon field.

Conflict of interest statement

The authors declare that they have no conflict of interest in relation to this research, whether financial, personal, authorship or otherwise, that could affect the research and its results presented in this paper.

CRediT author statement

Ibrayev N.Kh.: supervision, resources, conceptualization, validation; **Menshova E.P.**: formal analysis, investigation writing - original draft, visualization. All authors have read and agreed to the published version of the manuscript.

Acknowledgements

This research is funded by the Science Committee of the Ministry of Science and Higher Education of the Republic of Kazakhstan (Grant No. AP23490195).)

References

1 Sagadevan A., Hwang K.C., Su M.D. (2017) Singlet oxygen-mediated selective C–H bond hydroperoxidation of ethereal hydrocarbons. *Nature Communications*, 8(1), 1812. https://doi.org/10.1038/s41467-017-01906-5

2 Schmidt R. (2006). Photosensitized generation of singlet oxygen. *Photochemistry and Photobiology*, 82(5), 1161–1177. https://doi.org/10.1562/2006-03-03-IR-833

3 Ishchenko A.A., Syniugina A.T. (2023) Structure and photosensitiser ability of polymethine dyes in photodynamic therapy: *A review. Theoretical and Experimental Chemistry*, 58(6), 373–401. https://doi.org/10.1007/s11237-023-09754-9

4 Singleton D. A., Hang C., Szymanski M. J., Meyer M. P., Leach A. G., Kuwata K. T., Chen J. S., Greer A., Foote C.S., Houk K.N. (2003) Mechanism of the reactions of singlet oxygen: A two-step no-intermediate mechanism. *Journal of the American Chemical Society,* 125(5), 1319–1328. https://doi.org/10.1021/ja027225p

5 Aerssens D., Cadoni E., Tack L., Madder A. (2022) A photosensitized singlet oxygen (1O2) toolbox for bio-organic applications: Tailoring $^{1}O_{2}$ generation for DNA and protein labelling, targeting and biosensing. *Molecules*, 27(3), 778. https://doi.org/10.3390/molecules27030778

6 Bregnhøj M., Prete M., Turkovic V., Petersen A. U., Nielsen M.B., Madsen M., Ogilby P.R. (2019) Oxygen-dependent photophysics and photochemistry of prototypical compounds for organic photovoltaics: Inhibiting degradation initiated by singlet oxygen at a molecular level. *Methods and Applications in Fluorescence*, 8(1), 014001. https://doi.org/10.1088/2050-6120/ab4edc

7 Pibiri I., Buscemi S., Palumbo Piccionello A., Pace A. (2018) Photochemically produced singlet oxygen: Applications and perspectives. *ChemPhotoChem*, 2(7), 535–547. https://doi.org/10.1002/cptc.201800076

8 Wang Y., Lin Y., He S., Wu S., Yang C. (2024). Singlet oxygen: Properties, generation, detection, and environmental applications. *Journal of Hazardous Materials,* 461, 132538. https://doi.org/10.1016/j.jhazmat.2023.132538

9 Khan A., Alam M., Rehman S. U., Khan G. S., Khan F.A., Khan M., Zhang Y. (2019) Rhodamine-based fluorescent probes for bioimaging applications. *Chemical Reviews*, 119(19), 10504–10555. https://doi.org/10.1021/acs.chemrev.9b00230

10 Rao D., Singh P., Jain R. (2020) Applications of singlet oxygen in photodynamic therapy enhanced by plasmonic nanostructures. *Journal of Biomedical Nanotechnology,* 16(5), 843–856. https://doi.org/10.1166/jbn.2020.2914

11 Ogawa K., Kobuke Y. (2016) Heavy atom effects in photochemical and photobiological applications. *Accounts of Chemical Research*, 49(5), 712–721. https://doi.org/10.1021/acs.accounts.6b00027

12 Lakowicz J.R. (2006) Principles of fluorescence spectroscopy (3rd ed.). Springer. https://doi.org/10.1007/978-0-387-46312-4

13 Chowdhury M.H., Ray K. (2008) Plasmon-controlled fluorescence towards high-sensitivity optical sensing. *Advances in Biochemical Engineering/Biotechnology*, 116, 29–72. https://doi.org/10.1007/10_2008_9

14 Ray K., Chowdhury M.H., Zhang J., Fu Y., Szmacinski H., Nowaczyk K., Lakowicz J.R. (2009) Plasmon-controlled fluorescence towards high-sensitivity optical sensing. *Advances in Biochemical Engineering/Biotechnology*, 116, 29–72. https://doi.org/10.1007/10_2008_9

15 Zhang Y., Xu C., Hao Y. (2015) Influence of heavy atoms on intersystem crossing and singlet oxygen generation in photodynamic systems. *Journal of Photochemistry and Photobiology A: Chemistry*, 306, 44–52. https://doi.org/10.1016/j.jphotochem.2015.04.006

16 Ibrayev N.K., Valiev R.R., Seliverstova E.V., Menshova E.P., Nasibullin R.T., Sundholm D. (2024) Molecular phosphorescence enhancement by the plasmon field of metal nanoparticles. *Physical Chemistry Chemical Physics*, *26*(20), 14624–14636. https://doi.org/10.1039/d4cp01281j

17 Ibrayev N., Seliverstova E., Valiev R., Aymagambetova A., Sundholm D. (2024). The effect of heavy atoms on the *deactivation of electronic excited states of dye molecules near the surface of metal nanoparticles. Physical Chemistry Chemical Physics,* 26(40), 25986–25993. https://doi.org/10.1039/D4CP02621G

18 DeRosa M.C., Crutchley R.J. (2002). Photosensitized singlet oxygen and its applications. *Coordination Chemistry Reviews,* 233–234, 351–371. https://doi.org/10.1016/S0010-8545(02)00034-6

19 Kamalova D.I., Abdrazakova L.R., Salakhov M.Kh. (2020) Poly(vinyl butyral)/poly(ethylene glycol) blends for gas separation membranes: Coefficients of diffusion and permeability of oxygen. *Journal of Non-Crystalline Solids*, 532, 120304. https://doi.org/10.1016/j.jnoncrysol.2020.120304

20 Ibrayev N., Seliverstova E., Temirbayeva D., Ishchenko A. (2022) Plasmon effect on simultaneous singlet-singlet and triplet-singlet energy transfer. *Journal of Luminescence,* 251, 119203. https://doi.org/10.1016/j.jlumin.2022.119203

21 Minaev B.F. (2007) Electronic mechanisms of molecular oxygen activation. *Russian Chemical Reviews*, 76(11), 988–1010. https://doi.org/10.1070/RC2007v076n11ABEH003720

22 Seliverstova E., Ibrayev N., Omarova G., Ishchenko A., Kucherenko M. (2021) Competitive influence of the plasmon effect and energy transfer between chromophores and Ag nanoparticles on the fluorescent properties of indopolycarbocyanine dyes. *Journal of Luminescence*, 235, 118000. https://doi.org/10.1016/j.jlumin.2021.118000

23 Kanapina A., Seliverstova E., Ibrayev N., Derevyanko N., Ishchenko A. (2023) Features of the decay of excited states of ionic dyes in the near field of metal nanoparticles. *Eurasian Physical Technical Journal,* 20, 2(44), 106–111. https://doi.org/10.31489/2023No2/106-111

24 Temirbayeva D., Ibrayev N., Kucherenko M. (2022). Distance dependence of plasmon-enhanced fluorescence and delayed luminescence of molecular planar nanostructures. *Journal of Luminescence*, 243, 118642. https://doi.org/10.1016/j.jlumin.2021.118642

25 Gehlen M. H. (2020) The centenary of the Stern–Volmer equation of fluorescence quenching: From the single line plot to the SV quenching map. *Journal of Photochemistry and Photobiology C: Photochemistry Reviews,* 42, 100338. https://doi.org/10.1016/j.jphotochemrev.2019.100338

26 Krasnovsky A.A. (2008) Luminescence and photochemical studies of singlet oxygen photonics. *Journal of Photochemistry and Photobiology A: Chemistry*, 196(2–3), 210–218. https://doi.org/10.1016/j.jphotochem.2007.12.015

AUTHORS' INFORMATION

Ibrayev, Niyazbek – Doctor of Physics and Mathematical Sciences, Professor, Professor-researcher, Director of the Institute of Molecular Nanophotonics, Buketov Karaganda University, Karaganda, Kazakhstan; SCOPUS Author ID: 9333698600, https://orcid.org/0000-0002-5156-5015; niazibrayev@mail.ru.

Menshova, Evgeniya – Master (Eng.), Junior Research Fellow, Institute of Molecular Nanophotonics, Buketov Karaganda University, Karaganda, Kazakhstan; SCOPUS Author ID: 57283853000, https://orcid.org/0000-0003-3646-3763; menshovayevgeniya@gmail.com

EURASIAN PHYSICAL TECHNICAL JOURNAL

2025, Volume 22, No. 2 (52)

https://doi.org/10.31489/2025N2/13-24

Received: 04/03/2025 Revised: 18/05/2025 Accepted: 24/06/2025 Published online: 30/06/2025

Research Article

UDC 535.37; 535.217; 544.525.2; 546.21; 577.336

MULTIPULSE LUMINESCENCE DETECTION OF THE SPATIAL DISTRIBUTION OF REAGENTS AND THE DIFFUSION FLOW OF O_2 MOLECULES INTO POLYMER LAYER

Kucherenko M.G., Rusinov A.P.*

Orenburg State University, Orenburg, Russia
*Corresponding author: sano232@mail.ru

Abstract. *The problem of monitoring processes involving molecular oxygen in porous media still remains relevant due to the development of technologies based on the use of nanostructured systems. It is becoming important to study the characteristics of the reactions in nano cells with different morphologies and connectivity. The specifics of the localization and transport of reagents, which determine the yield of the product during transformations, provide valuable information for analyzing the process and optimizing its flow conditions. In this regard, it is necessary to improve the methodology for measuring photoinduced signals of oxygen-containing systems in non-stationary modes with time resolution to determine the current concentrations of reactant molecules. The kinetics of oxidative photoreactions in a colored polymer film was studied with multiple pulse activation of the system taking into account the layer-by-layer diffusion replenishment of the concentration of oxygen consumed in the reaction from the atmosphere. The process of chemical binding of oxygen molecules with immobilized anthracene molecules in an oxygen-permeable polymer film of polyvinyl butyral containing molecules of an organic dye (erythrosine) as a photosensitizer was recorded. A mathematical model is proposed that describes the kinetics of oxygen-dependent photoreactions in the film and the formation of luminescent response signals during its multi-pulse laser activation taking into account the diffusion replenishment of oxygen molecules in the intervals between the activating pulses. Based on a comparative analysis of the experimental and calculated luminescence signals, the nature of the non-uniform spatial distribution of the photosensitizer and the oxidized reagent in the polymer film is assessed.*

Keywords: Singlet oxygen, chemical traps, delayed fluorescence quenching, sensitized activation.

1. Introduction

Oxygen transport in tissues, its interaction with target biological molecules, the degree of tissue oxygenation, the role of active oxygen species in biological processes are the subject of close study in the field of biochemistry, physiology and medicine [1-8]. Oxygen permeability is an important characteristic in the design of biosimilar materials [2-3]. At the same time, the complexity of biological systems and their multi-level organization make many physical and chemical research methods directly inapplicable due to the possible disruption of the protein structure of tissues. One of the exceptions in terms of non-invasiveness are optical methods. Thus, in works [6-7] a luminescent microsensor introduced into tissues is considered, which allows determining local tissue saturation with oxygen, which is important in the treatment of ischemic diseases of the extremities.

In addition, the problem of monitoring processes involving molecular oxygen in porous nanostructured media remains relevant due to the development of a large number of different technologies based on the use of percolation systems with different morphology and connectivity of nanocells. It is becoming important to study the characteristics of the reactions in nanocells of such systems as reaction chambers. The specifics of the localization and transport of reagents, which determine the yield of the product during transformations, provide valuable information for analyzing the process and optimizing its flow conditions. In this regard, it is necessary to improve the methodology for measuring photoinduced signals of oxygen-containing systems in non-stationary modes with time resolution to determine the current concentrations of reactant molecules.

An alternative way to study the reaction mechanisms and diffusion processes of oxygen molecules is to use model systems where the polymer matrix is oxygen-permeable and is responsible only for its transport, and the binding of oxygen molecules is provided by an additional reagent, for example, as in this work – anthracene [9-10].

The excited singlet state of the oxygen molecule $^1\Delta_g(O_2)$ has the highest reactivity due to its specific orbital electron structure. The relatively high mobility of O_2 molecules in liquid and porous media, as well as the long lifetime of the state $^1\Delta_g(O_2)$, ensure effective transfer of electron excitation energy over fairly large, on a molecular scale, distances. Singlet oxygen is capable of destroying the native state of biological macromolecules, both through oxidative mechanisms - chemically binding to them, and by transferring excess energy to the macromolecule, which leads to disruption of its secondary and tertiary structure. Photogeneration of high concentrations of active oxygen in living cells leads to the death of the latter, which is the basis for photodynamic therapy of malignant tumors [11-18]. In studying the influence of singlet oxygen on biological systems, various experimental methods are used, based on measuring the characteristics of the intrinsic luminescence of O_2 in the infrared region of the spectrum, recording the influence of singlet oxygen on the signals of delayed fluorescence of dyes, and using chemical traps to immobilize excited O_2 molecules. In this paper, a variant of the combined use of the last two methods is proposed to determine the features of the spatial distribution of reagent molecules in an oxygen-permeable polymer layer and to record the diffusion flow of O_2 molecules from the air atmosphere into this layer. In order to adequately decipher the time-resolved signals recorded, a special mathematical model of the processes has been developed, on the basis of which their course in oxygen-permeable polymer films will be analyzed during pulsed laser activation of the system with different gating frequencies.

2. Experimental procedure

The experiments used an oxygen-permeable polymer film of polyvinyl butyral, into which molecules of an organic dye (erythrosine) and an aromatic hydrocarbon (anthracene) were embedded. Erythrosine acted as a photosensitizer, which upon activation ensured the transformation of oxygen molecules from the triplet to the singlet form. At the same time, it also acted as a luminescent probe, the signal of delayed fluorescence of which was used to estimate the concentration of oxygen in the system. This technique is original and was developed by the authors in a number of their previous works [19-23]. In this work, unlike in [21-22], anthracene molecules played the role of chemical traps for singlet oxygen molecules, effectively reducing its local concentration in the film. Anthracene molecules acted as chemical traps for singlet oxygen molecules, effectively reducing its local concentration in the film [19-23]. Experimental samples were prepared from alcohol solutions of polyvinyl butyral, anthracene and erythrosine by casting onto a glass substrate (Fig. 1), and after drying they were polymer films about 2 μm thick with a constant dye concentration (5 mM) and different anthracene concentrations (0, 0.5, 1.0, 2.5 and 5 mM).

24x24 mm cover glasses, a 3% ethanol solution of polyvinyl butyral and 0.1 mM alcoholic solutions of erythrosine and anthracene were used as substrates. Since the concentration and volume of the polymer solution were the same for all samples, the thickness of the films was also the same. For each concentration of anthracene, 4 film samples were produced, and their absorption and luminescence spectra were recorded to control the optical characteristics of the obtained samples. Thus, for samples from the same series, the differences in the spectra did not exceed 2-3%.

The films were then irradiated with a series of laser pulses with an energy of 1-2 mJ each and a duration of 10-12 ns at a wavelength of 532 nm (in the absorption band of erythrosine) with a delay between pulses of 0.1-0.2 s. Upon completion of each pumping pulse, a delayed fluorescence (DF) signal was recorded at a wavelength of 585 nm with a time resolution of 50 ns.

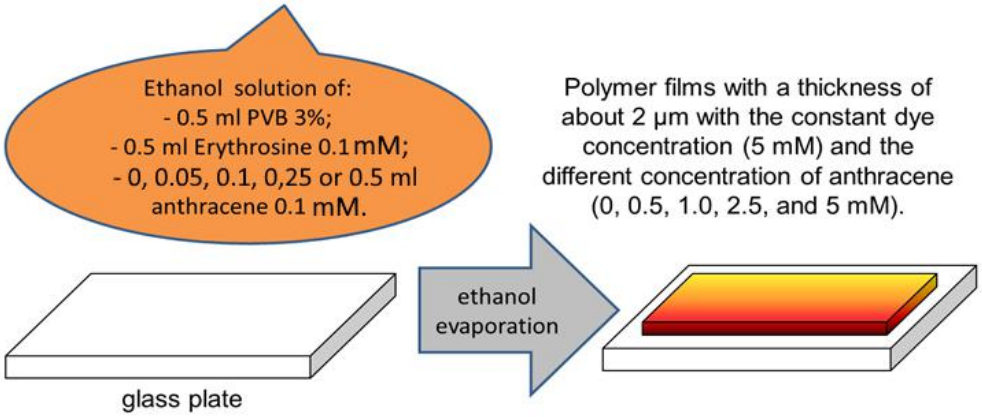

Fig.1. Sample preparation scheme.

To separate the DF signal from the "fast" fluorescence of the dye during laser pumping, the sensitivity of the PMT was modulated by applying an electric pulse of negative polarity to its first dynode ("locking" the PMT). The experimental design is shown in Fig. 2.

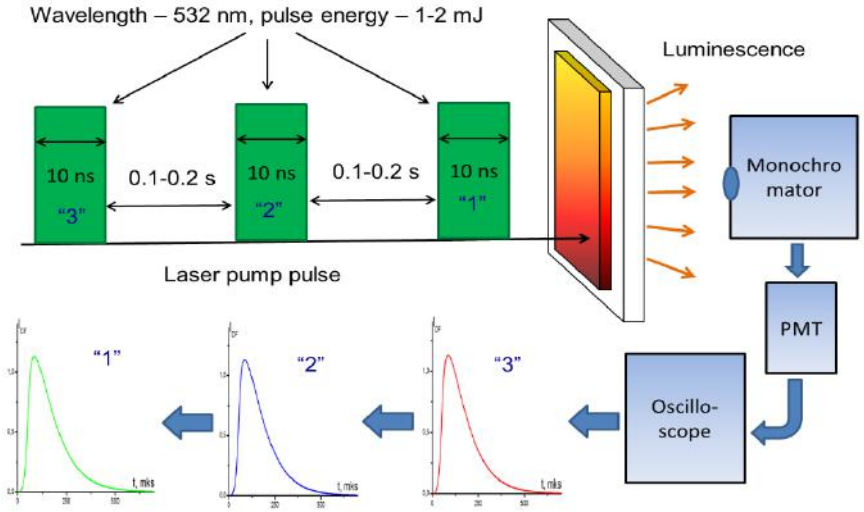

Fig.2. Experimental design.

3. Results and discussion of the experiment

In an oxygen-free environment, the decay time of the delayed fluorescence signal of erythrosine is about 800 μs, and in the presence of oxygen in the system under normal conditions for films without anthracene, the luminescence signal has a duration of about 50 μs, which is due to the active quenching of the triplet states of the dye by oxygen. In this case, the shape and duration of the signal do not change depending on the number of pump pulses, which indicates the absence of irreversible photochemical processes in the film. In samples containing anthracene molecules, the DF curve undergoes changes with each subsequent pump pulse: the signal amplitude decreases and its duration increases. From Fig. 3 it is clear that a smaller delay between pump pulses corresponds to a larger amplitude of the effect (about 20% for 0.1 s and 8-10% for 0.2 s).

The nature of the curves' change can be explained by a decrease in the oxygen concentration in the film when it is bound by anthracene and the subsequent comparatively slow replenishment of the O_2 molecule concentration due to their diffusion from the atmosphere. Accordingly, with a longer delay between pulses, the diffusion replenishment of oxygen in the polymer proceeds more effectively. This conclusion is also confirmed by the fact that after a pause of several seconds, the sample restores its initial parameters and, upon repeated exposure to a series of pulses, the effect of a decrease in the amplitude and an increase in the duration of the signal with an increase in the number of pumping pulses is also observed.

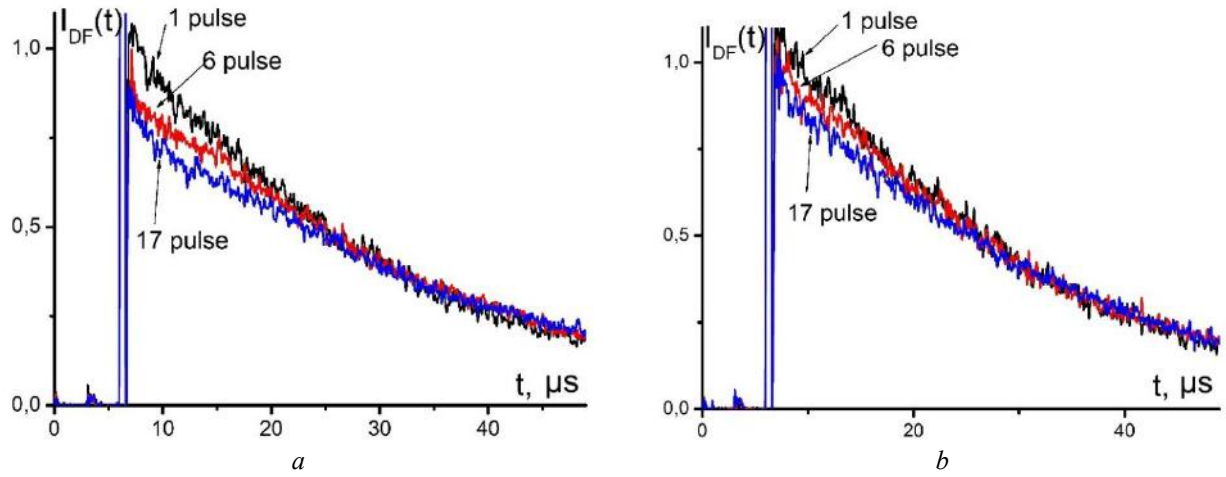

Fig.3. Kinetics of delayed fluorescence of erythrosine (C=5 mM) in a film of polyvinyl butyral with anthracene (C=0.5 mM) depending on the number of pumping pulses. Duration between pulses a) – 0.1 s, b) – 0.2 s.

Fig. 4 shows that with an increase in the anthracene concentration, the decrease in the amplitude of the delayed fluorescence signal of erythrosine is more pronounced (for a sample with the maximum anthracene concentration, this effect reaches values of 30-40%), and the duration of the glow increases, which also confirms the direct influence of anthracene molecules on the local concentration of free oxygen in the film. Fig. 5a shows the relative effect of anthracene in the system on the decrease in the maximum of delayed fluorescence signals when the sample is exposed to a series of pump pulses. It is evident from the graphs that with an increase in the anthracene concentration in the film, the magnitude of the effect increases, and the dependence $I_{DF}(N_{pulse})$ becomes nonlinear. The latter is due to the fact that with a significant decrease in the local concentration of oxygen in the film, the process of its replenishment due to diffusion from the external environment accelerates.

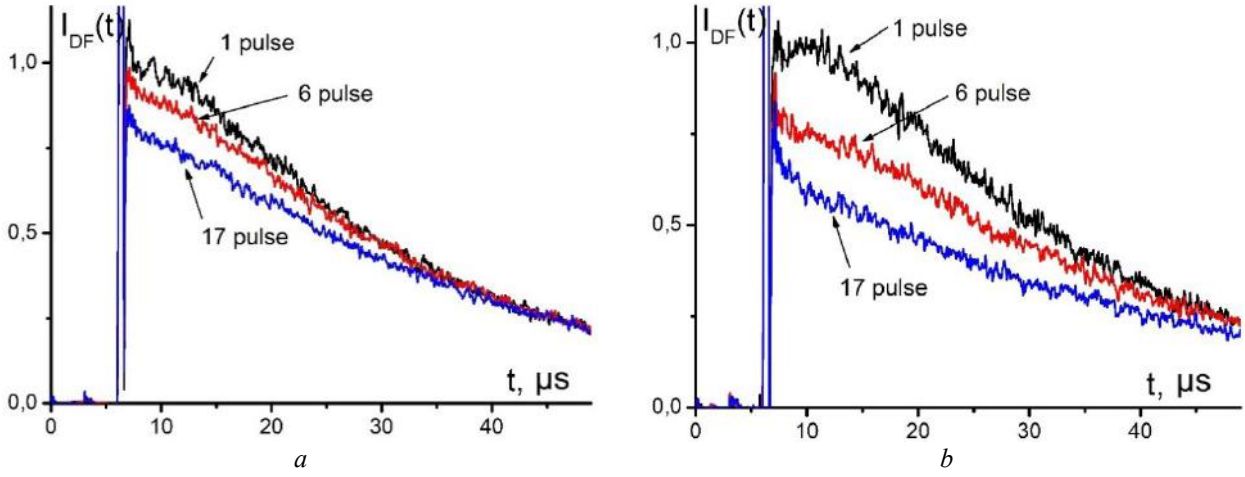

Fig.4. Kinetics of delayed fluorescence of erythrosine (C=5 mM) in a polyvinyl butyral film with anthracene with a concentration of a) – C=2.5 mM, b) – C=5.0 mM depending on the number of pump pulses (duration between pulses 0.1 s).

Since the kinetics of the delayed fluorescence signal in the presence of oxygen is non-exponential [10-12], the average duration of the delayed fluorescence signal, defined as

$$\tau_{eff} = \int t \cdot I_{DF}(t)dt \Big/ \int I_{DF}(t)dt .$$

It follows from Fig. 5b that with an increase in the total exposure, the duration of the glow signals increases, and in samples with a high concentration of anthracene, the dependence $\tau_{eff}(N_{pulse})$ becomes nonlinear. It is evident from Fig. 5b that the curve reaches a horizontal asymptote corresponding to the balance – mutual compensation of the processes of oxygen binding by anthracene in the polymer volume and its diffusion leakage from the outside.

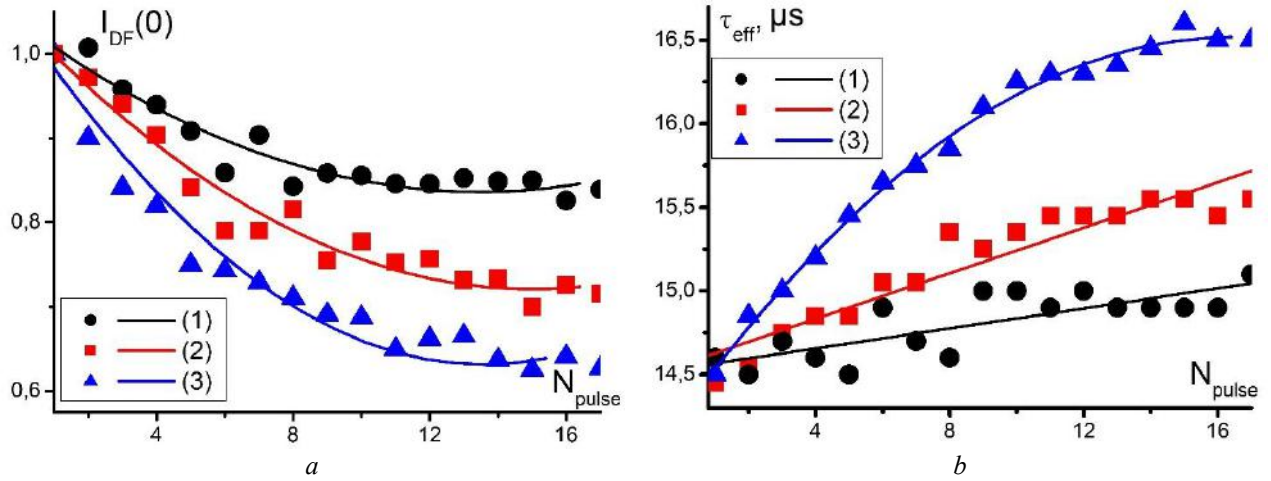

Fig.5. Intensity (a) and effective decay time (b) of the delayed fluorescence signal of erythrosine (C=5 mM) in a polyvinyl butyral film with different anthracene content (1) – 0.5, (2) – 2.5 and (3) – 5 mM depending on the number of pump pulses.

The obtained results allow us to estimate the proportion of oxygen molecules remaining in the system after the *k*-th pump pulse as

$$\frac{n_{Ox}(k)}{n_{Ox}(0)} \sim \frac{\tau_{eff}(0)}{\tau_{eff}(k)}.$$

Thus, in the film with the maximum anthracene content, about 3% of dissolved oxygen is bound under the action of the first pump pulse, and the maximum free oxygen deficit after 17 pulses is about 14%. These data allow us to determine the effective coefficient of oxygen diffusion into the film and the efficiency of oxygen binding by chemical traps. By analyzing the luminescence signals of samples placed in an oxygen-containing atmosphere and excited by a series of laser pulses, we can obtain information on the nature of the distribution of the oxidation product across the film thickness and estimate the value of the enrichment/depletion zone of the surface layers of the polymer film with the oxidized reagent.

4. Theoretical model

Considering the set of processes initiated by pulsed laser action in a polymer system containing immobile (bound to the matrix) photosensitizer molecules (Er - erythrosine) and oxygen molecule binding centers (chemical traps) (A - anthracene), they can be divided into separate groups according to characteristic times of occurrence. Thus, the duration of the process of interaction of sensitizer molecules with the optical pumping pulse and the formation of the resulting spatial distribution of T-centers $n_T(x)$ is tens of nanoseconds, the characteristic time of photoreactions involving O_2 molecules is tens of microseconds $t \sim \tau_T \sim \tau_\Delta$, and the diffusion influx of oxygen from the atmosphere unfolds on the scale of the T interval between adjacent laser pulses, i.e. on the order of tens to hundreds of milliseconds $t \sim T$.

Noting the short duration of the pump pulse compared to the characteristic time of photoreactions, we will omit a detailed analysis of the interaction of the light pulse with the dye molecules [16-17] here. Taking into account the high quantum yield of erythrosine in the triplet state and the incoherent saturation of absorption in the film, we will assume that the action of the pump pulse transfers all photosensitizer molecules from the ground energy state $S_0(Er)$ to a metastable one $T_1(Er)$.

In an oxygen-free environment, the decay of triplet states occurs according to an exponential law with its own lifetime τ_T. In an oxygen-permeable environment, the decisive role is played by the processes of quenching of excited triplet centers by oxygen molecules in the ground state

$$T_1(Er) + {}^3\Sigma_g^-(O_2) \rightarrow S_0(Er) + {}^1\Delta_g(O_2) \quad (1)$$

and subsequent cross-annihilation of excited oxygen molecules with triplet states of dye molecules, accompanied by the emission of a quantum of delayed fluorescence

$${}^1\Delta_g(O_2) + T_1(Er) \rightarrow {}^3\Sigma_g^-(O_2) + S_1(Er) \rightarrow S_0(Er) + h\nu_{DF}. \quad (2)$$

In the presence of anthracene molecules (chemical traps) in the system, singlet oxygen reacts with them in an oxidation reaction to form a stable compound – anthraquinone [19]

$$^1\Delta_g(O_2) + A \rightarrow AO_2, \quad (3)$$

which leads to a decrease in the overall concentration of oxygen molecules in the film.

First pulse. Upon completion of the action of the first initiating laser pulse, as a result of oxidation of molecules A by singlet oxygen $O_2(^1\Delta_g)$ on the time scale $t<<T$, a non-uniform distribution $n_{ox}(x)$ (x-profile) of oxygen molecules in the ground (unexcited) state will be formed.

Then, in the first-time interval T_0, up to the beginning of the action of the second pulse, as a result of the resulting gradient $n_{ox}(x)$, diffusion leakage of O_2 molecules from the atmosphere into the film begins. It occurs at times $\tau_T \sim \tau_\Delta \le t \le T_0$ and forms a new, resulting x-profile $n_{ox}(x,T)$ by the end of the time interval $T=T_0$.

To analyze the kinetics of large-scale time diffusion of oxygen inflow into a film of thickness L, a boundary value problem is set for the function $n(x,t)$ – the density of O_2 molecules in layer x

$$\frac{\partial n}{\partial t} = D\frac{\partial^2 n}{\partial x^2}, \quad 0 < x < L, \quad 0 < t < T_0 \quad (4)$$

$$n(0,t) = n_{ox}^{(0)}, \quad 0 < t < T_0$$
$$\left(\frac{\partial n}{\partial x}\right)_{x=L} = 0, \quad 0 < t < T_0 \quad (5)$$
$$n(x,0) = f_1(x) = n_{ox}^{(1)}(x), \quad 0 < x < L$$

The solution to the boundary value problem (4)-(5) upon completion of the first j=1 time stage $T=T_0 j$ takes the form

$$n^{(1)}(x,T) = n_{ox}^{(0)} + \sum_{k=0}^{\infty}\left\{a_k^{(1)} - \frac{4}{\pi}\frac{n_{ox}^{(0)}}{(2k+1)}\right\}\exp\left[-\frac{(2k+1)^2\pi^2}{4L^2}D\cdot T\right]\sin\left[\frac{(2k+1)\pi}{2L}x\right], \quad (6)$$

where

$$a_k^{(j)} = \frac{2}{L}\int_0^L f_j(x')\sin\left[\frac{(2k+1)\pi}{2L}x'\right]dx'. \quad (7)$$

At the moment $t_2=T_0$ of the beginning of the second pulse, oxygen is distributed non-uniformly in the film in accordance with expression (6), which now serves as the initial distribution of O_2 molecules in the layer x at the second time stage $j=2$, $T_0<t<2T_0$. For the function $n^{(2)}(x,t)$ of the density of O_2 molecules at this stage, formula (6) is still valid, but with the replacement $a_k^{(1)} \rightarrow a_k^{(2)}$, where $a_k^{(2)}$ is determined by formula (7), but with $f_2(x) = n^{(1)}(x,T)$, given by formula (6), and $T=2T$. Then this procedure can be continued an arbitrary number of times - depending on the size of the series of laser pulses initiating the system. After the pulse with number N, we obtain the function of the density of molecules $n^N(x, NT < t < (N+1)T)$, which will determine the kinetics of photo-processes in the film, including oxidation, as well as the pulse shape and the luminescence intensity of sensitizers – phosphorescence and cross-annihilation delayed fluorescence initiated by singlet oxygen.

Note that under conditions of a uniform initial distribution of oxidizable molecules in the film and insignificant Bouguer attenuation of the light beam, the kinetics of photo-processes after the first laser pulse and after the pulses following it will differ significantly. This is due to the fact that after the first pulse, the molecules of singlet oxygen uniformly distributed over the entire thickness of the film are bound. And after the second and subsequent pulses, previously formed non-uniform profiles $n_{ox}(x,T)$ already manifest themselves in the thickness of the film. Non-uniform concentration profile $n_T(x,T+t)$ is either formed initially or, like the profile $n_\Delta(x,T+t)$, after the first laser pulse.

Within the kinetic approach, which does not take into account the features of the microdiffusion of oxygen molecules in the polymer, we introduce the bimolecular rates of the following reactions: K_Σ – triplet

state quenching, K_Δ – cross-annihilation and K_A – anthracene oxidation, and the lifetimes of: τ_Δ – the excited singlet state of the oxygen molecule and τ_Δ – the triplet state of the photosensitizer molecule. We denote the average volume concentrations of triplet and trap centers by $n_T(t)$ and $n_A(t)$, and the concentrations of oxygen molecules in the ground and excited states by $n_\Sigma(t)$ and $n_\Delta(t)$, respectively.

Time j-stages after the first pulse. At each stage $j \cdot T_0 \le t \le (j+1)T_0$ after the end of the action of the next pulse, photo-processes unfold, the kinetics of which is determined by the following system of equations (8).

Assuming that the rate constants of quenching and cross-annihilation of T-states of the sensitizer are close in magnitude $K_\Sigma \approx K_\Delta = K$, we write the system of kinetic equations after the end of the action of the *j*-th laser pulse in the form *((j+1)T₀>t>jT₀)* [10-13]

$$\begin{cases} \dfrac{\partial n_T(x,t)}{\partial t} = -\left(\dfrac{1}{\tau_T} + K\left[n_\Sigma(x,t) + n_\Delta(x,t) \right] \right) n_T(x,t) \\ \dfrac{\partial n_\Sigma(x,t)}{\partial t} = -K\left[n_\Sigma(x,t) - n_\Delta(x,t) \right] n_T(x,t) + \dfrac{1}{\tau_\Delta} n_\Delta(x,t) \\ \dfrac{\partial n_\Delta(x,t)}{\partial t} = -\left(\dfrac{1}{\tau_\Delta} + K_A n_A(x,t) + K n_T(x,t) \right) n_\Delta(x,t) + K n_T(x,t) n_\Sigma(x,t) \\ \dfrac{\partial n_A(x,t)}{\partial t} = -K_A n_A(x,t) n_\Delta(x,t) \end{cases} \quad (8)$$

By integrating the last equation of the system, we obtain a quasi-stationary *x*-distribution of the oxidized A-reagent on the *j*-th time interval

$$n_A^{(j)}(x, j \cdot T_0 + 3\tau_T) = n_A^{(j)}(x, j \cdot T_0) \exp\left(-K_A \int_0^{3\tau_T} n_\Delta^{(j)}(x,t) dt \right) \quad (9)$$

The upper integration limit in (9) is chosen for convenience in the form $3\tau_T$, since upon its completion the population of the T-state of the sensitizer is practically empty, and the sensitization processes under consideration are completed. When implementing a specific computational procedure, the upper integration limit can tend to infinity. If the exponential expression is small enough $K_A \int_0^{3\tau_T} n_\Delta^{(j)}(x,t) dt << 1$, then the approximate equality holds $n_A^{(j)}(x, jT_0 + 3\tau_T) \approx n_A^{(j)}(x, jT_0) \left(1 - K_A \int_0^{3\tau_T} n_\Delta^{(j)}(x,t) dt \right)$, or $n_\Sigma(x, T+t) + n_\Delta(x, T+t) \approx n_{ox}^{(j)}(x,T) - n_A^{(j)}(x) K_A \int_0^\infty n_\Delta^{(j)}(x,t)\, dt$.

In the time interval $j \cdot T_0 \le t \le j \cdot T_0 + 3\tau_T$, provided that the number of oxidized molecules $n_A^{(j)}(x) K_A \int_0^\infty n_\Delta^{(j)}(x,t)\, dt$ during the time $j \cdot T_0 \le t \le j \cdot T_0 + 3\tau_T$ is sufficiently small, it can be assumed that the total concentration of O_2 molecules does not depend on the «fast» time.

$$n_\Sigma(x, T+t) + n_\Delta(x, T+t) = n_{ox}^{(j)}(x,T). \quad (10)$$

Then the solution to the system of equations

$$\begin{cases} \dfrac{\partial n_T(x,T+t)}{\partial t} = -\left(\dfrac{1}{\tau_T} + Kn_{ox}(x,T)\right) n_T(x,T+t) \\ \dfrac{\partial n_\Delta(x,T+t)}{\partial t} = -\left(\dfrac{1}{\tau_\Delta} + K_A n_A(x,T+t) + 2Kn_T(x,T+t)\right) n_\Delta(x,T+t) + \\ +Kn_T(x,T+t) n_{ox}(x,T) \end{cases} \tag{11}$$

at the *j*-th stage of laser activation, expressions for the concentrations of excited molecules in metastable states T- and $^1\Delta_g(O_2)$ can be written in the following form [10]

$$n_T^{(j)}(x, j\cdot T + t) = n_0^{(j)}(T)\exp\left\{-\frac{t}{\tau_T} - Kn_{ox}(x, j\cdot T_0)\cdot t\right\}, \tag{12}$$

$$n_\Delta^{(j)}(jT_0 + t \mid n_0^{(j)}, n_{ox}^{(j)}) = Kn_{ox}^{(j)}(x, j\cdot T_0)\times$$
$$\times \int_0^t n_T^{(j)}(x, jT_0 + \tau \mid n_0^{(j)}, n_{ox}^{(j)})\exp\left[\frac{\tau - t}{\tau_\Delta} - 2K\int_0^t n_T^{(j)}(x, jT_0 + \tau' \mid n_0^{(j)}, n_{ox}^{(j)})d\tau'\right]d\tau \,. \tag{13}$$

The intensities of the cross-annihilation delayed fluorescence $I_{DF}^{(N)}(t)$ and phosphorescence $I_{Ph}^{(N)}(t)$ signals of the sensitizer after a series of *N* laser pulses are determined by the following integrals over the thickness of the dye-containing film

$$I_{DF}^{(N)}(T+t) \sim K_\Delta \int_0^L n_T^{(N)}(x,T+t) n_\Delta^{(N)}(x,T+t)dx\,, \tag{14}$$

$$I_{Ph}^{(N)}(T+t) \sim \int_0^L n_T^{(N)}(x,T+t)dx\,. \tag{15}$$

Then, we can study the amplitude and shape of the pulse signals (14)-(15) from the number of laser pulses *N* in a series and compare the calculation results with the experiment. An important feature of the proposed model is that it considers the possible non-uniformity of the distribution of triplet and "trap" centers across the film thickness. Non-uniform distribution of reagents in the film can be obtained purposefully by layer-by-layer pouring of the film with solutions with the required ratio of anthracene and erythrosine. Then, in addition to the simplest case of uniform distribution, other characteristic variants of the x-distribution of reagents are of interest: a near-surface zone of the polymer layer enriched in trap or triplet centers and, accordingly, a case of a depleted near-surface zone. By analyzing the luminescence signals of samples placed in an oxygen-containing atmosphere and excited by a series of laser pulses, we can obtain information on the nature of the distribution of reagents across the film thickness and estimate the size of the enrichment/depletion zone.

Fig. 6 shows model calculations of the average volume concentrations of excited triplet centers, triplet and singlet oxygen and anthracene molecules by the first and 17-th pumping pulses. Fig. 6b shows a multiple decrease in oxygen concentrations compared to Fig. 6a, which leads to an increase in the effective lifetime of excited T-centers.

Calculations using the model show that the kinetics of photoreactions reacts weakly to the specific distribution of triplet and trap centers in the film. The diffusion of oxygen molecules in the film at the end of the next pumping pulse, on the contrary, reflects well the initial distribution of the reagents. Moreover, the enrichment of some characteristic region of the film with trapping centers or photosensitizer leads to similar results for the picture of the diffusion influx of oxygen (Fig. 7).

This is explained by the fact that it is in the enrichment region (no matter with anthracene or photosensitizer) that the oxygen binding reactions proceed most intensively and form a region with a deficiency of O_2, which is then filled by diffusion. The kinetics of luminescent signals, depending on the number of pumping pulses, also changes with a change in the nature of the distribution of reagents in the film (Fig. 8).

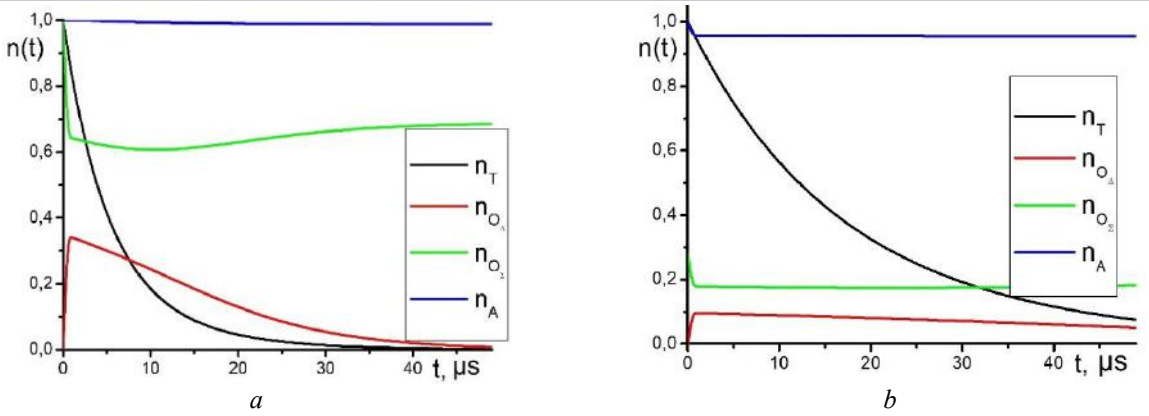

a *b*

Fig.6. Kinetics of reagent concentrations in the film upon activation by the first (a) and 17-th (b) pump pulses (uniform initial distribution of reagents).

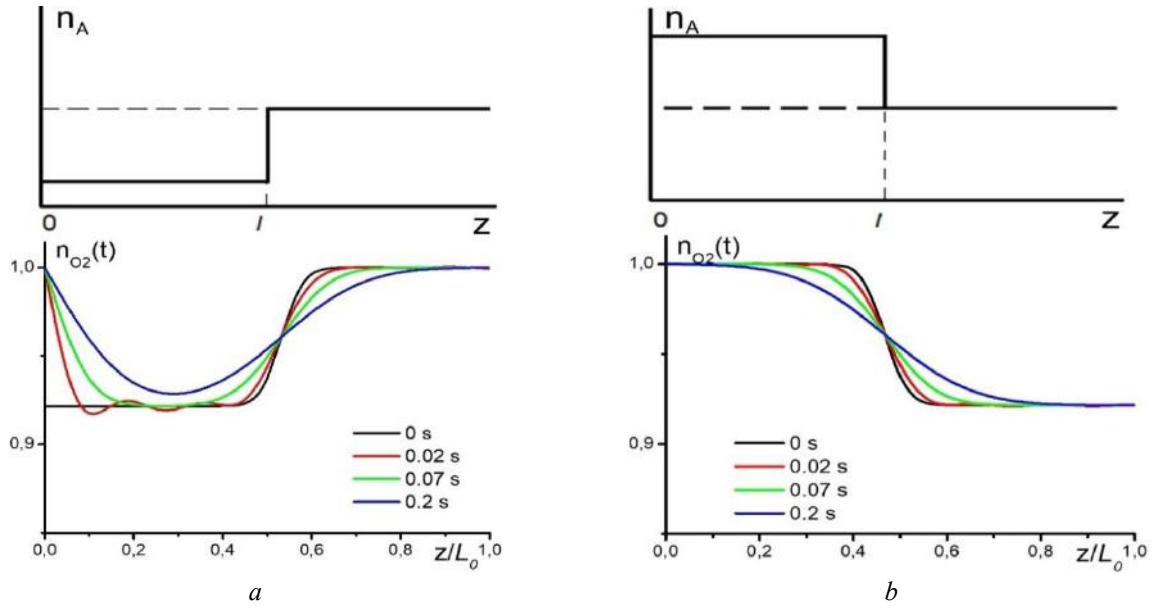

a *b*

Fig.7. Approximation of the non-uniform distribution of sensitizer molecules by piecewise constant functions. Below: diffusion kinetics of oxygen molecules into the film after the first pump pulse is completed with enrichment of the surface layers of the film (a) and deep layers (b) by trapping centers.

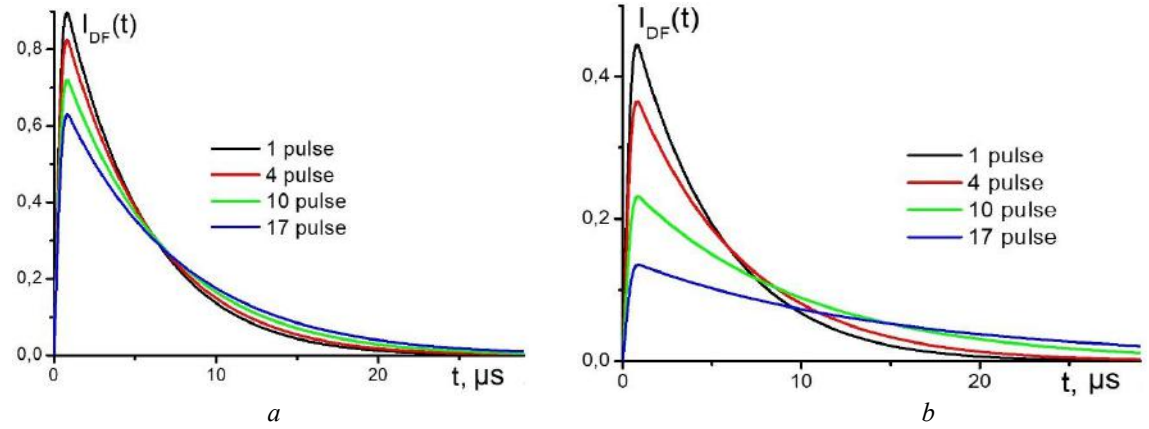

a *b*

Fig.8. Calculated pulse signal of delayed fluorescence of dye in the film depending on the total number of pump pulses during enrichment of capture centers of the surface layers of the film (a) and deep layers (b).

Considering the maximum intensity (Fig. 9a) and the effective decay time (Fig. 9b) as the parameters of the change in the delayed fluorescence signals, it can be noted that with enrichment of the surface layer with T-centers or deep layers with A-centers (curves 2 and 5), the amplitude of the effect is minimal (the luminescence signal changes slightly with an increase in the number of pulses).

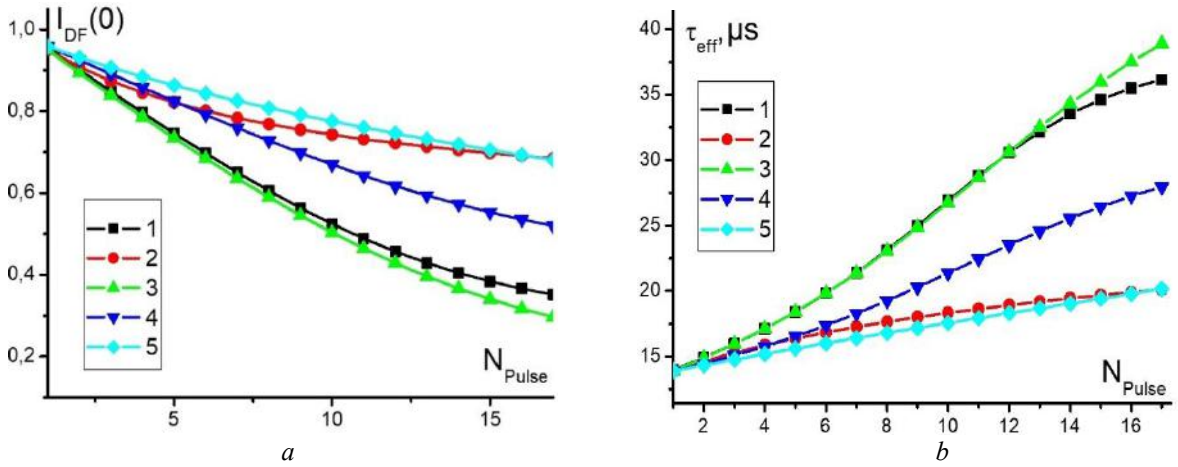

Fig.9. Intensity amplitude (a) and effective decay time (b) of the pulsed signal of delayed fluorescence of the dye in the film depending on the total number of pump pulses. (1) – uniform distribution of T- and A-centers; (2) – surface region of the film enriched in T-centers; (3) – deep region of the film enriched in T-centers; (4) – surface region of the film enriched in A-centers; (5) – deep region of the film enriched in A-centers.

The maximum change in the luminescence signals is observed with a deep distribution of T-centers. By varying the nature of the distribution of reagents over the film thickness as a model parameter, it is possible to obtain good agreement between the calculated and experimental dependences for the delayed fluorescence signals. In our case, this was achieved under the assumption of enrichment of the surface region of the film with capture centers by 35-45% of its thickness with a concentration ratio of the enriched and unenriched regions of 3:1.

4. Conclusion

The kinetics of oxidative photoreactions in a polymer film was studied with multiple pulse activation of the system considering the layer-by-layer diffusion replenishment of the concentration of oxygen consumed from the atmosphere.

To study the diffusion and reaction properties of O_2 molecules in an oxygen-permeable polyvinyl butyral film, it was proposed to use anthracene molecules, which act as "trap" centers for singlet oxygen $^1\Delta_g(O_2)$. Activation of O2 molecules in the $^1\Delta_g$-state was carried out in a sensitized manner from photoexcited erythrosine molecules accumulated in the long-lived triplet (T) state. At the same time, the photosensitizer also acted as a luminescent probe, the delayed fluorescence signal of which was used to estimate the oxygen concentration in the system at the moment of arrival of the next laser pulse.

It has been shown experimentally that an increase in the concentration of anthracene molecules in the polymer leads to a decrease in the maximum of the delayed fluorescence signal and an increase in the effective decay time of the luminescence signal with an increase in the number of pump pulses, which indicates a decrease in the local oxygen concentration in the film.

A mathematical model is proposed that describes the kinetics of oxygen-dependent photoreactions in the film and the formation of luminescent response signals during its multi-pulse laser activation, taking into account the diffusion replenishment of oxygen in the intervals between activating pulses. Based on a comparison of experimental luminescence signals and calculated curves, the nature of the placement of reagents across the film thickness is analyzed and the sizes of the enrichment/depletion region of the near-surface layers of the polymer film with the oxidizable reagent are estimated.

Conflict of interest statement

The authors declare that they have no conflict of interest in relation to this research, whether financial, personal, authorship or otherwise, that could affect the research and its results presented in this paper.

CRediT author statement

Kucherenko, M.G.: Conceptualization, Methodology, Validation, Writing - review and editing. **Rusinov, A.P.:** Software, Investigation, Visualization, Writing- original draft. All authors discussed the results and contributed to the manuscript. The final manuscript was read and approved by all authors.

Funding

The work was performed as part of the state assignment of the Ministry of Science and Higher Education of the Russian Federation within the framework of scientific project No. FSGU-2023-0003.

References

1 Bartz R.R., Piantadosi C.A. (2010) Clinical review: Oxygen as a signaling molecule. *Crit. Care,* 14, 234. https://doi.org/10.1186/cc9185

2 Babcock G., Wikström M. (1992) Oxygen activation and the conservation of energy in cell respiration. *Nature,* 356, 301–309. https://doi.org/10.1038/356301a0

3 Acker H. (1983) *Tissue Oxygen Transport in Health and Disease*. In: Pallot, D.J. (eds) Control of Respiration. Springer, Boston, MA. https://doi.org/10.1007/978-1-4684-1487-5_5

4 Pittman R.N. (2011) Regulation of tissue oxygenation. *Colloquium Series on Integrated Systems Physiology*, 3, 1- 81. https://doi.org/10.4199/C00029ED1V01Y201103ISP017

5 Habler O.P., Messmer K.F. (1997) The physiology of oxygen transport. *Transfus Sci.* 18(3), 425-435. https://doi.org/10.1016/S0955-3886(97)00041-6

6 Babcock G. (1999) How oxygen is activated and reduced in respiration. *Proc. Nat. Acad. Sci. USA*, 12971–12973. https://doi.org/10.1073/pnas.96.23.12971

7 Filatov M.A., Heinrich E., Busko D. Ilieva I.Z., Landfester K., Baluschev S. (2015) Reversible oxygen addition on a triplet sensitizer molecule: protection from excited state depopulation. *Phys. Chem. Chem. Phys.,* 17, 6501–6510. https://doi.org/10.1039/c4cp05025h

8 Montero-Baker M.F., Au-Yeung K.Y., Wisniewski N.A., Gamsey S., Morelli-Alvarez L., Mills Sr J.L., Campos M., Helton K.L. (2015) The First-in-Man "Si Se Puede" study for the use of micro-oxygen sensors (MOXYs) to determine dynamic relative oxygen indices in the feet of patients with limb-threatening ischemia during endovascular therapy. *J Vasc Surg.,* 61, 1501-1509. https://doi.org/10.1016/j.jvs.2014.12.060

9 Chien J.S., Mohammed M., Eldik H., Ibrahim M.M., Martinez J., Scott P.N., Wisniewski N., Klitzman B. (2017) Injectable Phosphorescence-based Oxygen Biosensors Identify Post Ischemic Reactive Hyperoxia. *Scientific reports,* 7, 8255. https://doi.org/10.1038/s41598-017-08490-0

10 Yang Y., Ronson T., Hou D., Zheng J., Jahović I., Luo K., Nitschke J.R. (2023) Hetero-Diels-Alder Reaction between Singlet Oxygen and Anthracene Drives Integrative Cage Self-Sorting *ChemRxiv.* https://doi.org/10.26434/chemrxiv-2023-st339

11 Krasnovsky A.A. (2004) Photodynamic activity and singlet oxygen. *Biofizika*, 49(2), 305-321. Available at: https://www.researchgate.net/publication/8575395

12 Briviba K., Klorz l-O. Sics H. (1997) Toxic and signaling effects of photochemically or chemically generated singlet oxygen in biological systems. *Bio. Chem.,* 378, 1259-1265. Available at: https://www.scirp.org/reference/referencespapers?referenceid=723051

13 Uzdensky A.B. (2010) *Cellular and molecular mechanisms of photodynamic therapy*, St. Petersburg: Nauka, 326. Available at: https://ozon.kz/product/kletochno-molekulyarnye-mehanizmy-fotodinamicheskoy-terapii-uzdenskiy-anatoliy-borisovich-1362599002 [in Russian]

14 Krasnovsky A.A. (1999) Photosensitized phosphorescence of singlet molecular oxygen: measurement methods and application to analysis of photodestructive processes in cells. *Uspekhi Biologicheskoy Khimii*, 39, 255-288. Available at: https://www.researchgate.net/publication/280976073 [in Russian]

15 Letuta S.N., Pashkevich S.N., Alidzhanov E.K., Lantukh Yu.D., Razdobreev D.A., Chakak A.A., Ishemgulov A.T. (2019) Monitoring of Changes in Oxygen Concentration in Tissues by the Kinetics of Delayed Fluorescence of Exogenous Dyes. *Optics and spectroscopy,* 127, 1169 – 1176. https://doi.org/10.1134/S0030400X19120129

16 Liu W., Zhang H.I., Liu K.P., Zhang S.D., Duan Y.X. (2013) Laser-induced fluorescence: Progress and prospective for in vivo cancer diagnosis. *II Chinese Science Bulletin*, 58, 2003 – 2016. https://doi.org/10.1007/sll434-013-5826-y

17 Roussakis E., Li Z., Nichols A.J., Evans C.L. (2015) Bright, "Clickable" Porphyrins for the Visualization of Oxygenation under Ambient Light. *II Angew. Chem.Int.Edit,* 54, 8340 – 8362. https://doi.org/10.1002/anic.201506847

18 Grether-Beck S.; Buettner R.; Krutman J. (1997) Ultraviolet A radiation-induced expression of human genes: molecular and photobiological mechanism, *Bio. Chem.,* 378, 1231-1236. PMID: 9426182

19 Rusinov A.P., Kucherenko M.G. (2006) Kinetics of photochemical recording of stationary gratings in oxygen-permeable polymers with triplet sensitization. *Bulletin of the Russian Academy of Sciences. Physical Series*, 70, 1262–1266. Available at: https://www.researchgate.net/publication/290035289

20 Kucherenko M.G. (1997) Kinetics of nonlinear photo-processes in condensed molecular systems. Orenburg: OSU, 386. Available at: https://scholar.google.ru/citations?user=-N16cjEAAAAJ&hl=ru [in Russian]

21 Kucherenko M.G., Ketzle G.A. (1999) Suppression of Singlet Oxygen Generation by a Powerful Laser Pulse. *Bulletin of the Russian Academy of Sciences. Physical Series*, 63, 1149 – 1154. Available at: https://www.researchgate.net/publication/290027656

22 Kucherenko M.G. (2001) On the Kinetics of the Reaction of Singlet Oxygen with Immobile Sensitizers. *Chemical Physics*, 20, 31-36. Available at: https://www.researchgate.net/publication/295126232

23 Kucherenko M.G., Chmereva T.M. (2010) *Processes with Participation of Electronically Excited Molecules on the Surfaces of Solid Adsorbents*. Orenburg: Orenburg State University, 346. Available at: www.osu.ru/doc/1041/kaf/820/prep/196 [in Russian]

AUTHORS' INFORMATION

Kucherenko, Michael Gennadievich – Doctor of Physical and Mathematical Sciences, Professor, Director of the Center for Laser and Information Biophysics, Professor of the Department of Radiophysics and Electronics, Orenburg State University, Orenburg, Russia; SCOPUS Author ID: 7003581468, https://orcid.org/0000-0001-8821-2427; clibph@yandex.ru

Rusinov, Alexander Petrovich – Candidate of Physical and Mathematical Sciences, Associate Professor, Head of the Department of Radiophysics and Electronics, Senior Researcher of the Center for Laser and Information Biophysics, Orenburg State University, Orenburg, Russia; SCOPUS Author ID: 6603807908, https://orcid.org/0000-0001-6735-8216; sano232@mail.ru

EURASIAN PHYSICAL TECHNICAL JOURNAL

2025, Volume 22, No.2 (52)

https://doi.org/10.31489/2025N2/25-32

Received: 30/11/2024 Revised: 27/03/2025 Accepted: 12/05/2025 Published online: 30/06/2025

Research Article

UDC 535.37

PROPERTIES OF Ag/TiO_2 AND Ag/SiO_2 NANOPARTICLES AND THEIR EFFECT ON THE PHOTOCATALYTIC PROPERTIES OF A SEMICONDUCTOR NANOCOMPOSITE

Sharapov I., Omarova G., Sadykova A., Seliverstova E.*

Institute of Molecular Nanophotonics, Karaganda Buketov University, Karaganda, Kazakhstan

*Corresponding author: genia_sv@mail.ru

Abstract. *The optical properties and the electric field distribution around silver nanoparticles coated with TiO_2 or SiO_2 shell have been studied. It is demonstrated that the presence of a shell around a plasmonic nanoparticle leads to a bathochromic shift in the maximum of its absorption band. The maximum electric field intensity around metal nanoparticles is radially concentrated, predominantly near the surface of the nanoparticles. The quantum efficiency, representing the ratio of emitted photons to absorbed photons, is nearly 50% higher for Ag/TiO_2 nanoparticles compared to Ag/SiO_2. In the presence of Ag/TiO_2 and Ag/SiO_2 core/shell nanoparticles the photocatalytic activity of the TiO_2/rGO nanocomposite increases by 2.7 and 1.7 times, respectively. These changes are associated with improved charge transport properties of TiO_2/rGO and possible hot electron injection from the nanoparticles into the semiconductor.*

Keywords: plasmon, nanoparticles, optical properties, photocatalysis, nanocomposite.

1. Introduction

Localized surface plasmon resonance (LSPR) refers to the collective oscillation of conduction electrons in metallic nanoparticles (NPs) under the influence of external electromagnetic excitation [1]. This phenomenon has attracted significant attention from researchers due to its unique properties. For instance, the capability of plasmon NPs to efficiently absorb and scatter light in a various spectral ranges makes them highly promising for a wide variety of applications, including photocatalysis [2], optical devices [3], and solar energy [4]. Of particular interest for practical applications are core/shell nanostructures, where a metallic core, such as Ag or Au NPs, is surrounded by a dielectric or semiconductor shell. These structures exhibit several advantages over the monocomponent NPs. Specifically, the shell provides stability of the metallic core against external influences, enables control over local electromagnetic fields near the NPs, and modifies its interaction with incident radiation. Additionally, the shell can create conditions for efficient electron transfer [5] that is essential for photovoltaic processes, and optimize the spatial configuration between plasmon NPs and interacting particles.

The influence of core/shell nanostructures on photovoltaic processes has been extensively studied in Ref. [6]. It has been shown that the presence of such NPs enhances the efficiency of dye-sensitized solar cells (DSSC) by 20%. Spectral-luminescent measurements revealed that while the optical density of the dye remained nearly unchanged, the fluorescence intensity increased twofold upon the addition of Ag NPs. The enhancement in DSSC efficiency is attributed to the LSPR effect of Ag NPs, which modifies the absorption

properties of the dye molecules. $Au/SiO_2/TiO_2$ particles have been used to increase the light absorption coefficient in solar cells. It has been demonstrated that the dielectric shell stabilizes the metallic core and prevents charge carriers' recombination that results in generation of more photons and growth of overall device performance [7, 8].

Core/shell NPs were also widely applied in photocatalysis. The authors of Ref. [9] synthesized Au NPs of various sizes and integrated them into core/shell structures with TiO_2 or SiO_2 shells. During the degradation of salicylic acid under visible light irradiation, samples containing Au NPs exhibited significantly higher catalytic activity compared to neat TiO_2. Notably, the highest activity was observed for Au NPs with a diameter of 3 nm, while for core/shell structures with SiO_2 shells, the best photocatalytic performance was achieved with 17 nm Au particles. In the first case, effective charge separation and the sensitization effect due to LSPR played a dominant role in enhancement of catalytic activity. In the second case, the dielectric shell of SiO_2 hindered charge carrier separation and the injection of hot electrons, suggesting that the observed increase in catalytic activity was primarily due to the local enhancement of the electric field around the Au NPs.

Additionally, Pt/CeO_2 and Ni/TiO_2 NPs have demonstrated high activity and stability in methane reforming and CO_2 conversion processes. The plasmon effect in such systems minimizes catalyst deactivation at high temperatures, which is particularly crucial for industrial applications. Moreover, the adjustable shell structure enables selective reaction control, making these materials promising candidates for sustainable chemistry [10, 11]. The authors of [12] also investigated the effect of Au NPs' size on the photocatalytic degradation of Methylene blue dye. Detailed microstructural studies concluded that the enhancement of photodegradation is predominantly driven by electron transfer mechanisms and the interface structure. This suggests that the photocatalytic efficiency is primarily influenced by the quantity and transport of charge carriers at the semiconductor/metal interface. However, unresolved questions remain regarding to the plasmon effect on the charge transfer processes.

This study presents theoretical and experimental investigations of the optical properties of core/shell NPs and their effect on the photocatalytic properties of TiO_2/rGO nanocomposite. Structures consisting of Ag NPs as cores and TiO_2 or SiO_2 as shells were selected. It was assumed that changes of the material of shell from a semiconductor to a dielectric could reveal whether the hot electrons of Ag NPs contribute to the enhancement of photocatalytic activity in TiO_2/rGO nanocomposites.

2. Materials and methods

The synthesis of Ag/TiO_2 NPs was performed according to method described in Ref. [13]. All reagents were of analytical grade and purchased from Sigma Aldrich. Silver NPs were prepared as cores by dissolving of 0.5 g of polyvinylpyrrolidone in 25 mL of ethylene glycol with the addition of 0.1 mmol of silver nitrate. The Ag NPs were separated from the ethylene glycol by centrifugation and washed twice sequentially with acetone and ethanol. Subsequently, 1 mL of TIPT ($Ti(OCH(CH_3)_2)_4$) was added to the ethanol solution of Ag NPs. According to dynamic light scattering data (Nanosizer S90, Malvern), the average size of silver NPs was 24±4 nm, while the size of core/shell structures was 44±8 nm (Fig. 1).

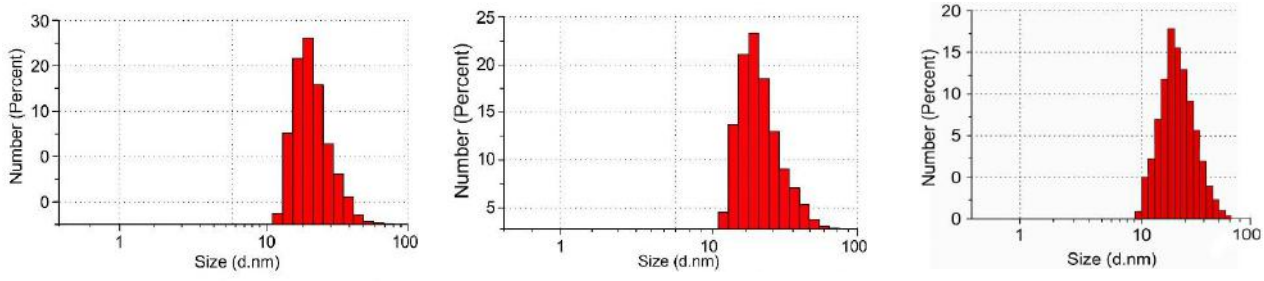

Fig.1. Size distribution of Ag NPs and core/shell NPs.

The synthesis of Ag/SiO_2 NPs followed to the procedure described in Ref. [14]. Tetraethyl orthosilicate (TEOS) was used as the SiO_2 precursor. The synthesized particles had cores with an average diameter of 24±4 nm, while the core/shell structures had an average diameter of 45±10 nm. The resulting solutions of core/shell NPs were incorporated into a TiO_2/rGO nanocomposite paste and mixed with a magnetic stirrer for

24 hours. The core/shell NPs concentration in the TiO_2/rGO nanocomposite was equal to 1 wt% according to the previous study [6]. For this concentration the greatest enhancement of photovoltaic parameters of the studied cells was recorded.

The TiO_2/rGO nanocomposite was synthesized via a hydrothermal method as described in Ref. [15, 16]. In particular, 40 mg of reduced graphene oxide (rGO) was sonicated in 160 mL of a water-ethanol mixture (1:3) for 1 hour. Subsequently, 400 mg of TiO_2 was added and the suspension was stirred for 2 hours. The light-gray suspension was autoclaved at 120°C for 24 hours, followed by cooling to room temperature. The TiO_2/rGO precipitate was centrifugated at 6000 rpm and washed with deionized water and ethanol. The obtained precipitate was dried at 60°C to produce a powder. To deposit TiO_2/rGO onto solid substrates, pastes were prepared from the resulting powder. For this, 300 mg of TiO_2/rGO powder was mixed with 2 mL of ethanol and mixed for 12 hours. The paste was spin-coated onto FTO substrates at 3000 rpm. The prepared TiO_2/rGO films, both with and without core/shell NPs, were annealed in an Ar atmosphere for 2 hours at 450°C.

The absorption spectra of the prepared samples were measured using a Cary-300 spectrophotometer (Agilent). The photocatalytic activity of the samples was evaluated by measuring the photoinduced current over 1 cm^2 of an illuminated area in a standard three-electrode cell with a potentiostat/galvanostat CS350 with an integrated EIS analyzer (CorrtestInstr.) according to the methodology described in [15]. Measurements were conducted in a 0.1 M NaOH electrolyte solution. A 300 W/cm^2 xenon lamp (Newport) was used as the light source. Impedance spectra were measured in steady-state mode. The amplitude of the applied signal was 15 mV and the frequency range was varied from 1 MHz to 100 mHz. To analyze the experimental curves and evaluate the electrotransport properties of the films, a simplified equivalent electrical circuit of the electrochemical cell was used (Fig. 2), which is a special case of the circuit from the Ref. [17].

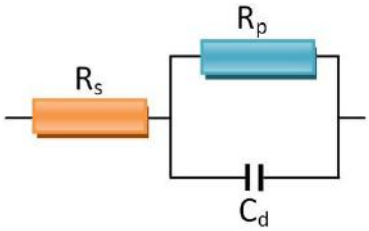

Fig. 2. Equivalent electrical circuit.

The optical properties of core/shell NPs were simulated using the finite-difference time-domain (FDTD) method, based on the Yee algorithm for solving Maxwell's equations. This algorithm involved discretizing of the computational domain into a rectangular grid, where electric fields were located along the grid boundaries, and magnetic fields were directed toward the cell centers.

The simulation domain was employed with Cartesian coordinate system with perfectly matched layer (PML) boundary conditions. To ensure maximum accuracy, a grid with an index of 8 and a step size of 0.5 nm was used. Grid refinement was achieved using the conformal0 method. Simulation parameters were set to 1000 femtoseconds and 300 K. Spherical Ag NPs with SiO_2 and TiO_2 shells were placed within the simulation domain. The radius of the Ag core was 13 nm, and the shell thickness was 5 nm. Material data for silver were sourced from [18], for SiO_2 from [13], and for TiO_2 from [19] and the open database refractiveindex.info. A total-field scattered-field (TF-SF) source was used as the radiation source. For NPs in a homogeneous medium, the incident radiation from the source represented a p-polarized plane wave propagating along the z-axis, with a wavelength range of 300–800 nm was used.

3. Results and discussion

The synthesized Ag/TiO_2 nanoparticles exhibited a spherical shape, as it was confirmed by SEM image (Mira 3LMU, Tescan). The absorption spectra of Ag and Ag/TiO_2 NPs revealed that before the shell synthesis, the absorption band of Ag NPs had a maximum at approximately 405 nm (Fig. 3). After coating with the TiO_2 shell, a bathochromic shift in the spectrum was observed. Additionally, from the short-wavelength region of the spectrum exhibits an absorption corresponding to the TiO_2, with the absorption edge located around ~380 nm. Similar data were obtained for Ag/SiO_2 NPs. The calculated optical properties and electric field intensity distributions around the studied NPs (Fig. 4) showed that the maximum of

calculated absorption band of Ag NPs exhibits at 380 nm. As experiments have shown, coating of the metal NPs with a shell caused a bathochromic shift in the absorption spectra. For Ag/SiO_2 NPs, the absorption maximum appeared at 390 nm, while for Ag/TiO_2, it shifted to 410 nm. The calculated absorption band positions correlated well with experimental data.

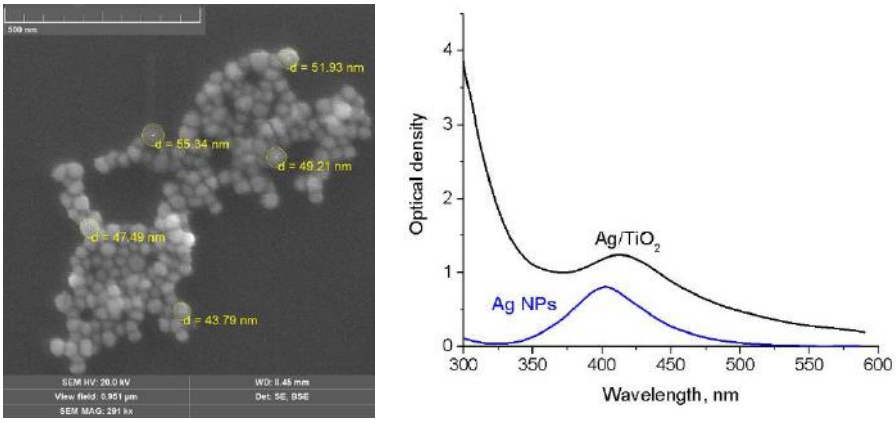

Fig. 3. SEM images of Ag/TiO_2 NPs (a) and (b) the absorption spectra of Ag and Ag/TiO_2 NPs.

The bathochromic shift in the calculated absorption spectra of NPs with the shell, relative to their absorption spectra in ethanol, can be attributed to the dependence of absorption plasmon NPs on the properties of the surrounding environment. According to Mie theory [1] the polarizability (α) of the metallic NPs is defined by the Clausius-Mossotti relation [20]:

$$\alpha = 4\varepsilon_0 \pi R^3 \frac{\varepsilon - \varepsilon_m}{\varepsilon + 2\varepsilon_m} \quad (1)$$

where ε is the permittivity of vacuum, ε_m is the dielectric constant of surrounding medium, ε is the dielectric function of the metall NP and R is the radius of spherical NP.

The intensity of absorption of light by the NPs (δ_{abs}) is proportional to the imaginary part of the polarizability [1]:

$$\delta_{abs}(\omega) \sim \mathrm{Im}[\alpha(\omega)] \quad (2)$$

I.e., the absorption maximum of NPs corresponds to the frequency at which the imaginary part of polarizability is maximal. Hence, it is seen that the optical properties of plasmon NPs are determined by both the properties of the environment and its individual properties. The quantum efficiency, defined as the ratio of emitted photons to absorbed photons, was also calculated (Fig. 4b).

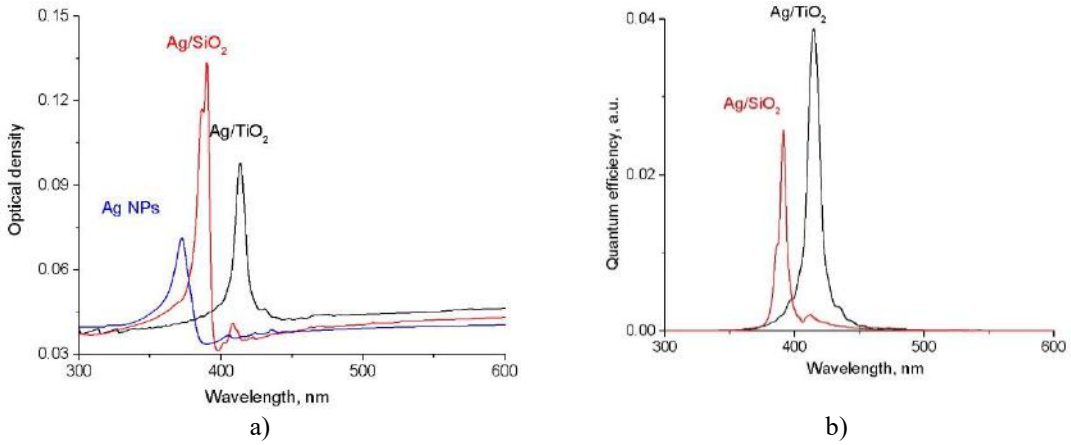

Fig. 4. Calculated absorption (a) and quantum efficiency (b) spectra of Ag and core/shell NPs.

The results showed that the quantum efficiency of Ag/TiO_2 NPs was approximately on 50% higher than that of Ag/SiO_2 NPs. This difference may be attributed to the fact that a greater number of free electrons are transferred from Ag NP to the semiconductor environment upon light irradiation compared to the SiO_2 layer. This hypothesis is supported by the 2D electric field intensity distribution patterns (Fig. 5).

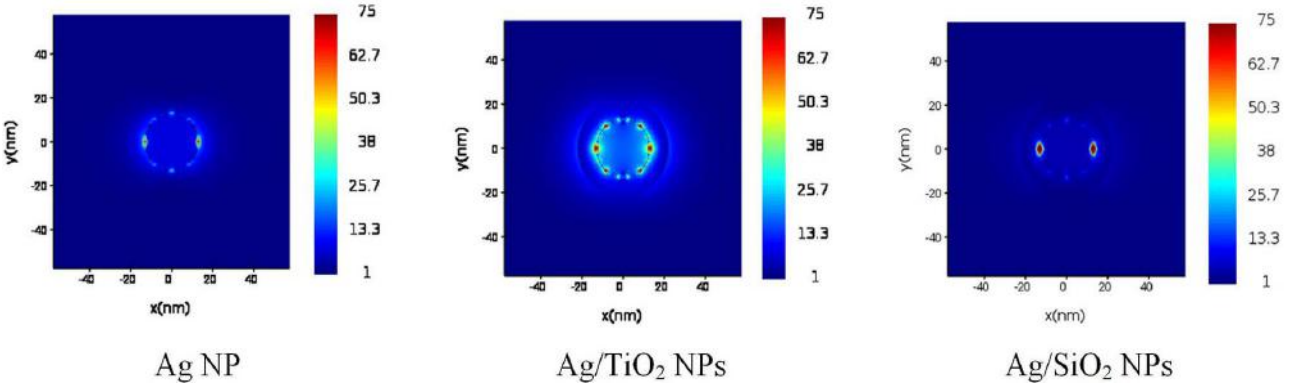

Fig. 5. 2D electric field intensity (in V/m) distributions around Ag and core/shell NPs.

The data revealed that the maximum electric field intensity is radially concentrated, predominantly near the surface of NPs along the OX direction. The magnitude of the field strength around the NP is varied from 1 to 75 V/m. For Ag/TiO_2 NPs, the electric field was more pronounced and uniformly distributed across the entire plasmon surface of NPs, unlike of Ag/SiO_2 NP.

Photocurrent measurements of the TiO_2/rGO nanocomposite with plasmon NPs confirmed the observed differences in optical properties and electric field distributions. The photocurrent density (Fig. 6) increased upon the addition of core/shell NPs to the TiO_2/rGO nanocomposite. For the pure TiO_2/rGO film, the current density was I=0.17 mA/cm^2, while it increased to I=0.45 mA/cm^2 for samples with Ag/TiO_2 NPs. In the case of Ag/SiO_2 NPs, the maximum photocurrent enhancement (1.7 times) was lower than that for Ag/TiO_2 (2.7 times). The photocurrent profile can be explained as follows: upon light irradiation, rapid photoinduced separation of electron-hole pairs occurs, resulting in a spike in the photocurrent curve. This is clearly visible for samples with core/shell NPs. This spike then diminishes as charge carriers migrate to the film surface. The subsequent decrease in photocurrent indicates that charge carriers recombination occurs within the film. The constant photocurrent level is achieved when the rates of charge carrier generation and recombination are balanced. During subsequent irradiation cycles the photocurrent increases with time and reaches saturation in the TiO_2/rGO samples. This shape of the curve could be resulted by the slow charge transport as well as the presence of traps in the TiO_2 and rGO, which leads to the gradual accumulation of charge carriers until the dynamic equilibrium was established [16]. The previously described behavior of the photocurrent curve was observed for nanocomposite samples with core/shell NPs. This may be due to the plasmon effect of silver NPs, which contributes to a more efficient separation of charge carriers and the enhanced local electromagnetic field and generation of hot electrons [15]. In all cases, a long-term relaxation of the amplitude of photocurrent pulses is observed, which indicates the presence of slow processes of accumulation of residual charges in the TiO_2/rGO structure between illumination cycles.

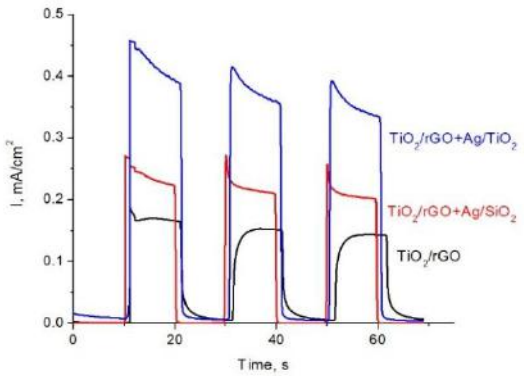

Fig. 6. Photocurrent profiles of the TiO_2/rGO nanocomposite with core/shell NPs.

The observed changes in the photocurrent value may be associated with an improvement in their charge-transport properties, data on which were obtained using impedance spectroscopy (Table 1). The electrophysical parameters were assessed using the methodology of Refs. [15,21], where τ_{eff} is the effective lifetime of an electron in a nanocomposite material; R_s characterizes the equivalent resistance of the film from the entire volume of the nanocomposite and the intercontact resistance between the layers. R_p corresponds to the resistance of charge carrier transfer at the interface between the layer under study and the electrode.

Table 1. Electrophysical parameters of TiO_2/rGO nanocomposite with Ag/TiO_2 and Ag/SiO_2 NPs

Sample	R_s, Ohm	R_p, Ohm	τ_{eff}, s
TiO_2	37.20	969.22	0.0078
TiO_2+ Ag/TiO_2	17.81	118.65	0.0051
TiO_2+ Ag/SiO_2	20.28	131.71	0.0033

The data indicate that nearly all parameters related to the resistance of nanocomposite films decrease in the presence of core/shell NPs. A significant reduction in recombination resistance (R_p) is observed for f Ag/TiO_2 NPs. Moreover, the shortest effective electron transit time was recorded. These results indicate that the addition of core/shell NPs effectively reduces the electron lifetime in the semiconductor, which enhances charge generation and separation, prevents recombination, and facilitates rapid electron migration and extraction from the semiconductor surface, enabling them to participate in photocatalytic reactions.

4. Conclusion

The results of this study demonstrate that the presence of Ag/TiO_2 and Ag/SiO_2 core/shell NPs enhances the photocatalytic activity of the TiO_2/rGO nanocomposite by 2.7 and 1.7 times, respectively. These changes can be attributed to improved charge transport properties in TiO_2/rGO and the potential injection of hot electrons from the metal NPs into the semiconductor. This process is notably hindered when a dielectric SiO_2 shell surrounds the Ag NPs.

The results of the studies show that the presence of Ag/TiO_2 and Ag/SiO_2 NPs enhances the photocatalytic activity of TiO_2/rGO nanocomposite by 2.7 and 1.7 times, respectively. The introduction of metal NPs into the composite increases the generation of charge carriers and promotes its separation, preventing their recombination, allowing them to participate in photochemical reactions. The possibility of injection of hot electrons from plasmon NPs as well as resonant energy transfer or charge tunneling from plasmon NPs also have to be taken into account. However, the latter processes are unlikely or significantly limited in this system. A more detailed study of the mechanism of the plasmon influence of metal NPs will be carried out by us in further studies.

The calculated with the FDTD method absorption spectra and electric field intensities revealed that the maximum absorption band of Ag NPs exhibits at 380 nm. Coating of the metal NPs with a shell induced a bathochromic shift in the absorption spectra, with the maximum absorption band at ~390 nm for Ag/SiO_2 and at 410 nm for Ag/TiO_2. These calculated results correlated well with experimental data. The maximum electric field intensity around plasmon NPs is radially concentrated, predominantly near the surface. For Ag/TiO_2, the electric field was more pronounced and distributed across the entire surface of the NPs. The quantum efficiency, defined as the ratio of emitted photons to absorbed photons, was approximately 50% higher for Ag/TiO_2 than for Ag/SiO_2 NPs. The findings of this study can be used to materials with enhanced photocatalytic and optoelectronic properties for applications in photoelectrochemical cells, hydrogen generation, organic compound photodegradation, and related areas.

Conflict of interest statement

The authors declare that they have no conflict of interest in relation to this research, whether financial, personal, authorship or otherwise, that could affect the research and its results presented in this paper.

CRediT author statement

Sharapov I.: software, calculations, writing – original draft; **Omarova G**.: visualization, validation; **Sadykova A**.: investigation, formal analysis; **Seliverstova E**.: conceptualization, methodology, resources, writing – review and editing. The final manuscript was read and approved by all authors

Funding

This work was supported by the Science Committee of the Ministry of Science and Higher Education of the Republic of Kazakhstan [Grant No. AP19680241].

References

1 Mayer K.M., Hafner J.H. (2011) Localized surface plasmon resonance sensors. *Chemical Reviews*, *111*, 3828–3857. https://doi.org/10.1021/cr100313v

2 Lin K.-T., Lin H., Jia B. (2020) Plasmonic nanostructures in photodetection, energy conversion and beyond. *Nanophotonics*, *9*(10), 3135–3163. https://doi.org/10.1515/nanoph-2020-0104

3 Barbillon G. (2019). Plasmonics and its applications. *Materials*, *12*(9), 1502. https://doi.org/10.3390/ma12091502

4 Ai B., Fan Z., Wong Z.J. (2022). Plasmonic–perovskite solar cells, light emitters, and sensors. *Microsystems Nanoengineering*, *8*, 5. https://doi.org/10.1038/s41378-021-00334-2

5 Kasani S., Curtin K., Wu N. (2019). A review of 2D and 3D plasmonic nanostructure array patterns: Fabrication, light management and sensing applications. *Nanophotonics*, *8*(12), 2065–2089. https://doi.org/10.1515/nanoph-2019-0158

6 Ibrayev N., Seliverstova E., Omarova G. (2020) The influence of plasmons of Ag nanoparticles on photovoltaics of functionalized polymethine dye. *Materials Today: Proceedings*, *25*, 39–43. https://doi.org/10.1016/j.matpr.2019.11.01

7 Chiozzia V., Rossi F. (2020) Inorganic–organic core/shell nanoparticles: Progress and applications. *Nanoscale Advances*, 2, 5090-5105. https://doi.org/10.1039/D0NA00411A

8 Rusdan N.A., Timmiati Sh.N., Yaakob Z., Lim K.L., Khaidar D. (2022) Recent application of core-shell nanostructured catalysts for CO_2 thermocatalytic conversion processes. *Nanomaterials*, 12(21), 3877. https://doi.org/10.3390/nano12213877

9 Turakova M., Salmi T., Eränen K., Warnå J., Murzin D.Y., Kralik M. (2015) Liquid phase hydrogenation of nitrobenzene. *Applied Catalysis A: General*. 499, 66-76. https://doi.org/10.1016/j.apcata.2015.04.002

10 Gawande M. B., Goswami A., Asefa T., Guo H., Biradar A.V., Peng D.-L., Zboril R., Varma R.S. (2015) Core–shell nanoparticles: Synthesis and applications in catalysis and electrocatalysis. *Chemical Society Reviews,* 44, 7540-7590. https://doi.org/10.1039/C5CS00343A

11 Das S., Pérez-Ramírez J., Gong J., Dewangan N., Hidajat K., Gates B.C., Kawi S. (2020) Core–shell structured catalysts for thermocatalytic, photocatalytic, and electrocatalytic conversion of CO2. *Chemical Society Reviews,* 49, 2937-3004. https://doi.org/10.1039/C9CS00713J

12 Lin L., Zhong Q., Zheng Y., Cheng Y., Qi R., Huang R. (2021) Size effect of Au nanoparticles in Au-TiO_2-x photocatalyst. *Chemical Physics Letters*, *770*, 138457. https://doi.org/10.1016/j.cplett.2021.138457

13 Afanasyev D.A., Ibrayev N.K., Serikov T.M., Zeinidenov A.K. (2016) Effect of the titanium dioxide shell on the plasmon properties of silver nanoparticles. *Journal of Physical Chemistry A*, *90*(4), 833–837. https://doi.org/10.1134/S0036024416040026

14 Alikhaidarova E., Afanasyev D., Ibrayev N., Nuraje N. (2022) Plasmonic enhanced polymer solar cell with inclusion of $AgSiO_2$ core-shell nanostructures. *Polymer Advanced Technologies*, *33*(3), 1000–1008. https://doi.org/10.1002/pat.5574

15 Seliverstova E., Serikov T., Nuraje N., Ibrayev N., Sadykova A., Amze M. (2024) Plasmonic effect of metal nanoparticles on the photocatalytic properties of TiO_2/rGO composite. *Nanotechnology*, *35*, 325401. https://doi.org/10.1088/1361-6528/ad3e02

16 Zhumabekov A., Seliverstova E., Ibrayev N. (2019). Investigation of photocatalytic activity of TiO2-GO nanocomposite. *Eurasian Physical Technical Journal*, 16(1(31)), 42–46. https://doi.org/10.31489/2019No1/42-46

17 Zhang B., Wang D., Hou Y., Yang S., Yang X. H., Zhong J. H., Liu J., Wang H. F., Hu P., Zhao H. J., Yang H. G. (2013). Facet-dependent catalytic activity of platinum nanocrystals for triiodide reduction in dye-sensitized solar cells. *Scientific Reports, 3,* 1836, https://doi.org/10.1038/srep01836

18 Johnson P.B., Christy R.W. (1972). Optical constants of noble metals. *Physical Review B*, *6*, 4370. https://doi.org/10.1103/PhysRevB.6.4370

19 Polyanskiy M.N. (2024). Refractive index.info database of optical constants. *Scientific Data*, *94*, 19. https://doi.org/10.1038/s41597-024-01102-5

20 Ibrayev N.Kh., Seliverstova E.V., Kanapina A.E. (2022) Transient absorption of gold nanoparticles of various diameters. *European Physical Technical Journal*, *19*(4), 73–77. https://doi.org/10.31489/2022No4/73-77

21 Adachi M., Sakamoto M., Jiu J., Ogata Y., Isoda S. (2006) Determination of parameters of electron transport in dye-sensitized solar cells using electrochemical impedance spectroscopy. *Journal of Physical Chemistry B*, *110*, 13872–13880. https://doi.org/10.1021/jp060976l

AUTHORS' INFORMATION

Sharapov, Ivan – Master's student, Buketov Karaganda University, Karaganda, Kazakhstan; https://orcid.org/0009-0000-6614-0338, ivan.sharapov.2001@mail.ru

Omarova, Gulden – PhD, Associate Professor, Head of the Department of Physics and Nanotechnology, Buketov Karaganda University, Karaganda, Kazakhstan; SCOPUS Author ID:56669661100, https://orcid.org/0000-0003-2900-2168; guldenserikovna@mail.ru

Sadykova, Aigul – Master (Sci.), Department of Physics and Nanotechnology, Buketov Karaganda University, Karaganda, Kazakhstan; SCOPUS Author ID: 57200382854; https://orcid.org/0000-0003-0148-3078; sadikova-aigul@mail.ru

Seliverstova, Evgeniya – PhD (Phys.), Associate Professor, Senior Research Fellow, Institute of Molecular Nanophotonics, Buketov Karaganda University, Karaganda, Kazakhstan; SCOPUS Author ID: 35323255400, https://orcid.org/0000-0002-9507-8825; genia_sv@mail.ru

EURASIAN PHYSICAL TECHNICAL JOURNAL

2025, Volume 22, No. 2 (52)

https://doi.org/10.31489/2025N2/33-41

Received: 26/02/2025 Revised: 16/04/2025 Accepted: 23/06/2025 Published online: 30/06/2025
Research Article

UDC 539.171

A COMPREHENSIVE PHENOMENOLOGICAL, SEMI-MICROSCOPIC, AND CRC ANALYSIS OF ^{15}N ELASTIC SCATTERING FROM ^{13}C AND ^{19}F NUCLEI

Akhat R.[1,3], Amangeldi N.[1,2], Baratova A. A.*[1], Anuar A.[1], Raiymbekov Ye. [1,3], Yergaliuly G. [1,3]

[1] L. N. Gumilyov Eurasian National University, Astana, Kazakhstan
[2] Institute of Nuclear Physics, Almaty, Kazakhstan
[3] National Laboratory Astana, Nazarbayev University, Astana
*Corresponding author: baratova_aa@enu.kz

Abstract. *In the present study, the angular distributions obtained at beam energies E_{lab} = 30.0, 32.0 and 45.0 MeV for the ^{15}N+ ^{13}C reaction and E_{lab} = 23.0, 26.0 and 29.0 MeV for the ^{15}N+ ^{19}F system were subjected to a comprehensive reanalysis using the optical model, the double folding model, and the coupled reaction channel (CRC) method. The main objective of the study was to establish the optimal optical potential through phenomenological and semi-microscopic analysis. Through careful calculations, the acceptable parameters of the potentials and their energy dependencies were derived for both nuclear systems. Notably, the angular distributions were well reproduced, indicating the effectiveness of the theoretical models used. In back angle scattering analysis, the CRC has very good agreement with the experimental values. As a result of the analysis, spectroscopic amplitudes were extracted for the $^{15}N \rightarrow {}^{13}C + d$ and $^{19}F \rightarrow {}^{15}N + \alpha$ configurations at different energies of the incident ^{15}N ions. The obtained results of spectroscopic amplitudes were subsequently compared with previously reported values, facilitating an assessment of the consistency and accuracy of the present work.*

Keywords: elastic scattering, optical model, double-folding model, elastic transfer, spectroscopic amplitude.

1. Introduction

Elastic scattering in nuclear physics is a key method for studying nuclear structure and nucleon-nucleon interactions. The angular distribution of scattered particles, resembling light diffraction by an opaque disk, is effectively analyzed using the optical model (OM), which provides a reliable framework for describing scattering phenomena [1]. Elastic scattering data helps map nuclear matter distribution and understand nuclear properties. Among various theoretical models, including the shell and cluster models, the OM has been a cornerstone in analyzing charged particle scattering for decades. The OM is commonly used to describe the scattering of different systems, including elastic [2–7] and elastic transfer [8–11] scattering.

In this study, OM is applied to analyze the angular distribution of elastic scattering for the ^{15}N+ ^{13}C and ^{15}N+ ^{19}F nuclear systems. The goal is to identify the optimal optical potential, refine its parameters, and determine reaction cross sections. Early investigations in this field began with Gamp A. [12] in 1975, who studied ^{15}N+ ^{13}C scattering at energies of 30.0, 32.0, and 45.0 MeV, using phenomenological Woods-Saxon potentials. Later, Gamp A. in [13] extended work to ^{15}N+ ^{19}F scattering at energies of 23.0, 26.0, and 29.0 MeV, analyzing differential cross sections with a range of complex potentials. By incorporating OM into the analysis, this study provides deeper insights into the nuclear interactions of these systems. In practice,

multiple parameters set often provide equally good fits to the data, raising the critical question of whether some are more physically meaningful than others, and, if so, which should be prioritized. This emphasizes the need to assess the physical relevance of each parameter set and choose the most suitable one to ensure the results are both reliable and easy to interpret.

Accurately determining the optical potential through phenomenological analysis alone is challenging due to ambiguities in the complex parameter space. Thus, it is essential to constrain the potential within physical boundaries before parameter optimization. To address this, the double-folding model (DF) is employed to identify physically meaningful optical potential parameters [14–17].

In this study, we investigate the ^{15}N+ ^{13}C and ^{15}N+ ^{19}F nuclear systems using the standard optical model, combining both phenomenological and semi-microscopic approaches. Experimental angular distribution data were analyzed with the FRESCO and SFRESCO codes [18] to derive nuclear potentials and reaction cross-section parameters. The organization of the manuscript is as follows: section 1 Introduction, section 2 research within the framework of OM and DF with suitable optical parameters of the potentials. Section 3 analyzes the data within the CRC, presenting the results and leading the discussion. The conclusion is presented in section 4.

2. OM, DF analysis of ^{15}N +^{13}C, ^{15}N+ ^{19}F

The experimental data for the ^{15}N+ ^{13}C and ^{15}N+ ^{19}F nuclear systems were reanalyzed phenomenologically and semi-microscopically under the standard OM. In the first approach, the differential cross-sections were calculated in the framework of the phenomenological OM, and the interaction potential was found by fitting the computed cross-sections to the experimental data.

Within this model, the total interaction potential has a shape:

$$U(r) = -V_0\left[1+\exp\left(\frac{r-R_V}{a_V}\right)\right]^{-1} - iW_0\left[1+\exp\left(\frac{r-R_W}{a_W}\right)\right]^{-1} + V_c(r), \quad (1)$$

where V_0 real potential depth, W_0 imaginary potential depth, a_W, a_V are the diffuseness of real and imaginary potential parts; r_V, r_W: the reduced radii of these potential parts. These six parameters were allowed to vary independently.

$V_c(r)$ the Coulomb potential is defined as follows [19]:

$$V_C(r) = \begin{cases} \dfrac{Z_1 Z_2 e^2}{2R_C}\left(3-\dfrac{r^2}{R_C}\right) & \text{for r}<R_C \\ \dfrac{Z_1 Z_2 e^2}{r} & \text{for r} \geq R_C \end{cases}, \quad (2)$$

where R_C -Coulomb potential radius.

The optical potential can also be determined using semi-microscopic methods [20], which incorporate the internal structure of the interacting nuclei. In this approach, the nuclear-nuclear potential is derived from the nucleon-nucleon (NN) interaction [21, 22]. Effective NN interaction takes into account even and odd components of the central forces. The real potential is the sum of direct and exchange potentials[23]:

$$\vec{V} = V^D + V^{EX}. \quad (3)$$

The direct term of folding potential is given by:

$$V^D(R) = \iint \rho^{(1)}(r_1) v_D(s) \rho^{(2)}(r_2) dr_1 dr_2, \quad (4)$$

where, $v^D(s)$ - is the direct component of the effective NN interaction, $\rho^{(1)}$, $\rho^{(2)}$ - densities of colliding nuclei, R -distance between nucleus $\left|\vec{R}\right|$.

Exchange term of folding potential is given by the expression:

$$V^{EX}(R) = \iint \rho^{(1)}(r_1, r_1+s) v_{EX}(s) \rho^{(2)}(r_2, r_2+s) \exp\left[ik(R)s/M\right] dr_1 dr_2, \quad (5)$$

where $v_{EX}(s)$ - is the exchange component of the effective NN - interaction, $\rho^{(i)}(r,r')$ is the density matrix of colliding nuclei, $s = \left|\vec{r}_2 - \vec{r}_1 + \vec{R}\right|$ is the distance between interaction nucleons, M is reduced mass, $k(R)$ - local momentum of relative motion.

M3Y-Reid interaction is given in terms of Yukawa potential as follows [24]:

$$v_D(s) = 7999.0\frac{e^{-4s}}{4s} - 2134.25\frac{e^{-2.5s}}{2.5s}$$
$$v_{EX}(s) = 4631.4\frac{e^{-4s}}{4s} - 1787.87\frac{e^{-2.5s}}{2.5s} - 7.8474\frac{e^{-0.7072s}}{-0.7072s}, \quad (6)$$

The equation of state of the optical potential is constructed depending on the density:

$$v_{D(EX)}(\rho,s) = f(\rho)v_{D(EX)}(s), \quad (7)$$

where ρ - is the density of the medium in which the nucleons is located. $f(\rho)$ - density dependence factor.

Density dependence factor takes the following form:

$$f(\rho) = C(1 + \alpha\exp(-\beta\rho) - \gamma\rho), \quad (8)$$

C, α, β, γ -parameters of factor which reproduce the saturation process of nuclear matter in the calculations. The values are given in the Table 1.

The modified harmonic oscillator (MHO) model was used to calculate the matter density distribution of nuclei ^{13}C, ^{15}N [25]:

$$\rho(r) = \rho_0(1 + \alpha(r/a)^2\exp(-(r/a)^2), \quad (9)$$

where a =1.81 fm and α =1.25 fm for ^{15}N and a =1.635 fm and α =1.403 fm for ^{13}C respectively.

The nucleon density distribution in the ^{19}F nucleus is expressed as a two-parameter Fermi [25] function as follows:

$$\rho(r) = \rho_0/(1 + \exp(r - c)/z), \quad (10)$$

where c =2.59 fm and z =0.564 fm for ^{19}F.

Experimental data for the ^{15}N+ ^{13}C system are analyzed at energies E_{lab}=30.0, 32.0, and 45 MeV, and for ^{15}N+ ^{19}F are analyzed at energies E_{lab}=23.0, 26.0 and 29.0 MeV in the framework of OM, DF. The density dependent parameters included in the folding potentials are shown in Table 1.

Table 1. M3Y-Reid potentials coefficients

Density dependence	C	A	β(fm^3)	γ(fm^3)	K (MeV)
CDM3Y1-Reid	0.3429	3.0232	3.5512	0.5	188

In the framework of the optical model of DF, the real part of the optical potential is created by folding the NN interaction with the nuclear matter density distribution in the ground state of projectile nuclei $\rho^{(1)}(r_1)$ and target nuclei $\rho^{(2)}(r_2)$. Total interaction potential has DF potential is for the real part and WS volume potential is for the imaginary part:

$$U(r) = N_r\left[V^D(r) + V^{EX}(r)\right] - iW_0\left[1 + \exp\left(\frac{r - R_W}{a_W}\right)\right]^{-1} + V_c(r), \quad (11)$$

where N_r - is the renormalization factor of the real potential part.

The obtained optimal potential parameters for ^{15}N+ ^{13}C and ^{15}N+ ^{19}F elastic scattering, together with the values of χ^2/N are presented in Table 2.

Table 2. Identified parameters as a result of the analysis of OM and DF for the ^{15}N+ ^{13}C and ^{15}N+ ^{19}F systems. Coulomb radius fixed: r_c=1.25fm

E MeV	Model	V_0 MeV	rv fm	av fm	W_0 MeV	r_W fm	a_W fm	`χ^2/N up to 90°	χ^2/N up to 180°	N_r
	^{15}N+ ^{13}C									
30.0	OM	133.09	1.09	0.54	9.92	1.18	0.49	6.5±0.01	23.93±0.8	-
	DFOM	CDM3Y1- Reid			9.79	1.24	0.49	7.74±0.01	29.62±0.5	0.92
32.0	OM	130	0.8	0.63	14.36	0.8	0.31	3.7±0.01	32.0±0.4	-
	DFOM	CDM3Y1- Reid			14.3	1.2	0.59	5.25±0.01	43.0±1.2	0.90
45.0	OM	124. 78	1.02	0.704	21.12	1.13	0.2	17.76±0.6	27.81±0.8	-
	DFOM	CDM3Y1- Reid			21.12	1.13	0.2	20.74±0.8	34.11±0.6	1.21
	^{15}N+ ^{19}F									
23.0	OM	83.55	1.19	0.53	33.53	1.34	0.29	0.17±0.01	1.94±0.08	-
	DFOM	CDM3Y1- Reid			33.64	1.4	0.39	1.05±0.01	2.02±0.01	0.817
26.0	OM	79.95	1.09	0.59	34.35	1.2	0.39	0.81±0.03	8.39±0.1	-
	DFOM	CDM3Y1- Reid			33.64	1.4	0.39	1.06±0.01	2.02±0.1	0.804
29.0	OM	78.93	1.16	0.57	36.0	1.31	0.28	1.65±0.01	5.52±0.08	-
	DFOM	CDM3Y1- Reid			36.64	1.37	0.39	1.69±0.02	6.3±0.2	0.812

Figures 1 and 2 depict the phenomenological and semi-microscopic cross sections (respectively) derived from the parameters of the ^{15}N+ ^{13}C system at E_{lab} =30.0, 32.0, 45.0 MeV, as well as the ^{15}N+ ^{19}F system at incident energies E_{lab} =23.0, 26.0, 29.0 MeV. Despite obtaining optimal parameters in the framework of OM and DF which will describe the experimental data in the forward angles, the description in the full angular range is difficult (it shows χ^2/N up to 180°).

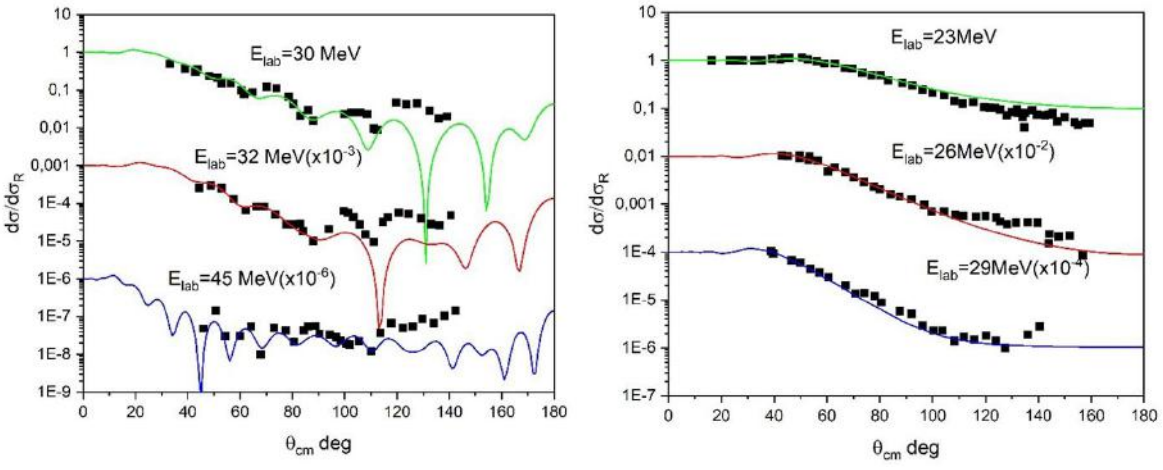

Fig.1. OM cross-sections for ^{15}N+ ^{13}C (left) and ^{15}N+ ^{19}F (right) nuclear systems

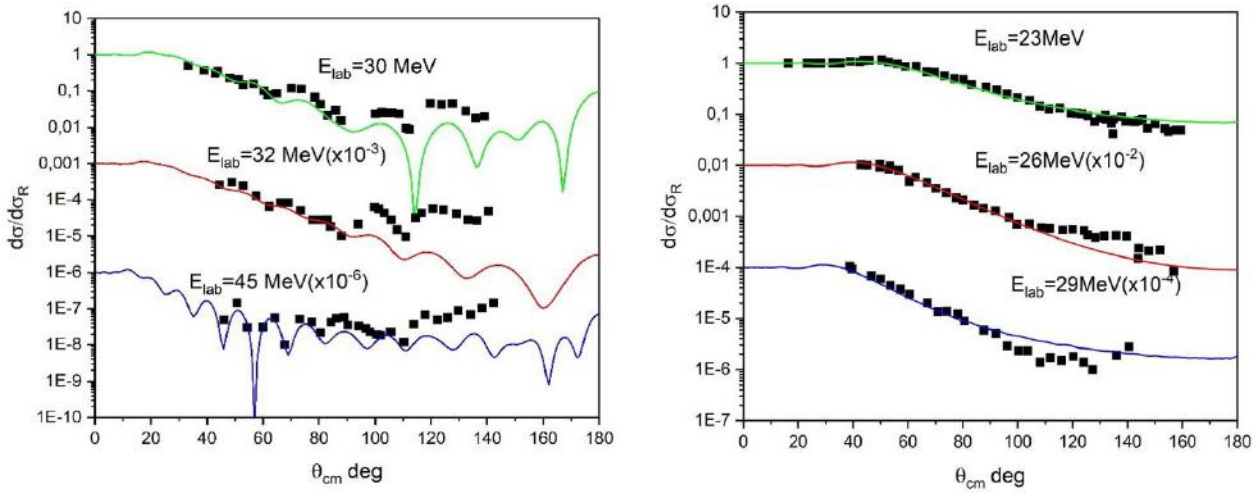

Fig.2. DF cross-sections for ^{15}N+ ^{13}C (left) and ^{15}N+ ^{19}F (right) nuclear systems

3. CRC analysis of ^{15}N +^{13}C, ^{15}N+ ^{19}F

The figures 3,4 demonstrate a significant increase in differential cross sections at backward angles, likely attributed to particle transfer processes. Such phenomena, involving the transfer of protons, deuterons, or alpha particles, have been extensively studied in previous works [26–29].

To accurately describe experimental data over the full angular range, the Coupled Reaction Channel (CRC) method is commonly employed. This approach extends the coupled channel framework to include nuclear rearrangement or transfer reactions, where one or more nucleons or composite particles (α, d particles) are transferred between the projectile and target nuclei. In this scenario, a composite projectile nucleus A=(a+x) interacts with a target nucleus b, transferring the particle x to form the final system B=(b+x). The nuclei a and b are referred to as cores. To compute the necessary wave functions, two critical parameters are needed: the number of nodes (N) in the radial wave function and the spectroscopic amplitudes (SA), which describe the decomposition of A and B into their constituent components a+x and b+x, respectively.

The Talmi-Moshinski transformation [30, 31] was employed to determine the quantum numbers of the cluster state, using the following formula:

$$2(N-1)+L=\sum_{i=1}^{n}2(n_i-1)+l_i\,, \tag{12}$$

where N is the number of nodes of the radial wave function of relative motion (taking into account the node at $r=0$) and L is the corresponding orbital momentum of the cluster, n_i, l_i are quantum numbers of components of a cluster of nucleons in harmonic oscillator model, Σ denotes the sums of similar quantities for nucleons entering a cluster in a bound state.

The differential cross section is the square of the sum of amplitudes from the pure elastic scattering and the exchange mechanism of the cluster transfer, as follows [8]:

$$\frac{d\sigma}{d\Omega}=\left|f_{el}(\theta)+e^{i\alpha}Sf_{tr}(\pi-\theta)\right|^2, \tag{13}$$

here $f_{el}(\theta)$ is the elastic scattering amplitude, f_{tr} is the transfer amplitude calculated using the distorted wave method with the replacement $\theta=\pi-\theta$, S is the product of the two spectroscopic amplitudes (SA), parameter $\alpha=pi$ (coherence of amplitudes).

Experimental data for the ^{15}N+ ^{13}C system are analyzed at energies E_{lab} =30.0, 32.0, 45 MeV and for ^{15}N+ ^{19}F are analyzed at energies E_{lab} =23.0, 26.0, 29.0 MeV in the framework of CRC. The cluster quantum numbers for the overlap used in CRC calculations are listed in Table 3.

Table 3. Cluster quantum number for the overlaps for the $^{15}N+ ^{13}C$ and $^{15}N+ ^{19}F$ systems used in our calculations.

Overlap	N	L	S	J=L+S	Binding Energy (MeV)
$<^{13}C+d\|^{13}C>$	3	2	1	1	16.16
$<^{15}N+\alpha\|^{15}N>$	2	1	0	1	4.01

The OM potentials presented in Table 2 were also used in the study of the elastic transfer of d for the $^{15}N+ ^{13}C$ system and α cluster transfer in the $^{15}N+ ^{19}F$ scattering. These calculations were performed using only one adjustable parameter SA (for the $^{15}N \rightarrow ^{13}C$ + d -configuration and $^{19}F \rightarrow ^{15}N$ + α-configuration). Parameter SA is shown in Table 4 for each nuclear system.

Table 4. Data of SA parameters for each nuclear system.

E_{lab} MeV	SA	χ^2/N up to 180°
$^{15}N+ ^{13}C$		
30	0.35±0.001	7.95±0.01
32	0.3±0.006	16.05±0.001
45	0.35±0.004	20.8±0.2
$^{15}N+ ^{19}F$		
23	0.3±0.008	1.85±0.01
26	0.3±0.006	7.84±0.3
29	0.3±0.004	4.45±0.2

The extracted average SA values for $^{15}N \rightarrow ^{13}C$ + d, $^{19}F \rightarrow ^{15}N$ + α -configuration are 0.33 and 0.3. As shown in Figure 3 the agreement between the experimental data at large angles and the CRC calculations, which took into account the mechanism of the transfer of the d - cluster transfer in the $^{13}C(^{15}N, ^{13}C)^{15}N$ reaction and α - cluster transfer in the ^{19}F (^{15}N, ^{19}F) ^{15}N reaction is quite good.

The values of SA we derived for the above systems are in good agreement with the data from the publications of Rudchik et al [31] and [13]. In the present work, the energy dependencies are found for the real and imaginary parts of the potential (figure 4). For the potential set, energy dependencies are described by the linear functions V = 147.09–0.499E and W = −8.59 + 0.66E for $^{15}N+ ^{13}C$ and V = 88.85–0.22E and W = 22.92 + 0.41E for the $^{15}N+ ^{19}F$ scattering system.

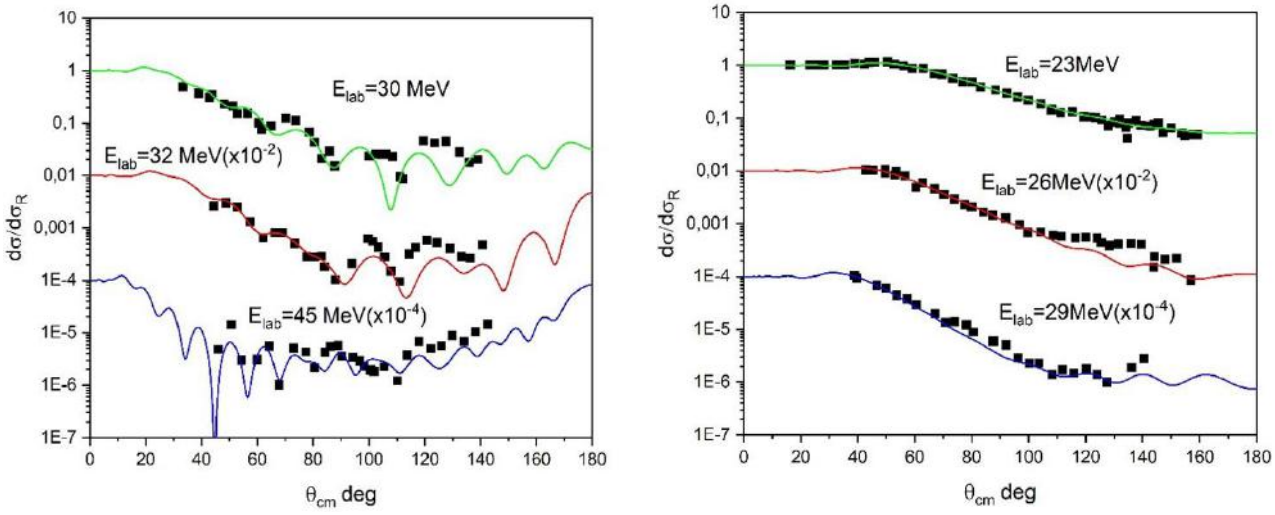

Fig.3. CRC cross-sections for $^{15}N + ^{13}C$ (left) and $^{15}N + ^{19}F$ (right)

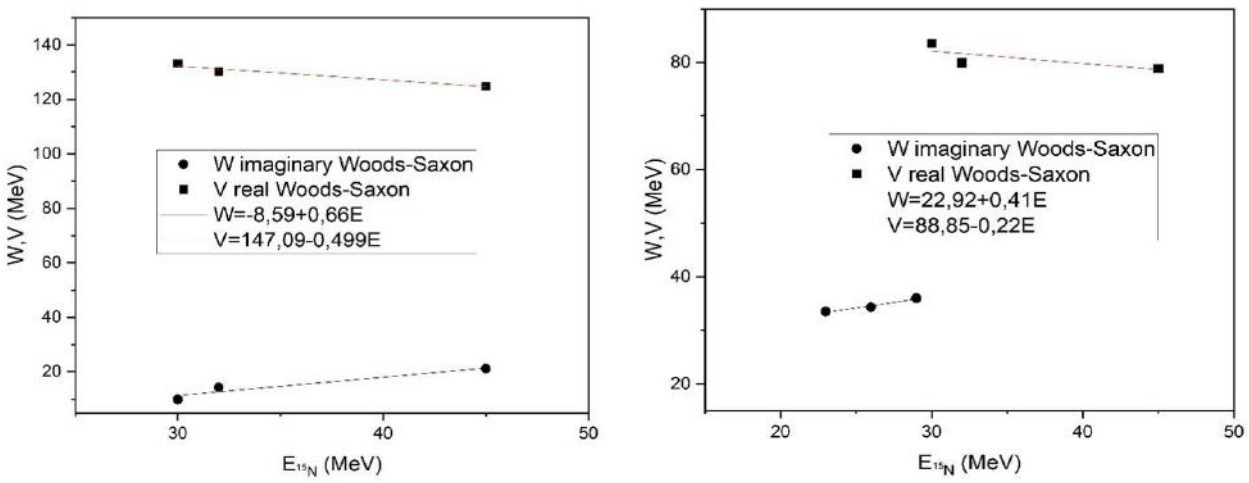

Fig.4. Energy dependence of $^{15}N + ^{13}C$ (left) and $^{15}N + ^{19}F$ (right)

4. Conclusion

New information on the parameters of optical potentials and reaction cross sections was obtained from the analysis of experimental data on the angular distributions of elastic scattering for the $^{15}N + ^{19}F$ and $^{15}N + ^{13}C$ systems. The energy dependences of the real and imaginary components of the nuclear potential depth were determined. A more physically meaningful set of optical potential parameters was also obtained by employing the DF model and the CRC.

Within the semi-microscopic framework, a folding potential based on the CDM3Y1-Reid interaction was constructed using the double-folding (DF) model. The phenomenological analysis revealed relative errors ranging from 0.17 to 1.6 for $^{15}N + ^{19}F$ and from 3.7 to 17.6 for $^{15}N + ^{13}C$ when comparing experimental and theoretical cross-sections. In the semi-microscopic analysis, the renormalization coefficients (Nr) of the microscopic potentials were determined to be 0.8–0.817 for $^{15}N + ^{19}F$ and 0.92–1.21 for $^{15}N + ^{13}C$. To fully describe the experimental data across the entire angular range, calculations were conducted using the Coupled Reaction Channel (CRC) method implemented in the FRESCO program. This approach incorporated elastic scattering, modeled using the optical model (OM), and the exchange mechanism, which accounted for cluster transfer—an α-cluster for $^{15}N + ^{19}F$ and a d-cluster for $^{15}N + ^{13}C$ — calculated with the distorted wave method.

As a result of this analysis, spectroscopic amplitude (SA) values were determined for the configurations $^{19}F \rightarrow ^{15}N + \alpha$ (average SA=0.3) and $^{15}N \rightarrow ^{13}C + d$ (average SA=0.33). These SA values show strong consistency with data reported by other researchers, underscoring the reliability of the findings.

Conflict of interest statement

The authors declare that they have no conflict of interest in relation to this research, whether financial, personal, authorship or otherwise, that could affect the research and its results presented in this paper.

CRediT author statement

Akhat R. - conceptualization, methodology, investigation; **Amangeldi N.** - supervision, project administration; **Baratova A.**- writing-original draft, writing-review, editing; **Anuar A. -** vizualization; **Raiymbekov Ye.** - software, investigation; **Yergaliuly G.** - conceptualization, formal analysis.

Acknowledgements

This work was carried out by the Science Committee of the Ministry of Science and Higher Education of the Republic of Kazakhstan (Grant No. AP19680284).

References

1 Soldatkhan D., Amangeldi N., Baltabekov A.S., Yergaliuly G., Mauyey B. (2022).= Investigation of the energy dependence of the interaction potentials of the $^{16}O+^{12}C$ nuclear system with a semi-microscopic method. *Eurasian Physical Technical Journal*, *19, 3(41),* 39-44, https://doi.org/10.31489/2022No3/39-44

2 Amar A., Hamada A., Burtebayev N., Amangeldy N. (2011) Study of scattering ^{1}H, ^{12}C and ^{16}O nuclei on 1P-shell at energy near the Coulomb barrier. *Int. J. Mod. Phys. E*, *20*, 980–986, https://doi.org/10.1142/S0218301311019106

3 Wang K., Yang Y.Y., Guimarães V., Pang D.Y., Duan F.F., Sun Z.Y. (2023) Elastic scattering investigation of radioactive ^{13}B and ^{13}O projectiles on a ^{208}Pb target at intermediate energies. *Phys. Rev. C*, *105*, 054616, https://doi.org/10.1103/PhysRevC.105.054616

4 Yang G., Duan F.F., Wang K., Yang Y.Y., Sun Z.Y., Guimarães V., Pang D.Y., Chen W.D., Jin L., Xu S.W., Ma J.B., Ma P., Bai Z., Wang L.H., Liu Q., Ong H.J., Lv B.F., Guo S., Raju M.K., Wang X.H., Li R.H., Zhang Y.H., Zhou X.H., Hu Z.G., Xu H.S. (2023) Elastic scattering of ^{13}C and ^{14}C isotopes on a ^{208}Pb target at energies around five times the Coulomb barriers. *Chin. Phys. C*, *3*, 034001, https://doi.org/10.1088/1674-1137/ad1678

5 Kundalia K., Gupta D., Ali S.M., Saha S.K., Tengblad O., Ovejas J.D., Perea A., Martel I., Cederkall J., Park J., Szwec S., Moro A.M. (2022) Study of elastic and inelastic scattering of ^{7}Be + ^{12}C at 35 MeV. *Phys. Lett. B*, *833*, 137294, https://doi.org/10.1016/j.physletb.2022.137294

6 La Fauci L., Spatafora A., Cappuzzello F., Agodi C., Carbone D., Cavallaro M., Lubian J., Acosta L., Amador-Valenzuela P. (2021) ^{18}O +^{76}Se elastic and inelastic scattering at 275 MeV. *Phys. Rev. C*, *104*, 054610, https://doi.org/10.1103/PhysRevC.104.054610

7 Nassurlla M., Burtebayev N., Karakozov B.K., Sakuta S.B., Boztosun I., Amangeldi N., Morzabayev A.K., Yergaliuly G., Alimov D.K., Burtebayeva J., Nassurlla M., Mauyey B., Kucuk Y., Hamada S., Sabidolda A., Khojayev R. (2021) New measurements and analysis of elastic scattering of ^{13}C by ^{9}Be nuclei in a wide energy range. *Eur. Phys. J. A*, *57*, 1–9, https://doi.org/10.1140/epja/s10050-021-00539-z

8 Hamada S., Burtebayev N., Gridnev K.A., Amangeldi N. (2011) Analysis of alpha-cluster transfer in $^{16}O+^{12}C$ and $^{12}C+^{16}O$ at energies near Coulomb barrier. *Nucl. Phys. A*, *859*, 29–38, https://doi.org/10.1016/j.nuclphysa.2011.04.006

9 Burtebayev N., Nassurlla M., Sabidolda A., Sakuta S.B., Karakhodzhaev A.A., Ergashev F., Rusek K., Piasecki E., Trzcinska A., Wolińska-Cichocka M., Mauyey B., Janseitov D., Zalewski B., Hamada S., Kemper K.W., Ibraheem A.A. (2019) Measurement and analysis of ^{10}B +^{12}C elastic scattering at energy of 41.3 MeV. *Int. J. Mod. Phys. E*, *28*, 1950028, https://doi.org/10.1142/S0218301319500289

10 Phuc N.T.T., Phuc N.H., Khoa D.T. (2018) Direct and indirect α transfer in elastic ^{16}O + ^{12}C scattering. *Phys. Rev. C*, *98*, 1–13, https://doi.org/10.1103/PhysRevC.98.024613

11 Gamp A., Braun-Munzinger P., Gelbke C.K., Harney H.L., Bohlen H.O., Bohn W., Hildenbrand K.D., Kuzminski J., von Oertzen W., Tserruya I. (1975) Interfering proton and neutron transfer in the reaction ^{13}C (^{15}N, ^{14}N)^{14}C. *Nucl. Phys. A*, *250*, 341–350, https://doi.org/10.1016/0375-9474(75)90264-X

12 Gamp A., von Oertzen W., Bohlen H.G., Feil M., Walter R.L., Marquardt N. (1973) Elastic Scattering of ^{15}N on ^{19}F, ^{19}F on ^{18}O and ^{19}F on ^{16}O at low energies and elastic transfer. *Z. Phys. A*, *304*, 283–304, https://doi.org/10.1007/BF01399327

13 Nassurlla M., Burtebayev N., Sakuta S.B., Karakozov B. K., Nassurlla M., Burtebayeva J., Khojayev R., Sabidolda A., Yergaliuly G. (2022) Deuteron scattering and (d, t) reaction on ^{11}B at an energy of 14.5 MeV. *Nuclear Physics A*, *1023*, 122448. https://doi.org/10.1016/j.nuclphysa.2022.122448

14 Ibraheem A.A., Al-Amri H. (2022) Analysis of $^{4,6,8}He+^{208}Pb$ elastic scattering at E = 22 MeV using various potentials. *Rev. Mex. Fis.*, *58*, 4–10, https://doi.org/10.31349/revmexfis.68.051201

15 Khoa D.T., von Oertzen W., Bohlen H.G. (1994) Double-folding model for heavy-ion optical potential: Revised and applied to study ^{12}C and ^{16}O elastic scattering. *Phys. Rev. C*, *49*, 1652–1668, https://doi.org/10.1103/PhysRevC.49.1652

16 Alsaif N.A.M., Hamada S., Farid M.E.A., Alotaibi B.M., Alotiby M., Mohammed A., Awad A. (2023) Elastic scattering of $^{7}Li+^{58}Ni$: a phenomenological and microscopic analysis. *Rev. Mex. Fis.*, *69*, 1–11, https://doi.org/10.31349/revmexfis.69.021201

17 Thompson I.J. (1988) Coupled reaction channels calculations in nuclear physics. *Comput. Phys. Rep.*, *7*, 167–212, https://doi.org/10.1016/0167-7977(88)90005-6

18 Boztosun I., Dagdemir Y., Bayrak O. (2005) The examination of the $^{12}C+$ ^{24}Mg elastic scattering around the Coulomb barrier. *Physics of Atomic Nuclei, 68*, 1153-1159. https://doi.org/10.1134/1.1992570

19 Khoa D.T., Satchler G.R. (2000) Generalized folding model for elastic and inelastic nucleus–nucleus scattering using realistic density dependent nucleon–nucleon interaction. *Nucl. Phys. A*, *668*, 3–41, https://doi.org/10.1016/S0375-9474(99)00680-6

20 Khoa D.T., Satchler G.R., von Oertzen W. (1997) Nuclear incompressibility and density dependent NN interactions in the folding model for nucleus-nucleus potentials. *Physical Review C, 56*, 954–969, https://doi.org/10.1103/PhysRevC.56.954

21 Khoa D.T., von Oertzen W. (1995) Refractive alpha-nucleus scattering: a probe for the incompressibility of cold nuclear matter. *Phys. Lett. B*, *342*, 6–12, https://doi.org/10.1016/0370-2693(94)01393-Q

22 Khoa D.T. (2001) α-nucleus optical potential in the double-folding model. *Physical Review C*, 63, 034007. https://doi.org/10.1103/PhysRevC.63.034007

23 Soldatkhan D., Yergaliuly G., Amangeldi N., Mauyey B., Odsuren M., Ibraheem A. A., Hamada S. (2022) New Measurements and Theoretical Analysis for the ^{16}O+ ^{12}C Nuclear System. *Brazilian Journal of Physics*, *52,* 152. https://doi.org/10.1007/s13538-022-01153-0

24 De Vries H., De Jager C.W., De Vries C. (1987) Nuclear Charge-Density-Distribution Parameters From Elastic Electron Scattering. *At. Data Nucl. Data Tables*, *36*, 495–536, https://doi.org/10.1016/0092-640X(87)90013-1

25 Amangeldi N., Burtebayev N., Sakuta S.B., Nassurlla M., Burtebayeva J., Nassurlla M., Yergaliuly G., Sabidolda A., Rusek K., Trzcinska A., Wolińska-Cichocka M., Mauyey B. (2020) Study of elastic scattering of 10B ions on ^{12}C nuclei at the energy of 17.5 MeV. *Acta Phys. Pol. B*, *51*, https://doi.org/10.5506/APhysPolB.51.757

26 Takai H., Koide K., Bairrio Nuevo A., Dietzsch O. (1988) α-transfer contribution to ^{10}B+^{14}N elastic scattering. *Phys. Rev. C*, *38*, 741–747, https://doi.org/10.1103/PhysRevC.38.741

27 Rudchik A.T., Budzanowski A., Chernievsky V.K., Czech B., Głowacka L., Kliczewski S., Mokhnach A.V., Momotyuk O.A., Omelchuk S.E., Pirnak Val.M., Rusek K., Siudak R., Skwirczyńska I., Szczurek A., Zemło L. (2001) The ^{11}B+^{12}C elastic and inelastic scattering at Elab(^{11}B) = 49 MeV and energy dependence of the ^{11}B+^{12}C interaction. *Nucl. Phys. A*, *695*, 51–68, https://doi.org/10.1016/S0375-9474(01)01106-X

28 Gridnev K.A., Mal'tsev N.A., Burtebaev N., Amangel'dy N., Hamada S. (2012) Role of the inelastic transfer channel in elastic ^{16}O+ ^{12}C scattering over a wide range of energies. *Bulletin of the Russian Academy of Sciences: Physics*, *76*, 934-937. https://doi.org/10.3103/S106287381208014X

29 Burtebayev N., Sadykov T.K., Boztosun I., Amangeldi N., Alimov D., Kerimkulov Z., Burtebayeva J., Maulen Nassurlla, Kurakhmedov A., Sakuta S.B., Karakoc M., Ibraheem Awad A., Kemper K.W., Hamada Sh. (2020). New measurements and reanalysis of ^{14}N elastic scattering on ^{10}B target. *Chinese Physics C, 44*, 115-123. https://doi.org/10.1088/1674-1137/abab89

30 Keeley N., Alamanos N., Kemper K.W., Rusek K. (2009) Elastic scattering and reactions of light exotic beams. *Prog. Part. Nucl. Phys.*, *63*, 396–447, https://doi.org/10.1016/j.ppnp.2009.05.003

31 Rudchik A.T., Rudchik A.A., Kutsyk O.E., Kemper K.W., Rusek K., Piasecki E., Trzcińska A., Kliczewski S., Koshchy E.I., Pirnak Val.M., Ponkratenko O.A., Strojek I., Plujko V.A., Sakuta S.B., Siudak R., Ilyin A.P., Stepanenko Yu.M., Shyrma Yu.O., Uleshchenko V.V. (2019) ^{12}C(^{15}N, ^{14}C)^{13}N reaction at 81 MeV. Competition between one and two particle transfers. *Nucl. Phys. A*, *992*, 121638, https://doi.org/10.1016/j.nuclphysa.2019.121638

AUTHORS' INFORMATION

Raimbek, Akhat – PhD student, Eurasian National University, National Laboratory Astana, Astana, Kazakhstan; Scopus Author ID: 57226571776; https://orcid.org/0000-0002-7634-0525; akhat.raimbek22@gmail.com

Amangeldi, Nurlan – PhD, Assistant Professor, Department of Nuclear Physics, New Materials and Technologies, L.N. Gumilyov Eurasian National University, Astana, Kazakhstan; Scopus Author ID: 37065699200; https://orcid.org/0000-0002-9416-5425 ; Nur19792@mail.ru

Baratova, Aliya – Candidate of physical and mathematical sciences, Senior Lecturer, Department of Nuclear Physics, New Materials and Technologies, L.N. Gumilyov Eurasian National University, Astana, Kazakhstan; Scopus Author ID: 55221822500; https://orcid.org/0000-0002-7015-3657 , baratova_aa@enu.kz

Anuar, Aida – PhD student, Eurasian National University, Astana, Kazakhstan, https://orcid.org/0009-0006-8587-8673 ; Aeedaassylbekova6@gmail.com

Raiymbekov, Ye. – PhD student, Eurasian National University , National Laboratory Astana, Astana, Kazakhstan, Scopus Author ID: 58532271000; https://orcid.org/0000-0003-3380-9263; esimray@mail.ru

Yergaliuly, Gani – PhD, National Laboratory Astana, Kazakhstan, Scopus Author ID: 57216951648; https://orcid.org/0000-0002-7443-8561; yergaliuly.gani@gmail.com

EURASIAN PHYSICAL TECHNICAL JOURNAL

2025, Volume 22, No. 2 (52)

https://doi.org/10.31489/2025N2/42-53

Received: 02/12/2025 Revised: 10/04/2025 Accepted: 25/05/2025 Published online: 30/06/2025

Research Article

UDC 537.311.33; 620.82

ENHANCED EFFICIENCY OF DYE-SENSITIZED SOLAR CELLS USING ZNO NANOPARTICLE DOPING CU FROM PINEAPPLE PEEL EXTRACT WITH MODIFIED NATURAL DYE SOLUTION

Rohmawati L.[1*], Ferdianto S.P.[1], Ma'arif M.S.[1], Ardiansyah F.F.[1], Muadhif F.I.[2,3], Setyarsih W.[1], Supardi Z.A.I.[1], Darminto D.[4]

[1] Universitas Negeri Surabaya, Ketintang, Surabaya, Indonesia
[2] Graduated School, Institut Teknologi Bandung, Bandung, Indonesia
[3] Research Center for System Nanotechnology, National Research and Innovation Agency, Tangerang Selatan, Banten, Indonesia
[4] Institut Teknologi Sepuluh Nopember, Keputih, Surabaya, Indonesia

*Corresponding author: lydiarohmawati@unesa.ac.id

Abstract. *Photoanodes and dye solutions are indispensable in the stability and efficiency of Dye-Sensitized Solar Cells' performance. In this study, the photoanode uses a ZnO sample doped with Cu, made using a green synthesis technique with bio-reduction from pineapple skin extract. Meanwhile, using the maceration method, the dye solution is made from mulberry fruit extract and moringa leaves. For Dye-Sensitized Solar Cells applications, ZnO photoanodes doped with 1%, 3%, 5%, and 10% Cu were each depleted on ITO glass and immersed in the dye solution for one day. The results were then tested for electrical conductivity and performance in Dye-Sensitized Solar Cells. Adding Cu doping concentration to the ZnO photoanode can affect the performance of the Dye-Sensitized Solar Cell. In this work, the ZnO sample doped with 5% Cu as a photoanode showed the highest efficiency at 1.67% with an electron lifetime of 12 ms, compared to the photoanode without Cu doping or with Cu doping at concentrations of 1%, 3%, and 10%. Thus, Cu-doped ZnO nanoparticles and dye solutions from natural materials can be further developed for Dye-Sensitized Solar Cells applications.*

Keywords: Dye-Sensitized Solar Cells, ZnO nanoparticles, Cu Doping, Dye Solution, Green synthesis.

1. Introduction

Dye-sensitized solar Cells (DSSC) are third-procreation solar cells with low outlay, simplicity, and high efficiency. These advantages make DSSCs attractive to industry because they offer renewable energy solutions with low pollution levels and are environmentally friendly. However, DSSCs have weaknesses in the type of dye solution, namely ruthenium, where the availability in nature is minimal (0.0001 ppm) [1] so it is not practical for large-scale use even in the long term, although this material has a high energy conversion value, reaching 13%. It is a consideration for large-scale DSSC applications, so an alternative to using dye solutions from natural materials is needed.

Natural pigments such as chlorophyll, carotenoids, anthocyanins, lutein, rutin, and betalains extracted from various parts of plants, including flowers, fruits, and leaves, can be used as sensitizers in DSSC [2]. Black mulberry fruit (*Morus nigra L.*) and moringa leaves (*Moringa oleifera*) are rich in anthocyanins and chlorophyll. Black mulberry fruit contains anthocyanin pigments of 570.10 ± 77.09 mg/100 g [3] and a light absorption peak of 550 nm. That absorption is similar to ruthenium's, even showing a power conversion

efficiency of 1.3% [4]. Likewise, Moringa leaves have a chlorophyll content of 10.19-16.51 mg/liter [5] and a peak light absorption of 665 nm [6].

Not only dye solutions but also semiconductor materials, such as photoelectrodes, also affect the efficiency of DSSC performance. One of these materials is ZnO, which features a bandgap of 3.37 eV with an exciton binding energy of 60 meV [7]. This value is higher than other metal oxides, making ZnO efficient for various applications, including antibacterial medication, dye removal, gas sensors, and photoanodes for water splitting [8]. Compared to TiO_2, ZnO can absorb energy at a larger wavelength and higher electron mobility [9]. However, using ZnO on a large scale still needs improvement, given its low efficiency in visible light and the rapid recombination of electron-hole pairs [10]. In addition, ZnO tends to form an agglomeration layer on the surface [11]. Therefore, doping with cationic elements such as Cu is needed to enhance the ZnO sample's ability to absorb visible light, reduce charge pair recombination, and increase electron mobility [11].

Cu metal has an ionic radius similar to Zn, allowing Cu to enter the ZnO matrix and change its optical properties [12]. Several methods, including co-precipitation, have successfully synthesized Cu-doped ZnO nanoparticles for DSSC photoanode applications [8], Layered Double Hydroxide (LDH) [13], sol-gel [14], hydrothermal [11], adsorption, and successive ionic layer reaction (SILAR) [2]. Nevertheless, these methods generally use special and toxic chemicals as intermediaries to reduce the size and stabilize nanoparticles, so they are not environmentally friendly. The use of green synthesis pathways is very relevant to in the manufacture of nanoparticles today because the toxicity level of the synthesis process can be reduced so much that the negative impact on the environment [15] and does not even require high temperatures and excessive energy and is environmentally friendly [16]. Khan et al. [17] reported using the green synthesis method to synthesize Cu-doped ZnO from horsetail leaf extract (*Stachytarpheta jamaicensis*). However, the study only focused on antibacterial applications, and the fabrication results still contained Cu ions with a 5 wt% doping composition. In previous studies [18], they successfully synthesized nanoparticles of ZnO through green synthesis using bioreduction from pineapple peel extract. However, that study was only for photocatalyst applications. In contrast, DSSC applications have never been reported, let alone the material used: ZnO nanoparticles doped with Cu, which is manufactured using the green synthesis method.

This research focuses on manufacturing Cu-doped ZnO nanoparticle photoanodes using the green synthesis method from pineapple peel extract with dye solution modification from black mulberry fruit extract and moringa leaves for DSSC applications. Pineapple peel has been considered organic waste, and its utilization can be even better besides being used as animal feed. It should be noted that pineapple peel contains bioactive compounds such as saponins, flavonoids, tannins, anthocyanins, vitamin C, carotenoids, and bromelain enzymes, which can reduce Zinc ions into ZnO nanoparticles [18]. In addition, these compounds can also function as stabilizers in metal solutions by binding to hydroxyls and carboxylates, forming a protective layer around metal particles, preventing aggregation, and even maintaining particle size and distribution [19]. This study was conducted to determine how adding Cu doping to ZnO nanoparticles affects the efficiency and absorption of photon energy in DSSC.

2. Materials and Methods

2.1 Materials

The following are the materials that need to be prepared in this study: Moringa leaves (*Moringa Olivera*), black mulberry fruit (*Morus Nigra L.*), distilled water, ethanol (Merck), $CuSO4.5H_2O$ (Merck), $Zn(CH_3COO)_2.2H_2O$ (Sigma Aldrich), NaOH (Sigma Aldrich), acetic acid (Merck), potassium iodide 0.5 M (Merck), KCl 3 M (Merck), acetonitrile (Emsure), iodine 0.05 M (Emsure), 8B pencil (Staedtler), PVA (Merck), and ITO glass (Sigma Aldrich, 8-12 Ohm-Sq). The equipment used in this study included a mortar pestle, digital balance, dry oven, magnetic bar, hotplate stirrer, beaker glass, petri dish, funnel glass, universal indicator pH, Whatman filter paper, erlenmeyer flask, pipette, spatula, separatory funnel, scotch tape and clamp.

2.2 Preparation of Cu-doped ZnO nanoparticles

Before making ZnO nanoparticles by doping with Cu using the green synthesis method, ZnO nanoparticles were prepared, as described in previous research [18]. Pineapple fruit was separated from the skin to take the pericarp, and the pulp was washed with distilled water. Furthermore, 10 g of pineapple skins were soaked in distilled water and stirred at 75 °C for 1 hour at 350 rpm. The lateness was then left open and filtered to obtain a yellow filtrate. After that, the solution was mixed with 3 g of Zn $(CH_3COO)_2 \cdot 2H_2O$ and

$CuSO_4 \cdot 5H_2O$ at concentrations of 1, 3, 5, and 10 wt.%. It was then added to distilled water and sonicated at 40°C for 90 minutes. The result was blended with 4 g of NaOH and 100 mL of distilled water, then centrifuged at 3000 rpm for 5 minutes. The result was heated at 120°C for 12 hours and then calcined at 500°C for 2 hours.

2.3 Preparation of dye-sensitizer solution

A total of 10 g of Moringa oleifera leaves (*Moringa oleifera*) and black mulberry fruit (*Morus nigra L.*) were crushed with a blender. After that, each ingredient was dissolved with ethanol for the maceration process, left for one day, and then strained using Whatman paper. Black mulberry extract and Moringa leaves were combined in a 1:1 ratio. Then, the natural dye extract was gradually dripped with HCl until a pH of 5 was reached. Furthermore, filtration was carried out, and a dye solution was obtained from a mixture of Moringa leaves and black mulberry fruit.

2.4 Fabrication of DSSC

In the fabrication of DSSC, the first step is to make a photoanode by coating ZnO nanoparticle powder, either without doping or with Cu doping, on the conductive surface of ITO glass using the doctor blade method. Before the coating was carried out, 1.5 g of PVA was dissolved in distilled water and stirred for 30 minutes at 80°C, forming a gel. After that, the gel was mixed with 0.5 g of ZnO, either without or with Cu doping, and then stirred using a mortar and pestle until each formed a paste. Before the paste was applied to the ITO glass surface, it was first cleaned with ethanol. The side of the ITO glass was coated with tape, leaving a 2 cm x 2 cm area open in the middle. The ZnO paste, doped with Cu and without Cu doping, was applied to the middle part that was not covered with tape and then heated on a hot plate at 450 °C for 30 minutes. After that, it was soaked in a dye solution for 24 hours to achieve maximum absorption. The counter electrode in this study was made by referring to previous research [20], specifically by shading an 8B pencil graphite on the ITO conductive glass section until evenly distributed.

Furthermore, 0.8 g potassium iodide was dissolved in 10 ml of acetonitrile to make the electrolyte solution. After that, 0.127 g of iodine was mixed with the liquid until it was homogeneous, and an I^-/I_3^- electrolyte solution was obtained. The DSSC construction process uses a sandwich system with two glass substrates, one serving as the working electrode and the other as the counter electrode. The electrolyte solution of I^-/I_3^- ions is dripped between the two sides of the glass and clamped using a clamping clip

2.5 Characterization

Phase identification of Cu-doped ZnO samples can be determined using the Smartlab Rigaku type X-ray Diffraction (XRD) characterization tool, which works using Bragg-Brentano optical rays with a Cu anode radiation source, 40 kV, 30 mA, and a CuKα wavelength of 1.54 Å with a testing angle of 20-80°. The diffraction pattern of the sample, as determined from the characterization results, was then analyzed qualitatively using Match! Software with the search and match technique. The size of the sample's crystallite could be reckoned using the Debye-Scherrer formula. The surface morphological structure of the sample can be identified using Scanning Electron Microscopy (SEM) characterization, type SU3500, brand Hitachi, with a voltage of 15 kV. SEM of characterization results can measure the sample's grain size distribution using a bar scale as a reference, which is then processed using ImageJ software by considering 150 grains. The absorbance of the sample can be measured using a Hitachi UH-5300 type Ultraviolet-visible spectroscopy (UV-Vis) characterization tool at wavelengths of 400-700 nm. The absorbance data from the characterization can be used to determine its bandgap energy using the Tauc Plot method analysis.

The electrochemical properties of DSSC can be determined through Electrochemical Impedance Spectroscopy (EIS) characterization using Gamry Instruments, equipped with Reference 3000. This characterization provides an impedance response to electrical signals at 0.1 Hz - 10 kHz. Electrical resistance in EIS testing is expressed as impedance, a circuit's ability to withstand the flow of electric current. In the Nyquist graph, the x-axis shows the sample's response data for a given frequency range, specifically the real impedance value ($Z' = Z_{real}$), while the y-axis represents the imaginary impedance ($Z'' = Z_{img}$). The elements that form the equivalent circuit consist of series resistance (R_s), Constant Phase Element (CPE), charge transfer resistance (R_{ct}), and Warburg impedance (W), which are used to determine electrochemical and physical phenomena in the cell. R_{ct} is the difference between the highest and lowest values of the semicircle formed on the graph or can be calculated from the starting point to the end point of the semicircle formation. The R_s value is known from the lowest point on the graph, which is caused by the presence of electrolytes. On the Bode

phase plot graph, the value of the effective mass of an electron in the solar cell system (τ) can be determined according to Equation (1) by knowing the maximum frequency peak (f_{max}) in Hertz units.

$$\tau = \frac{1}{2\pi f_{max}}, \quad (1)$$

Solar simulator test using ABET Technology equipped with Source meter model 2400 Keithley that simulates sunlight to test the performance of photovoltaic devices, such as solar cells. The test was conducted at a voltage range of 0 to 2 V, an irradiation area of 0.25 cm^2, and a light intensity of 100 mW/cm^2. The efficiency of converting light energy into electricity (η) and the fill factor in DSSC (FF) can be calculated using Equations (2), where J_{SC} is the current density (mA/cm^2), V_{OC} is the open circuit voltage (Volt), and P_{in} is the light power received from the light source (solar simulator).

$$\eta = \frac{J_{SC} \times V_{OC} \times FF}{P_{in}} \times 100\%, \quad (2)$$

3. Result and Discussion

3.1 Analysis of phase

The XRD test produced data with diffraction peaks on ZnO samples, both with and without Cu doping (ZnO-Cu) at concentrations of 1%, 3%, 5%, and 10%, as shown in Figure 1(a). The sample had diffraction peaks at two theta angles, namely 31.73, 34.42, 36.23, 47.53, 56.52, 62.84, 66.30, 67.88, and 69.05°. Each of these diffraction peaks indicates the wurtzite phase with the orientation of the crystal planes in sequence at (100), (002), (101), (102), (110), (103), (200), (112), and (201). The highest intensity at an angle of 36.23° (101) indicates that the ZnO and ZnO-Cu samples have formed a single phase, according to the Joint Committee on Powder Diffraction Standards (JCPDS) card number 36-1451. Previous studies reported that the maximum peak intensity of the wurtzite phase occurs at an angle of 36.32°, corresponding to the orientation of the crystal planes (101) [17].

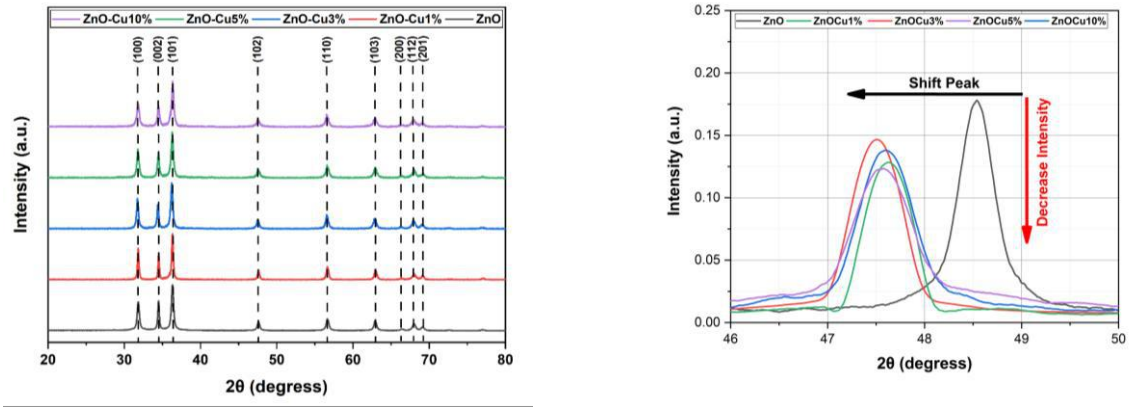

(a) (b)

Fig.1. (a) Diffraction patterning of Cu doped and undoped ZnO samples, (b) Shift lattice diffraction pattern of the ZnO samples doping Cu

Adding Cu doping to the ZnO sample reduces the intensity and shifts the angle of the diffraction peaks, as seen in Figure 1(b). At angles 31.73, 34.42, 36.23, 47.53, 56.52, 62.84, 66.30, 67.88, and 69.05°, there is an angular shift to 30.76, 33.48, 35.25, 46.60, 55.59, 61.91, 65.37, 67.01, and 68.14° after the addition of Cu doping. This change is due to the replacement of Zn^{2+} ions by Cu^{2+} ions at the ZnO site, where it is known that the radii of the Zn^{2+} and Cu^{2+} ions are similar, namely 0.74 Å and 0.73Å. The addition of doping Cu can also reduce the crystallite size in ZnO samples and even increase the number of electrons and the rate of electron movement in the conduction band [14]. The crystallite size of ZnO samples without Cu doping was 28.64 nm, whilst ZnO samples with Cu doping concentrations of 1%, 3%, 5%, and 10% are 22.52 nm, 22.27 nm, 19.65 nm, and 18.86 nm, respectively, calculated using the Debye-Scherrer formula. The smaller crystallite size in the Cu-doped ZnO sample is caused by lattice deformation and increased defect density, possibly due to strain from ion substitution [21]. Additionally, the presence of copper as a dopant can put stress on the doped samples [11].

3.2 Analysis of morphology and particle size

The morphology of the ZnO sample in this study, with a magnification of 30,000 times, shows a spherical shape with nanocrystallite oligomerization, as seen in Figure 2(a). Increasing the concentration of Cu doping in the ZnO sample, as seen in Figure 2(b-e), shows changes in shape and morphology. That is due to substituting Cu^{2+} ions into Zn sites. At a magnification of 35,000 times, the morphology of the Cu-doped ZnO sample shows a mixture of spherical and rod-shaped grains, as seen in Figure 2(b-e).

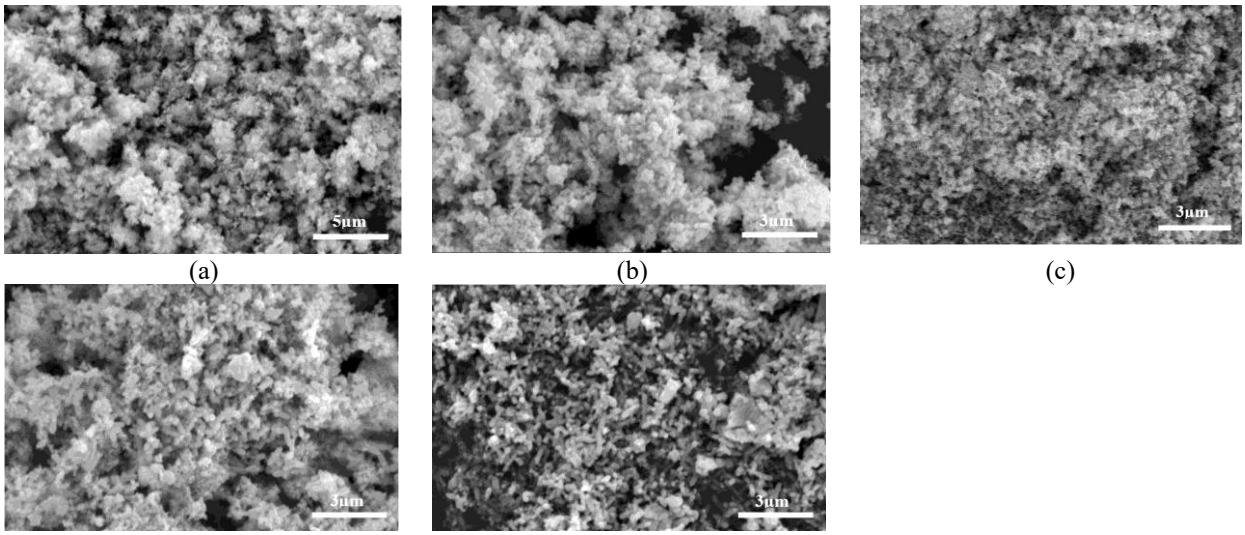

Fig.2. Morphology of samples (a) ZnO, (b) ZnO with 1% Cu doping, (c) ZnO with 3% Cu doping, (d) ZnO with 5% Cu doping, and (e) ZnO with doping 10%

The particle size distribution can be calculated using ImageJ software, the results are shown in Figure 3. Based on Figure 3, the particle size distribution for the ZnO sample without doping is 87.49 nm, while for the ZnO sample with Cu doping at concentrations of 1, 3, 5, and 10%, it is 77.77, 62.75, 59.42, and 57.80 nm, respectively.

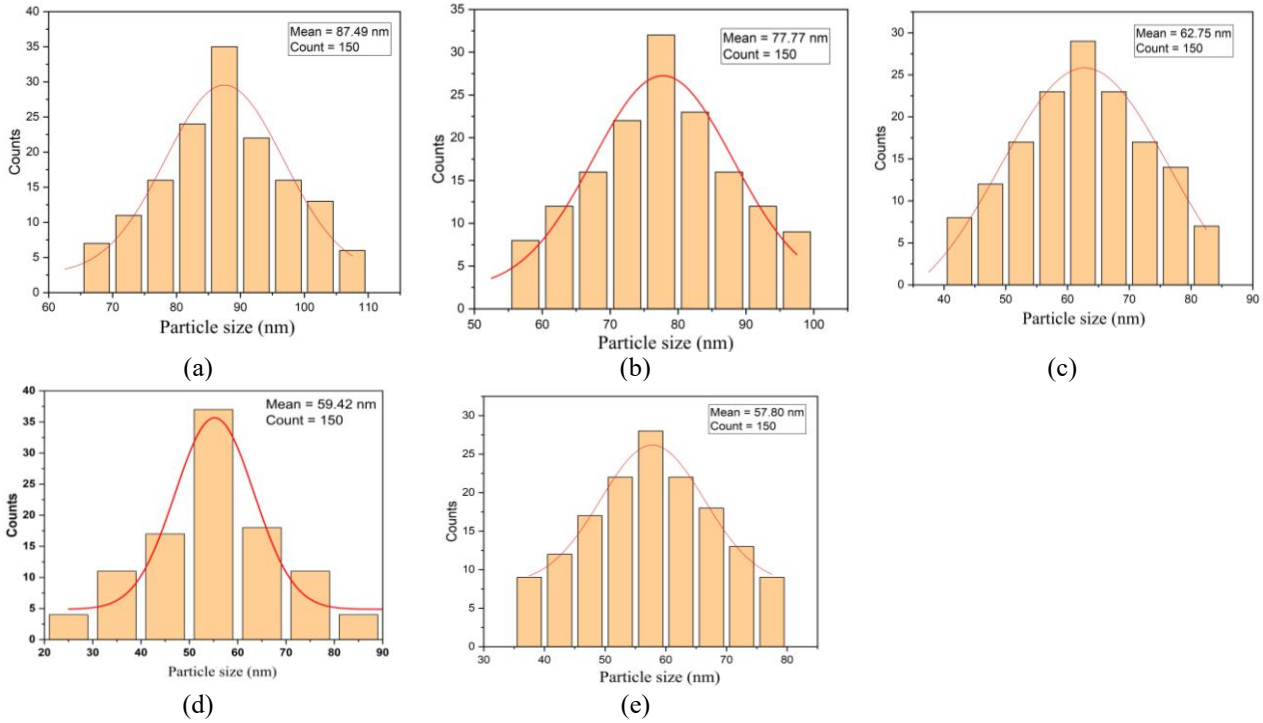

Fig.3. Particle size distribution of the sample (a) ZnO, (b) ZnO with 1% Cu doping, (c) ZnO with 3% Cu doping, (d) ZnO with 5% Cu doping, and (e) ZnO with doping Cu 10%

The difference in particle size in the ZnO sample without and with the addition of doping, which appears smaller, is due to the exchange of Cu^{2+} and Zn^{2+} ions in the ZnO lattice, and this is synchronous with the smaller crystallite size of the ZnO sample after being doped with Cu, thus affecting the efficiency of DSSC performance. Ge et al. [13] reported that a small particle is associated with a large surface area. So, it has the potential to increase the performance of DSSC, where the electrode absorbs more dye solution, which strengthens the light scattering.

3.3 Absorption UV-Vis and bandgap energy analysis

The peak of the UV-Vis absorption spectrum in Figure 4(a) for the ZnO sample is at a wavelength of 358 nm. However, with Cu doping in the ZnO sample, the absorption peak shifts to 368, 369, 370, and 372 nm for concentrations of 1, 3, 5, and 10%. The change in the absorption peak from blue-shifted to red-shifted is caused by the increasing concentration of Cu doping in the ZnO sample, resulting in changes in the electronic structure, namely the broadening of optical absorption in the ultraviolet region. Figure 4(b) shows the UV-vis spectrum at wavelengths from 400 to 700 nm for the dye solution from black mulberry fruit extract and moringa leaves, with two absorption peaks at 536 nm and 663 nm. According to previous studies, anthocyanin compounds have a wavelength absorption peak of around 450-600 nm [4], while chlorophyll pigments are found at wavelengths of 431-680 nm [22]. Mixing dyes containing anthocyanins and chlorophyll causes a bathochromic shift, also known as a red shift, so that the absorption peak of the mixed dye shifts to a longer wavelength [22]. Thus, the dye solution from this study can be used as a photosensitizer for DSSC. Because it has light absorption in the visible spectrum, even a mixture of dyes from chlorophyll and anthocyanin can increase absorption and expand the light absorption range [23].

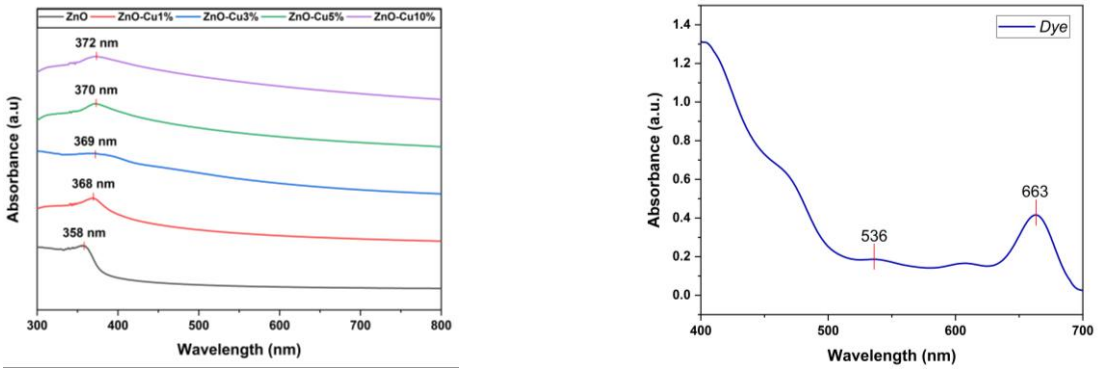

(a) (b)

Fig.4. UV-vis spectrum of samples (a) ZnO and ZnO-Cu, (b) natural dye solution

In this study, the bandgap energy for ZnO samples, both undoped and doped with Cu, can be determined from Tauc plot analysis, as shown in Figure 5(a). The ZnO sample and Cu doped ZnO 1%, 3%, 5%, and 10% have bandgap energies of 3.26, 3.00, 2.92, 2.82, and 2.59 eV, respectively. The decrease in band gap energy due to doping causes a shift in the red absorption edge, which can increase the electron mobility rate and reduce the recombination of charge carriers [24].

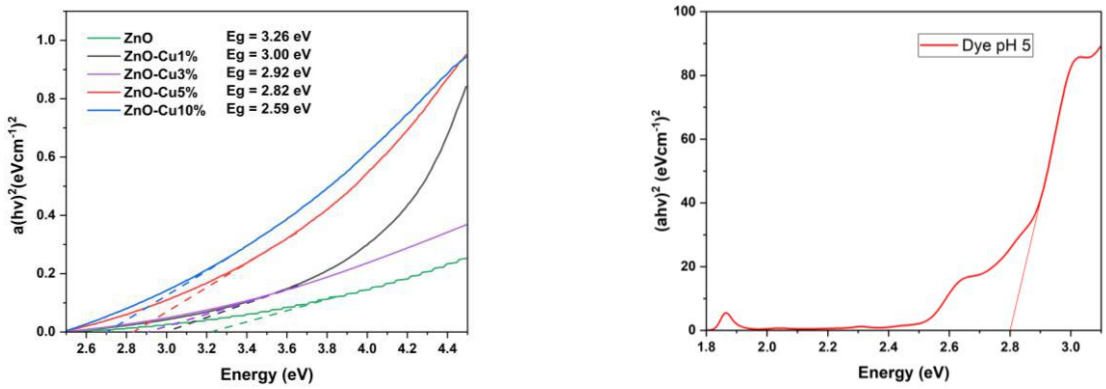

(a) (b)

Fig.5. Bandgap energy of (a) ZnO and ZnO-Cu samples, (b) natural dye solution

Figure 5(b) shows that the bandgap energy of the dye solution from black mulberry fruit extract and moringa leaves is 2.8 eV. Combining anthocyanins and chlorophyll from these plant extracts can produce a broader absorption spectrum, allowing more energy absorption from sunlight. This wider absorption wavelength can reduce the energy required for electron excitation to the conduction band, allowing the mixture of two dyes in this study to increase the photosensitizer's absorbance coefficient.

3.4 Performance DSSC

EIS measurements in dark conditions were carried out on the DSSC prototype with photoanode, counter electrode, and electrolyte to detect the possibility of electrochemical processes, especially in the charge transport process that occurs in the DSSC. The EIS test results are a Nyquist graph and a Bode phase plot, shown in Figure 6. The first semicircle (R_{ct}-CE) in the Figure 6(a) represents the charge transfer resistance at the counter electrode/electrolyte interface. In contrast, the second semicircle (R_{ct}-photoanode) describes the recombination resistance at the photoanode/electrolyte interface.

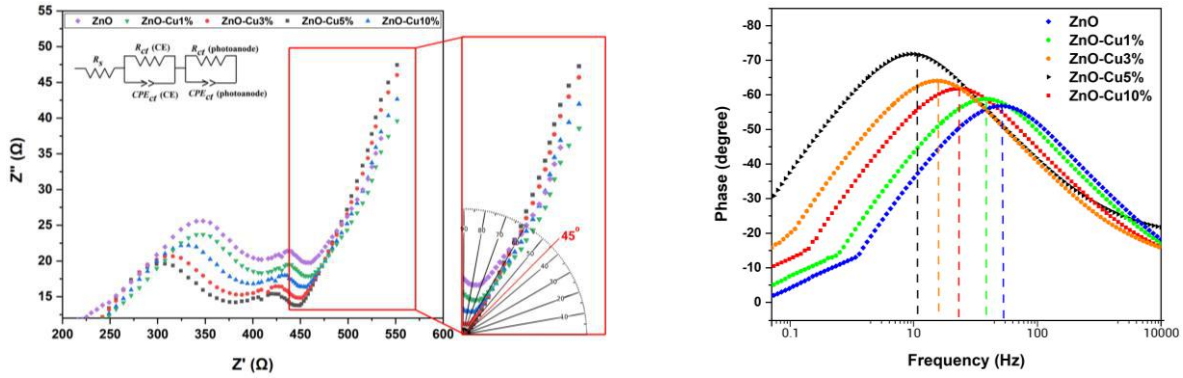

(a) (b)

Fig.6. (a) Nyquist curve, (b) Bode plot phase of ZnO nanoparticles doped Cu photoanodes

The shape of the Nyquist curve in DSSCs consists of three semicircles located in the low, mid, and high-frequency regions. In the mid-frequency range, a slope exceeding 45° (a specific angle) in the curve indicates the Warburg diffusion resistance related to the diffusion of charge carriers in the electrode material. This Warburg diffusion is an essential factor in the performance of electrochemical cells because it involves the movement of ions or molecules in the electrolyte, which shows the balance between resistance and reactance in DSSCs. This balance indicates good system stability, which can optimize the conversion of sunlight energy into electricity in solar cells. In the future, the R_s value will indicate the series resistance value associated with the system's external circuit. Electrodes with R_s values lower than the semicircle (R_{ct}) have better electrochemical energy storage performance. The DSSC on the ZnO photoanode has the largest giant semicircular shape compared to the ZnO photoanode doped with Cu. It indicates a less efficient electron transfer process because the resistance to electron flow is quite significant, thus reducing system performance and energy conversion efficiency in solar cells.

However, with the addition of Cu doping to the ZnO photoanode, the R_{ct} resistance value becomes lower, as seen in 5% Cu doping, which has a minor semicircular shape among 1%, 3%, and 10% Cu doping, which indicates that a lower of the resistance to electron transfer, so that the electron mobility is high [13]. Figure 6(b) shows the Bode phase plot curve, where the frequency peak shifts to a lower value with Cu doping on the ZnO photoanode. It shows that the charge carrier recombination rate decreases with Cu doping, allowing more light energy to be converted into electrical energy and increasing photoconversion efficiency. Cu doping at 5% has a lower frequency peak than doping at 1%, 3%, and 10%. The lifetime value of charge carriers is also an essential aspect of a solar cell's performance.

The lifetime of electrons in the cell system (τ) can be determined from the Bode phase plot curve using Equation (1), with the results presented in Table 1. Table 1 shows a significant difference in the electron lifetime in DSSCs of doped and undoped Cu photoanodes. The smaller the maximum frequency (f_{max}), the longer the electron lifetime (τ). Undoped and Cu-doped ZnO photoanodes with concentrations of 1%, 3%, 5%, and 10% have f_{max} of 74.25, 65.14, 25.74, 12.31, and 36.23 Hz, respectively, with electron lifetimes of 2.1, 2.4, 6.1, 12, and 3.6 ms.

Table 1. EIS parameters of research results of DSSC photoanodes

Photoanode Types	R_s (Ω)	R_{ct} (Ω)		f_{max} (Hz)	τ (ms)
		CE	Photoanode		
ZnO	1.11 ± 0.29	7.29 ± 0.15	4.63 ± 0.50	74.25	2.1
ZnO-Cu 1%	0.97 ± 0.27	7.01 ± 0.16	4.28 ± 0.54	65.14	2.4
ZnO-Cu 3%	0.79 ± 0.44	6.23 ± 0.14	3.98 ± 0.49	25.74	6.1
ZnO-Cu 5%	0.70 ± 0.26	5.52 ± 0.18	3.86 ± 0.53	12.31	12
ZnO-Cu 10%	0.85 ± 0.21	6.36 ± 0.26	4 ± 0.41	36.23	3.6

A high τ value indicates a longer lifetime of electrons generated by photons in the cell, meaning that electrons survive longer before being trapped or returning to the ground state, allowing more electrons to contribute to generating an electric current. Increasing the concentration of Cu doping in the ZnO photoanode can increase the efficiency of the DSSC. However, the performance efficiency of the DSSC doped with 10% Cu decreased. It can be seen from the increase in the R_{ct} values on the photoanode and counter electrode (CE) and the electron lifetime, which were 6.36 Ω, 4 Ω, and 3.6 ms, respectively. Cu doping with a high concentration (10%) has the potential to create more trap states in the ZnO semiconductor, thus limiting the number of free electrons that can move. As a result, the flow of electrons is reduced, impacting the DSSC's performance and reducing its efficiency. Cu doping in the DSSC photoanode improves its electrochemical performance in energy conversion compared to the ZnO photoanode alone. Ge et al. [13] in their research reported that ZnO photoanodes with 1% Cu doping, produced through the hydrothermal method, have an electron lifetime of 1.06 ms, which is lower than that of research carried out using the green synthesis method for producing Cu-doped ZnO photoanodes. It has been proven that 1% Cu-doped ZnO in this work has an electron lifetime of 2.4 ms. Even the electrochemical performance of ZnO photoanodes without Cu doping in this study was also better, at 2.1 ms, compared to ZnO prepared through the coprecipitation method (1.96 ms) [25] and commercial ZnO (1.32 ms) [13]. It shows that synthesizing ZnO nanoparticles using the green synthesis pathway improves electrochemical performance in DSSC.

The solar simulator test can evaluate the efficiency (η) of DSSC performance, which reflects its ability to convert sunlight into electrical energy. The results showing the relationship between voltage (V) and current density (J_{SC}) are presented in Figure 7. The figure allows further analysis of the DSSC performance efficiency, which is given in Table 2. The ZnO-Cu5% DSSC photoanode shows the highest short-circuit current (J_{SC}) of 1.11 mA/cm^2, while the open-circuit voltage (V_{OC}) of all samples is almost the same due to the very similar structure, chemical reactivity, and optical properties between Cu^{2+} and Zn^{2+} ions [11].

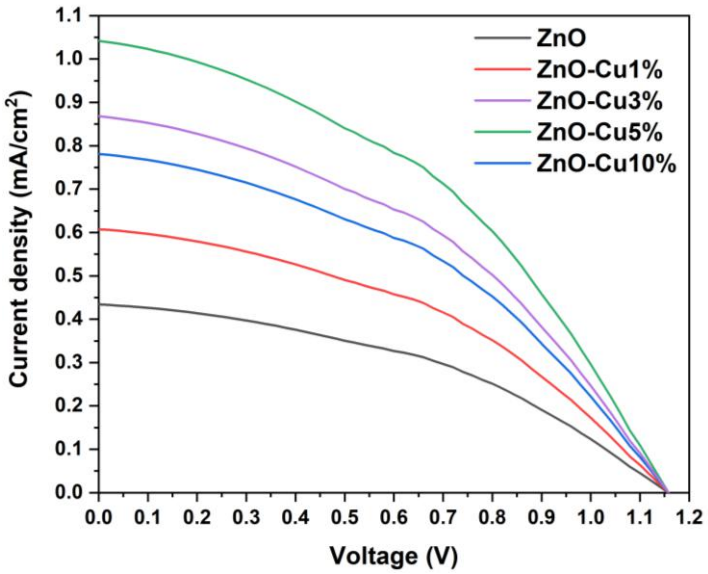

Fig.7. J-V curve of DSSC with ZnO doped Cu photoanode

The DSSC efficiency value on the ZnO-Cu5% photoanode is 1.67%, higher than that of ZnO-Cu10%, which is 1.48%. The excessive influx of Cu ions into ZnO causes a decrease in the effectiveness of the transition process and electron transfer in the DSSC [13].

The efficiency of DSSC with Cu-doped ZnO photoanode synthesized through green synthesis using pineapple peel extract has a higher energy conversion efficiency in DSSC than the results of several previous researchers, as shown in Table 3.

Table 2. DSSC photovoltaic performance with photoanodes and dye solution

Photoanoda	J_{SC} (mA/cm^2)	V_{OC} (Volt)	FF	η (%)
ZnO	0.46 ± 0.03	1.14 ± 0.05	0.23 ± 0.01	0.48 ± 0.04
ZnO-Cu1%	0.65 ± 0.04	1.14 ± 0.05	0.32 ± 0.01	0.95 ± 0.01
ZnO-Cu3%	0.84 ± 0.05	1.14 ± 0.05	0.42 ± 0.02	1.60 ± 0.01
ZnO-Cu5%	1.11 ± 0.08	1.14 ± 0.05	0.33 ± 0.02	1.67 ± 0.01
ZnO-Cu10%	0.93 ± 0.07	1.14 ± 0.05	0.35 ± 0.01	1.48 ± 0.02

Table 3. The efficiency of Cu doped ZnO based DSSCs from green synthesis results compared with previous research results.

Synthesis Method	Photoanode Type	Dye	DSSC Efficiency, η (%)	References
Sequential Ion Layer Adsorption and Reaction (SILAR)	ZnO-Cu 1%	Hypericum perforatum L. flowers	0.42	[2]
co-precipitation	ZnO-Cu 3%, ZnO-Cu 5%	N3	1.34, 1.09	[26]
co-precipitation	ZnO-Cu 5%	N719	0.34	[8]
co-precipitation	ZnO-Cu 5%	N3	1.09	[26]
Radio Frequency (RF) sputtering in room temperature	ZnO, ZnO-Cu	$H_2PtCl_6.6H_2O$ in 2-propanol .	0.16, 0.56	[27]
Layered Double Hydroxide (LDH)	ZnO-Cu 1%	D149	0.83	[13]
sol-gel	ZnO-Cu 5%	Xanthene	0.78	[14]
Green synthesis	ZnO, ZnO-Cu 1%, ZnO-Cu 5%	Moringa leaves and black mulberry fruit	0.48, 0.95, 1.67	This work

Cu-doped ZnO photoanodes from various methods that several researchers have reported, as in Table 3, show different DSSC efficiency values. ZnO photoanodes without and with Cu doping, from the results of synthesis through the green synthesis method in this study, showed better DSSC performance, where the efficiency value was higher than the results of previous studies. In addition, dye solutions from natural materials, namely black mulberry extract, and moringa leaves, also play an essential role as sensitizers in absorbing photons, so they can be used to replace synthetic sensitizer dyes.

4. Conclusion

In this study, the ZnO nanoparticles doped with Cu were well synthesized using bioreduction from pineapple peel extract with the green synthesis method. This sample has a wurtzite phase with a nanocrystallite size. Increasing the concentration of Cu doping in ZnO samples can cause a decrease in the bandgap energy value, where it is known that the bandgap before Cu doping is 3.26 eV, and after Cu doping is 3, 2.92, 2.82, and 2.59 eV for doping concentrations of 1, 3, 5, and 10%.

Combining anthocyanin and chlorophyll from black mulberry fruit extract and moringa leaves produces a broader absorption spectrum at 536 and 663 nm, with a bandgap of 2.8 eV. Cu-doped ZnO photoanode

increases the performance efficiency of DSSC, as evidenced by the results of electrochemical tests, where the electron lifetime for the ZnO photoanode without doping is 2.1 ms. Conversely, ZnO photoanodes doped with Cu at concentrations of 1%, 3%, 5%, and 10% had electron lifetimes of 2.4 ms, 6.1 ms, 12 ms, and 3.6 ms, respectively. Cu doping at a concentration of 5% on the ZnO photoanode provided an efficiency DSSC of 1.67%, higher than that of the ZnO photoanode without doping (0.48%) and with Cu doping at concentrations of 1% (0.95%), 3% (1.6%) and 10% (1.48%). Thus, a Cu-doped ZnO photoanode synthesized by the green route shows good electrochemical performance.

Conflict of interest statement

The authors declare that they have no conflict of interest in relation to this research, whether financial, personal, authorship or otherwise, that could affect the research and its results presented in this paper.

CRediT author statement

Rohmawati, L.: Conceptualization, Methodology, Investigation, Writing-Original Draft; **Ferdianto, S.P.**: Methodology, Investigation, Software; M Samsul M.: Methodology, Software; Fadhil F.A.: Methodology, Software; Fariz I.M.: Methodology, Software; **Setyarsih, W.**: Conceptualization, Methodology, Writing-Original Draft; **Supardi, Z.A.I.**: Conceptualization, Writing-Original Draft; **Darminto, D.**: Conceptualization, Writing-Original Draft.
The final manuscript was read and approved by all authors.

Acknowledgements

This research can be completed according to the author's expectations thanks to the assistance of various parties, mainly from institutions that have supported the implementation of this research.

The authors would like to thank the Director Riset Teknologi and Pengabdian Masyarakat (DRTPM) of the Kementerian Pendidikan, Kebudayaan, Riset, dan Teknologi for the funds provided through research on the Regular Fundamental scheme with the Decree of the Rector of Universitas Negeri Surabaya, Number 841/UN38/HK/2024.

References

1 Neikov O.D., Naboychenko S.S., Murashova I.B. (2019) Production of rare metal powders. *Handbook of Non-Ferrous Metal Powders (Second Edition)*, Chapter 24, 757-829. https://doi.org/10.1016/B978-0-08-1005439.00024-5.

2 Göde F., Balpinar N. (2023) Dye-sensitized solar cells fabricated using ZnO:Cu thin films and dye extracted from Hypericum perforatum L. flowers. *Dig. J. Nanomater. Biostruct*. 18(1), 389-402. https://doi.org/10.15251/DJNB.2023.181.389.

3 Huo J., Ni Y., Li D., Qiao J., Huang D., Sui X., Zhang Y. (2023) Comprehensive structural analysis of polyphenols and their enzymatic inhibition activities and antioxidant capacity of black mulberry (*Morus nigra L.*). *Food Chem*., 427, 136605. https://doi.org/10.1016/j.foodchem.2023.136605.

4 Yildiz Z.K., Atilgan A., Atli A., Özel K., Altinkaya C., Yildiz A. (2019) Enhancement of efficiency of natural and organic dye sensitized solar cells using thin film TiO_2 photoanodes fabricated by spin-coating. *J. Photochem. Photobiol. A Chem*., 368, 23-29. https://doi.org/10.1016/j.jphotochem.2018.09.018.

5 Rotulung J.C., Djarkasi G.S.S., Taroreh M.I.R. (2023) Pengaruh Penambahan Sari Daun Kelor Terhadap Kadar Kalsium Dan Sifat Sensoris Pada Susu Kenari. *Jurnal Teknologi Pertanian*., 14(2), 110-118. https://doi.org/ https://doi.org/10.35791/jteta.v14i2.51877

6 Fajri, Rahmatu R., Alam N. (2018) Kadar Klorofil Dan Vitamin C Daun Kelor (Moringa Oleifera Lam) dari Berbagai Ketinggian Tempat Tumbuh. *AGROTEKBIS: Jurnal Ilmu Pertanian*., 6(2), 152-158. Available at: http://jurnal.faperta.untad.ac.id/index.php/agrotekbis/article/view/270/263

7 Vaiano V., Matarangolo M., Murcia J.J., Rojas H., Navío J.A., Hidalgo M.C. (2018) Enhanced photocatalytic removal of phenol from aqueous solutions using ZnO modified with Ag. *Appl. Catal. B*, 225, 197-206. https://doi.org/10.1016/j.apcatb.2017.11.075.

8 Das A., Nair R.G. (2020) Effect of aspect ratio on photocatalytic performance of hexagonal ZnO nanorods. *J. Alloys Compd*., 817: 153277. https://doi.org/10.1016/j.jallcom.2019.153277.

9 Wu D., Wang Y., Ma N., Cao K., Zhang W., Chen J., Wang D., Gao Z., Xu F., Jiang K. (2019) Single-crystal-like ZnO mesoporous spheres derived from metal organic framework delivering high electron mobility for enhanced energy conversion and storage performances. *Electrochim. Acta*, 305, 474–483. https://doi.org/10.1016/j.electacta.2019.0

10 Kuang M., Zhang J., Wang W., Chen J., Liu R., Xie S., Wang J., Ji Z. (2019) Synthesis of octahedral-like ZnO/$ZnFe_2O_4$ heterojunction photocatalysts with superior photocatalytic activity. *Solid State Sci*., 96, 105901. https://doi.org/10.1016/j.solidstatesciences.2019.05.012.

11 Esgin H., Caglar Y., Caglar M. (2022) Photovoltaic performance & physical characterization of Cu doped ZnO nanopowders as photoanode for DSSC. *J.Alloys Compd*., 890, 161848. https://doi.org/10.1016/j.jallcom.2021.16184 8

12 Gaurav A., Beura R., Kumar J.S., Thangadurai P. (2019) Study on the effect of copper ion doping in zinc oxide nanomaterials for photocatalytic applications. *Mater. Chem. Phys*., 230, 162-171. https://doi.org/10.1016/j.matchemphys.2019.03.056.

13 Ge Z., Wang C., Chen T., Chen Z., Wang T., Guo L., Qi G., Liu J. (2021) Preparation of Cu-doped ZnO nanoparticles via layered double hydroxide and application for dye-sensitized solar cells. *J. Phys. Chem. Solids*, 150. https://doi.org/10.1016/j.jpcs.2020.109833.

14 Kumbhar D., Kumbhar S.S., Delekar S., Nalawade R., Nalawade A. (2019) Photoelectrochemical cell performance cu doped zno photoanode sensitized by xanthene dyes. *Nanosyst: Phys. Chem. Math*., 10(4), 466–474. http://doi.org/10.17586/2220-8054-2019-10-4-466-474.

15 Muthuvel A., Jothibas M., Manoharan C. (2020) Effect of chemically synthesis compared to biosynthesized ZnO-NPs using *Solanum nigrum* leaf extract and their photocatalytic, antibacterial and invitro antioxidant activity. *J. Environ. Chem. Eng.,* 8, 103705. https://doi.org/10.1016/j.jece.2020.103705.

16 Kazemi S., Hosseingholian A., Gohari S.D., Feirahi F., Moammeri F., Mesbahian G., Moghaddam Z.S., Ren Q. (2023) Recent advances in green synthesized nanoparticles: from production to application. *Mater. Today Sustain*., 24, 100500. https://doi.org/10.1016/j.mtsust.2023.100500.

17 Khan M.M., Harunsani M.H., Tan A.L., Hojamberdiev M., Poi Y.A., Ahmad N. (2020) Antibacterial Studies of ZnO and Cu-Doped ZnO Nanoparticles Synthesized Using Aqueous Leaf Extract of *Stachytarpheta jamaicensis*. *BioNanoScience*, 10(4), 1037–48. https://doi.org/10.1007/s12668-020-00775-5.

18 Rohmawati L., Lailia L.R., Putri N.P., Nasir M., Darminto D. (2024) Characterization of ZnO Nanoparticles Pineapple Skin Extract (*Ananas comosus L.*) as Photocatalytic Activity. *J. Water Environ. Nanotechnol*., 9(1), 112–123. http://doi.org/10.22090/jwent.2024.01.08.

19 Gaur J., Vikrant K., Him K.H., Kumar S., Pal M., Badru R., Masand S., Momoh J. (2023) Photocatalytic degradation of Congo red dye using zinc oxide nanoparticles prepared using Carica papaya leaf extract. *Mater. Today Sustain*., 22, 100339. https://doi.org/10.1016/j.mtsust.2023.100339.

20 Andari R. (2020) Distance Variation of Light Source Effects toward Dye Sensitized Solar Cell (DSSC) Performance using Anthocyanin Extract from Rosella Flower. *JPSE (Journal of Physics Science and Engineering),* 5(1), 31–35. http://doi.org/10.17977/um024v5i12020p031.

21 Nazim V.S., El-Sayed G.M., Amer S.M., Nadim A.H. (2023) Optimization of metal dopant effect on ZnO nanoparticles for enhanced visible LED photocatalytic degradation of citalopram: comparative study and application to pharmaceutical cleaning validation. *Sustain. Environ. Res*., 33(39), 1-16. https://doi.org/10.1186/s42834-023-00198-3.

22 Munandar M.R., Hakim A.S.R., Puspitadindha H.A., Andiyani S.P., Nurosyid F. (2022) The effect of mixing Chlorophyll-Antocyanin as a natural source dye on the efficiency of dye-sensitized solar cell (DSSC). *J. Phys. Conf. Ser*., 2190(1), 012042. https://doi.org/10.1088/1742-6596/2190/1/012042.

23 Sakshi, Singh P.K., Shukla V.K. (2022) Widening spectral range of absorption using natural dyes: Applications in dye sensitized solar cell. *Mater. Today Proc*., 49(8), 3235-3238. https://doi.org/10.1016/j.matpr.2020.12.287.

24 Kyaw K.K., Toe H. (2020) Characterization and Doping Effect of Cu-Doped ZnO Films. *Mater. Sci. Eng. A,* 10(3-4), 43-52. https://doi.org/10.17265/2161-6213/2020.3-4.001.

25 Ramya M., Nideep T.K., Nampoori V.P.N., Kailasnath M. (2021) The impact of ZnO nanoparticle size on the performance of photoanodes in DSSC and QDSSC: a comparative study. *J Mater Sci: Mater Electron*., 32, 3167-3179. https://doi.org/10.1007/s10854-020-05065-0.

26 Rajan A.K., Louis C. (2020) Localized surface plasmon resonance of Cu-doped ZnO nanostructures and the material's integration in dye sensitized solar cells (DSSCs) enabling high open-circuit potentials. *Journal of Alloys and Compounds,* 829, 154497. https://doi.org/10.1016/j.jallcom.2020.154497.

27 Alam M.W., Ansari M.Z., Aamir M., Waheed-Ur-Rehman M., Parveen N., Ansari S.A. (2022) Preparation and Characterization of Cu and Al Doped ZnO Thin Films for Solar Cell Applications. *Crystals*, 12, 128. https://doi.org/10.3390/cryst12020128.

AUTHORS' INFORMATION

Rohmawati, Lydia – Master (Sci.), Lecturer in Department of Physics, Faculty of Mathematic and Sciences, Universitas Negeri Surabaya, Surabaya, Indonesia; Scopus Author ID: 57201676108; https://orcid.org/0000-0002-0047-3487; lydiarohmawati@unesa.ac.id

Ferdianto, Sandy Prayoga – Bachelor(Sci.), Department of Physics, Faculty of Mathematic and Sciences, Universitas Negeri Surabaya, Surabaya, Indonesia; Scopus Author ID: 59483385500; https://orcid.org/0009-0004-1530-6421; sandy.20026@mhs.unesa.ac.id

Ma'arif, M Samsul – Bachelor(Sci.), Department of Physics, Faculty of Mathematic and Sciences, Universitas Negeri Surabaya, Surabaya, Indonesia; Scopus Author ID: 59484056700; https://orcid.org/0009-0003-6442-4793; msamsul.20038@mhs.unesa.ac.id

Ardiansyah, Fadhil Figo – Bachelor(Sci.), Department of Physics, Faculty of Mathematic and Sciences, Universitas Negeri Surabaya, Surabaya, Indonesia; Scopus Author ID: 59483930300; https://orcid.org/0009-0004-9974-5949; fadhil.20027@mhs.unesa.ac.id

Muadhif, Fariz Irkham – M.Sc Student,- Post graduate student, Department of Nanotechnology, Institut Teknologi Bandung, Bandung; Researcher in the Research Center for System Nanotechnology, National Research and Innovation Agency (BRIN), Tangerang Selatan, Indonesia; Scopus Author ID: 58821604300; https://orchid.org/0009-0004-7357-2912; 28723005@mahasiswa.itb.ac.id

Setyarsih, Woro – Master (Sci.), Lecturer in Department of Physics, Universitas Negeri Surabaya, Surabaya, Indonesia. Scopus Author ID: 57193132412; https://orcid.org/0000-0001-8344-2768; worosetyarsih@unesa.ac.id

Supardi, Zainul Arifin Imam – Ph.D, Lecturer in Department of Physics, Universitas Negeri Surabaya, Surabaya, Indonesia. Scopus Author ID: 6508147948; https://orcid.org/0000-0002-9150-6378; zainularifin@unesa.ac.id

Darminto, Darminto – Ph.D, Professor, Lecturer in Department of Physics, Institut Teknologi Sepuluh Nopember, Surabaya, Indonesia. Scopus Author ID: 6602346156; https://orcid.org/0000-0002-6269-9246; darminto@physics.its.ac.id

EURASIAN PHYSICAL TECHNICAL JOURNAL

2025, Volume 22, No. 2 (52)

https://doi.org/10.31489/2025N2/54-59

Received: 16/11/2024 Revised: 12/04/2024 Accepted: 25/06/2025 Published online: 30/06/2025
Research Article

UDC 53.097; 539.893; 621.3.07

STUDY OF OPTIMAL ENERGY PARAMETERS OF ELECTRO-HYDROPULSE TREATMENT FOR EFFICIENT EXTRACTION OF VALUABLE COMPONENTS FROM ORGANIC WASTE

Duisenbayeva M.S.[1*], Schrager E.R.[2], Sakipova S.E.[1], Nussupbekov B.R.[3]

[1] E.A. Buketov Karaganda University, Karaganda, Kazakhstan
[2] National Research Tomsk State University, Tomsk, Russia
[3] Abylkas Saginov Karaganda Technical University, Karaganda, Kazakhstan
*Corresponding author: m_o_l_d_i_r_89@mail.ru

Abstract. *The article considers some aspects of solving the urgent problem related to waste processing, in particular, renewable biowaste from the food industry. Development and implementation of modern technologies for processing and recycling various organic waste will reduce dependence on fossil energy sources, achieve carbon neutrality and maintain environmental safety. The object of the study is organic waste of the agro-industrial complex in the form of bone mass. The possibilities of efficient extraction of the valuable component using electro-hydro-pulse processing were experimentally studied. A description of the basic diagram of the electro-hydro-pulse installation and testing methods for different processing modes are given. Optimum values of electrical parameters are determined, allowing to increase the degree of extraction of valuable components from organic raw materials while reducing the processing time.*

Keywords: electro-hydro-pulse installation, spark discharge, treatment, organic waste, bone mass, valuable components.

1. Introduction

Despite the rapid development of renewable (alternative) energy, almost 80% of the world's demand for electricity is still met by using traditional fossil fuels, which are still economically viable. At the same time, the exponential growth of the world's population is causing unprecedented crises. Of particular concern are energy security and environmental issues such as air pollution, greenhouse gas emissions, the emergence of mass diseases among the population, etc. [1-3]. One possible solution to these problems is a strategy of innovative development and cost-effective use of bioenergy for the production of energy from renewable biological sources such as agricultural and food industry waste. Bioenergy could be considered as a steady and environmentally energy source alternative to fossil fuel [1].

The need to use energy from waste is due to the fact that improper disposal of agricultural waste in the open air and burning of residues also contribute to greenhouse gas emissions [1]. The energy obtained during the processing and recycling of various types of waste, such as metal and plastic waste, organic waste, etc., can be used to produce heat and electricity [4-6]. The use of modern biomass processing technologies allows not only to produce an alternative energy source in the form of biofuel, but also to extract valuable components from food industry waste, such as organic raw materials in the form of bone mass.

In recent years, various types of force effects have been used to improve the efficiency of heat and mass transfer processes in the processing of organic waste, including ultrasonic, electrical, pulse and discrete-pulse [7-11]. The main attention in the development of such methods is focused on changing the structure of the

cellular material in order to increase its diffusion permeability. In [8], the technological equipment and processes occurring during heat treatment of agricultural raw materials of various structures using electromagnetic radiation energy were studied. However, most of these methods and technologies are at the stage of laboratory and pilot tests, which indicates the presence of a number of unsolved theoretical and applied problems.

An analysis of publications and developments using a vapor-liquid flow formed under the influence of electric discharges during the processing of organic raw materials revealed a number of unsolved problems. The work [9] is devoted to the study of discharge phenomena accompanying electro-explosive energy conversion. Issues related to the capacitive accumulation of energy and its release in the discharge channel formed by a breakdown of a liquid or an explosion of a conductor are considered. In works [10-12] it is shown that shock waves and cavitation phenomena occurring at the initial stage of an electric discharge as a result of the formation of a discharge channel have a significant effect on particles of secondary raw materials in aqueous suspensions. It is shown that these processes accompanying a high-voltage discharge pulse with a nanosecond front contribute to the disintegration of the material and determine the intensity of mass transfer during the extraction process. In [13-15] the effect of frequency and intensity of an electric field was studied. The structure of cells was studied using transmission electron microscopy. The efficiency of the method depends on various factors such as time, temperature, field strength, frequency, sample selection and preparation, and it is effective even at lower field strengths.

In [16] an important problem related to the features of high-voltage electrical discharges in water or air is considered. This is due to the fact that the use of electro-hydro-pulse (EHP) technologies can lead to various adverse effects - from injury to people and animals to damage to electrical systems, fires and other emergency situations. A deep understanding of the mechanisms underlying these phenomena allows us to develop effective protective measures and increase the level of safety when using such technologies. Nevertheless, the experience of successful practical application of electro-hydro-pulse action for intensification of heat exchange [17], destruction and grinding of mineral materials for enrichment of mineral raw materials [5], etc. determines the real prospect of creating an energy-efficient technology that implements the advantages of this method.

This article discusses the results of experimental studies to identify the most optimal modes of EHP treatment of organic waste in the form of bone mass, allowing for the efficient extraction of valuable components.

2. Materials and testing methods

A laboratory installation has been developed to conduct experimental studies using electro-hydro-pulse processing of organic waste and to determine optimal energy parameters, Fig. 1. The developed setup makes it possible to implement a method for processing organic waste from the agro-industrial sector in order to extract valuable components, degrease bone mass, produce biofuel, and process biological waste [18, 19]. Crushed organic waste 1, dissolved in water 2, are continuously heated through the metal wall of the main tank 3 by means of liquid located in the water jacket 4, which is connected by rubber hoses 5 to thermostat 6. Thermostat 6 has a contact thermometer that allows automatic maintenance and regulation of the «water jacket» temperature in the range from 20°C to 85°C.

Liquid is supplied to water jacket 4 from the upper part of the tank, covering the entire surface, and cooled water is discharged through tube 7 located in the lower part of the tank. The outer part of the tank is covered with felt 8 to maintain and preserve the temperature. The underwater spark discharge is carried out using electrodes. The positive electrode 9 is installed on the tank cover, and the second, the negative electrode 10, is located on the bottom of the main tank 3. The positive electrode 9 is connected by means of an antenna cable 11 to an electro-hydro-pulse installation 12, which includes a control panel, a generator with an air discharger, and a capacitor bank equipped with a protection system [20].

The essence of the EHP processing method is to use the impact of a pulsed shock wave, which accompanies spark discharges in the area of the material being studied and destroys the structure of organic waste. From the power grid with a standard voltage of 220 V through a transformer, energy is supplied to a capacitor bank. The capacitors are charged to a high voltage. Using the control panel, a signal is sent to the air spark gap, which causes an electric discharge breakdown between the electrodes immersed in the liquid. An electric discharge in a liquid medium (water) causes the formation of a shock wave. In addition to the impact of the resulting shock waves, cavitation and air bubbles collapsing in water contribute to the extraction of a valuable component in the form of fat through microcracks in solid organic waste materials.

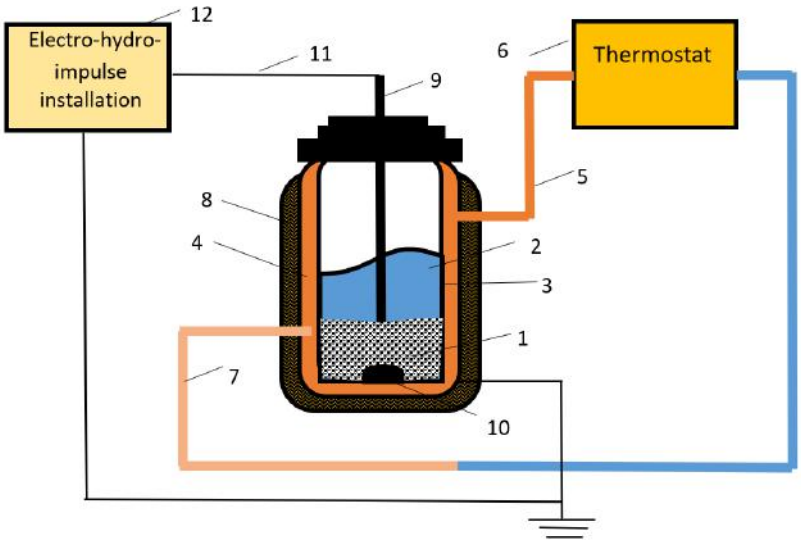

Fig. 1. General view of the laboratory EHP installation working cell.

Fig. 2 shows the dependence of the number of electric discharge pulses (n) on the change in the interelectrode distance l in the air spark gap (12), Fig.1. The number of electric discharge pulses was recorded using an electronic oscilloscope. It has been experimentally established that if the air gap electrodes are installed at a distance of 7 mm, then with a capacitor bank capacity of C2 = 0.25 μF, 720 electric discharge pulses can be produced in 5 minutes. With a capacity of C1=0.4 μF, the number of electric discharge pulses decreases to 600. For an interelectrode distance in an air gap equal to 9 mm with similar capacity values, the number of pulse discharges changes from 530 to 460, respectively.

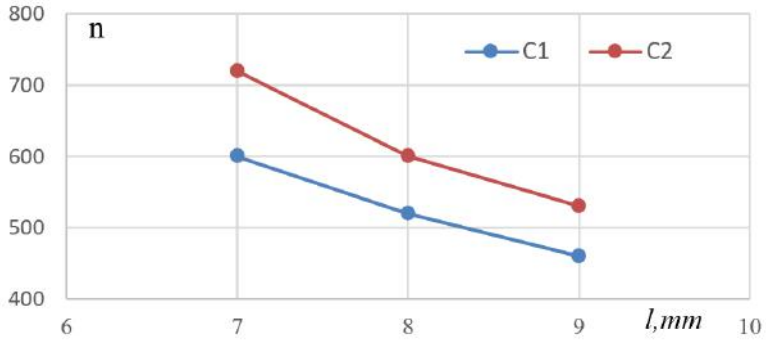

Fig.2. Dependence of the pulses number on the interelectrode distance in an air gap at different capacitance values.

It should be noted that the choice of this range of variation of the interelectrode distance *l* in the air spark gap is explained by achieving the optimal voltage value required to obtain a discharge breakdown. Multiple tests have shown that in this range of the interelectrode distance of the EHP air spark gap, the installation with this working cell operates in a stable mode. The probability of random premature discharges is reduced and complete discharge of the capacitors is ensured, which ensures obtaining a sufficient value of discharge energy to form shock waves. In the experiments, crushed cattle bones, which are waste from the food industry, were used as the processed organic raw material. To obtain raw material samples that are placed in a working container for EHP processing, the bones were crushed to particles of 2 mm to 10 mm in size and preliminarily placed in water.

In subsequent experiments, the duration of the EHP treatment was increased from 5 min to 30 min, while the number of received electric discharge pulses was from 1750 to 3000 with a specific energy of 1.8÷104 J/m. The difference of this EGI treatment technology is in the additional heating of the processed raw material using a water jacket in the temperature range from 32°C to 50°C. This is due to the fact that earlier the authors in the laboratory of hydrodynamics and heat transfer of the E.A. Buketov KarU conducted experiments with heating

the processed raw material in the temperature range from 32°C to 38°C [19]. However, a detailed analysis of the raw material samples after EHP treatment showed that the valuable component was not extracted from the bone fractions completely enough.

3. Results and discussion

Experiments to study the electrophysical parameters and determine the optimal values of the operation energy modes of the (EHP) installation were carried out in the Laboratory of hydrodynamics and heat exchange of the E.A. Buketov Karaganda University. Taking into account the previously obtained research results of the authors [20], in order to achieve more intensive extraction of the valuable component from the organic raw material, the mixture was heated using the so-called "water jacket" in the temperature range from 10°C to 50°C. The effect of the temperature mode of heating the samples of organic raw materials on the extraction of the valuable component in the absence and presence of EHP treatment is shown in Figure 3.

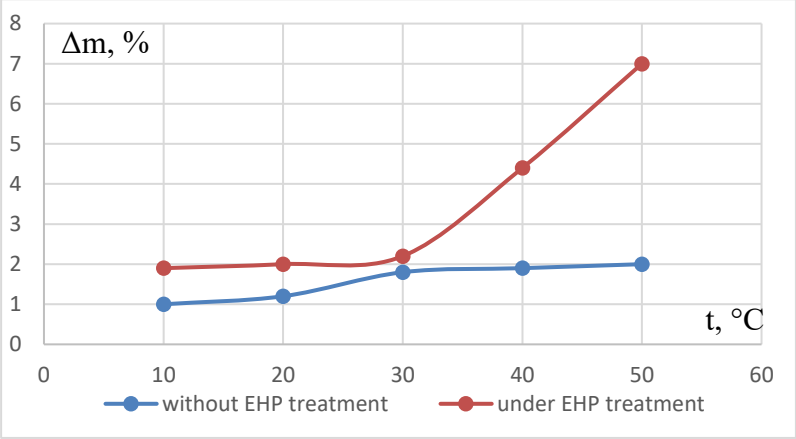

Fig.3. Dependence of a valuable component the extraction from organic waste materials on temperature without and under EHP treatment.

In the experiments, samples of two types of organic waste with solid bone fraction sizes of 2 mm were studied. These organic waste samples were pre-placed in water for 24 hours. This method for preparing samples from organic waste is described in detail in [17]. Figure 4 shows the change in the extracted mass of the valuable component (Δm, %) depending on the capacity of the capacitor bank during EHI processing of a mixture with crushed fractions of organic waste samples.

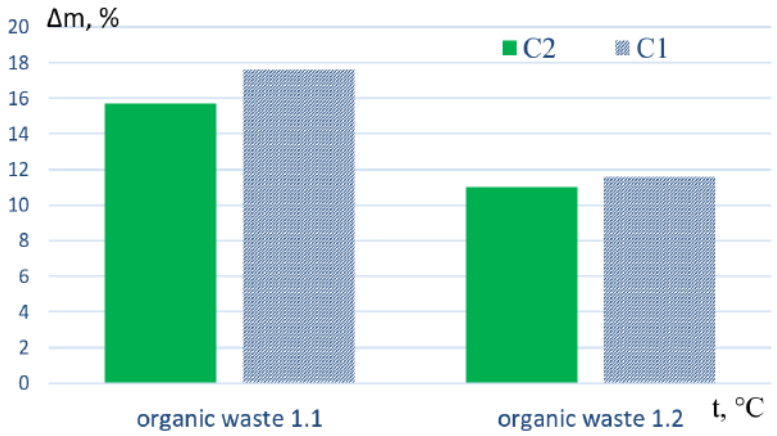

Fig.4. Dependence of extraction of valuable components from samples of two types organic waste at values of capacitor bank capacity C1 = 0.25 μF and C2 = 0.4 μF.

It is evident that water, which has saturated the bone mass structure, helps to enhance the destruction and extract valuable components from these organic wastes much more effectively. In organic waste 1.1, with a

capacitor capacity of 0.25 μF, the extraction was 15.7%. With an increase in the capacitor capacity to 0.4 μF, the extraction of organic waste increases to 17.6%. And in organic waste 1.2, with an increase in the capacitor capacity, the extraction rate increased from 11.0% to 11.6. The graphs show that the extraction intensity can stabilize with capacity growth. This allows us to determine the optimal capacity values required to reproduce the experiments. Each point of the experimental graph represents the average value of 5 consecutive measurements; the average deviation does not exceed 3%.

Similar dependencies were obtained for organic waste samples with solid fraction diameters of 5 mm and 10 mm. However, the value of extraction of the valuable component from organic waste with these solid fraction size values remained virtually unchanged.

4. Conclusion

The results of the conducted experimental studies showed that the use of technology based on the generation of an electric pulse discharge in a liquid medium has prospects for the intensification of extraction processes. As a result of multiple experimental tests, it was found that this mode of electro-hydro-pulse treatment with the specified parameters is implemented with the lowest energy costs, i.e. it is economically advantageous. It was experimentally established that for a given working capacity, the most energetically advantageous is EHP processing with a capacitor capacitance value 0.4 μF.

Optimization of the energy parameters of the electro-hydro-pulse installation for the efficient extraction of a valuable component from secondary raw materials requires an integrated approach, including the study of the influence of various factors, such as discharge energy, pulse frequency, electrode configuration and ambient temperature. The study showed that the correct combination of these parameters can significantly increase the efficiency of bone mass fraction destruction, which contributes to an increase in the yield of the valuable component with minimal energy costs.

Conflict of interest statement

The authors declare that they have no conflict of interest in relation to this research, whether financial, personal, authorship or otherwise, that could affect the research and its results presented in this paper.

Credit author statement

Duisenbayeva, M.S.: investigation, formal analysis; writing-original draft; **Schrager E.R.:** supervision, conceptualisation; **Sakipova S.E.:** data curation, writing – review & editing; **Nussupbekov B.R.:** project administration, methodology.
The final manuscript was read and approved by all authors.

Funding

This research is funded by the Science Committee of the Ministry of Science and Higher Education of the Republic of Kazakhstan (AP26102107).

References

1 Gielen D., Boshell F., Saygin D., Bazilian M.D., Wagner N., Gorini R. (2019) The role of renewable energy in the global energy transformation. *Energy Strategy Reviews,* 24, 38 -50. https://doi.org/10.1016/j.esr.2019.01.006

2 Sharma R., Choudhary P., Thakur G., Pathak A., Singh S., Kumar A., Lo Sh-L., Kumar P. (2025) Sustainable management of biowaste to bioenergy: A critical review on biogas production and techno-economic challenges. *Biomass and Bioenergy*, 196, 107734. https://doi.org/10.1016/j.biombioe.2025.107734

3 Kudimov Yu.N., Kazub V.T., Golov E.V. (2022) Electric discharge processes in liquids and kinetics of extraction of biologically active components. *Bulletin of TSTU*, 8, 2, 253 – 264. Available at: http://vestnik.tstu.ru/rus/t_8/pdf/82010.pdf [in Russian]

4 Sakipova S.E., Nussupbekov B.R., Ospanova D.A., Khassenov A.K., Sakipova Sh.E. (2015) Effect of electric pulse processing on physical and chemical properties of inorganic materials. *IOP Conf. Ser.: Materials Science and Engineering,* 81, 12051 – 12056. https://doi.org/10.1088/1757-899X/81/1/012051.

5 Nussupbekov B., Sakipova, S., Edris, A., Khassenov, A., Nussupbekov, U., Bolatbekova, M. (2022) Electrohydraulic method for processing of the phosphorus containing sludgers. *Eurasian Physical Technical Journal*, *19*, 1(39), 99–104. https://doi.org/10.31489/2022No1/99-104

6 Kazub V.T., Orobinskaya V.N., Pisarenko O.N. The advantages of modern nonthermal of processing the technology of organic raw material. M*odern science and innovations*. 2013; (3). 82-93. Available at: https://msi.elpub.ru/jour/article/view/1266 [in Russian]

7 Panov V. A., Vasilyak L.M., Vetchinin S.P., Pecherkin V.Ya., Son E.E. (2016) Pulsed electrical discharge in conductive solution. *Journal of Physics D: Applied Physics*, 49, 38, 385 – 202. https://doi.org/10.1088/0022-3727/49/38/385202

8 Khavari M., Priyadarshi A., Morton J., Porfyrakis K., Pericleous K., Eskin D., Tzanakis I. (2023) Cavitation-induced shock wave behaviour in different liquids. *Ultrasonics Sonochemistry*, 94 106328, 1 – 11. https://doi.org/10.1016/j.ultsonch.2023.106328

9 Kondrat O., Shumilin T. (2023) Electrohydraulic Yutkin effect and electrospark discharges in liquids. *Prospecting and Development of Oil and Gas Fields,* https://doi.org/10.69628/pdogf/3.2023.61

10 Budagova N.V. (2024) Analysis of characteristics of electric discharges in a water-air environment. *Bulletin of Science*, 5 (74), 2, 757 – 762. Available at: https://www.вестник-науки.рф/article/14442 [in Russian]

11 Gershman S., Belkind A. (2010) Time-resolved processes in a pulsed electrical discharge in argon bubbles in water. *The European Physical Journal D*, 60, 3, 661–672. https://doi.org/10.1140/epjd/e2010-10258-0

12 Tereshonok D., Babaeva N.Yu., Naidis G. V. &Smirnov B.M. (2016) Hydrodynamical flows in dielectric liquid in strong inhomogeneous pulsed electric field. *Journal of Physics D: Applied Physics*, 49, 50, 505501. https://doi.org/10.1088/0022-3727/49/50/505501

13 Gürgül S., Erdal N., Yilmaz S.N., Yildiz A., Ankarali H. (2008) Deterioration of bone quality by long-term magnetic field with extremely low frequency in rats. *Bone,* 42(1), 74 - 80. https://doi.org/10.1016/j.bone.2007.08.040

14 Mankowski J, Kristiansen M. (2000) A review of short pulse generator technology. *IEEE Transactions on Plasma Science*, 28. 102-108. https://doi.org/10.1109/27.842875

15 Schoenbach K.H., Katsuki S., Stark R.H., Buescher E.S., Beebe S.J. (2002) Bioelectrics-new applications for pulsed power technology. *IEEE Trans Plasma Sci*., 30(1). 293–300. https://doi.org/10.1109/TPS.2002.1003873

16 Babaeva N.Y., Tereshonok D.V., Naidis G.V. (2015) Initiation of breakdown in bubbles immersed in liquids: pre-existed charges versus bubble size. *Journal of Physics D: Applied Physics*, 48, 35, 355201. https://doi.org/10.1088/0022-3727/48/35/355201

17 Nussupbekov B.R., Duisenbayeva M.S. (2023) Processing of organic waste by electrohydroimpulse method. *Bulletin of the Karaganda University. Physics Series,* 111(3), 156 – 162. https://doi.org/10.31489/2023PH3/156-162

18 Nussupbekov B.R., Duisenbayeva M.S., Kartbayeva G.T., Kurmanaliev A.B., Abduvakhidov M.I., Sabit R.D. (2024) Method for degreasing crushed bone. Patent for Utility Model, No. 9548, 2024/0768.2 Publ. 14.06.2024. Available at: https://gosreestr.kazpatent.kz/Utilitymodel/DownLoadFilePdf?patentId=400715&lang=ru [in Russian]

19 Kartbayeva G., Duisenbayeva M., Nussupbekov B., Mussenova E., Smagulov Z., Kurmanaliev A. (2024) Identification of the energy parameters of an electrohydroimpulse plant for the production of valuable components from organic raw materials. *Eastern-European Journal of Enterprise Technologies*, 3, 11 (129), 6 – 13. https://doi.org/10.15587/1729-4061.2024.306787

AUTHORS' INFORMATION

Duisenbayeva, Moldir Sekikbekovna – PhD student, Master (Sci.), Department of Engineering Thermophysics named after professor Zh.S. Akylbayev, E.A. Buketov Karaganda University, Karaganda, Kazakhstan; Scopus Author ID: 57211793991; https://orcid.org/0000-0003-3733-7662 ; m o l d i r 89@mail.ru

Schrager, Ernst Rafailovich - Doctor of Physical and Mathematical Sciences, Professor, National Research Tomsk State University, Tomsk, Russia; Scopus Author ID: 55956811200; https://orcid.org/0000-0002-7178-4071, sher@mail.tsu.ru

Sakipova, Saule Erkeshevna - Candidate of Physical and Mathematical Sciences, Professor, Department of Engineering Thermophysics named after professor Zh.S. Akylbayev, E.A. Buketov Karaganda University, Karaganda, Kazakhstan; Scopus Author ID: 6504154211; https://orcid.org/0000-0002-7505-8413; sakipova1607@gmail.com

Nussupbekov, Bekbolat Rakishovich - Candidate of Technical Sciences, Professor, Vice Rector for Academic Affairs of Karaganda Technical University named after Abylkas Saginov, Karaganda, Kazakhstan; Scopus Author ID: 56289675900, https://orcid.org/0000-0003-2907-3900 , bek_nr1963@mail.ru

EURASIAN PHYSICAL TECHNICAL JOURNAL

2025, Volume 22, No.2 (52)

https://doi.org/10.31489/2025N2/60-69

Received: 03/02/2025 Revised: 05/05/2025 Accepted: 25/06/2025 Published online: 30/06/2025

Original Research Article

UDC 532.517.4

STUDY OF THERMOPHYSICAL DYNAMICS IN BIOFUEL DROPLET ATOMIZATION AND COMBUSTION

Askarova A.[1], Bolegenova S.[1], Ospanova Sh.[1*], Maxutkhanova A.[1], Bolegenova K.[1], Baidullayeva G.[2]

[1] Al-Farabi Kazakh National University, Almaty, Kazakhstan
[2] Asfendiyarov Kazakh National Medical University, Almaty, Kazakhstan
*Corresponding author: Shynar.Ospanova@kaznu.edu.kz

Abstract. *The article presents a study of computer modeling of thermophysical processes occurring during atomization and turbulent combustion of biofuel (biodiesel) droplets in the combustion chamber of a direct injection engine. For this purpose, a complex computer model was developed, including mathematical, spatial, and numerical submodels for calculating a complex turbulent reacting flow. Using the developed model, computational experiments were performed to investigate the thermal and aerodynamic properties of the reacting fuel-air mixture of biodiesel, focusing on the effects of temperature and pressure variations in the combustion chamber. The research results made it possible to obtain a visualization of the reacting flow with temperature and concentration characteristics of harmful emissions during biodiesel combustion. The numerical data obtained during the modeling were compared with the results for traditional diesel fuel.*

Keywords: bioenergetics, biofuel, atomization, complex model, common rail system, visualization, harmful emissions.

1. Introduction

Biodiesel production is experiencing rapid growth globally, driven by the increasing demand for eco-friendly fuels. Derived from vegetable oils, animal fats, or waste, biodiesel is a renewable energy source. Key producers include the United States, Brazil, Germany, and Indonesia, where transesterification technologies are employed to convert oils into biodiesel [1-4]. The widespread adoption of biodiesel plays a crucial role in reducing dependence on fossil fuels and cutting greenhouse gas emissions, thereby contributing to the improvement of the global environmental landscape.

Biodiesel production in Kazakhstan is developing in response to the growing interest in renewable energy sources and environmentally friendly technologies. The country has significant agricultural potential, which allows the use of vegetable oils such as rapeseed and sunflower oil, as well as agricultural waste, to produce biodiesel. Biodiesel in Kazakhstan is used in such industries as transport and energy, helping to reduce dependence on fossil fuels and improve the environmental situation. However, the development of this sector faces several challenges, including high initial costs, insufficient infrastructure, and the lack of full legislative support. Nevertheless, given global trends in the field of ecology and energy, Kazakhstan is actively working to improve biodiesel production technologies and create conditions for its widespread implementation in the future.

In 2013, specific targets were set for the development of the renewable energy sector, which made it possible to determine the market size and potential for reducing greenhouse gas emissions. Within the framework of the Concept of Kazakhstan's Transition to a "Green" Economy and the "Kazakhstan-2050

Strategy", the desire was set to increase the share of alternative and renewable energy sources in the country's energy balance to 15% by 2030 and to 50% by 2050 (Figure 1) [5].

In this regard, Bio Operations LLP is the flagship for deep grain processing in Kazakhstan. The company produces high-tech products: biodiesel, bioethanol, wheat gluten, and starch. The products are certified by FSSC 22000 and ISCC, and exported to India, the USA, Colombia, Norway, the CIS countries, and the EU. The plant is the largest producer of gluten and starch in Kazakhstan and bioethanol in the CIS [6].

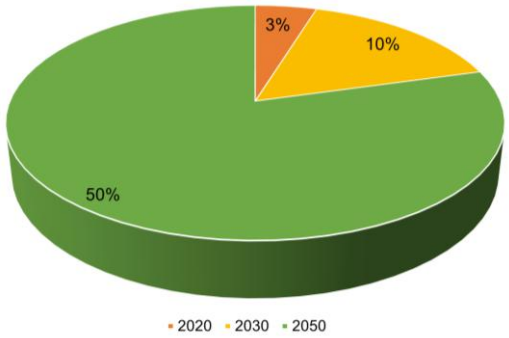

Fig.1. Development of renewable energy sources in Kazakhstan [5]

In this work, the thermophysical processes of atomization and combustion of biodiesel droplets in the model chamber of a direct injection engine are studied. Based on the developed complex computer model, studies of the thermal, aerodynamic, and concentration characteristics of biodiesel droplets during their spraying in a reacting flow were carried out.

2. Mathematical, spatial and physical models of the problem

The mathematical model of liquid fuel droplet combustion includes equations of continuity, momentum, energy, and concentration of reacting components in a two-phase flow [7-9].

The continuity equation for the gas phase of a dispersed system has the following form:

$$\frac{\partial \rho}{\partial t} + \mathrm{div}(\rho \mathbf{u}) = S_{mass}, \tag{1}$$

where u fuel drop velocity, S_{mass} is a local change in gas density caused by evaporation or condensation processes in a two-phase flow.

The equation of conservation of momentum for a gas is written as follows:

$$\rho \frac{\partial u}{\partial t} + \rho(\mathrm{grad}\mathbf{u})\mathbf{u} = \mathrm{div}\boldsymbol{\xi} + \rho\mathbf{g} + S_{mom}, \tag{2}$$

where S_{mom} represents the local rate of change of momentum in the gas phase caused by the movement of droplets.

The equation for the conservation of internal energy has the following form:

$$\rho \frac{\partial E}{\partial t} = \boldsymbol{\tau}:\mathbf{D} - \rho \mathrm{div}\mathbf{u} - \mathrm{div}\mathbf{q} + S_{energy}, \tag{3}$$

where **q** is the specific heat flux corresponding to Fourier's law of heat transfer, and S_{energy} means the contribution to the change in internal energy caused by the sprayed liquid or phase.

The equation for the conservation of concentration of component m is written in the following form:

$$\frac{\partial(\rho c_m)}{\partial t} = -\frac{\partial(\rho c_m u_i)}{\partial x_i} + \frac{\partial}{\partial x_i}\left(\rho D_{c_m} \frac{\partial c_m}{\partial x_i}\right) + S_{mass}, \tag{4}$$

where ρ_m is the mass density of a component m, which denotes the amount of mass of this component contained in a unit volume, ρ is the total mass density, which is the sum of the masses of all components contained in a unit volume of the systemю

The k-ε turbulence model is used to simulate turbulent flow in various engineering problems, including fuel-air mixtures. In this model, two transport equations describe the turbulent kinetic energy (k) and its dissipation (ε), which allows the prediction of turbulence parameters such as the velocity and distribution of turbulent flows [10, 11]:

$$\rho\frac{\partial k}{\partial t}+\rho\frac{\partial \overline{u}_j k}{\partial x_j}=\frac{\partial}{\partial x_j}\left[\left(\mu+\frac{\mu_t}{\sigma_k}\right)\frac{\partial k}{\partial x_j}\right]\frac{\partial \overline{u}_i}{\partial x_j}+G-\frac{2}{3}\rho k\delta_{ij}\frac{\partial \overline{u}_i}{\partial x_j}-\rho\varepsilon, \quad (5)$$

$$\rho\frac{\partial \varepsilon}{\partial t}+\rho\frac{\partial \overline{u}_j \varepsilon}{\partial x_j}-\frac{\partial}{\partial x_j}\left[\left(\mu+\frac{\mu_t}{\sigma_\varepsilon}\right)\frac{\partial \varepsilon}{\partial x_j}\right]=c_{\varepsilon_1}\frac{\varepsilon}{k}G-\left[\left(\frac{2}{3}c_{\varepsilon_2}-c_{\varepsilon_3}\right)\rho\varepsilon\delta_{ij}\frac{\partial \overline{u}_i}{\partial x_j}\right]-c_{\varepsilon_2}\rho\frac{\varepsilon^2}{k}. \quad (6)$$

Constant parameters of the calculation model, such as c_{ε_1}, c_{ε_2}, c_{ε_3}, σ_k, σ_ε, are typically determined through experimental methods [12]. This is important for more accurate modeling of combustion, fuel atomization, and aerodynamic characteristics in engines.

In this study, a prototype of the common rail fuel injection system, commonly employed in modern diesel engines, was utilized. In such a system, fuel is supplied under high pressure to a common manifold, from where it is evenly distributed to the injectors, which spray it into the combustion chamber. This fuel system refers to direct injection injectors with multiple holes. The schematic design of this system is shown in Figure 2 [13]. Due to the precise dosage of fuel and the ability to change the injection time, the common rail system allows the reduction of harmful emissions such as nitrogen oxides and carbon compounds, which helps to comply with environmental standards.

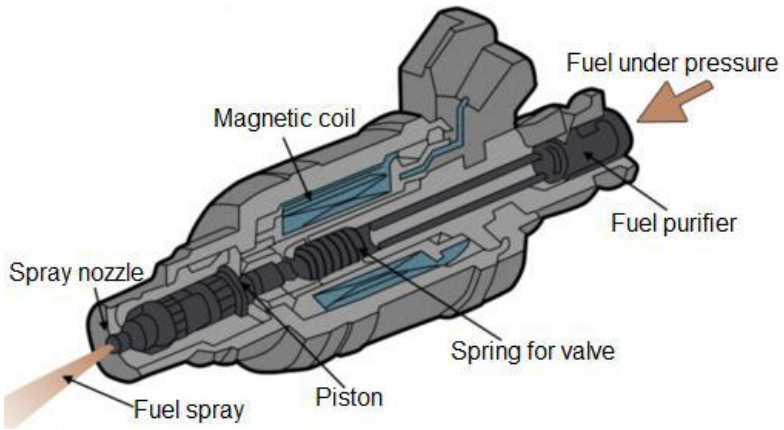

Fig.2. The cross-section of a common rail fuel injector [13]

The system uses a fuel filter to clean the fuel before it enters the system, and a high-pressure cylinder pump to increase the fuel pressure needed for the injectors to operate properly. All these components work together to ensure optimal combustion, increased power, and minimized harmful emissions in modern diesel engines. The CHEMKIN program was used to model the chemical kinetics of biodiesel combustion, which allows the creation of a reaction mechanism that describes the thermodynamics and kinetics of biodiesel combustion, as well as the interaction of fuel with an oxidizer [14, 15]. The system takes into account such parameters as temperature, pressure, and flow rate, which allows for accurate modeling of the combustion process, including the formation of pollutants (CO, CO_2) and evaluation of combustion efficiency.

In this work, pure rapeseed biodiesel Biofuel RME B100 was used as biofuel, which is a mixture of fatty acid methyl esters (FAME) obtained from rapeseed oil. The main component is methyl oleate ($C_{19}H_{36}O_2$) - a monounsaturated ester, which makes up to 90% of the total composition, with admixtures of saturated and polyunsaturated esters. The use of RME in the conditions of Kazakhstan is justified, since it has increased resistance to low temperatures, which is critically important for the northern regions of the country. In addition, the agroclimatic resources of Kazakhstan are favorable for growing rapeseed, which makes RME production sustainable and economically feasible at the national level.

Dodecane ($C_{12}H_{26}$) was used as a model diesel fuel because its combustion characteristics, as well as its physicochemical properties such as boiling point, viscosity and cetane number, are closest to those of biodiesel among simple hydrocarbons. Due to these properties, dodecane is widely used in research as a reference compound for modeling combustion processes of diesel fuel.

The equations for the complete combustion of biodiesel and petroleum diesel fuel under internal combustion engine conditions with the participation of air are presented as follows:

$$C_{19}H_{36}O_2+27O_2+101{,}52N_2=19CO_2+18H_2O+101{,}52N_2\,,$$

$$C_{12}H_{26}+18.5O_2+69.56N_2=12CO_2+13H_2O+69.56N_2.$$

In the engine, biodiesel burns with the formation of CO_2 and H_2O, releasing thermal energy sufficient for its operation, but having a slightly lower energy density compared to petroleum diesel fuel.

For comparison purposes, Table 1 presents the values of the physicochemical characteristics of the fuels (biodiesel and diesel fuel) used in the computational experiments [12].

Table 1. Physicochemical characteristics of biodiesel and diesel fuel

Parameter	Diesel fuel	Biodiesel
Chemical formula	$C_{12}H_{26}$	$C_{19}H_{36}O_2$
Chemical class	alkanes (paraffins)	esters (methyl esters)
Flash point	46°C	130°C
Viscosity (at t=20°C)	1.3–1.5 cSt	4.0–5.0 cSt
Density (at t=15°C)	0.752–0.765 g/cm^3	0.86–0.88 g/cm^3
Surface tension (at t=20°C)	~26.0–28.0 mN/m	~30.0–32.0 mN/m
Cetane number	52	52
Compression ratio	18	18

3. Modeling results and analysis

This paper presents a comprehensive study of computer modeling of the thermophysical processes of atomization and combustion of biodiesel droplets in a model combustion chamber. A comparatives analysis is conducted aimed to determine the efficient fuel combustion parameters that ensure maximum combustion efficiency. Figure 3 shows the temperature distribution of biodiesel and petroleum diesel droplets at 50 mm from the injector nozzle. The results of computer modeling showed that the maximum combustion temperature of the biodiesel fuel-air mixture reaches approximately 3000 K, while the highest combustion temperature of diesel fuel does not exceed 1400 K [16]. From these data, it follows that biodiesel has a significantly higher combustion temperature, which can lead to higher combustion efficiency and heat transfer. Because biodiesel has a high flash point, which makes it safer to handle than conventional diesel fuel. During the study of the distribution of aerodynamic characteristics of fuels depending on the pressure in the combustion chamber, it was found that with increasing pressure, the velocities of biodiesel and diesel droplets also increase. It follows that an increase in pressure in the combustion chamber contributes to an increase in the droplet velocity, which can affect the combustion process and the efficiency of the heat engine. The results of computational experiments showed that at a pressure of 60 bar, the maximum velocity of biodiesel droplets reaches 33 m/s, while diesel droplets have a velocity of 25 m/s, which confirms the greater mobility of biodiesel droplets (Figure 4).

Increasing the pressure and temperature in the combustion chamber increases the speed of the fuel droplets. This can affect the atomization, mixing, and combustion processes of the fuel. Biodiesel has greater droplet mobility, confirmed by a higher droplet speed. This indicates better atomization and more efficient mixing with air, which can improve combustion processes and lead to more complete combustion. Also, the efficiency of a heat engine can be improved when using biodiesel due to better atomization of the droplets, which contributes to more efficient combustion of the fuel and, possibly, to a reduction in carbon emissions and other harmful substances.

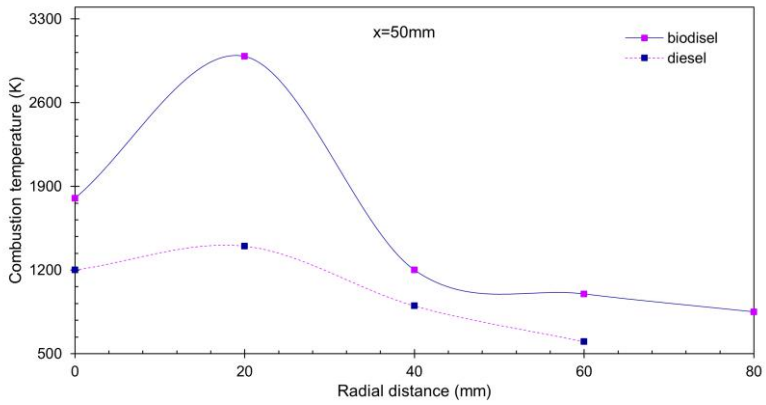

Fig.3. Combustion temperature distribution of fuel droplets

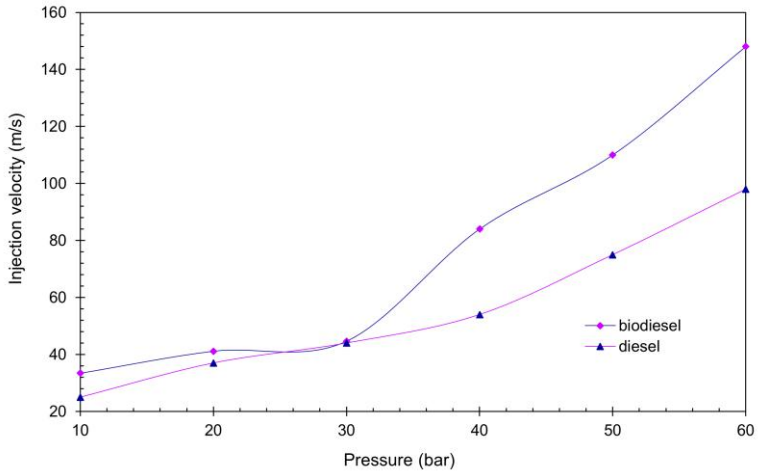

Fig.4. Distribution of biodiesel and diesel droplet velocities as a function of combustion chamber pressure

The spray area of both fuels is between 0.43 and 1.3 cm along the combustion chamber height (Fig.5). Since biodiesel droplets have a higher velocity, their spray area is located higher than that of petroleum diesel droplets. The reason for this phenomenon is that biodiesel droplets have a higher velocity, which allows them to travel a greater distance in the combustion chamber before they interact with air. The higher spray velocity contributes to the longer droplet spread, which leads to their location higher along the combustion chamber height compared to petroleum diesel droplets (Fig.5).

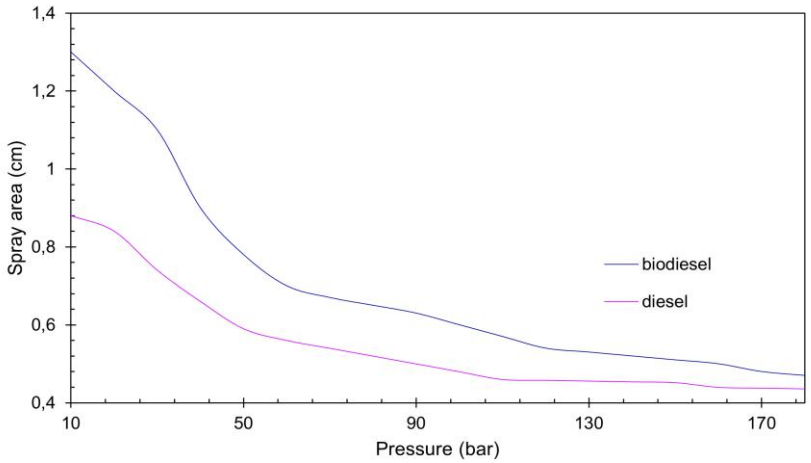

Fig.5. Spray areas of biodiesel and conventional diesel droplets

Based on the computational experiments conducted, a visualization of the reacting flow was obtained. Figure 6 shows the temperature profiles of biodiesel fuel at a time of 3 ms. It is evident from the figure that in the core of the torch the temperature reaches its maximum, about 3000 K. The height of the temperature torch is 4.2 cm of the combustion chamber, and in the rest of the chamber, the temperature remains within 2300-2500 K. Figure 7 shows the distribution of concentration fields of carbon dioxide CO_2 during combustion of biodiesel droplets at a time of 3 ms. The maximum concentration of CO_2 reached 0.183 g/g, while the minimum value was 0.012 g/g. The maximum concentration of carbon dioxide will be observed in the center of the combustion chamber, in the area where the main combustion of the fuel occurs. This is because, in the center of the torch, the temperature and density of the reactive substances are maximum, which contributes to the more intensive formation of carbon dioxide. However, at the exit from the combustion chamber, the concentration of carbon dioxide will be somewhat reduced since the processes of cooling and dilution of gases are already taking place here. Reducing CO_2 emissions from heat engines is an important step towards improving the environmental situation and combating climate change [17]. Biofuels emit significantly less carbon dioxide when burned than traditional fuels. Moreover, some biofuels can be carbon neutral if their production and use are optimized.

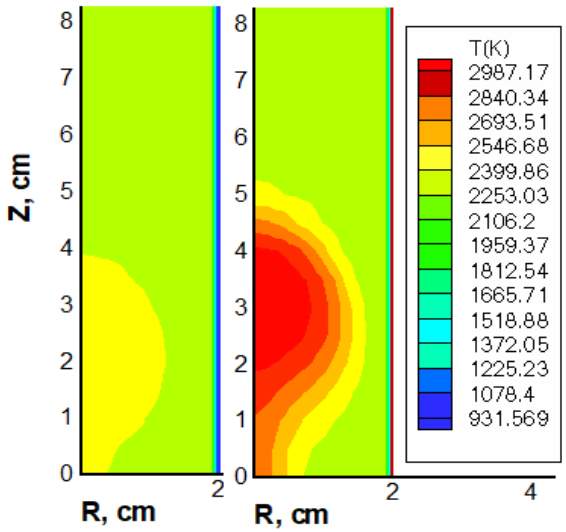

Fig.6. Temperature profiles of biodiesel droplets at t=3 ms

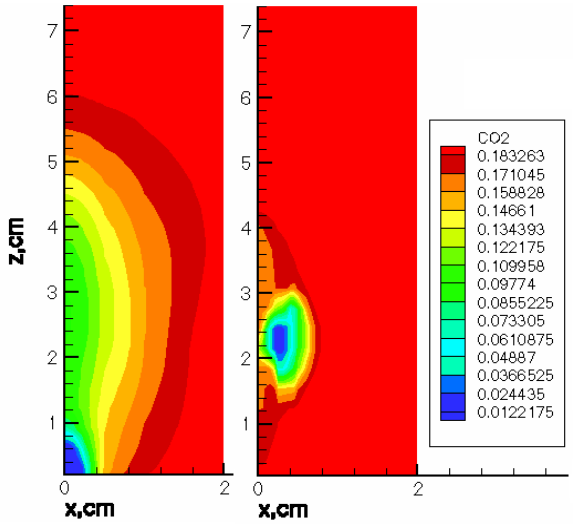

Fig.7. Concentration fields of carbon dioxide during combustion of biodiesel at t=3 ms

Figure 8 shows the dispersion of biodiesel droplets by specific temperature. In the upper part of the combustion chamber, the maximum specific temperature of biodiesel droplets reaches 655 K, while in the lower part, there are droplets with a temperature of 300-400 K.

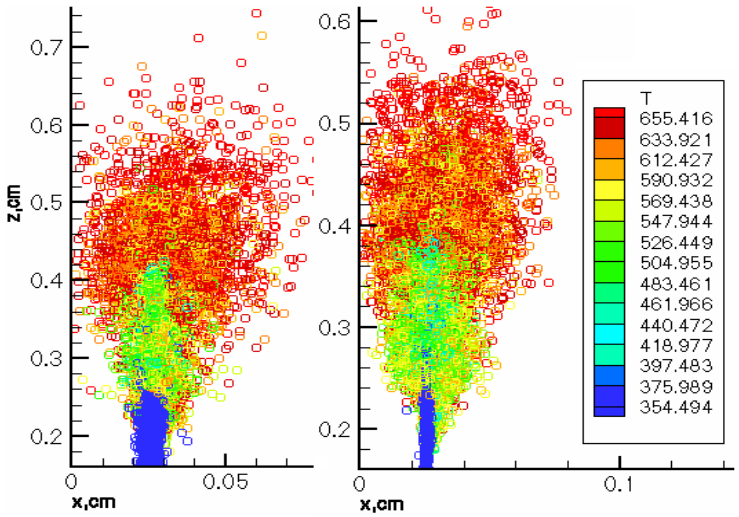

Fig.8. Dispersion of biodiesel droplets by specific temperature at t=3 ms

This is because, in the upper part of the combustion chamber, biodiesel droplets are exposed to a more intense effect of high temperatures formed in the core of the torch, where the main combustion occurs. While in the lower part of the chamber, the temperature is lower due to a more remote location from heat sources and less exposure to high-temperature gases.

Figure 9 shows the distribution of carbon monoxide concentration CO during biodiesel combustion. As can be seen, the concentration of CO remains low enough, which confirms the complete combustion of the fuel with the oxidizer without residual products. It follows that the combustion process of biodiesel occurs efficiently and completely, without the formation of significant amounts of intermediate products, such as carbon monoxide. This indicates high combustion quality and minimal emissions of harmful substances.

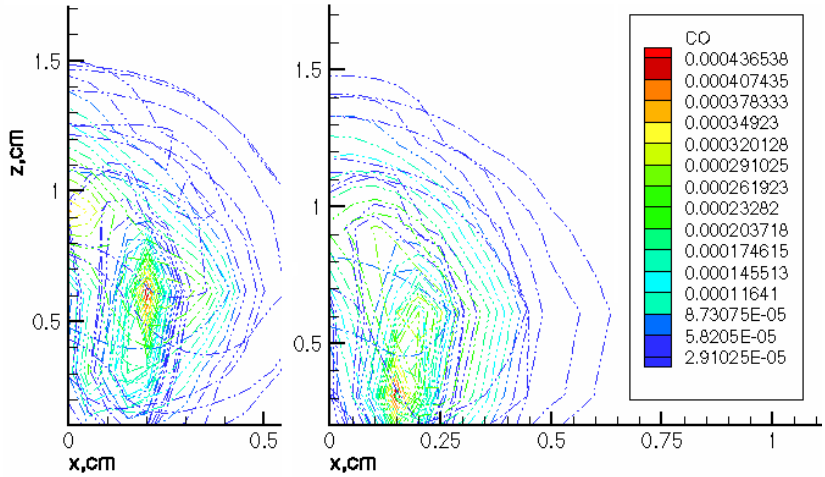

Fig.9. Concentration fields of carbon monoxide during biodiesel combustion at t=3 ms

Complete combustion of biodiesel with minimal emissions of carbon monoxide has a positive effect on the operation of the heat engine. This contributes to more efficient use of fuel energy, improves the thermal performance of the engine, and reduces environmental pollution [18]. In addition, the absence of incomplete combustion residues reduces the risk of carbon deposits accumulating in the combustion chamber, which can extend the service life of the engine and reduce the need for maintenance.

Figure 10 shows the results of computational experiments showing the change in the time distributions of the Sauter mean diameter (SMD) of diesel and biodiesel fuel droplets at 40 mm from the injector nozzle. The Sauter mean diameter is the average volume-surface diameter of the droplets. The same figure presents a comparison between the calculated data for diesel fuel [19] and the experimental results provided in [20].

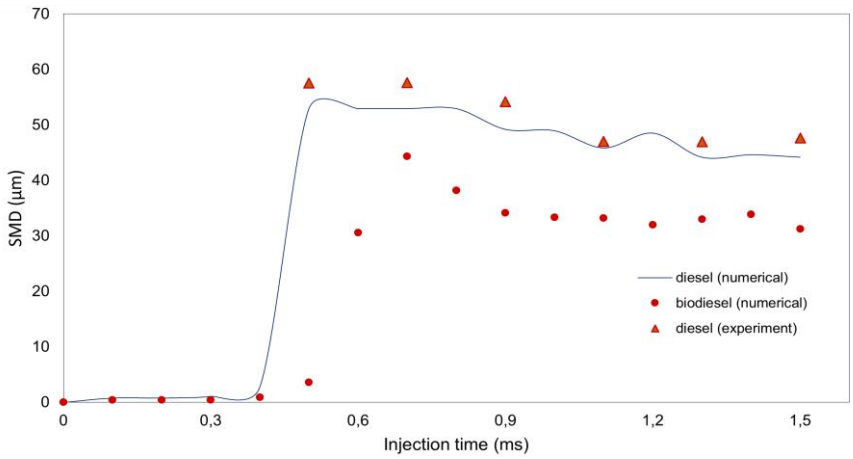

Fig. 10. Comparison of time distributions of the Sauter mean diameters (SMD) of diesel and biodiesel droplets with an experiment at 40 mm from the injector nozzle

As can be seen from the graph, the calculated data for diesel fuel is in good agreement with the experimental results. Biodiesel droplets exhibit a smaller volume-surface diameter compared to diesel droplets, which can be attributed to the lower surface tension coefficient and distinct molecular structure of biodiesel. These characteristics promote finer atomization. Additionally, biodiesel's improved flow properties contribute to the formation of smaller droplets during atomization. Together, these factors enhance atomization efficiency and result in a smaller Sauter mean droplet diameter.

4. Conclusions

Based on the research conducted on modeling of thermophysical processes of spraying and combustion of biodiesel fuel droplets, the following conclusions can be made:

1. The maximum combustion temperature of the fuel-air mixture of biodiesel reaches about 3000 K, while for diesel fuel this temperature does not exceed 1400 K. This indicates a higher combustion temperature of biodiesel, which can lead to improved combustion efficiency and heat transfer;

2. At a combustion chamber pressure of 60 bar, the maximum speed of biodiesel droplets is 33 m/s, while for diesel droplets it is 25 m/s. This confirms the greater mobility of biodiesel droplets, which contributes to better atomization and more complete mixing with air, which improves combustion processes and the efficiency of the heat engine;

3. The spray area for both fuels varies from 0.43 to 1.3 cm in the combustion chamber height. Biodiesel droplets, due to their higher speed, have a higher spray area, which allows them to reach more distant areas of the combustion chamber;

4. In the flame core, the temperature of the biodiesel fuel reaches a maximum value of about 3000 K. The temperature in the upper part of the combustion chamber flame is 2300-2500 K, which confirms the high combustion temperature in the center of the flame and lower temperatures in the rest of the chamber;

5. The concentration of carbon dioxide (CO_2) during biodiesel combustion reaches a maximum of 0.183 g/g in the center of the combustion chamber, where the temperature and density of the reactants are maximum, and a minimum of 0.012 g/g after the gases leave the chamber. At the same time, the concentration of carbon monoxide (CO) remains low, which confirms the complete combustion of the fuel with the oxidizer and the absence of significant carbon monoxide residues. These data indicate high efficiency of biodiesel combustion and minimal emissions of harmful substances;

6. From the computational experiments, it is evident that biodiesel droplets have a smaller Sauter mean diameter compared to diesel droplets. This is explained by the lower surface tension coefficient and molecular structure of biodiesel, which contributes to finer atomization and improved mixing with air. The computational results show that biodiesel has better atomization characteristics, which leads to more efficient combustion;

7. The reduction of CO_2 and carbon monoxide emissions from biodiesel combustion contributes to a better environmental situation. Biodiesel not only emits less CO_2 than diesel fuel, but can also be carbon neutral if its production and use are optimized. It also contributes to improved efficiency of heat engines and a lower environmental impact.

Conflict of interest statement

The authors declare that they have no conflict of interest in relation to this research, whether financial, personal, authorship or otherwise, that could affect the research and its results presented in this paper.

Credit author statement

Askarova A.S.: Supervision; **Bolegenova S.A.:** Conceptualization, Funding acquisition**; Ospanova Sh.S.:** Investigation, Writing Reviewing and Editing; **Maxutkhanova A.:** Resources, Software; **Bolegenova K.:** Data curation, Methodology, Investigation; **Baidullayeva G.:** Visualization, Validation.

The final manuscript was read and approved by all authors.

Funding

This work was supported by the Science Committee of the Science and Higher Education Ministry of the Republic of Kazakhstan (No AP19679741).

References

1 Macheli L., Malefane M.E., Jewell L.L. (2025) Waste-derived calcium oxide catalysts in biodiesel production: Exploring various waste sources, deactivation challenges, and improvement strategies, *Bioresour. Technol*., 29, 102021. https://doi.org/10.1016/j.biteb.2025.102021

2 Ogunkunle O., Ahmed N.A. (2019) A review of global current scenario of biodiesel adoption and combustion in vehicular diesel engines, *Energy Reports*, 5, 1560–1579. https://doi.org/10.1016/j.egyr.2019.10.028

3 Pranta M.H., Cho H.M. (2025) A comprehensive review of the evolution of biodiesel production technologies, *Energy Convers. Manage*., 328, 119623. https://doi.org/10.1016/j.enconman.2025.119623

4 Bajwa K., Bishnoi N.R., Selven S.T. (2024) Green Gold: Sustainable Biodiesel Production and Bioactive Compounds Extraction from Microalgae, *J. Energy Res. Rev*., 16, 19–36. https://doi.org/10.9734/jenrr/2024/v16i12384

5 Advantages and effectiveness: Kazakhstan's progress in developing new energy sources. Available at: https://qazaqgreen.com/en/news/kazakhstan/1750/

6 Kazakhstan has good prospects for the development of the biofuel market. Available at: https://www.apk-inform.com/ru/news/1533576

7 Askarova A., Bolegenova S., Ospanova S., Bolegenova S., Baidullayeva G., Berdikhan K., Nussipzhan A. (2024) Determining the optimal oxidation temperature of non-isothermal liquid fuels injections using modeling based on statistical droplet distribution, *East.-Eur. J. Enterp. Technol*., 6, 8 (132), 44-55. https://doi.org/10.15587/1729-4061.2024.316100

8 Oruganti S.K., Gorokhovski M.A. (2024) Stochastic models in the under-resolved simulations of spray formation during high-speed liquid injection, *Phys. Fluids,* 36, 052105. https://doi.org/10.1063/5.0206826

9 Askarova A., Bolegenova S., Ospanova Sh., Slavinskaya N., Aldiyarova A., Ungarova N. (2021) Simulation of non-isothermal liquid sprays under large-scale turbulence, *Phys. Sci. Technol*., 8, 28-40. https://doi.org/10.26577/phst.2021.v8.i2.04

10 Gorokhovski M.A., Oruganti S.K. (2022) Stochastic models for the droplet motion and evaporation in under-resolved turbulent flows at a large Reynolds number, *J. Fluid Mech*., 932, 18. https://doi.org/10.1017/jfm.2021.916

11 Gorokhovski M., Zamansky R. (2018) Modeling the effects of small turbulent scales on the drag force for particles below and above the Kolmogorov scale, *Phys. Rev. Fluids.,* 3, 034602. https://doi.org/10.1103/PhysRevFluids.3.034602

12 Amsden A.A., O'Rourke P.J., Butler T.D. (1989) *KIVA-II: A computer program for chemically reactive flows with sprays*, Los Alamos, 160 p. Available at: https://www.lanl.gov/projects/feynman-center/deploying-innovation/intellectual -property/software-tools/kiva/_assets/docs/KIVA2.pdf

13 Mishra Y.N. (2018) Droplet size, concentration, and temperature mapping in sprays using SLIPI-based techniques Lund: Division of Combustion Physics, Department of Physics, Lund University. *Thesis for Ph.D*., 85 p. Available at: https://portal.research.lu.se/en/publications/droplet-size-concentration-and-temperature-mapping-in-sprays-usin

14 Liang L., Reitz R., Iyer C., Yi J. (2007) Modeling Knock in Spark-Ignition Engines Using a G-equation Combustion Model Incorporating Detailed Chemical Kinetics, *SAE Tech. Pap.*, 2007-01-0165. https://doi.org/10.4271/2007-01-0165

15 Ra Y., Reitz R.D. (2008) A reduced chemical kinetic model for IC engine combustion simulations with primary reference fuels, *Combust. Flame*, 155, 713–738. https://doi.org/10.1016/j.combustflame.2008.05.002

16 Askarova A.S., Bolegenova S.A., Ospanova Sh.S., Rakhimzhanova L.A., Nurmukhanova A.Z., Adilbayev N.A. (2024) Optimization of fuel droplet sputtering and combustion at high turbulence flows, *Russ. Phys. J.*, 67, 2, 167-170. https://doi.org/10.1007/s11182-024-03104-5

17 Bolegenova S., Askarova A., Ospanova S., Zhumagaliyeva S., Makanova A., Aldiyarova A., Nurmukhanova A., Idrissova G. (2024) Technology of reducing greenhouse gas emissions for decarbonization and decreasing anthropogenic pressure on the environment, *Phys. Sci. Technol*, 11, 1-2, 64-75. https://doi.org/10.26577/phst2024v11i1a8

18 Azad A.K., Doppalapudi A.T., Khan M.M.K., Hassan N.M.S., Gudimetla P. (2023) A landscape review on biodiesel combustion strategies to reduce emission, *Energy Reports,* 9, 4413–4436. https://doi.org/10.1016/j.egyr.2023.03.104

19 Bolegenova S., Askarova A., Ospanova S., Makanova A., Zhumagaliyeva S., Nurmukhanova A., Adilbayev N., Shalkar A. (2024) Simulation of liquid fuel spray formation and distribution in a reacting turbulent flow, *Eurasian Phys. Tech. J.*, 21, 22–30. https://doi.org/10.31489/2024No2/22-30

20 Gavaises M., Arcoumanis C., Theodorakakos A., Bergeles G. (2001) Structure of high-pressure diesel sprays, *SAE Tech. Pap*., 2001-24-0009. https://doi.org/10.4271/2001-24-0009.

AUTHORS' INFORMATION

Askarova, Aliya Sandybayevna – Doctor of Phys. and Math. Sciences, Professor, Department of Thermophysics and Technical Physics, al-Farabi Kazakh National University, Almaty, Kazakhstan; SCOPUS Author ID: 6603209318; https://orcid.org/0000-0003-1797-1463; Aliya.Askarova@kaznu.edu.kz

Bolegenova, Saltanat Alikhanovna - Doctor of Phys. and Math. Sciences, Professor, Head of the Department of Thermophysics and Technical Physics, al-Farabi Kazakh National University, Almaty, Kazakhstan; SCOPUS Author ID: 57192917040; https://orcid.org/0000-0001-5001-7773; Saltanat.Bolegenova@kaznu.edu.kz

Ospanova, Shynar Sabitovna - PhD, Senior Lecturer, Department of Thermophysics and Technical Physics, al-Farabi Kazakh National University Almaty, Kazakhstan; Scopus Author ID: 55988678700; https://orcid.org/0000-0001-6902-7154; Shynar.Ospanova@kaznu.edu.kz

Maxutkhanova, Ardak Maxutkhanova - Senior Lecturer, Department of Thermophysics and Technical Physics, al-Farabi Kazakh National University Almaty, Kazakhstan; Scopus Author ID:56943471700; https://orcid.org/0000-0001-7703-4610; ardak.maxutkhanova@kaznu.edu.kz

Bolegenova, Karlygash Alikhanovna – PhD student, Department of Thermophysics and Technical Physics, al-Farabi Kazakh National University Almaty, Kazakhstan; https://orcid.org/0009-0003-3341-9772; karla836@mail.ru

Baidullayeva, Gulzhakhan Yeltayevna - Candidate of Phys. and Math. Sciences, Associate Professor, Department of Normal Physiology with a Biophysics Course, Asfendiyarov Kazakh National Medical University, Almaty, Kazakhstan; SCOPUS Author ID: 59187653000; https://orcid.org/0000-0002-1998-1617; G.baydullaeva@mail.ru

EURASIAN PHYSICAL TECHNICAL JOURNAL

2025, Volume 22, No.2 (52)

https://doi.org/10.31489/2025N2/70-78

Received: 12/02/2025 Revised: 17/04/2025 Accepted: 23/06/2025 Published online: 30/06/2025

Original Research Article

UDC 536.75; 620.92

GENERALIZATION OF THE LOCAL APPROACH APPLICATION TO THE ASSESSMENT OF TRANSFER PROCESSES IN HEAT POWER EQUIPMENT

Suprun T.T.

Institute of Engineering Thermophysics, National Academy of Sciences of Ukraine, Kyiv, Ukraine,
*Corresponding author: suprun@secbiomass.com

Abstract. *In order to develop measures to improve the thermal efficiency of working surfaces and the coolant supply system, it is necessary to examine and analyze the results of comprehensive studies of transfer processes under complex conditions of interaction of external (increased turbulence) and internal (separation) turbulent effects typical for heat power equipment. The aim of the work is to develop methods for assessing transfer processes in such equipment based on local control of thermophysical parameters in characteristic zones of the working environment. The object of the study is heat exchange surfaces of power, chemical and electronic equipment, as well as coolant supply systems. The research method is physical modeling of turbulent effects of various natures and processes of heat, momentum and mass transfer using hot-wire, electro-calorimetric methods, and heat and mass analogy methods. The article considers the generalization of the local approach application on examples of assessing the influence of increased turbulence, local closed separations and unsteady flows on transfer processes in the flow part of heat power equipment for various purposes. A local approach to the development of an effective coolant supply system for the technology of final drying of plant waste fragments is also considered. The use of a local approach, which allows recording thermophysical parameters in any characteristic zone of the working space, provides the ability to control the most thermally stressed areas. These results are the basis for developing measures to increase the thermal efficiency of working surfaces.*

Keywords: local thermophysical parameters, local aerodynamic characteristics, heat exchange surfaces, coolant supply system.

2. Introduction

It is known that processes in heat power, technological and electronic equipment occur under complex conditions of interaction of various natures turbulent effects. On the one hand, external disturbances caused by turbulence of the medium, pressure gradients, velocity non-stationarity, etc. are primarily associated with the geometry and design of the flow part. On the other hand, there are internal sources of disturbances on the working surface, caused by both natural causes (e.g., roughness, separation) and special artificial measures aimed at improving the transfer process (e.g., blowing to cool the surface, holes to increase heat dissipation, riblets to reduce hydraulic resistance, etc.). In addition, many technical applications are characterized by the installation of prismatic elements on a flat surface.

The progressive trend of increasing the efficiency and operational reliability of equipment requires constant improvement of methods for control and management of working processes. This is achieved by penetrating into the complex mechanism of boundary layers (BL) development on streamlined surfaces and targeted impact on their internal structure. Based on the above, it follows that it is relevant to conduct complex experimental studies in laboratory conditions on controlling the structure of boundary layers by means of

different nature disturbances, in particular, studying the features of a bypass laminar-turbulent transition. It concerns first gas turbine engines. The blade boundary layers are subjected to a combination of variables including free-stream turbulence, pressure gradient, unsteady periodic wakes of the upstream blade rows. These conditions have a significant influence on the BL transition process.

The increased interest of the electronics industry in the development of methods for calculating heat exchange of elements and units of electronic equipment confirms the relevance of studying the features of heat exchange in a pseudolaminar boundary layer developing on the surface of a prismatic element. Previously, the calculation of electronic equipment units was based on the average flow rate determined by the fan performance and constant for all prisms installed on a flat surface. This approach ignores information about the velocity and temperature fields and does not sufficiently take into account the influence of the size and location of the prismatic elements on the hydrodynamic structure of the flow. The local approach allows us to determine the temperature state of individual prismatic elements and the entire structure as a whole.

Due to the rapid development of computer technology in the last decade, there has been a disproportionate increase in numerical modeling compared to physical experiment, in particular direct numerical modeling of separated flow [1]. Therefore, experimental studies of heat transfer and hydrodynamics of complex flows, including separated flows, are of particular relevance. Analysis of the results of these studies helps to determine the characteristics of transfer processes when separations occur, allows evaluating the actual course of processes and helps to improve numerical modeling.

The organization of optimal distribution of the coolant flow for various heat technologies, in particular for the technology of final drying of plant waste fragments, is an important factor in energy saving. Improving the aerodynamic characteristics of the drying process based on a local approach is an urgent task.

2. Analysis of recent research and publications

As the analysis of recent studies and publications shows, the number of studies devoted to the influence of disturbances of various nature on the laminar-turbulent transition has now significantly increased. The relevance of this part of the work is evidenced by the volume of studies devoted to the problems of the bypass transition due to its wide distribution in various technical applications, primarily in gas turbines [1, 2]. In particular, the review [3] describes models of various types transition for flows in the boundary layer of streamlined surfaces in turbomachines. Unsteady flow initiates special type of laminar-turbulent boundary layer transition: wake-induced transition, which is also typical for gas turbine engines. The conclusions of the works [4, 5], which present a study of the simultaneous influence of the intensity and scale of turbulence on the onset of the bypass laminar-turbulent transition, indicate that the intensity of turbulence is the main factor affecting the transition, and the scale of turbulence has a secondary effect. Studies devoted to the problems of the bypass transition mainly relate to the numerical modeling of the hydrodynamic bypass transition using various turbulence models.

Most of the experimental and computational work deals with the case of momentum transfer. The problems associated with the influence of turbulence, periodic velocity non-stationarity and separation on heat transfer remain unclear.

Despite numerous attempts to penetrate into the separation mechanism in the recirculation, reattachment and relaxation zones, some aspects of complex separated flows remain unpredictable to date. Thus, universal criteria for assessing the intensity of separation and methods for diagnosing its type (laminar, transitional or turbulent) have not been developed. There are no reliable recommendations for determining the size (length and height) of the separation bubble and the length of the relaxation zone behind it. Data on the influence of the degree of turbulence on the formation of separation and the development of BL in the relaxation zone behind it are limited. Since friction practically disappears in the separation zone, there is a significant violation of the Reynolds analogy in it, extending to the relaxation zone.

There are enough articles devoted to the development of effective methods for drying various agricultural products and fragments of plant waste. In the study [6], an indirect solar dryer was proposed and developed, which accelerates the drying process of agricultural products. The work [7] describes an automatic control system for the drying process, which ensures sufficient heat flows depending on the type of product being dried. Impact jets, as in the present study, are often used in industry to dry, cool or heat various products. Impact drying and cooling is especially common for continuous sheets such as paper, textiles and metals. For example, results described in [8] for heat transfer mechanism of a slit jet impingement, will help to optimize cooling equipment and controlled parameters for the industrial-scale hot steel strip/plate cooling technology.

To determine the patterns of this complex transfer process, careful experimental data obtained under conditions as close as possible to the conditions in the flow section of full-scale equipment are required. Taking into account all of the above, the purpose of the study is to develop methods for assessing transfer processes in such equipment based on local control of thermophysical parameters in characteristic zones of the working environment.

3. Materials and research methods

The research method is physical modeling of turbulent effects of various natures and processes of heat, momentum and mass transfer using hot-wire, electro calorimetric methods, and heat and mass analogy methods. Since physical modeling is one of the most promising methods for studying transfer processes occurring under complex conditions, the studies were carried out in specially manufactured experimental samples of installations that completely reproduce the operating conditions of a full-scale installation in terms of geometric parameters and air supply system. The studies of the influence of increased turbulence, local closed separations, and velocity non-stationarity on the transfer processes in the flow path of heat power equipment were conducted in the T-5 wind tunnel of the IET NASU. The generator for creating turbulence had the form of a perforated plate. The working surface was a flat plate, the length of which made it possible to implement a mixed flow regime in the boundary layer. The velocity of the external flow, the shape of the leading edge of the plate and the length of the interceptor installed at the end of the wind tunnel test section controlled the type of separation (laminar, transitional or turbulent). Experimental investigations of a flat plate heat transfer in the presence of unsteady flows were carried out in a wind tunnel using various wake generators (a still and hesitating cylinder, a still and rotating "squirrel" wheel).

The studies of the transfer processes in the pseudolaminar boundary layer developing on the surface of a prismatic element were carried out in the aerodynamic stand ADS-1. The layout included four rows of prismatic elements installed on a flat surface (Fig.1). To study the heat transfer of prismatic elements, the method of heat and mass analogy was used, in particular the method of sublimation of matter in air.

The design of the experimental model, specially manufactured for the aerodynamic improvement of final drying of plant waste fragments, completely reproduced the operating conditions of the full-scale installation in terms of geometric parameters and air supply system (Fig.4) [9].

4. Results and discussion

4.1 Local approach for assessing the impact of increased turbulence

Such studies were conducted under conditions of nonlinear interaction of external (increased turbulence) and internal (separation at the leading edge) disturbances on two types of different working surfaces – flat and prismatic, therefore the results of two parts of the studies are considered.

For the first part, when studying the bypass laminar-turbulent transition, the local approach means determining the local coefficients of heat transfer and friction at the local velocity, as well as the fields of velocity, temperature and their pulsations in various sections along the length of the flat working surface.

The use of a local approach made it possible to explain the reason for the formation of a pseudolaminar boundary layer (PLBL), which precedes the bypass transition. This is caused by the simultaneous manifestation of two mutually related processes: selective penetration of turbulent pulsations from the external flow into the boundary layer (BL) and the development of powerful pulsations within the BL itself. Depending on the scale of turbulence, the development of PLBL at $Tu > 0$ can be accompanied by an increase in the coefficients of friction and heat transfer due to an increase in the velocity and temperature gradients near the wall with a simultaneous change in the internal structure of the BL. This also allowed us to evaluate the fact that in the pseudolaminar boundary layer the increase in heat transfer (up to 70%) significantly outpaces the increase in friction (up to 17%). The reasons for the intensification of heat transfer in the pseudolaminar boundary layer, significantly outstripping friction, are associated with higher rates of growth of the energy loss thickness compared to the momentum loss thickness; closer to the wall location of the temperature pulsation maxima compared to the longitudinal velocity pulsation maxima; high degree of correlation (up to 90%) between them. Methods for predicting the type of flow in the boundary layer and determining the coordinates of the bypass laminar-turbulent transition were also developed. Control of heat removal in the pseudolaminar boundary layer and monitoring of the length and location of the bypass transition zone make it possible to avoid the occurrence of dangerous heat-stressed areas.

The second part of the work is devoted to the features of heat transfer in the pseudolaminar boundary layer developing on the surface of a prismatic element. As is known, prisms are typical elements of electronic equipment boards. To develop an effective cooling system for such equipment, it is necessary to assess the thermal state of the elements of a specific layout and develop measures to improve it.

The thermal efficiency of individual prismatic elements was tested for the arrangement shown in Fig. 1, which included four rows of prismatic elements. Turbulence in the first row was created by the input conditions and in the second, third and fourth rows - by the traces of the previous rows; flow separation occurred when flowing around the input edges of the elements.

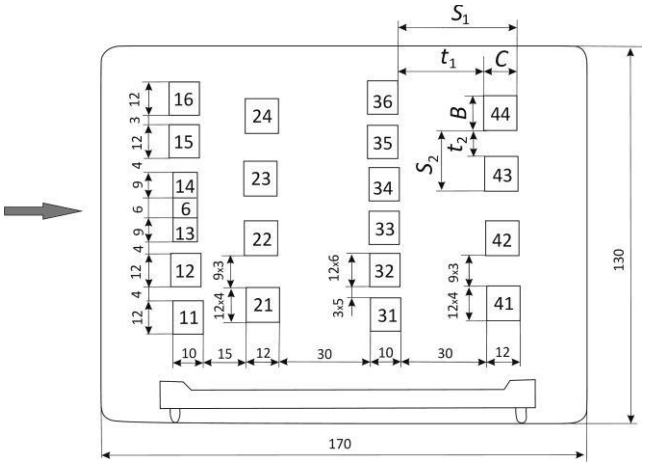

Fig.1. Flat surface with prismatic elements

The local approach for this part of the work is to determine the average surface heat transfer coefficient from the local velocity measured over each prismatic element. The analysis of the results showed that the intensity of the average heat transfer for the prisms located in positions 1 (prism No. 23) and 2 (prism No. 43) is different, which is associated with the aerodynamic features of their flow. The average heat transfer of the last row of prisms is less intense than for the first three rows. Thus, when constructively developing a flat surface with prismatic elements, the most heat-stressed of them should be located in conditions of maximum heat removal. In this case, such conditions turned out to be the flow conditions 1. This is a very important practical conclusion. Similarity equations were proposed for calculating the local heat transfer of each face of the prism separately and the average surface heat transfer Tabl. 1.

Table 1. Recommendations for calculating the average heat transfer of a prismatic element and its faces in 1-3 rows gap-free installed on a flat surface in a stream

General view of the similarity equation	$\overline{Nu} = C\,\mathrm{Re}^n$			
Average heat transfer	Defining size	Heat exchange surface	C	n
The element as a whole	C	$\sum F$	0.536	0.6
The upper face	C	$C \times B$	0.536	0.6
The side face	C	$C \times h$	0.487	0.6
The frontal face	h	$B \times h$	0.75-0.89	0.5
The back face	h	$B \times h$	0.116	0.667

This approach allows us to single out the role of each face in the total heat transfer and leads to the fact that the total heat transfer coefficient practically coincides with the average heat transfer coefficient on the upper face. This allows us to estimate the spatial temperature heterogeneity of the layout and carry out

measures to change the temperature in the required direction. The use of a local approach contributed to the implementation of a more accurate prediction of the reliability of electronic equipment components, taking into account their operating conditions in uneven temperature fields. Thus, the use of a local approach leads to a reduction in product development costs, allows for a more accurate selection of the required power for the cooling system, improves the design of equipment, and increases their reliability and service life [10].

4.2 Local approach for assessing the impact of flow separation

In the flow part of heat power equipment, conditions are often created that promote the occurrence of local closed separations. The occurrence of separations leads to a redistribution of heat transfer coefficients and a change in hydrodynamic resistance along the length of the working surfaces and is accompanied by significant disruptions in the structure of the thermal and hydrodynamic BL in the relaxation zones and the separation itself. Experiments using a local approach, conducted at the IET NAS of Ukraine, confirmed extremely slow recovery to" classical" turbulent boundary layer after various types of a separation with various rates of this gradual process, which made it possible to identify zones of "fast" and "slow" relaxation in the outer and inner parts of the BL. The separation "works" as a generator of external turbulence, because of which the length of the relaxation zone in the outer part of the BL is much greater than in the inner one. Moreover, the relaxation zone of the thermal BL is shorter than the hydrodynamic one due to the conservative reaction of the thermal BL to various disturbances, including separation.

A generalization of experimental data on heat transfer intensification confirmed the effectiveness of using turbulent viscosity to assess the transport properties of complex flows. Due to this approach, the turbulent viscosity at the outer boundary of the dynamic boundary layer in the section of reattachment $\nu_{t\delta r}/\nu$ is chosen as the main criterion determining, in the first approximation, the type of separation (laminar, transitional or turbulent) and its intensity. Laminar separation occurs at $\nu_{t\delta r}/\nu$=5, with increasing $\nu_{t\delta r}/\nu$ transitional separation occurs and, finally, at $\nu_{t\delta r}/\nu$>30 - turbulent separation. The value of this viscosity can be calculated based on the "energy-dissipation" turbulence model. For this purpose, it is advisable to use the decay law of longitudinal velocity pulsations at the outer boundary of the dynamic boundary layer developing behind the separation. In the first approximation, in the relaxation zone, the intensification of heat exchange can be described by the following equation:

$$St / St_o = f(\nu_{t\delta r} / \nu_{to}) \quad (1)$$

where St_o are determined by equation (2) for a turbulent boundary layer:

$$St_o = 0.0144 \cdot \mathrm{Re}^{**-0.25} \quad (2)$$

Equation (1) also contains the turbulent viscosity generated near the wall in the turbulent boundary layer, which can be calculated based on known recommendations:

$$\nu_{to} = 0.0168 \cdot U_e \cdot \delta^* \quad (3)$$

It should be noted that the choice of comparison conditions is very important when assessing the intensification of heat transfer and generalizing the experimental results. Relation (3) is recommended for the condition $Re^{**} = const$, the use of which is more acceptable for local representation of experimental data, when many uncertainties associated with the initial conditions are eliminated by using the momentum thickness δ^{**} as the determining dimension, rather than the current length x. The application of the local approach expanded the ideas regarding the non-traditional and sometimes unpredictable transformation of many important characteristics of the dynamic and thermal BL in the relaxation zone: distributions of friction and heat transfer coefficients, average velocities and temperatures, velocity and temperature pulsations at the outer boundary of the BL.

4.3 Local approach for assessing the impact of unsteady flow

It should be noted that there are different types of wake generators [11]. As already noted in the section "Materials and research methods", for modeling the unsteady flow with wake in this work such types of generators were installed in a wind tunnel: a still and hesitating cylinder, a still and rotating "squirrel" wheel. Based on the application of a local approach to determining the distribution of local heat transfer coefficients on a flat surface, the occurrence of a wake-induced laminar-turbulent transition initiated by stationary and moving wakes is confirmed. In this case, pre-transitional BL was pseudolaminar and characterized by substantial heat transfer growth in comparison with laminar boundary layer. By means of such wakes, it is

possible to change the intensity of heat transfer in the pseudo laminar boundary layer up to 80%, while simultaneously controlling the location and length of the wake-induced transition.

As experimental results have shown, a peripheral shear zone and a non-uniform turbulence field characterize the external flow with periodic non-stationarity. To evaluate the characteristics of such an external flow, it was replaced by a shear equivalent and a method for separating the total pulsations into turbulent and non-stationary components was proposed. For dividing turbulent and nonstationary components the additional measurement was conducted after still "squirrel cage". The method of dividing was based on two following assumptions: 1. rotation does not substantially influence on turbulent component; 2. energies of disturbances of different nature are not correlated, i.e. $\overline{u_e'^2} = \overline{u_t'^2} + \overline{u_n'^2}$.

The distributions of total fluctuations (u_e') including turbulent (u_t') and nonstationary (u_n') components differ by peaks (fig.2), amplitude of which decreases downflow. As shown at fig.3 the decay law of averaged total fluctuations $u_e'/U_e = f(x)$ was similar to the one after traditional still grids widely used for generation of turbulence in aerodynamic tubes. The values of total fluctuations changed from $u_e'/U_e \approx$ 15% to $u_e'/U_e \approx$ 4.3% at x=50 and 600 mm respectively.

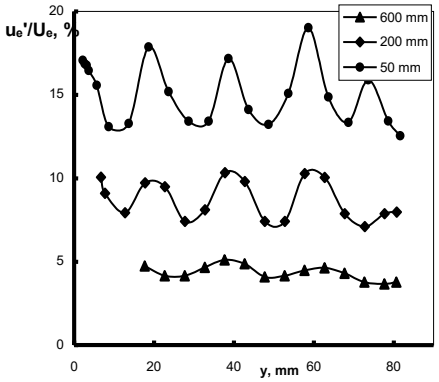

Fig.2. Total velocity fluctuations behind rotating "squirrel cage"

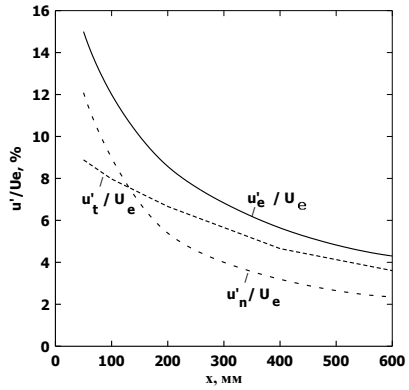

Fig.3. Distribution of components of velocity fluctuations

The decay law of total energy of longitudinal velocity fluctuations of shearless equivalent permits to estimate the transport properties of turbulized flow in the working part of aerodynamic tube. For that, it is possible to use the traditional form of decay laws behind stationary generators of turbulence:

$$\frac{U_e^2}{u_e'^2} = A(x + x_0)^m, \qquad (4)$$

where the exponent values (m) usually are chosen in the range of m =1,2-1,4, while virtual distance (x_0) and coefficient (A) are determined in the results of experimental investigations. On the base of decay law (4) it is possible to calculate the kinetic energy of fluctuations, their dissipation and characteristic scale as well as to estimate turbulent viscosity of turbulized flow ν_{te} in the frames of "energy – dissipation" turbulence model. Preliminary calculations show that values of the latter change from $\nu_{te} \approx 2{,}7.10^{-3}$ to $\nu_{te} \approx 1{,}4.10^{-3}$ м^2/с along the length of working part, i.e. exceed values of molecular viscosity almost into 200 times at x =50 mm.

The analysis of the obtained results (Fig. 3) demonstrates that the non-stationary component decreases significantly faster than the turbulent one. In the initial sections of the plate, the main contribution to the longitudinal fluctuations in the external flow is made by the non-stationary component, while in the middle and final sections of the plate, the turbulent component became prevailing. The revealed fact is important from a practical point of view, since it allows one to control the intensity of transfer processes using separately the parameters of non-stationarity (frequency, amplitude) or turbulence. The application of the local approach allows one to calculate the kinetic energy of fluctuations, dissipation and characteristic scale, and to estimate the turbulent viscosity of a turbulized flow with periodic non-stationarity. These data are necessary for calculating transfer processes in flows with periodic non-stationarity, for example, in turbomachines, based on turbulence models.

4.4 Local approach to improving the coolant supply system

Another example of the local approach application to the control of transfer processes in heat power equipment was the work to improve the aerodynamic characteristics of the coolant supply system in the technology of final drying and technological conditioning of plant materials [9]. The design of the full-scale installation was preceded by an aerodynamic calculation of the coolant supply system. However, as further tests showed, this calculation did not sufficiently take into account the influence of the installation structural elements on the hydrodynamic structure of the flow. To improve the aerodynamic characteristics of the coolant supply system, studies were conducted on a specially manufactured experimental model of the installation, which completely reproduces the operating conditions of a full-scale installation in terms of geometric parameters and air supply system (Fig. 4). The main difference was that the experiments were carried out without heating the coolant (air) and with a fixed working line.

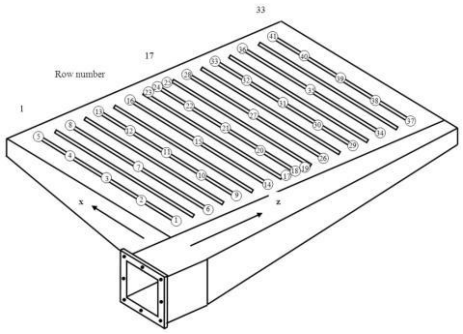

Fig. 4. Scheme of air supply to the working line

The processed plant material is placed on a fixed working line, which is a thin metal plate perforated with holes. The working line is blown with vertical air jets flowing from the system of longitudinal slots. The non-uniformity of the flow velocity field as well as the degree of turbulence were estimated based on the results of measurements at characteristic points of the working space. The results of the experiments confirmed that the initial design of the installation does not satisfy the optimal parameters of the coolant supply system. For this installation, the recommended values are U_{av}~0.5-0.8 m/s with a permissible degree of non-uniformity of velocity field 0.6-1.8.

Specific measures are proposed to improve the design of this system, namely: significant changes have been made to the size of the slots; the sections of the slots are partially covered at the ends of the rows; minimized leakage in the distribution box and others. As a result of these measures in final modification the velocity field non-uniformity coefficient k changed by no more than ~1.8 at an average velocity U_{av}=0.77 m/s (Fig. 5a). Thus, a significant improvement in the velocity field was observed both along the rows and along their length. The measurement results also showed that in final modification there is an increase in the degree of flow turbulence, reaching at some points u'/U = 52% at an average level of ~30% (Fig. 5 b).

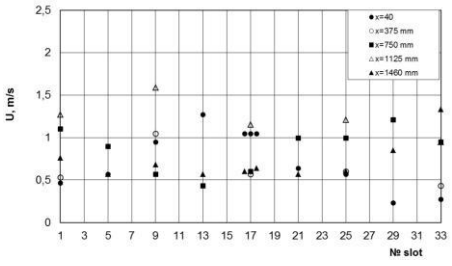

Fig.5a. Velocity distribution in final modification

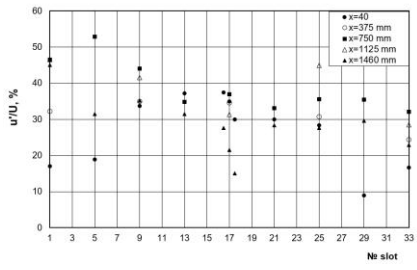

Fig.5b. Longitudinal pulsations distribution in final modification

An increase in both the average flow velocity of the coolant and its degree of turbulence contributes to the intensification of the heat and mass transfer process. This will improve the quality of the product and reduce the drying time. Analysis of the results of these studies allows us to develop a more rational design option for a full-scale installation. The use of the local approach consisted in estimating the value of average velocities and non-uniformity in local velocity distributions, as well as determining the degree of flow turbulence at characteristic points of the working space. Aerodynamic improvement of the coolant supply system contributes to the intensification of heat and mass transfer, and, as a result, increases productivity while reducing the time of the final drying process of plant raw materials.

5. Conclusion

The article presents a generalized study of a local approach application to assessing transfer processes in heat power equipment for various purposes. The advantage of the local approach is the possibility of fixing the thermophysical parameters of the process in any characteristic zone of the working space. Based on the data obtained, methods for calculating complex flows were developed and methods for monitoring and controlling work processes in heat power equipment were improved.

The scientific novelty and practical significance of the application of the local approach is as follows:

1) To generalize data on heat transfer intensification using turbulent viscosity in assessing the transport properties of complex flows.

2) The reason for the formation of a pseudolaminar boundary layer is formulated, which is caused by the simultaneous manifestation of two mutually related processes: selective penetration of turbulent pulsations from the external flow into the boundary layer (BL) and the development of powerful pulsations inside the BL itself.

3) The reasons for the significantly faster intensification of heat transfer in a pseudolaminar boundary layer compared to friction are substantiated.

4) Methods for predicting the type of flow in the boundary layer and determining the coordinates of the bypass laminar-turbulent transition region have been developed.

5) Conditions for controlling the most dangerous heat-stressed areas during the development of mixed flow regimes are created.

6) A bank of new experimental data on the intensity of the processes occurring for a flat surface with prismatic elements has been obtained, which allows taking into account the spatial unevenness of the temperature field and organizing measures to eliminate the unevenness.

7) To obtain many important characteristics of the dynamic and thermal BL in the relaxation zone, which can be used in the development of promising engineering and numerical methods for calculating complex flows in heat power equipment.

8) To justify the possibility of controlling the location and length of the wake-induced transition using stationary and moving wakes.

9) To evaluate the turbulent viscosity of a turbulent flow with periodic non-stationarity for the development of numerical methods for calculating flow transfer processes in heat power equipment.

10) To improve the aerodynamic characteristics of the coolant supply system, to ensure the required quality of material processing while reducing the time for the final drying process of plant raw materials.

Conflict of interest statement
The author declares that she has no conflict of interest in relation to this research, whether financial, personal, authorship or otherwise, that could affect the research and its results presented in this paper.

References

1 Wissink J.G., Zaki T.A., Rodi W., Durbin P. (2014) The Effect of wake Turbulence Intensity on Transition in a Compressor Cascade. *Flow Turbulence Combust*., 93, 555–576. https://doi.org/10.1007/s10494-014-9559-z

2 Simoni D., Ubaldi M., Zunino P., Bertini F. (2012) Transition mechanisms in laminar separation bubbles with and without incoming wakes and synthetic jet effects. *Exp Fluids*., 53, 173 – 186. https://doi.org/10.1007/s00348-012-1281-9

3 Dick E., Kubacki S. (2017) Transition Models for Turbomachinery Boundary Layer Flows: A Review. *International Journal of Turbomachinery, Propulsion and Power*, 2, 2, 1-45. https://doi.org/10.3390/ijtpp2020004

4 Shahinfar S., Fransson J.H.M. (2011) Effect of free-stream turbulence characteristics on boundary layer transition. *J. Phys. Conf. Ser.*, 318, 032019. Available at: https://iopscience.iop.org/article/10.1088/1742-6596/318/3/032019

5 Grzelak J., Wiercinski Z. (2017) Length scale of free stream turbulence and its impact on bypass transition in a boundary layer. *Journal of Applied Fluid Mechanics*, https://doi.org/10.18869/acadpub.jafm.73.238.27159

6 Alkahdery L.A., Yurchenko A.V., Mohammed J.A.-K., Mekhtiyev A.D., Neshina Y.G. (2023) Performance improvement of solar dryer using an auxiliary heat source under different values of airflow rates. *Eurasian phys. tech. j.* 20(1(43), 42–50. https://doi.org/10.31489/2023No1/42-50

7 Alkahdery L.A., Yurchenko A.V., Mohammed J.A.-K., Neshina Y.G. (2023) Automated temperature and humidity control and monitoring system for improving the performance in drying system. *Eurasian phys. tech. j.*, 20(2(44), 32–40. https://doi.org/10.31489/2023No2/32-40

8 Wang B., Liu Zh., Zhang B., Wang Zh., Wang G. (2019) Heat Transfer Characteristic of Slit Nozzle Impingement on High-temperature Plate Surface. *ISIJ International*., 59, 5, 900 – 907. https://doi.org/10.2355/isijinternational.ISIJINT-2018-576

9 Suprun T.T. (2022) Local approach to improve the aerodynamic characteristics of the final drying process. *Eurasian phys. tech. j*., 19, 2 (40), 65 – 70. https://doi.org/10.31489/2022No2/65-70

10 Suprun T.T. (2021) Local approach for evaluating heat transfer of prismatic elements on a flat surface. *Eurasian phys. tech. j.,* 18, 3 (37), 43 - 47. https://doi.org/10.31489/2021No3/43-47

11 Funazaki K. (1996) Unsteady boundary layers on a flat plate disturbed by periodic wakes: part I – Measurements of wake-affected heat transfer and wake-induced transition model. *J. Turbomach*., 118, 327 – 336 https://doi.org/10.1115/1.2836643

AUTHORS' INFORMATION

Supsun, Tetiana Tarasovna – Candidate of Technical Sciences, Senior Researcher, Institute of Technical Thermophysics of the National Academy of Sciences of Ukraine, Kiev, Ukraine; Scopus Author ID: 6602978555; https://orcid.org/0000-0002-5360-388X, suprun@secbiomass.com

EURASIAN PHYSICAL TECHNICAL JOURNAL

2025, Volume 22, No. 2 (52)

https://doi.org/10.31489/2025N2/79-87

Received: 19/12/2024 Revised: 29/04/2025 Accepted: 23/06/2025 Published online: 30/06/2025

Original Research Article

UDC 533.6

AERODYNAMIC IMPROVEMENT OF A TWO-BLADE MAGNUS WIND TURBINE: NUMERICAL AND EXPERIMENTAL ANALYSIS OF AERODYNAMICS AND PRESSURE DISTRIBUTION

Shaimerdenova K.M.[1], Tleubergenova A.Zh.[1,2], Tanasheva N.K.[1,2], Dyusembaeva A. N.[1,2], Minkov L. L.[3], Bakhtybekova A. R.[1,2*]

[1] E.A. Buketov Karaganda University, Karaganda, Kazakhstan
[2] Scientific Center "Alternative Energy", Karaganda, Kazakhstan
[3] Tomsk State University, Tomsk, Russia
*Corresponding author: asem.alibekova@inbox.ru

Abstract. *Improving wind power plant efficiency is crucial due to the increasing demand for renewable energy. This study analyzes the aerodynamic characteristics of a wind power plant equipped with two combined blades that integrate fixed blades and rotating cylinders. The object of the study is a wind power plant model designed to optimize airflow direction and enhance lift. The methodology involves numerical modeling using the Ansys Fluent software package, as well as experimental testing under laboratory conditions. The main results show that as when the air-flow velocity increases from 3 to 12 m/s, and thrust force rises from 0.5 N to 3.85 N. Comparative analysis of the minimum and maximum pressure on the blade surfaces demonstrates a strong correlation between increasing rotational speed and elevated pressure differentials: p_{max} rises from approximately 0.4 Pa to 0.7 Pa, while p_{min} increases from about 0.15 Pa to 0.4 Pa. The thrust coefficient decreases from 1.45 to 1.05 as the Reynolds number (Re) increases, indicating improved aerodynamic characteristics during the transition to turbulent flow. A comparative analysis of numerical and experimental data reveals a deviation of no more than 5%, confirming the model's reliability and the soundness of the research methodology. The conclusions indicate that employing combined blades can enhance the aerodynamic efficiency of a wind power plant by 8–10% compared with traditional designs. This improvement may foster the development of more efficient and stable wind energy systems, particularly in regions with low to medium wind potential.*

Keywords: wind power plant, combined blades, pressure distribution, aerodynamic characteristics, numerical modeling.

1. Introduction

In the context of growing global energy consumption and the need to reduce dependence on fossil energy sources, the development of renewable energy technologies, in particular wind energy, is becoming particularly relevant [1]. Modern wind power plants (wind turbines) are constantly being improved to increase the efficiency of converting kinetic wind energy into electrical energy [2]. By 2022, the total number of installed wind power capacities in the European Union countries amounted to 202.8 GW, which demonstrates the stable growth of this sector in recent years. Denmark and Sweden occupy the leading positions in terms of wind energy capacity per capita, which underlines the significant potential of Northern Europe in the development of this area [2].

There are various types of wind turbines, among which special attention is paid to vertical and horizontal structures [3]. However, vertical wind turbines have significant disadvantages that limit their wide application

[4]. The main problems include low efficiency, power surges, and maintenance complexity, which negatively affect the efficiency and reliability of such installations. Additionally, vertical turbines often encounter instability of aerodynamic forces due to turbulence and changes in wind direction [5]. This leads to an uneven load on the blades and other components, increasing wear and shortening the service life of the equipment [6].

Horizontal wind turbines, being the most common type, are characterized by higher efficiency and stable operation [7]. Their peak power factor can reach 50%, whereas for vertical turbines this figure is about 40% [8]. However, they are not designed to operate efficiently at low wind speeds. For example, at a wind speed of 6 m/s, a horizontal turbine with a capacity of 20 kW produces about 3 kW, while a vertical turbine under the same conditions generates about 1.8 kW. At speeds below 5 m/s, the performance of horizontal turbines is significantly reduced, which limits their use in regions with low wind potential and reduces the overall efficiency of the power system.

In this regard, horizontal turbines using the Magnus effect are of particular interest [9]. The use of rotating cylinders in the turbine design creates additional lift, which increases the overall efficiency of the installation, especially at low wind speeds. Studies show that such turbines are capable of operating efficiently in a wide range of wind speeds from 2 to 40 m/s, whereas traditional blade turbines are usually effective at speeds from 5 to 25 m/s [10]. The improved aerodynamic characteristics of these turbines reduce turbulence and flow pulsations, which contribute to stable and reliable operation. Nevertheless, the optimization of such systems requires an in-depth study of aerodynamic characteristics and the influence of various design parameters [11].

In recent years, many studies have been conducted to improve the aerodynamics of wind turbines using various methods, including numerical simulations and experimental studies [12,13]. Nevertheless, the issue of combining fixed blades with rotating cylinders to stabilize the flow and increase efficiency remains insufficiently studied [14].

The purpose of this study is to analyze the aerodynamic characteristics of a wind power plant with two combined blades using the Magnus effect. This includes the development and research of a new turbine design that combines the advantages of traditional fixed blades and rotating cylinders to improve the efficiency of wind energy conversion.

The novelty of the work lies in the combination of fixed blades with rotating cylinders in a single wind turbine design. This combination is aimed at improving aerodynamic performance and increasing lift, especially at low wind speeds. Unlike previous studies, this paper proposes a new geometry of the blades and optimization of their location to achieve maximum efficiency.

As part of the study, numerical simulations were carried out using the Ansys Fluent software package, as well as experimental tests in laboratory conditions at air flow velocities from 3 to 12 m/s. A comparative analysis of numerical and experimental data confirmed the effectiveness of the proposed design and the reliability of the model used.

2. Main part

2.1 Numerical studies

To study the aerodynamic characteristics, a mathematical model of a wind turbine with two combined blades was created. The wind turbine model includes structural elements that ensure the conversion of kinetic wind energy into mechanical energy. The main components of the system are fixed blades and cylinders mounted on the central shaft. These elements are fixed to the mast, which supports the main shaft, creating the necessary strength and stability of the entire installation.

The cylinders located around the circumference of the wind wheel have a length of 205 mm and a diameter of 50 mm, and the fixed blades, 225 mm long and 25 mm wide, serve to stabilize the flow and optimize the direction of the air flow, which increases the efficiency of energy conversion. The diameter of the wind wheel is 500 mm, which contributes to a significant capture of the air flow, providing the power for the installation. The 420 mm long mast serves as the basis for the installation of the main shaft, creating a reliable basis for the operation of the structure in various meteorological conditions (Figure 1a).

In contrast to conventional, non-combined cylindrical blades, the combined power elements employ stationary guide vanes interacting with rotating cylinders to induce a controlled swirl, diminish the recirculation zone, and raise the lift coefficient, while the fixed blades—set at an angle to the rotation axis—simultaneously stabilize the airflow, minimize wake distortions, and thereby maximize the Magnus effect, collectively boosting the turbine’s aerodynamic efficiency.

Initially, a computational domain was created around a mathematical model of a wind power plant to set boundary conditions and rotation conditions (Figure 1b). A cylindrical subdomain (type 1) with a thickness of 5 mm was formed around each power element to set the conditions for the rotation of the blades. To stabilize the flow and create an area of rotation around this subdomain, a cylindrical area (type 2) with a radius of 0.1 m around the z-axis was added. An external area in the form of a parallelepiped with dimensions of 0.7 m × 0.7 m × 3 m has been created around the cylindrical subdomain (type 2), which provides the necessary conditions for modeling the rotation of the entire wind wheel.

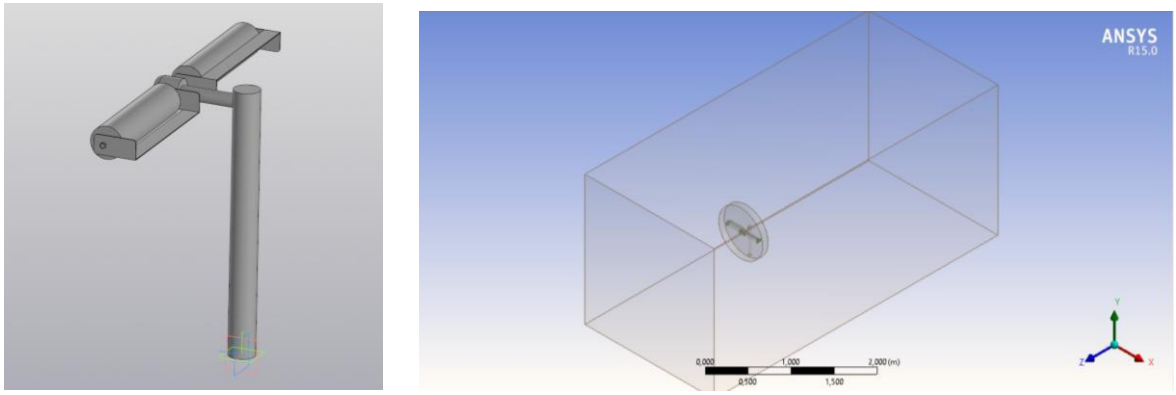

a) b)

Fig.1. Wind turbine with 2 combined blades: a) a mathematical model, b) the calculated area around the wind turbine.

Basic assumptions:

1. Incompressibility of the flow: At low values of Mach numbers (M << 0.1), air is considered as an incompressible medium.

2. Turbulence of the flow: At high values of the Re > 10^4, the flow is considered turbulent.

3. Isothermicity: Due to the low Mach numbers and small temperature differences near the wind wheel, the current is assumed to be isothermal.

To calculate the turbulent flow, the Realizable k−ε model was chosen, taking into account turbulent energy and dissipation. The system of equations was solved in Ansys Fluent using the finite volume method and the SIMPLE scheme for matching pressure and velocity fields.

For incompressible flow, the continuity equation is expressed as:

$$\frac{\partial x_i}{\partial u_i} = 0$$

where u_i represents the velocity components of the flow, and x_i represents the spatial coordinates.

The Reynolds-averaged momentum equations for turbulent flow are given by:

$$\frac{\partial(\rho u_i)}{\partial t} + \frac{\partial(\rho u_i u_j)}{\partial x_j} = \frac{\partial p}{\partial x_i} + \frac{\partial}{\partial x_j}(\mu \frac{\partial u_i}{\partial x_j}) - \frac{\partial}{\partial x_j}(\rho \overline{u_i' u_j'})$$

where, ρ is the fluid density; p is the pressure; μ is the dynamic viscosity; $\overline{u_i' u_j'}$ are the Reynolds stresses that model the turbulent stresses arising from velocity fluctuations.

The Realizable $k-\varepsilon$ model is applied in this study, which improves upon the standard $k-\varepsilon$ model by imposing realizability constraints on the turbulent kinetic energy and dissipation rate. This approach enhances accuracy for complex turbulent flows, such as rotating and recirculating flows around the wind turbine's cylindrical elements.

The transport equation for turbulent kinetic energy k is given by:

$$\frac{\partial(\rho k)}{\partial t} + \frac{\partial(\rho u_i k)}{\partial x_i} = \frac{\partial}{\partial x_j}[(\mu + \frac{\mu_t}{\sigma_k})\frac{\partial k}{\partial x_j}] + Pk - \rho\varepsilon$$

where, k is the turbulent kinetic energy; μ_t is the turbulent viscosity; σ_k is the turbulent Prandtl number k; P_k is the production of turbulent kinetic energy; ε is the dissipation rate of turbulent kinetic energy.

The transport equation for the dissipation rate ε is:

$$\frac{\partial(\rho\varepsilon)}{\partial t}+\frac{\partial(\rho ui\varepsilon)}{\partial x_i}=\frac{\partial}{\partial x_j}[(\mu+\frac{\mu_t}{\sigma_\varepsilon})\frac{\partial\varepsilon}{\partial x_j}]+\rho C_1 S\varepsilon-\rho C_2 k+\frac{\varepsilon^2}{\sqrt{\nu\varepsilon}}$$

where σ_ε the turbulent Prandtl number for ε epsilonє, C_1 and C_2 are empirical constants, and S is the modulus of the mean rate-of-strain tensor.

The turbulent viscosity μ_t is computed as:

$$\mu_t=\rho C_\mu\frac{k^2}{\varepsilon}$$

where C_μ is a model constant.

The boundary conditions are presented in Table 1.

Table 1. Boundary conditions.

Parameter	Condition	Value/Description
Domain Inlet	Turbulence intensity, I	0.1
	Hydraulic diameter of the inlet region	1 m
	Velocity	3,5,7,9,12 m/s
Domain Outlet	Pressure at the outlet	$p=p_{p\ external}$
Rotor Walls	Wall movement speed	Depends on the rotational speed of the cylinders around their longitudinal axis and the rotor axis
Near-Wall Region	Boundary conditions for turbulent kinetic energy	k=0
	Turbulent kinetic energy dissipation rate	Calculated based on equality of production and dissipation of turbulent energy (logarithmic velocity profile)
	Constant κ for the logarithmic profile	0.42
	Distance from the center of the cell to the wall, yp	If $y_p<11.06$, k=0 if $y_p\geq11.06$, turbulent dissipation is considered

2.2 Experimental studies

Experimental studies were conducted in the laboratory "Aerodynamic measurements" of the scientific center "Alternative Energy" of the E. A. Buketov Karaganda University. A model of a combined wind turbine with rotating 2 cylindrical blades was developed, which was then studied at various wind speeds in a transverse air flow from 3 to 12 m/s (Figure 2). The laboratory layout allows for experimental tests to evaluate aerodynamic characteristics and confirm the results of numerical modeling.

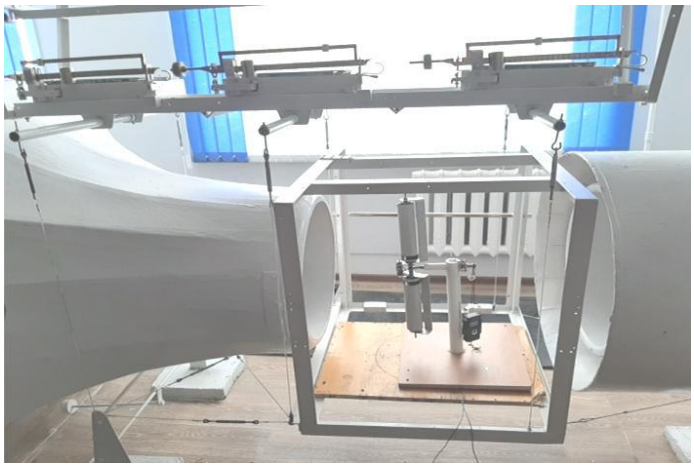

Fig.2. Laboratory layout of a wind turbine.

Air-flow velocity was measured with a cup anemometer JDC Skywatch Atmos (range 2–150 km h^{-1}, accuracy ± 3 %), while the three orthogonal components of aerodynamic force and moment acting on the model were resolved by a mechanical three-component balance (Fig. 2) whose overall measurement uncertainty does not exceed 5–7 %. The rotational speed of the cylinders was monitored with a contact/non-contact laser photo-tachometer CEM AT-8 (2–99 999 rev min^{-1}, resolution 0.1 rev min^{-1} below 10 000 rev min^{-1}, accuracy ± 0.05 %).

Each point represents the mean of five consecutive runs; the standard deviation never exceeded 0.04 N (1.2 %) for forces and 0.02 m/s (0.6 %) for velocity.

3. Results and discussion

This section provides a comparative analysis of the aerodynamic characteristics of a two-bladed wind power plant based on numerical and experimental data. Figure 3 shows a comparative graph of the drag force for a two-bladed wind power plant.

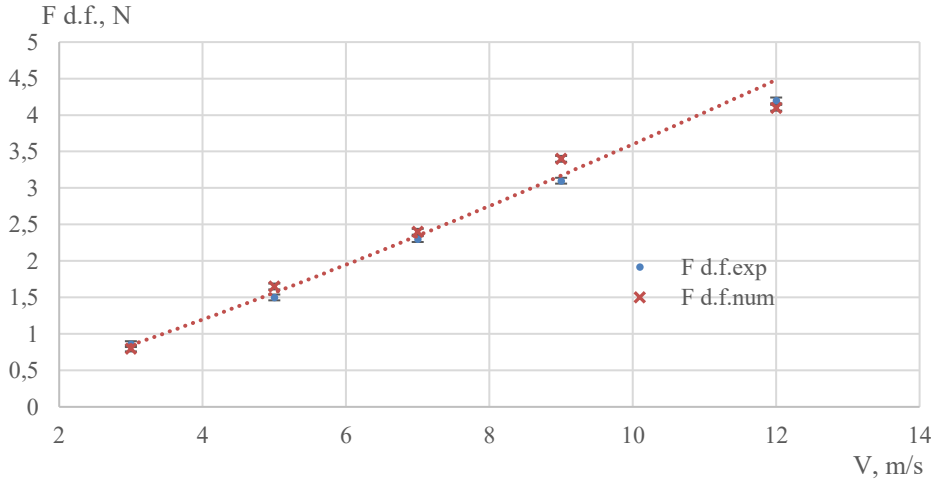

Fig. 3. A comparative graph of the drag force for a two-bladed wind power plant.

Figure 3 shows how the drag force of a two-bladed wind turbine increases with increasing air flow velocity. The values of $F_{d.f.\ num}$= 4.1 N and $F_{d.f.\ exp}$ = 4.2 N was obtained at a speed of 12 m/s. The drag force increases with increasing speed due to increased pressure on the front surface of the blades. The resulting resistance of 4.1–4.2 N is almost twice as low as that of diffuser microturbines of similar diameter [15]. The comparison of experimental and numerical data demonstrates a good match, which confirms the adequacy of the model used in describing the aerodynamic properties of the turbine. Error bars denote ±1 σ experimental uncertainty: ±0.04 N for forces (1 %–2 % of the value).

The numerical data of the drag force are approximated by a power function:

$$F_{d.f.num} = 0{,}2262V^{1{,}2018}$$

Figure 4 below shows a comparative graph of the thrust force for a two-bladed wind power plant.

As can be seen from Figure 4, the thrust force increases linearly with increasing flow velocity. The values of $F_{t..num}$ = 3.85 N and $F_{t.exp}$ = 3.8 N were obtained at a speed of 12 m/s. The thrust force associated with the lift generated by the Magnus effect increases with increasing wind speed. This indicates an increase in the efficiency of converting wind energy into mechanical work. The consistency of the numerical and experimental results confirms the accuracy of the model.

It is established that the thrust force is approximated by a power function:

$$F_t = 0{,}1624\ V^{1{,}2881}$$

Figure 5 shows a comparative graph of the drag coefficient for a two-bladed wind power plant.

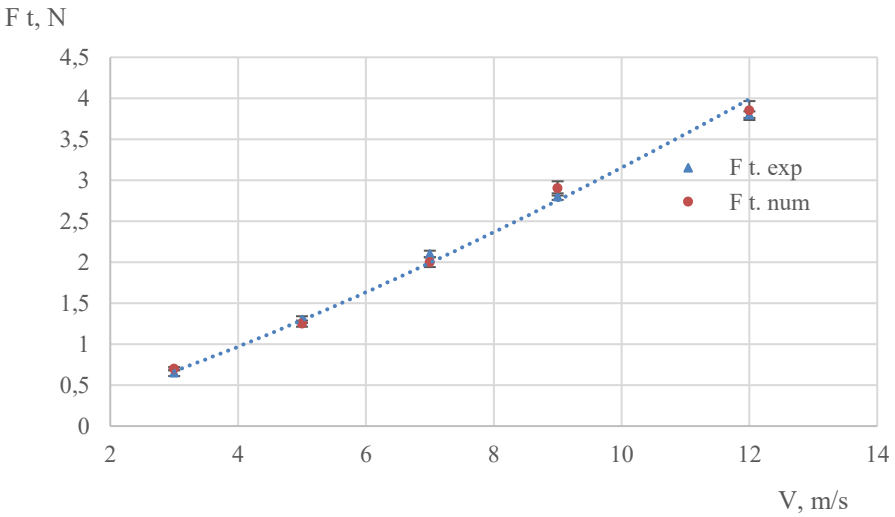

Fig. 4. Comparative graph of the thrust force for a two-bladed wind power plant.

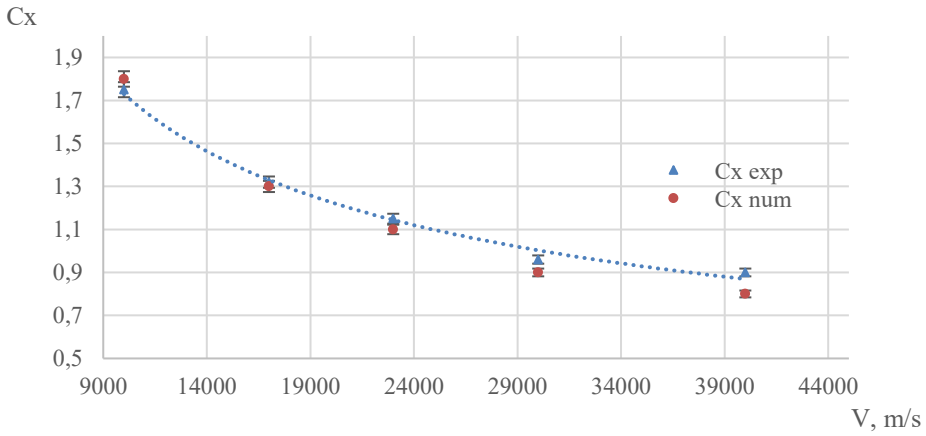

Fig. 5. Comparative graph of the drag coefficient for a two-bladed wind power plant.

As can be seen from Figure 5, with increasing Re, the coefficient of drag force decreases. The maximum experimental data at Re = 10000 is 1.75, and the numerical data is 1.8.

The decrease in the coefficient with an increase in the Re indicates an improvement in the aerodynamic properties of the blades at higher flow velocities, which is associated with the transition to a turbulent regime, reducing the relative magnitude of resistance.

In comparison, it was found that the coefficient of resistance in similar conditions turned out to be 12-15% lower than that of a traditional Magnus wind turbine with two blades [16]. This is because the addition of a fixed blade helps to minimize drag.

Figure 6 shows a comparative graph of the drag coefficient for a two-bladed wind power plant. As can be seen from Figure 6, the coefficient of thrust decreases with increasing Re. The maximum values of the coefficient of thrust obtained experimentally are 1.42 and numerically, 1.45. The thrust coefficient of 1.42–1.45 exceeds the range of 1.20–1.30 typical for vertical-axis turbines with Gurney flaps, and lies within the lower limit of the 15 percent increase demonstrated by active flow control on large HAWT profiles [17]. Error bars denote ±2 % for aerodynamic coefficients.

The decrease in the coefficient with an increase in the Re is associated with a change in the ratio between the lifting force and the dynamic pressure of the flow. This reflects the peculiarities of the aerodynamic behavior of the combined blades under different flow regimes. The obtained results of the lift coefficient turned out to be 8-10% higher than in the work [16]. This improvement can be explained by a more optimal ratio of length to diameter of rotating cylinders, as well as the use of fixed blades, which made it possible to use the Magnus effect more effectively at low air flow speeds.

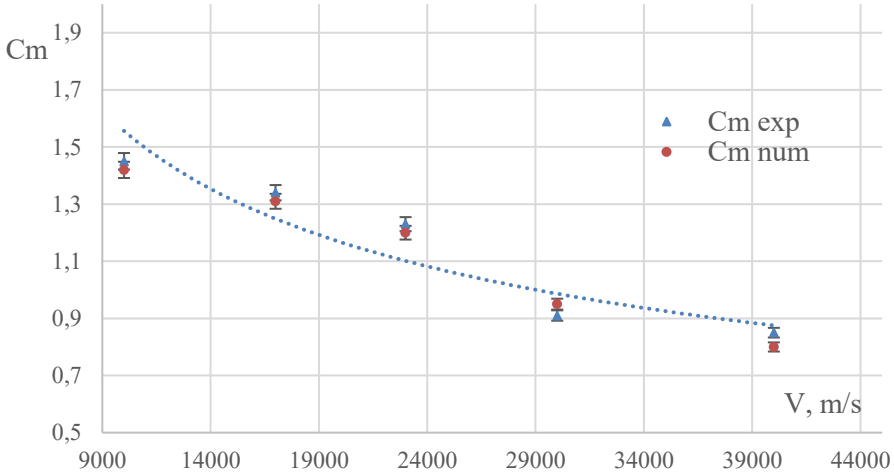

Fig.6. Comparative graph of the coefficient of drag force for a two-bladed wind power plant.

Figure 7 below shows a comparison of experimental and numerical data of minimum and maximum pressure depending on the rotation speed.

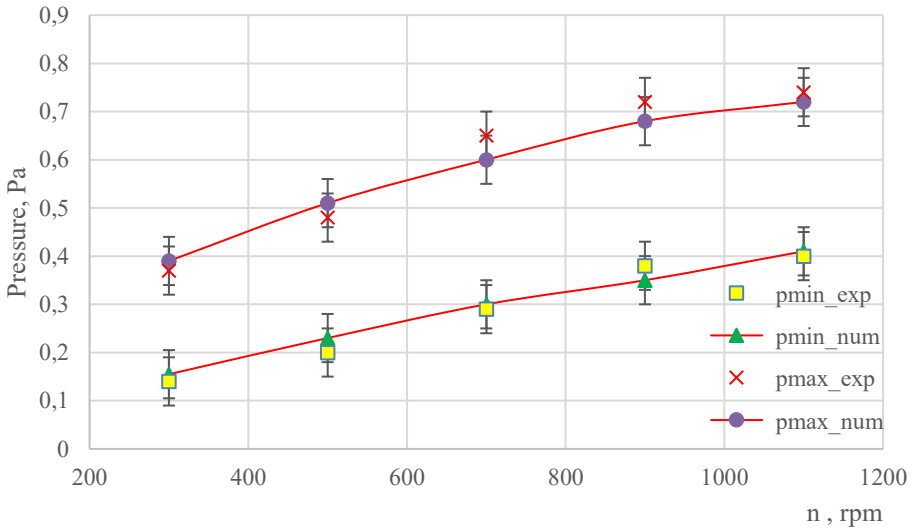

Fig. 7. Comparison of experimental and numerical data of minimum and maximum pressure depending on the rotation speed.

As can be seen from Figure 7, a good convergence of the experimental points with the results of numerical modeling is visible, indicating the correctness of the mathematical model used and the boundary conditions. As the rotation speed increases, the installation shows an increase in p_{max} from 0.4 Pa to 0.7 Pa, which is due to the increasing pressure action of the air flow on the front surface of the blade, while p_{min} increases from 0.15 Pa to 0.4 Pa due to increased vacuum on the back side. The increase in pressure drop to only 0.3 Pa remains approximately twice as low as the 0.6–0.8 Pa levels recorded on diffusor-reinforced rotors of a similar radius, which indicates a softer load profile of the proposed installation [18]. An essential factor that can change these indicators is the air temperature, since when it increases, the density of the working medium decreases, which leads to a decrease in pressure gradients and may slightly reduce the observed pressure values; on the contrary, at a lower temperature, air density increases, and pressures at the same rotational speeds may increase. The combined expanded uncertainty of pressure measurements (k = 2) does not exceed 0.10 Pa.

4. Conclusion

In the course of the study, it was found that the use of combined blades, combining fixed blades and rotating cylinders, contributes to a significant increase in the aerodynamic efficiency of a wind power plant. The analysis showed an increase in the coefficient of thrust by 8-10% compared to traditional designs at identical air flow speeds. In addition, it was found that the addition of a fixed blade reduces the drag coefficient by 12-15% relative to turbines equipped exclusively with cylindrical blades. As demonstrated by the pressure distribution measurements at varying rotational speeds, the maximum pressure on the front surface of the blades increases from approximately 0.4 Pa to 0.7 Pa, while the minimum pressure rises from around 0.15 Pa to 0.4 Pa. This trend correlates with a more uniform airflow around the rotating and fixed elements and aligns well with numerical predictions. The total combined uncertainty remains below 3 %, therefore the observed 8–10 % improvement is statistically significant.

These improvements are due to a more uniform distribution of air flow and minimization of turbulence zones behind the blades, which has a positive effect on the aerodynamic characteristics of the installation.

The results obtained confirm the expediency of using the proposed design for the development of highly efficient wind energy systems, especially in regions with low wind potential. Prospects for further research include optimizing the geometry of the blades and scaling the design for industrial implementation.

Conflict of interest statement

The authors declare that they have no conflict of interest in relation to this research, whether financial, personal, authorship or otherwise, that could affect the research and its results presented in this paper.

CRediT author statement

According to the requirements for publications indexed in the SCOPUS database, if there is more than one author, it is necessary to briefly indicate the contribution of each author to the preparation of the article, using the recommendations of Elsevier - https://www.elsevier.com/researcher/author/policies-and-guidelines/credit-author-statement

Funding

This research was funded by a grant from Science Committee of the Ministry of Science and Higher Education of the Republic of Kazakhstan (AP22785282 “Automation process detecting errors and improving efficiency operation compact combined power plant based on solar panels and wind generators”).

References

28 Hassan Q., Algburi S., Sameen A.Z., Salman H.M., Jaszczur M. (2023) A review of hybrid renewable energy systems: Solar and wind-powered solutions: Challenges, opportunities, and policy implications. *Results in Engineering*, 101621. https://doi.org/10.1016/j.rineng.2023.101621

29 Wolniak R., Skotnicka-Zasadzień B. (2023) Development of wind energy in EU countries as an alternative resource to fossil fuels in the years 2016–2022. *Resources*, 12(8), 96. https://doi.org/10.3390/resources12080096

30 Xie F., Aly A.M. (2020) Structural control and vibration issues in wind turbines: A review. *Engineering Structures*, 210, 110087. https://doi.org/10.1016/j.engstruct.2019.110087

31 Ahmad M., Shahzad A., Qadri M.N.M. (2023) An overview of aerodynamic performance analysis of vertical axis wind turbines. *Energy & Environment*, 34(7), 2815-2857. https://doi.org/10.1177/0958305X221121281

32 Hand B., Kelly G., Cashman A. (2021) Aerodynamic design and performance parameters of a lift-type vertical axis wind turbine: A comprehensive review. Renewable and Sustainable *Energy Reviews*, 139, 110699. https://doi.org/10.1016/j.rser.2020.110699

33 Maheshwari Z., Kengne K., Bhat O. (2023) A comprehensive review on wind turbine emulators. Renewable and Sustainable *Energy Reviews*, 180, 113297. https://doi.org/10.1016/j.rser.2023.113297

34 Li Y., Yang S., Feng F., Tagawa, K. (2023) A review on numerical simulation based on CFD technology of aerodynamic characteristics of straight-bladed vertical axis wind turbines. *Energy Reports*, 9, 4360-4379. https://doi.org/10.1016/j.egyr.2023.03.082

35 Al-Rawajfeh M.A., Gomaa M.R. (2023) Comparison between horizontal and vertical axis wind turbine. *International Journal of Applied*, 12(1), 13-23. https://doi.org/10.11591/ijape.v12.i1.pp13-23

36 Bai X., Ji C., Grant P., Phillips N., Oza U., Avital E.J., Williams J.J. (2021) Turbulent flow simulation of a single-blade Magnus rotor. *Advances in Aerodynamics*, 3, 1-22. https://doi.org/10.1186/s42774-021-00068-9

37 Dyusembaeva, A., Tanasheva, N., Tussypbayeva, A., Bakhtybekova, A., Kutumova, Z., Kyzdarbekova, S., & Mukhamedrakhim, A. (2024) Numerical Simulation to Investigate the Effect of Adding a Fixed Blade to a Magnus Wind Turbine. *Energies*, 17(16), 4054. https://doi.org/10.3390/en17164054

38 Tanasheva, N.K., Dyusembaeva A.N., Bakhtybekova A.R., Minkov L.L., Burkov M.A., Shuyushbayeva N.N., Tleubergenova A.Z. (2024) CFD simulation and experimental investigation of a Magnus wind turbine with an improved blade shape. *Renewable Energy*, 121698. https://doi.org/10.1016/j.renene.2024.121698

39 Mohammed O.A., Mohammed S.A., Ghazaly N.M. (2024). Influence of moisture condition and silica sand on friction coefficient of wind turbine brake system. *Eurasian Physical Technical Journal*, 21(3 (49)), 117-124. https://doi.org/10.31489/2024No3/117-124

40 Yershina A.K., Sakipova S.E., Manatbayev R.K. (2019) Some design features of the carousel type wind turbine Bidarrieus. *Eurasian Physical Technical Journal*, 16(2 (32)), 63-67. https://doi.org/10.31489/2019No2/63-67

41 Dyusembaeva A.N., Tleubergenova A.Z., Tanasheva N.K., Nussupbekov B.R., Bakhtybekova A.R., Kyzdarbekova S.S. (2024) Numerical investigation of the flow around a rotating cylinder with a plate under the subcritical regime of the Reynolds number. *International Journal of Green Energy*, 21(5), 973-987. https://doi.org/10.1080/15435075.2023.2228394

42 Naji M.M., Jabbar B.A. (2024) Diffuser-augmented wind turbine: A review study. *AIP Conference Proceedings*, 3051(1), 100015. https://doi.org/10.1063/5.0191895

43 Demidova G.L., Anuchin A., Lukin A., Lukichev D., Rassõlkin A., Belahcen A. (2020) Magnus wind turbine: Finite element analysis and control system. *In 2020 International Symposium on Power Electronics, Electrical Drives, Automation and Motion (SPEEDAM) 59-64. IEEE.* https://doi.org/10.1109/SPEEDAM48782.2020.9161922

44 Lahoz M., Nabhani A., Saemian M., Bergada J. M. (2024) Wind turbine enhancement via active flow control implementation. *Applied Sciences*, 14(23), 11404. https://doi.org/10.3390/app142311404

45 Gujar S., Auti A., Kale S. (2025) Advancements in wind energy: Exploring the potential of diffuser-augmented wind turbines (DAWTs). *SSRG International Journal of Mechanical Engineering, 12*(1), 12–23. https://doi.org/10.14445/23488360/IJME-V12I1P102

AUTHORS' INFORMATION

Shaimerdenova, Kulzhan Meiramovna - Canditate of Technical Sciences, Associate Professor, E.A. Buketov Karaganda University, Karaganda, Kazakhstan; SCOPUS Author ID: 56604144400, ORCID iD: 0000-0002-9588-4886; gulzhan.0106@mail.ru

Tleubergenova, Akmaral Zharylkasynkyzy - PhD student, E.A. Buketov Karaganda University, Karaganda, Kazakhstan; SCOPUS Author ID: 58244448900, https://orcid.org/0009-0009-5152-0050; akmaral.tzh7@mail.ru

Tanasheva, Nazgul Kadyralievna- PhD, Associate Professor, E.A. Buketov Karaganda University, Karaganda, Kazakhstan; SCOPUS Author ID: 56604246200; https://orcid.org/0000-0002-6558-5383; nazgulya_tans@mail.ru

Dyusembaeva, Ainura Nurtaevna – PhD, Associate Professor, E.A. Buketov Karaganda University, Karaganda, Kazakhstan; SCOPUS Author ID: 57197806401, https://orcid.org/0000-0001-6627-7262 ; aikabesoba88@mail.ru

Minkov, Leonid Leonidovich - Doctor of Physical and Mathematical Sciences, Professor, Tomsk State University, Tomsk, Russia; SCOPUS Author ID: 57196438690; https://orcid.org/0000-0001-6776-6375; lminkov@ftf.tsu.ru

Bakhtybekova, Asem Ravshanbekovna – PhD, Scientific Researcher, E.A. Buketov Karaganda University, Karaganda, Kazakhstan; SCOPUS Author ID: 56604263200; https://orcid.org/0000-0002-2018-8966; asem.alibekova@inbox.ru

EURASIAN PHYSICAL TECHNICAL JOURNAL

2025, Volume 22, No. 2 (52)

https://doi.org/10.31489/2025N2/88-96

Received: 22/01/2025 Revised: 21/04/2025 Accepted: 23/06/2025 Published online: 30/06/2025

Research Article

UDC 543.421/424; 663.6/7

DEVELOPMENT OF LOW-TEMPERATURE CELL FOR IR FOURIER-SPECTROSCOPY OF HYDROCARBON MATERIALS

A. Kenbay[1,2], D. Yerezhep[1,2,*] A. Aldiyarov[1]

[1] al-Farabi Kazakh National University, Almaty, Kazakhstan
[2] Satbayev University, Almaty, Kazakhstan
* *Corresponding author:* darhan_13@physics.kz

Abstract. *This work introduces a technology for Fourier-Transform InfraRed spectroscopy of hydrocarbon materials at low temperatures and atmospheric pressure. This device allows to study optical properties of various substances at temperature range of 77 – 300 K without need of a vacuum and to obtain new fundamental data since there is insufficient research in this area. Described new techniques and methods are working with Fourier-Transform InfraRed spectrometer, diffuse reflection attachment and two Dewar vessels using for cooling with liquid nitrogen inside cryogenic capillary system and blowing with gaseous nitrogen to create InfraRed inactive environment. It makes this new technique a valuable method for obtaining fundamentally new data useful for various energy and infrastructure spheres along with education field as a theoretical information.*

Keywords: Fourier-Transform InfraRed spectroscopy, low temperature, cell, cryogenic capillary system, hydrocarbon materials.

1. Introduction

At the dawn of spectrometry and since the creation of technologies that allow studying hydrocarbon compounds using spectroscopic methods at low temperatures, the process was accompanied by the formation of a vacuum, without which it was difficult to study the nanostructure [1-2], molecular composition [3-4] and physical, chemical, thermal, and optical properties [5-9] of a substance due to the presence of moisture and other impurities in the air that prevent high-quality study and analysis of a substance by any of the spectroscopic methods, including FTIR (Fourier-Transform InfraRed) [10-13].

Low-temperature study of substances [14], in particular hydrocarbon compounds, which involves the use of InfraRed (IR) spectroscopy, presupposes the presence of ultra-low pressure [15], i.e. vacuum, in consequence of which the results of high-quality fundamental studies of the optical properties of hydrocarbon substances under atmospheric pressure are still very rare, since this issue is associated with a number of problems, such as the complexity of developing, maintaining and subsequently upgrading technologies for spectroscopic study that allow achieving low temperatures at atmospheric conditions, the difficulty of creating an inert and IR-inactive or IR-transparent environment [16-17] that helps to achieve accuracy due to the low noise level of spectra and high radiation intensity, as well as the lack of a developed accurate step-by-step research methodology.

Overall, there are very few technologies in the world to study hydrocarbon substances at low temperature and atmospheric pressure. Even though some research studies [18-21] include experiments of spectroscopy at atmospheric pressure and low temperatures, there is limited scientific research in this direction, due to the issues described above. We offer a technology [22] for FTIR spectroscopic study of

hydrocarbon fuels under atmospheric pressure, but at low (77 K) temperatures, which presents solutions to the above problems when studying outside of a vacuum.

The idea of the article is the proposed experimental setup of a cryogenic-capillary system with a low-temperature cell and a measurement technique on it, allowing to obtain profoundly new fundamental data on the properties and behavior of hydrocarbon materials at low temperatures and atmospheric pressure, representing valuable information that can contribute to the subsequent development of high-quality research in this direction, including more factual data related to the action of molecules under these conditions, which can further contribute to the development of more accurate technological equipment.

In this paper, we study kerosene – a hydrocarbon used in energy, technology and other industries as a fuel or solvent and this compound as a test sample, as well as comparison of its spectra with the results of other authors were chosen and carried out in order to confirm the effectiveness of this technique and setup. So, this research corresponds to the goals according to the Sustainable Development Goal (SDG) [23] SDG 4 – Quality education and SDG 9 – Industry, innovation and infrastructure adopted by the United Nations (UN). These new data can be used in writing academic textbooks for higher education students in technical universities with Science, Technology, Engineering, Mathematics (STEM) direction as well as theoretical data for innovative energy industry sphere.

2. Materials and methods

In order to obtain high-quality results of low-temperature spectroscopic research of hydrocarbon materials at atmospheric pressure, we conduct experiments using cryogenic capillary system with low-temperature measuring cell. To provide accurate information about spectroscopic data of hydrocarbons we use high-precision mid-IR Fourier-spectrometer from “Infraspec” with a spectral resolution of 0.125 cm^{-1} in the range of 370–7800 cm^{-1} (figure 1).

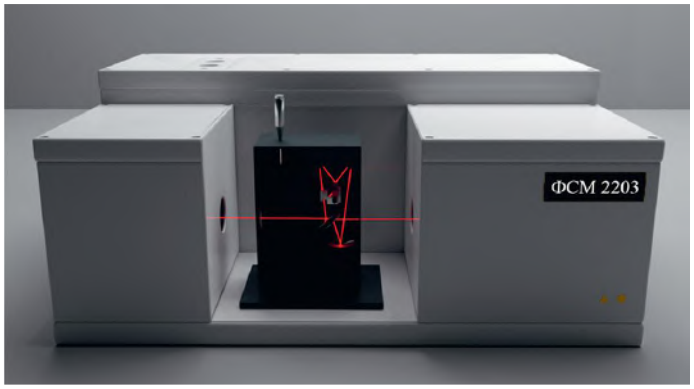

Fig.1. Infrared Fourier spectrometer “FSM 2203” with a diffuse reflection attachment.

To be able to conduct experiment of low-temperature diffuse reflection spectroscopy at atmospheric pressure we had to develop the installation allowing us to study hydrocarbon substances in these conditions. The focus shifts to enabling temperature control of the test sample within the diffuse reflection attachment (figure 2), where the sample is positioned in the cuvette compartment of the FSM 2203 spectrometer. Of utmost significance is the capability to lower the temperature to 77 K. The use of the diffuse reflection method entails minimal sample preparation requirements and allows for the examination of irregular surfaces and various coatings, including polymers. Furthermore, this method enables spectrum analysis across a broad range, offering an advantage over traditional transmission measurement techniques.

The central components of this accessory consist of a mirror system and an retractable sample holder (fig. 2, item 4) where the test samples are housed. A micrometer screw (fig. 2, item 1) is utilized to modify the vertical position of the sample holder, by moving the directive (fig. 2, item 5) along its way we can modify horizontal position. The radiation entering the accessory passes through its inlet and strikes a flat double-sided mirror (fig. 2, item 2). This beam is then reflected towards an elliptical mirror (fig. 2, item 3), which focuses it onto the test sample's surface within the retractable holder. The diffusely reflected light from the sample's surface is redirected back towards the elliptical mirror, which guides it to a spherical

mirror (fig. 2, item 6). The reflected beam further encounters the opposite side of the double-sided flat mirror before entering the detector chamber of the FSM 2203 spectrometer.

Initial processing of the obtained IR spectra is conducted using the FSpec software, with subsequent analysis carried out through the Origin software. In order to achieve temperature reduction of the test sample within the retractable holder's cell of this accessory, a specially designed modification was implemented based on the standard sample holder (figure 3). The enhanced holder's construction comprises two primary materials: polylactide and copper. The selection of these materials for specific holder components is based on their respective thermal conductivity properties. Polylactide, with a thermal conductivity ranging from about 0.11 to 0.19 W/m*K, is chosen to counteract the adverse impact of external atmospheric temperatures on both the copper bar and the samples housed in the measuring cells.

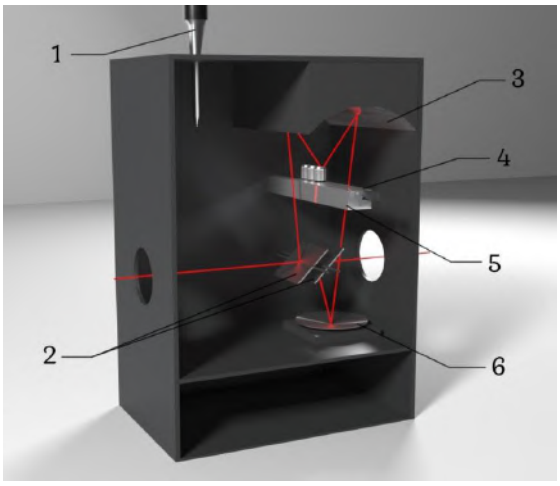

Fig.2. Schematic representation of the diffuse reflection attachment: 1 — micrometer screw; 2 — double-sided flat mirror; 3 — elliptical mirror; 4 — retractable sample holder; 5 — directive; 6 — spherical mirror.

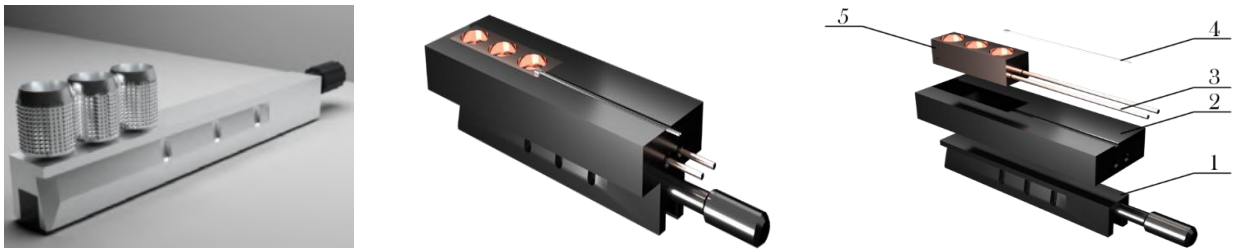

a) b) c)

Fig.3. Three-dimensional model of a retractable holder. a) standard retractable sample holder, b) modernized specialized retractable sample holder, assembled, c) modernized specialized retractable sample holder, disassembled. 1 – holder handle, 2 – heat insulating cover of the holder, 3 – cryogenic capillary system, 4 – temperature sensor (thermocouple), 5 – container

The bar with cylindrical cavities (cells) for sample placement (fig. 3, item 5) is crafted from copper, a high thermal conductivity material, to facilitate rapid and even distribution of temperature provided by the cryogenic capillary system. The cryogenic capillary system itself (fig. 3, item 3) is also constructed from copper for similar reasons.

Cooling the samples under study to a temperature of 77 K is facilitated by the continuous flow of liquid and gaseous nitrogen through the copper tube of the cryogenic capillary system. The close contact between the copper tube, copper bar, and the cells, along with copper's high thermal conductivity, enables swift cooling of the test material (such as hydrocarbon) to the desired temperature. The copper bar temperature is monitored using a thermocouple attached to the surface of the bar by the LakeShore PID controller (fig. 3, item 4). Heating the test samples is accomplished by halting the nitrogen circulation through the cryogenic capillary system, thereby restoring thermodynamic equilibrium between the sample and the surroundings. To circulate nitrogen through the copper tubes of the cryogenic capillary system, high pressure is established through heating in a specialized Dewar vessel. This process causes nitrogen to be expelled from the vessel into the cryogenic capillary system, enabling the cooling of the samples.

The cryogenic capillary system is connected to the Dewar vessel mentioned above through a hermetically sealing fastening system (figure 4). This installation is made to supply and cool samples at atmospheric pressure in the low-temperature cell with permanent liquid and gaseous nitrogen circulation (77 K) via copper capillaries. The installation consists of Dewar vessel (vacuum flask) (fig. 4, item 1), fastening system (fig. 4, item 3), copper capillary (fig. 4, item 4) covered with thermal insulating coating, manometer or pressure gauge (fig. 4, item 2), contacts for electrical clamp (fig. 4, item 6) to create electrical connection and provide with voltage from heater, check valve (fig. 4, item 5) to prevent exceeding pressure inside a flask.

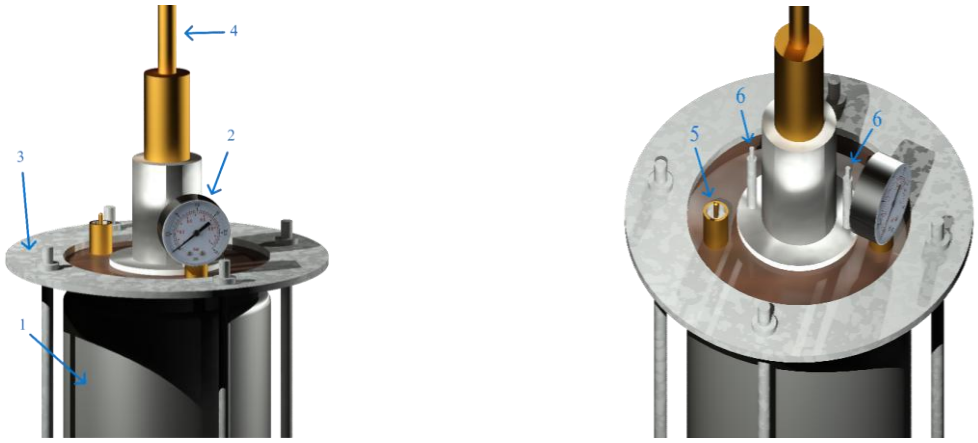

a) b)

Fig.4. Cryogenic capillary system and Dewar vessel (vacuum flask)

To start an experiment, we first need to ensure that the installation is ready:

1) Dewar vessel which is connected to the cryogenic capillary system is firmly hermetically sealed, a check valve is not stuck and the manometer (pressure gauge) indicates pressure at least 6 psi (0,4 atm)

2) Voltage supplied from the heater is reaching a contact element inside the vessel and heating a liquid nitrogen which is supposed to circulate inside capillary system by thermal expansion

3) There is no electrical contact with other metal parts of the installation to avoid short circuit

4) Thermocouple is working with LakeShore PID-controller

5) Capillaries are thoroughly covered with thermal insulating coating to avoid thermal conductivity with ambient environment while nitrogen is circulating inside them.

To ensure the experiment's purity, a blowing system was incorporated into the diffuse reflection attachment. By introducing gaseous nitrogen into the attachment, an inert environment is created, which not only safeguards the samples and the copper bar from frost formation but also supports the experiment's wholeness by creating IR-inactive environment. The next step of our experiment technique is preparation above mentioned blowing system, gasifier – ensuring hermetical sealing of the gasifier, pouring nitrogen into the gasifier's vessel, connecting it to the spectrometer's cuvette compartment with rubber hose in order to provide the diffuse reflection attachment, inside of which the IR radiation will pass, with inert IR-inactive environment that, in addition, lets us to avoid water vapor deposition on the samples while cooling. Preparation of gasifier is accurately described below:

1. Ensuring that the gasifier's Dewar vessel is empty and ready to get filled with nitrogen, being aware that manometer (pressure gauge) indicator is pointing to zero and only then opening the vessel's lid

2. The hose has to be attached firmly to both outlets and has no holes or another opening to avoid outflows

3. To check all radiators for frost absence, in order to provide quality gaseous nitrogen flow

4. When the gasifier is ready to be filled up, starting carefully pouring nitrogen into its vessel from another Dewar vessel

5. Closing the vessel's lid tightly and ensuring its manometer shows some additional pressure

6. Check the hose's outlet for the nitrogen to be flowing unhindered.

The gasifier's structure is shown in figure 5 – the vessel (fig. 5, item 1) is dedicated to store nitrogen since it is also a Dewar vessel, the manometer (pressure gauge) (fig. 5, item 4) shows overpressure inside the vessel and helps us to calculate approximate time of nitrogen exhaustion, the rubber hose (fig. 5, item 2)

connected to the spectrometer to provide diffuse reflection attachment with a nitrogen inert IR-inactive environment, the capillary tube (fig. 5, item 5) for nitrogen transfer, the radiators (fig. 5, item 3) that are meant to conduct a heat and help to provide with gaseous nitrogen particularly, the lid (fig. 5, item 8) to prevent nitrogen outflow, the valve (fig. 5, item 6) to regulate nitrogen flow and the check valve (fig. 5, item 7) to avoid excess pressure.

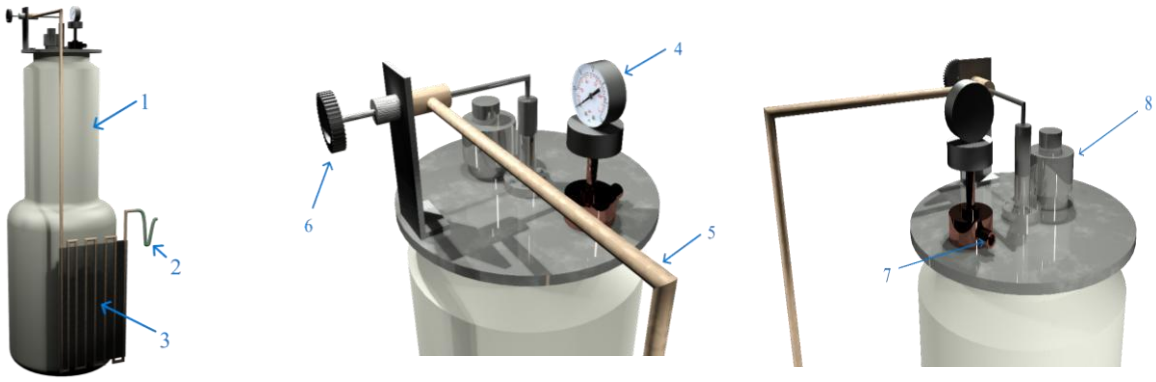

a) b) c)

Fig.5. Gasifier generating nitrogen for inert IR-inactive environment

Temperature of the samples in container's cells changes as we cool them with nitrogen flow or heat them by stopping nitrogen circulation. We need to know exact temperature of the samples while taking a spectrum. To measure the temperature of the sample we use E-type thermocouple (chromel and constantan) connected to the LakeShore Model 325 cryogenic temperature PID-controller. Within the controller's interface we can set initial temperature, room temperature, thermocouple type, an output (A or B) of thermocouple contact, etc.

The controller provides two separate proportional-integral-derivative (PID) control loops. The PID algorithm determines the control output by considering the temperature setpoint and feedback from the control sensor. With broad tuning parameters, it is compatible with most cryogenic cooling systems and many small high-temperature ovens. A high-resolution digital-to-analog converter ensures smooth control output. Users can manually set the PID values, or use the Autotuning feature to automatically adjust the tuning process.

By connecting cryogenic capillary system to the cell and putting it into diffuse reflection attachment inside of "FSM 2203" FTIR-spectrometer, we start our experiment. As temperature is going down after reaching crystallization point of hydrocarbon substance, we are taking spectra at every few certain temperatures. One of our goals is to study hydrocarbons' physical and chemical properties at atmospheric pressure and nitrogen boiling temperature (77 K) by taking spectra of samples in these conditions. Once the samples' temperature has reached its minimal point and the PID-controller shows 77 K we are taking Fourier-transform infrared spectra and starting heating process by stopping nitrogen flow and letting thermodynamical equilibrium to take place, and in the same way take spectra at every few certain temperatures.

After ensuring that all installations and instrumentation we need are ready, we start our experiment of studying optical properties of test substances (hydrocarbon compounds) at low temperature (77 K) and at atmospheric pressure. To conduct the experiment, we perform the following steps:

Stage 1: Filling up the gasifier and cryogenic capillary system with nitrogen and sealing them properly. Connect them to the following instrumentations: 1) gasifier to the spectrometer's inlet of cuvette compartment with rubber hose to supply with inert environment, 2) cryogenic capillary system to the LakeShore 325 temperature PID-controller with E-type (chromel-constantan) thermocouple, and to heater with wires via alligator clips to create additional pressure inside the flask and thereby enhance nitrogen circulation through capillary.

Stage 2: Covering cuvette compartment with polypropylene and polyethylene film to keep IR-inactive inert nitrogen environment inside the cuvette for obtaining more quality IR-spectra, with only some space for micrometer screw and retractable holder. Due to comparatively similar molecular weight of air and N_2, it does not seem difficult to keep such an environment.

Stage 3: Putting pre-pestled potassium bromide sample, which absorbs moisture from ambient, into first cell of retractable holder's container bar so we can obtain its spectrum and use as base that will then divide test substance's spectra. Preparation of the test sample (kerosene in this case) includes only few steps – opening properly sealed vessel, picking up 1 ml kerosene using new disposable syringe, putting it into second and third cells (0.5 ml each) and inserting the holder into diffuse reflection attachment. Syringe is used to take equal doses of kerosene for each experiment. The kerosene used in our experiment is from brand "Derzhava" with sulfur content 1% according to GOST 18499-73.

Stage 4: Finding out the holder's position with the strongest intensity of IR-beam by adjusting vertical micrometer screw for every cell separately. Once it is found, we stop adjusting and further use this position to register samples' spectra by "FSpec" and analyze them in "Origin" software.

Stage 5: Taking spectra while cooling samples starting from room temperature (290-300 K) and all the way down to the nitrogen boiling point (77 K), using temperature controller to real-time determine the sample temperature and applying heater to force nitrogen inside the flask flowing more intensively through capillary. It is important not to miss test substance's phase transition and record its spectra in each phase to further describe the differences. After passing phase transition temperature taking a few spectra every certain temperature until reaching lowest point – 77 K and registering samples spectra at this point. After that we stop the heater thereby reducing nitrogen circulation and let the thermal equilibrium to take place. This will force a sample to get heated and increase its temperature while we are taking spectra. Afterwards we compare sample's cooling and heating spectra and describe their differences.

Stage 6: After obtaining spectra we needed, stopping the experiment by removing the holder from attachment, electrical contacts from vacuum flask and PID-controllers thermocouple. Blowing spectrometers compartment with nitrogen to get rid of possible residual hydrocarbon vapors and thereby cleaning inside of diffuse reflection attachment and FSM 2203 spectrometer.

Afterwards we need to analyze spectra obtained by this experiment and draw up the results. These research and experiment can be used as fundamental information for many spectroscopic studies of hydrocarbon materials since results are obtained at low temperature but at atmospheric pressure. But before that it is important to compare our results with another data of obtaining spectra of hydrocarbons using low-temperature setups.

3. Results and discussion

Results of the experiment are shown in figure 6. Test substance is kerosene, a hydrocarbon used in energy, technological and other industries as a fuel or solvent. In this transmission spectrum, characteristic peaks of the functional groups of kerosene are visible, in particular, the stretching and bending of the C-H bonds, one can also notice a tendency to shift the peak of the C-H bond bending relative to the results of other authors, a difference in wave numbers is obvious during the stretching of the above-mentioned bond in the kerosene molecule, that is, a hypsochromic shift.

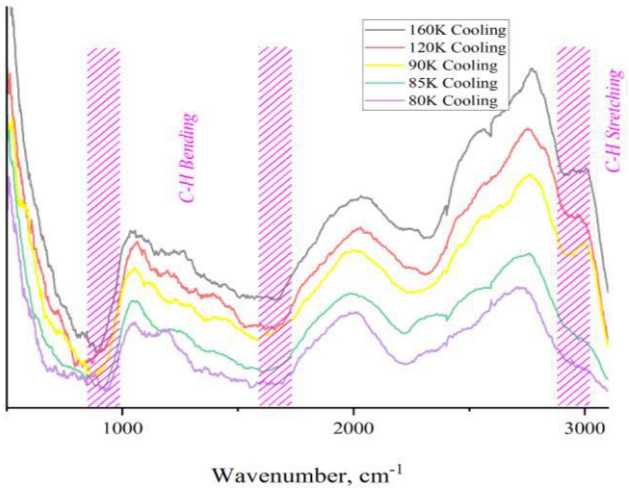

Fig.6. Spectra of kerosene while cooling from room temperature (only few temperatures are shown)

As we can see, there is the C-H stretching in the wavenumber range of 2800-3000 cm^{-1}, mild hypsochromic shift in the range of 1500-1700 cm^{-1} for the C-H bending (scissoring) and almost no shift in the range of 600-900 cm^{-1} for C-H bending (rocking and out-of-plane) relative to the results of other authors. Highlighted with dotted lines areas represent the peaks that indicate presence of kerosene key C-H group and its vibrations at specific wavenumber range. These lines are meant to give importance and significance to the vibrations. To show data in more clear way we are providing the table of our research and other authors research results of kerosene spectra (tab. 1).

Table 1. Comparison of spectra results

№	Authors	C-H stretching (cm^{-1})	C-H bending (scissoring) (cm^{-1})	C-H bending (rocking and out-of-plane) (cm^{-1})
1.	Our data	2800-3000	1500-1700	600-900
2.	Dollah, A., Zainol Rashid, Z. et al [24]	2800-3000	1300-1500	800
3.	Mirea, R., & Cican, G. [25]	2800-3100	1300-1500	650-800
4.	Biaktluanga, L., Lalhruaitluanga, J. et al [26]	2800-3000	1500	800

Results of authors [24] correspond to the wavelength under normal conditions: C-H stretching at 2800-3000 cm^{-1}, C-H bending (scissoring) at 1300-1500 cm^{-1} and C-H bending (rocking and out-of-plane) at 800 cm^{-1}. Other researchers' results [25] are given as well; they correlate well with our data what additionally confirms effectiveness of the measurement technique used in our research. More of other authors' results in this field [26] are given. We can see the same characteristic peaks we observed in previous comparisons, particularly C-H stretching at 2800-3000 cm^{-1}, C-H bending (scissoring) at 1500 cm^{-1} and C-H bending (rocking and out-of-plane) at 800 cm^{-1}. The physical meaning of this comparison is that we obtained spectral results of characteristic peaks of kerosene molecules' key functional groups, well-correlated with results of other respected authors in this field. This comparison confirms the effectiveness of our new cryogenic setup, used for obtaining FTIR-spectra of hydrocarbon fuels at low temperature and atmospheric pressure.

The kerosene spectra at low temperature shown in fig. 6 are obtained at atmospheric pressure, which undoubtedly influences the spectra and vibration wavenumbers of the sample, and that is proved by hypsochromic shift of C-H stretching, which was mentioned before. This result shows that conditions of test sample as well as the way of obtaining solid kerosene (below 226 K) directly affect FTIR-spectra, since other researchers' spectra being compared with our data [24-26] are received in vacuum.

We are truly sure that given comparison analysis proves the operability and effectiveness of our setup with low-temperature cell and cryogenic-capillary system being used in our experiments at low temperatures (down to 80 K) and atmospheric pressure (101,325 Pa, 1 atm).

4. Conclusions

In this paper, we have described an experimental setup and measurement technique for studying hydrocarbon compounds, particularly a kerosene, at low-temperatures and atmospheric pressure using the cryogenic-capillary system with nitrogen blowing system, the gasifier, and high resolution FTIR spectrometer. The verification performed by comparing the FTIR spectra of kerosene obtained using our setup with the results of FTIR spectra reported by other researchers allows us to conclude that there is a good correlation.

Also, we can say that kerosene being studied at atmospheric pressure has slightly different result in one characteristic peak of one vibration, related to the C-H stretching, from research results of kerosene under vacuum. That can be valuable fundamental information about kerosene (may be not only) properties and behavior. The presented setup has a number of advantages, such as a possibility to study low-temperature samples at atmospheric pressure, to obtain profoundly new fundamental data about properties and structure of hydrocarbon substances under unusual conditions and opportunity to present it to scientific community as a new operable device for cryogenic studies at atmospheric pressure.

Conflict of interest statement

The authors declare that they have no conflict of interest in relation to this research, whether financial, personal, authorship or otherwise, that could affect the research and its results presented in this paper.

CRediT author statement

Kenbay A: Methodology, Formal analysis, Investigation, Writing – Original Draft, Visualization; **Yerezhep D:** Writing – Review & Editing, Validation, Data Curation, Project administration; **Aldiyarov A:** Conceptualization, Resources, Supervision, Funding acquisition. The final manuscript was read and approved by all authors.

Funding

This research has been funded by the Science Committee of the Ministry of Science and Higher Education of the Republic of Kazakhstan (Grant No. AP27508001 "Study of the stability of perovskite materials under low-temperature conditions (15-100K) for further application in space research")

References

1 Shaalan N.M. (2024) An approach to fabricate nanomaterials using a closed low-temperature growth system. *Materials Chemistry and Physics*, 328, 129930. https://doi.org/10.1016/j.matchemphys.2024.129930

2 Sorokin N. I., Arkharova N. A., Karimov D. N. (2024) Synthesis of nano-sized solid electrolyte Pr1-ySryF3-y and the effect of heat treatment on the ionic conductivity of fluoride nanoceramics. *Crystallography Reports*, 69(4), 561–568. https://doi.org/10.1134/S106377452460145X

3 Carrascosa H., Muñoz Caro G. M., Martín-Doménech R., Cazaux S., Chen Y.-J., Fuente A. (2024) Formation and desorption of sulphur chains (H2S x and S x) in cometary ice: Effects of ice composition and temperature. *Monthly Notices of the Royal Astronomical Society,* 533(1), 967–978. https://doi.org/10.1093/mnras/stae1768

4 Kakkenpara Suresh S., Dulieu F., Vitorino J., Caselli P. (2024) Experimental study of the binding energy of NH 3 on different types of ice and its impact on the snow line of NH_3 and H_2O. *Astronomy & Astrophysics*, 682, A163. https://doi.org/10.1051/0004-6361/202245775

5 Sokolov D.Y., Yerezhep D., Vorobyova O., Ramos M.A., Shinbayeva A. (2022) Optical studies of thin films of cryocondensed mixtures of water and admixture of nitrogen and argon. *Materials,* 15(21), 7441. https://doi.org/10.3390/ma15217441

6 Sokolov D.Y., Yerezhep D., Vorobyova O., Golikov O., Aldiyarov A.U. (2022) Infrared analysis and effect of nitrogen and nitrous oxide on the glass transition of methanol cryofilms. *ACS Omega,* 7(50), 46402–46410. https://doi.org/10.1021/acsomega.2c05090

7 Yerezhep D., Akylbayeva A., Golikov O., Sokolov D.Y., Shinbayeva A., Aldiyarov A.U. (2023) Analysis of vibrational spectra of tetrafluoroethane glasses deposited by physical vapor deposition. *ACS Omega*, 8(22), 19567–19574. https://doi.org/10.1021/acsomega.3c00985

8 Golikov O.Yu., Yerezhep D.E., Sokolov D.Yu. (2023) Researching carbon dioxide hydrates in thin films via FTIR spectroscopy at temperatures of 11-180 K. *Scientific and Technical Journal of Information Technologies, Mechanics and Optics, 23(3),* 483–492. https://doi.org/10.17586/2226-1494-2023-23-3-483-492

9 Bhavani G., Durga Rao T., Niranjan M.K., Kumar K.R., Sattibabu B., Petkov V., Kannan E.S., Reddy B.H. (2024) Structural, magnetic, optical and electronic properties of Gd2NiIrO6. *Physica B: Condensed Matter*, 695, 416477. https://doi.org/10.1016/j.physb.2024.416477

10 Xu J., Liu Q., Zheng T., Xie M., Shen H., Li Y., Guo F., Zhang Q., Duan M., Wu K.-H. (2025) Comparing low-temperature NH3-SCR activity, operating temperature window and kinetic properties of the Mn-Fe-Nb/TiO2 catalysts prepared by different methods. *Separation and Purification Technology*, 356, 129906. https://doi.org/10.1016/j.seppur.2024.129906

11 Nishikino T., Sugimoto T., Kandori H. (2024) Low-temperature FTIR spectroscopy of the L/Q switch of proteorhodopsin. *Physical Chemistry Chemical Physics*, 26(35), 22959–22967. https://doi.org/10.1039/D4CP02248C

12 Yang Z., Su B., Ding H., Qiu Y., Zhong D. (2024) Prediction of asphalt low-temperature performance by FTIR spectra using comparative modelling strategy. *Road Materials and Pavement Design*, 1–16. https://doi.org/10.1080/14680629.2024.2383915

13 Moszczyńska J., Liu X., Wiśniewski M. (2022) Non-thermal ammonia decomposition for hydrogen production over carbon films under low-temperature plasma - In-situ ftir studies. *International Journal of Molecular Sciences*, 23(17), 9638. https://doi.org/10.3390/ijms23179638

14 Moody G., Kavir Dass C., Hao K., Chen C.-H., Li L.-J., Singh A., Tran K., Clark G., Xu X., Berghäuser G., Malic E., Knorr A., Li X. (2015) Intrinsic homogeneous linewidth and broadening mechanisms of excitons in monolayer transition metal dichalcogenides. *Nature Communications*, 6(1), 8315. https://doi.org/10.1038/ncomms9315

15 Golikov O. Yu., Yerezhep D., Sokolov D.Yu. (2023) Improvement of the automatic temperature stabilisation process in the cryovacuum unit. *Scientific and Technical Journal of Information Technologies, Mechanics and Optics*, 23(1), 62–67. https://doi.org/10.17586/2226-1494-2023-23-1-62-67

16 Dillinger S., Mohrbach J., Hewer J., Gaffga M., Niedner-Schatteburg G. (2015) Infrared spectroscopy of N 2 adsorption on size selected cobalt cluster cations in isolation. *Physical Chemistry Chemical Physics*, 17(16), 10358–10362. https://doi.org/10.1039/C5CP00047E

17 Fortes P.R., Da Silveira Petruci J.F., Wilk A., Cardoso A.A., Raimundo Jr I.M., Mizaikoff B. (2014) Optimized design of substrate-integrated hollow waveguides for mid-infrared gas analyzers. *Journal of Optics,* 16(9), 094006. https://doi.org/10.1088/2040-8978/16/9/094006

18 Serdyukov V.I., Sinitsa L.N., Lugovskoi A.A., Emel'yanov N.M. (2020) Liquid-nitrogen-cooled optical cell for the study of absorption spectra in a fourier spectrometer. *Atmospheric and Oceanic Optics*, 33(4), 393–399. https://doi.org/10.1134/S1024856020040144

19 Serdyukov, V. I., Sinitsa, L. N., Lugovskoi, A. A., & Emelyanov, N. M. (2019). Low-temperature cell for studying absorption spectra of greenhouse gases. Atmospheric and Oceanic Optics, 32(2), 220–226. https://doi.org/10.1134/S1024856019020106

20 Sung K., Mantz A. W., Smith M.A.H., Brown L. R., Crawford T.J., Devi V.M., Benner D.C. (2010) Cryogenic absorption cells operating inside a Bruker IFS-125HR: First results for 13CH4 at 7μm. *Journal of Molecular Spectroscop*y, 262(2), 122–134. https://doi.org/10.1016/j.jms.2010.05.004

21 Mantz A.W., Sung K., Brown L.R., Crawford T.J., Smith M.A.H., Malathy Devi V., Chris Benner D. (2014) A cryogenic Herriott cell vacuum-coupled to a Bruker IFS-125HR. *Journal of Molecular Spectroscopy,* 304, 12–24. https://doi.org/10.1016/j.jms.2014.07.006

22 Kenbay A.A., Golikov O.Yu., Aldiyarov A.U., Yerezhep D.E. (2023) Low-temperature cell for IR Fourier spectrometric investigation of hydrocarbon substances. *Scientific and Technical Journal of Information Technologies, Mechanics and Optics*, 23(4), 696–702. https://doi.org/10.17586/2226-1494-2023-23-4-696-702

23 Nguyen T.-D., Ngo T.Q. (2022) The role of technological advancement, supply chain, environmental, social, and governance responsibilities on the sustainable development goals of SMEs in Vietnam. *Economic Research-Ekonomska Istraživanja,* 35(1), 4557–4579. https://doi.org/10.1080/1331677X.2021.2015611

24 Dollah A., Zainol Rashid Z., Hidayati Othman N., Nurliyana Che Mohamed Hussein S., Mat Yusuf S., Shuhadah Japperi N. (2018) Effects of ultrasonic waves during waterflooding for enhanced oil recovery. *International Journal of Engineering & Technology,* 7(3.11), 232. https://doi.org/10.14419/ijet.v7i3.11.16015

25 Mirea R., Cican G. (2024) Theoretical assessment of different aviation fuel blends based on their physical-chemical properties. *Engineering, Technology & Applied Science Research*, 14(3), 14134–14140. https://doi.org/10.48084/etasr.6524

26 Biaktluanga L., Lalhruaitluanga J., Lalramnghaka J., Thanga H. H. (2024) Analysis of gasoline quality by ATR-FTIR spectroscopy with multivariate techniques. *Results in Chemistry*, 8, 101575. https://doi.org/10.1016/j.rechem.2024.101575

AUTHORS' INFORMATION

Alisher Kenbay – master of natural sciences, master of science in the field of training 16.04.01 Technical Physics, PhD student of Physical and Technical faculty, al-Farabi KazNU, Almaty, Kazakhstan; SCOPUS Author ID 58639681300, ORCID iD 0000-0001-6803-5873; mr.kenbay@gmail.com

Darkhan Yerezhep – PhD, Candidate of technical sciences, associate professor of Institue of Energy and Mechanical Engineering named after A. Burkitbayev, Satbayev University, Almaty, Kazakhstan; SCOPUS Author ID 57194012596, ORCID iD 0000-0002-2232-2911; darhan_13@physics.kz

Abdurakhman Aldiyarov – candidate of physical-mathematical sciences, associate professor, acting professor of Physical and Technical faculty, al-Farabi KazNU, Almaty, Kazakhstan; SCOPUS Author ID 16201950600, ORCID iD 0000-0002-5091-7699; abdurakhman.aldiyarov@kaznu.kz

EURASIAN PHYSICAL TECHNICAL JOURNAL

2025, Volume 22, No.2 (52)

https://doi.org/10.31489/2025N2/97-108

Received: 05/01/2024 Revised: 08/04/2024 Accepted: 17/06/2025 Published online: 30/06/2025

Research Article

UDC 539.232, 620.193; 669.2/.8

PREDICTION OF CORROSION RESISTANCE OF MAGNALIAS

Guchenko S.A., Seldyugaev O.B., Fomin V.N., Afanasyev D.A.*

E.A. Buketov Karaganda University, Karaganda, Kazakhstan
*Corresponding author: a.d.afanasyev2@gmail.com

Abstract. *In the presented work the factors influencing the strength and corrosion rate in seawater of magnalium aluminum-magnesium alloy were considered. It was shown that in unsaturated solid alpha solutions the main form of magnesium in the aluminium structure was the electronic compound Mg_2Al_4 entering the rhombic subsystem of aluminium cells. The calculation showed that the more aluminium cells contain Mg_2Al_4 group as a rhombic subsystem, the higher the strength of these alloys. The mechanism of destruction by halogen ions of pure aluminium cells and aluminium cells containing the Mg_2Al_4 group was determined by the PM3 method. Destruction of both types of cells occurred by the same scenario, through the detachment by halogen ions of the central atom in the upper edge of cells bordering. It was shown that in seawater the corrosion rate of aluminium cells containing Mg_2Al_4 group was higher than the corrosion rate of pure aluminium cells. A mathematical model has been developed that allows calculating the change in the corrosion rate of magnesium alloys with low magnesium mass fraction (up to 3.5 % magnesium inclusive) in seawater. The model allowed to take into account the change of influence of the mass fraction of the main alloying elements (Mg, Cr, Mn, Zn, Ti, Cu) on the corrosion rate. Change of corrosion rate in seawater of three aluminium-magnesium alloys variants was calculated using this model. These aluminium alloy variants include a magnesium content of 2.6 mass % with higher levels of the alloying elements Cr and Mn.*

Keywords: Corrosion, aluminum-magnesium alloy, magnalium, aluminium, cubic subsystem, halogens, quantum-chemical calculations.

1. Introduction

Aluminium alloys are used in various industries due to their low density, high corrosion resistance and low cost [1]. Modelling of the alloys structure depending on the quantitative composition of the alloy is one of the ways to accelerate the search and prediction of improved alloy compositions. For example, a hybrid model on a combination of neuro-fuzzy and physical models for predicting the flow stress and microstructural evolution during thermomechanical processing has been developed in the paper [2]. Comparison with experimental data have shown generally good agreement for Al -Mg alloy with 1 mass % of Mg deformed under thermomechanical processing conditions. Using of machine learning for molecular material modelling of Al, Mg and Al-Mg alloy samples is shown in [3]. Ability to create uniformly accurate models of potential energy surfaces with a minimum amount of reference data is shown on the basis of the active learning procedure.

Another example of a complex study (experimental and numerical) is the work [4]. Reducing the number and size of Al_3Fe intermetallic particles in aluminum alloy leads to an increase in the corrosion resistance of the material. This result was obtained on the basis of electron microprobe analysis and transmission electron microscopy. A large number of works [5- 9] have been devoted to the study of the

corrosion process and methods of protection against it. The works were carried out both experimentally [5-7] and with the involvement of numerical calculations and mathematical models [8, 9]. Therefore, the creation of calculation methods capable of predicting with good accuracy the corrosion resistance of new and modified alloys is an urgent task.

The purpose of this work was to develop a methodology for predicting the corrosion resistance of aluminium-magnesium alloys with a percentage of magnesium not exceeding 3.5 mass %. This allows to significantly reduce research costs and increase the speed of development of new alloy modifications.

2. Materials and experimental details

The structure of magnalium and other samples have calculated using the parametric method 3 (PM3), which was specially developed for calculations of compounds containing aluminum and halogen atoms [10]. In the aluminium unit cell model 14 atoms were used for the calculations. It was taken 14 atoms in the cell of AMg-aluminium-magnesium (AMg) alloys, as in the cell of pure aluminum.

Considering that the cells of AMg alloys have had the same number of atoms as in the cell of pure aluminum (14 atoms). The density of AMg alloys was calculated with different numbers of magnesium atoms in the structural cell. The calculation was started with the condition that all cells of the AMg alloy contain 1 magnesium atom, and all other atoms in the cells are aluminum atoms (13 aluminum atoms). A model of an aluminum cell consisting of 9 atoms have been used in order not to take into account the same aluminum atoms twice in the calculations. This sell was called a calculated aluminium cell. The number of magnesium atoms changed depending on the concentration of magnesium in the alloy. Only one halogen atom - chlorine was used for modeling interaction cells with seawater.

In order to clarify the corrosion resistance of AMg alloys in seawater, samples of pure aluminium (analytic grade - 99.99 % Al), AMg2, AMg3 and AMg6 identical in size and external surface area were placed for 72 hours in 5% iodine solution in ethanol. Samples with dimensions of 1cm*1.5cm*2 mm were used. The gravimetric method was used to measure the corrosion rate in the samples - the samples were weighed before and after being placed in iodine solution. The mass of samples was measured on electronic scales RADWAG AS 60/220.R2 with an accuracy of 10^{-4} grams.

3. Results and discussion

The structure of the pure aluminium cell has been known from X-ray diffraction analysis [11]. A schematic representation of the aluminum cell structure obtained as a result of the PM3 calculation is shown in Figure 1. The aluminium cell is a face- centred cubic lattice of 14 aluminium atoms, consisting of two subsystems: cubic and rhombic (Figure 1). There are no aluminium atoms in the centre of the aluminium cell, which accounts for the good ductility of pure aluminium. Under normal conditions, these aluminium cells on the surface of products are partially oxidised. The cubic subsystem of the aluminium cell lattice on the surface is oxidised. It is reason why pure aluminum does not corrode in fresh water. However, pure aluminium has low strength and hardness and has currently very limited use, e.g. for producing electrical wires.

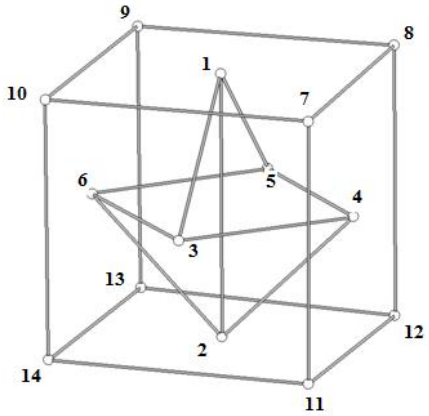

Fig.1. Structure of the pure aluminium cell (atoms 1-6 form the rhombic subsystem of the aluminium cell).

Alloys of aluminium with magnesium (magnalia) are widely used for technological purposes. These alloys have significantly higher hardness and strength than pure aluminium, Table 1 [12]. It is known that the

strength of magnesium increases with increasing magnesium content in the alloy in the series from AMg1, AMg2, AMg3, AMg4, AMg6 (the figure indicates the percentage of magnesium content in the aluminium alloy by mass). An almost linear dependence of magnesium strength increase on magnesium percentage is observed (Table 1).

Table 1. Mechanical characteristics of aluminium alloys [12]

	Tensile strength, MPa	Yield strength, MPa	Brinell hardness, Kgs/mm^2
Pure aluminium	70	25	25
AMg1	140	50	30
AMg2	170	80	45
AMg3	200	100	58
AMg4	250	120	75
AMg5	280	150	65
AMg6	320	160	100

There are 14 atoms in the cells of AMg alloys as in the cells of pure aluminium. There is a homogeneous distribution of magnesium and other alloying elements in AMg alloys, as is known from X-ray diffraction analysis [13]. It is believed that the increase in the strength of alloys of aluminium with magnesium (magnalium) compared to pure aluminium is due to the emergence of strengthening phases in these alloys in the form of intermetallic compounds of magnesium and aluminium [14].

In further, issues related to the structural formula of intermetallic compounds of magnesium with aluminum in each type of AMg alloy, their localization in the structure of cells and their influence on the strength of the alloys as a whole were considered. Table 2 presents data on the density of AMg alloys depending on the mass content of magnesium atoms [15]. A large mass fraction of magnesium in an aluminum alloy leads to a lower density of the alloy. The density of AMg alloys at different number of magnesium atoms in the structural cell was calculated taking into account that in the cells of AMg alloys the same number of atoms as in the cell of pure aluminium (14 atoms). As a starting calculation, the condition was adopted that each cell of the AMg alloy contains one atom of magnesium. All other atoms in the cells were aluminium atoms (13 aluminium atoms). Below, the algorithm for calculating the density of the AMg alloy containing a given number of magnesium atoms was considered.

Table 2. Basic initial parameters of pure aluminium and alloys (magnalias) and alloy cell modelling parameters

	PA*	AMg1	AMg2	AMg3	AMg4	AMg5	AMg6	AMn*
Density, kg/m^3	2700	2690	2680	2670	2660	2650	2640	2730
Average number of magnesium atoms N per cell of AMg alloy**	-	0,25	0,5	1	-	-	2	-
Percentage of cells containing Mg_2Al_4 group	0%	12%	25%	50%	-	-	100%	-
Alloy tensile strength	70 MPa	140 MPa	170 MPa	200 MPa	-	-	250 MPa	-
Corrosion, mm per year	0,75	-	0,4	-	0,73	-	1,5	0,32

Here
* - PA (pure aluminium) - aluminium with 99.99 % purity; AMn - aluminium-manganese alloy with percentage of manganese 1.5 mass %;
** - average number of magnesium atoms in each magnalium cell.

The calculation took into account the fact that the aluminum atoms forming cell faces of 14 atoms are simultaneously part of two bordering cells. The computational aluminium cell included the first 4 aluminium atoms (atoms 9, 10, 13, 14 in the Figure 1) of the cubic subsystem (there are 8 atoms in the cubic subsystem of the physical cell). The rhombic subsystem of the physical cell contained 5 aluminium atoms (atoms 1-3, 5, 6 in the Figure 1). Atoms 4, 7, 8, 11, 12 of the physical cell belonged in the computational model to the neighboring computational cell.

Then 8 aluminium atoms and one magnesium atom was used in the calculated aluminium cell model. Both types of cells (physical and the cell used for calculations) contained one magnesium atom. It was considered that the magnesium atom is localised in the rhombic subsystem of the physical cell.

1) The total mass of 1 m^3 of pure aluminum (Mone Al) is determined for all aluminum atoms occupying positions with a given number (e.g. atoms 10, Figure 1) in all calculated aluminium cells. The density of pure aluminium is 2700 kg/m^3.

$$M_{one\ Al}= 2700\ kg/\ 9\ aluminium\ atom= 300\ kg. \quad (1)$$

The total masses of aluminium atoms under any other numbers in all cells in 1m^3 are the same.

2) The total mass of magnesium atoms in 1 m^3 of AMg alloy was calculated, knowing the total mass of aluminum atoms under a certain number $M_{one\ Al}$, the mass of a magnesium atom, which is 0.901 of the mass of an aluminum atom, and the number of magnesium atoms N in aluminum cells. If 1 magnesium atom N in the cells equals 1, then all magnesium atoms in this case are 1/9 of the total number of atoms in the alloy:

$$M_{one\ Mg}= M_{one\ Al} * 0.901 * N = 270.3\ kg; \quad (2)$$

3) The total mass of aluminum atoms $M_{tot\ Al}$ in 1 m^3 of the AMg alloy was found for a given number of magnesium atoms N in the elementary cells of the alloy.

$$M_{tot\ Al}= M_{one\ Al} * (9 - N); \quad (3)$$

There were 270.3 kg of magnesium and 2400 kg of aluminium for 1 m^3 of AMg alloy containing 1 magnesium atom in each cell. When they were summed up, it turned out that in 1 m^3 there is 2670.3 kg of the total mass of aluminium and magnesium (add up 8 mass fractions of aluminium and one mass fraction of magnesium). That is the density of the alloy in which in 100% of structural cells there are 8 atoms of aluminium and 1 atom of magnesium will be 2670,3 kg/m^3. This density corresponds to the alloy AMg3 (Table 2).

Assuming that one magnesium atom is in every second real physical cell (N=0.5) of the alloy. It was got the density of the alloy 2682.15 kg/m^3. The number of magnesium atoms by condition is 2 times less than in the alloy AMg3 and the total mass of magnesium in 1 $m^3$of this alloy was 134.15 kg. The mass of aluminium in 1 $m^3$of this alloy was 2548 kg. The value is 2682.15 kg/m^3 which is close in density to the AMg2 alloy. In this case, it was assumed that only half of the cells of the AMg2 alloy contain a magnesium atom and the other half of the cells were pure aluminium cells.

If a magnesium atom was contained in every fourth physical cell of N= 0.25 aluminum, then alloy density would be 2692.6 kg/m^3. The number of magnesium atoms by the condition was 4 times less than in the alloy AMg3 and the total mass of magnesium in 1 m^3 of this alloy is 67,575 kg. The mass of aluminium in 1 m^3 of this alloy was 2625 kg, which is close to the density of the alloy AMg1. In this case, it is assumed that only 25% of the cells of the alloy contain a magnesium atom and 75% of the cells are pure aluminium cells.

Also consider the case when in all real physical cells of pure aluminium 2 atoms of aluminium out of 14 atoms of cells were replaced by atoms of magnesium (2 atoms of magnesium + 12 atoms of aluminium; N=2) in 1m^3 of AMg alloy there were 540,6 kg for magnesium and 2100 kg for aluminium. When they were summed up, it turned out that 1m^3 contains 2640.6 kg of the total mass of aluminium and magnesium, which corresponds in density to the alloy AMg6 (Table 2). At the average content of magnesium atoms in the cell N=2 it is unlikely that there are cells of pure aluminium in the alloy AMg6.

Taking into account the data of Table 1 and Table 3, we could conclude that the strength of AMg alloys increases as the number of aluminium cells containing magnesium atoms increases. Aluminium cells that containing a magnesium atom are the centres of strength. The situation is similar to the strengthening of iron structure by carbon. In steels, iron cells containing carbon compounds (carbides) are the centres of strength. The more cells containing carbon compounds (up to 2.14 % of the mass fraction), the harder and stronger is the iron structure.

Having determined the average statistical distribution of magnesium atoms in different AMg alloys (Table 2) it was necessary to determine the structural formula of compounds with aluminium atoms in AMg alloys. When considering the possible cell microstructure of AMg alloys, it should be taken into account that

aluminium atoms are trivalent and magnesium atoms are divalent. In this regard, the localisation of atoms in the cubic subsystem of the face-centred cubic lattice of aluminium is unlikely. The localisation of magnesium atom in the cubic subsystem of the aluminium cell would lead to the creation of lattice defects in the form of vacancies, which in turn would lead to a decrease in the strength of the crystal cells, which contradicts the experimental data that any alloy of aluminium with magnesium is stronger than pure aluminium (Table 1). It has been observed that the strength of aluminium cell-based alloys increases significantly when the mass fraction of magnesium in the alloys increases, and consequently the number of magnesium atoms in aluminium cells [12].

Due to the fact that the localisation of magnesium atoms in the cubic subsystem is difficult, hence the localisation of magnesium atoms in the alloy is very likely to occur in the rhombic subsystem of aluminium cells (atoms 1, 2, 3, 4, 5, 6, Figure 1). A fact showing that strengthening intermetallic compounds can be formed on the basis of the rhombic subsystem of the aluminium cell is the known intermetallic compound of manganese in aluminium Al_6Mn [16]. The manganese in Al_6Mn compound has embedded inside the rhombic subsystem of the aluminium cell. There are 6 aluminium atoms per one manganese atom in this Al_6Mn intermetallide. Exactly 6 aluminium atoms are located in the rhombic subsystem of the aluminium cell. The aluminium cell containing the Al_6Mn group contains 15 atoms - 14 aluminium atoms and one manganese atom. It was showed the possible configuration of this Al_6Mn intermetalide inside the aluminium cell at Figure 1, Supplementary Material.

It was revealed that in alloy AMg3 in all cells of the alloy contains on the average on 1 atom of magnesium after calculation of average statistical distribution of magnesium atoms. At the same time, all cells of the alloy still contain 14 atoms, of which the rhombic subsystem contains six atoms. If the embedded atoms of magnesium in AMg alloys led to an increase in the number of atoms in the unit lattice, an increase in the density of AMg alloys would be observed. However, this did not occur. For example, in the aluminium alloy AMn (containing 1.5 mass % manganese), 10% of the alloy cells have 15 atoms in their composition, which led to an increase in density to 2730 kg/m^3 (the density of pure aluminium is 2700 kg/m^3).

The analysis showed that five trivalent aluminium atoms and one divalent magnesium atom cannot form a one-position heterovalent solid solution. There is always one unoccupied valence bond and this makes the compound unstable. Therefore, if it assumes that in the alloy AMg3 in half of the cells there is no magnesium, in the other half of the cells there are two atoms each of magnesium in the rhombic subsystem of the AMg alloy cell in the form of solid solution Mg_2Al_4, then the average statistical distribution of magnesium atoms in the AMg3 alloy will still be as follows equal to one (Figure 2, Supplementary Material). Mg_2Al_4 is an electronically coupled alpha phase solid solution. There are 2 magnesium atoms and 4 aluminium atoms at the 6 atoms in the rhombic subsystem. Aluminium atoms 1 and 2, Figure 1 have been replaced by magnesium atoms in the rhombic subsystem. Half of the cells of AMg3 alloy not containing magnesium atoms are actually pure aluminium cells (Figure 2). In these cells, as in pure aluminium, the aluminium atoms of the rhombic subsystem are not completely oxidised. This is the reason for the corrosion of pure aluminium cells in seawater. Mg_5Al_8 compound was found in AMg10 alloys but it cannot be formed in AMg1, AMg2, AMg3 alloys due to low magnesium concentration and uniform distribution of magnesium in the alloy structure [13].

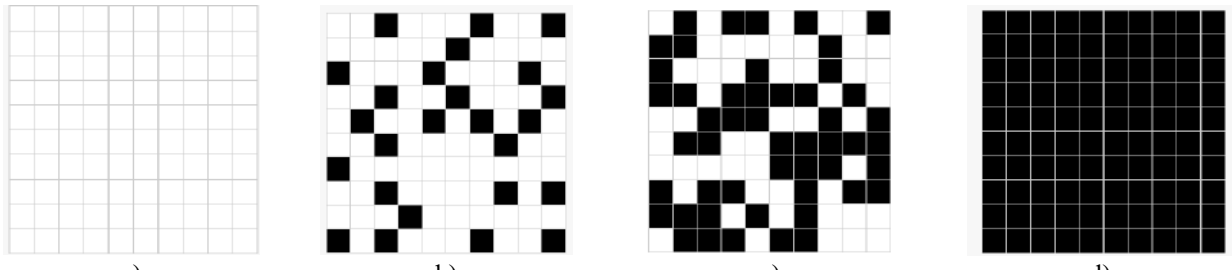

Fig.2. Variant of the average statistical distribution of aluminium cells containing Mg_2Al_4 groups in different AMg alloys. The cells containing Mg_2Al_4 groups are marked in black: a) pure Al; b) AMg2; c) AMg3; d) AMg6.

Then in the alloy AMg2, taking into account the average statistical distribution of magnesium atoms in the alloy cells (Table 2) and taking into account the structure of the compound Mg_2Al_4, two magnesium

atoms are contained in 25% of the alloy cells. On the other hand, the alloy AMg2 contains 75% of pure aluminium cells.

In the alloy AMg1 12% of cells contain the group Mg_2Al_4 and 88% of cells of pure aluminium. In alloy AMg6, on average, all cells of the alloy contain two magnesium atoms in the rhombic subsystem of aluminium Mg_2Al_4 cells. 100% of the cells of AMg6 alloy contain two magnesium atoms (Figure 2).

Thus, it is possible to assert that for magnesium from AMg1, AMg2, AMg3 to AMg6 the regularity is determined that the more aluminium cells contain the compound Mg_2Al_4 located in the solid solution of the rhombic subsystem, the higher the strength of the alloy (Table 2).

Corrosion of AMg alloys.

It is known that aluminium and all magnesiums have no corrosion in the atmosphere and in fresh water. In [12] data on corrosion of different AMg alloys in seawater were given. This data was showed in Table 2. Table 2 shows that the least corrosion in seawater in the range of alloys AMg (AMg2, AMg4, AMg5, AMg6) and PA (pure aluminium) for the alloy AMg2. According to Table 2, the corrosion rate of AMg2 alloy in seawater is 2.34 times less than that for pure aluminium. It is believed that the corrosion rate in seawater increases significantly when the mass fraction of magnesium in the alloy increases. The corrosion rate in seawater of AMg4 alloy is 45% higher than that of AMg2, while that of aluminium is 46.5% higher than that of AMg2. At the same time there is no direct dependence of corrosion rate in seawater on the magnesium content in the alloy.

The following questions arose when analysing the data in Table 2:

Why is the corrosion rate of AMg2 alloy much lower than in pure aluminium?

Why do alloys containing more magnesium than AMg2 alloy have significantly higher corrosion rates than AMg2 alloy?

It was shown in [17] that in pure aluminium cells, corrosion of aluminium cells was possible only through the central aluminium atom 1 of the upper plane of aluminium cells (Figure 1) bordering with seawater. Aluminium atom 1 is part of the rhombic subsystem of the cubic face-centred lattice of aluminium. It was shown in [17] that corrosion of pure aluminium in seawater is caused by corrosion of the rhombic subsystem of aluminium cells, in which aluminium atoms are not oxidised. At the same time, the cubic subsystem of pure aluminium on the surface of products is completely oxidised.

Comparative calculations of the structure of pure aluminium cells and aluminium cells containing the Mg_2Al_4 group were carried out using the PM3 method (Figure 3). Since corrosion occurs on the surface of the products, it was taken into account that both types of cells were partially oxidised (cubic subsystems of cells were oxidised).

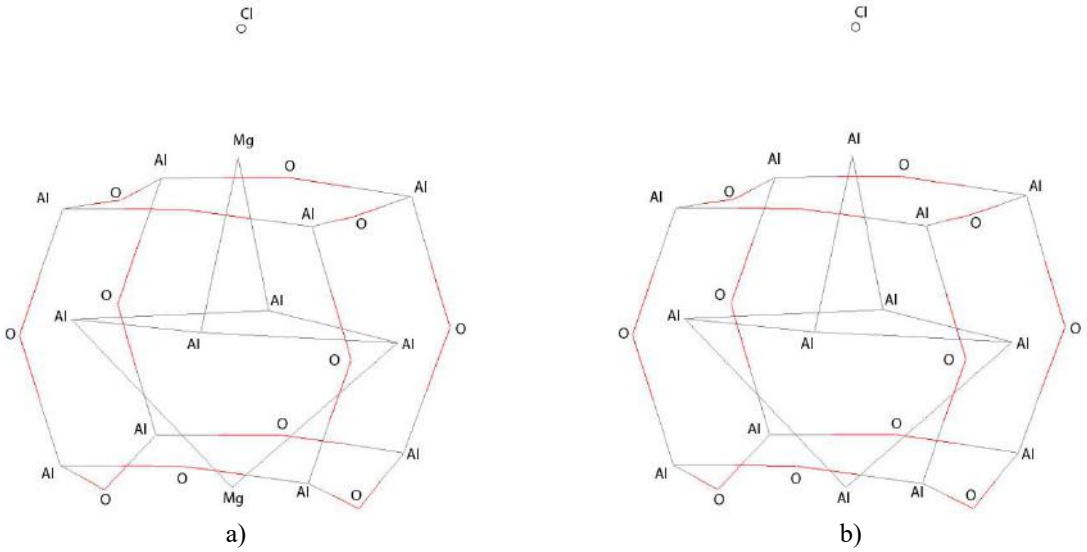

Fig.3. Proposed detachment mechanisms of atom 1 (see Figure 1) from aluminium cells containing Mg_2Al_4 group (a), from pure aluminium cells (b).

The experiment showed that AMg2 alloy is significantly more stable in halogen solution than AMg3 alloy and pure aluminium. The calculation by the PM3 method showed that negative halogen ions produce

detachment of magnesium atoms from the cells of aluminium containing the Mg_2Al_4 group. At the same time, the calculation showed that negative halogen ions produced detachment of atoms from the cells of pure aluminium in the case of pure aluminium cells (Figure 3, a), negative halogen ions could not destroy the cubic lattice subsystem in which each aluminium atom has three covalent bonds with oxygen atoms in partially oxidized cells containing Mg_2Al_4 group on the surface of products (Figure 3, b). At the same mechanism of destruction of cells in the alloy AMg2 in comparison with pure aluminium, a much lower corrosion rate was observed (Table 2). Given the data in Table 2, a question arised. If 25% of aluminium cells contain Mg_2Al_4 group, and 75% of cells are pure aluminium, and the corrosion mechanism in both types of cells is the same, then why in AMg2 alloy the corrosion rate in seawater is 46% lower than in pure aluminium?

In contrast to the works [5, 6], which focus on the corrosion processes in the interphase spaces of magnalium, our work investigates the corrosion process inside crystal grains of magnalium.

4. Experiment

In order to clarify the corrosion resistance of AMg alloys in seawater, the studied samples were placed for 72 hours in 5% iodine solution in ethanol. The experiment showed that the alloy AMg2 is significantly more resistant in halogen solution than pure aluminium and alloys AMg3, AMg6. The difference in weight loss between samples AMg2 and AMg3 was 16.8 %, between samples AMg2 and AMg6 the difference in weight loss was 23%. Between samples of AMg2 and pure aluminium (PA) the difference in weight loss was 42%, between samples of AMg6 and aluminium was 25%. The obtained results do not contradict the data of Table 2. It was necessary to consider in more detail the chemical composition of AMg2 and AMg3 alloys for explaining the obtained results, Table 3 [15]. The main alloying elements in AMg alloys are manganese, chromium, zinc, titanium. Copper in dosages from 0.15 to 0.22 has an anticorrosive effect [18].

Table 3. Chemical composition of aluminium alloys AMg2, AMg3.

Mass fraction of elements, mass %							
	Mg	Mn	Cr	Zn	Ti	Cu	Fe
AMg2	2.6	0.6	0.05	0.15	0.15	0.15	0.5
AMg3	3.8	0.6	0.05	0.2	0.1	0.1	0.5

One atom of alloying elements per cell is sufficient to either completely block the corrosion of the aluminium cell (manganese, chromium, titanium atoms) or to increase the rate of cell failure (iron). The influence of alloying element atoms was considered in more detail:

1) Aluminum cells containing manganese in the form of the intermetallic compound Al_6Mn are not destroyed in sea water, moreover, they are centers of strength, which increases the wear resistance and microhardness of AMg alloys. Also the Al_6Mn compound can capture iron atoms to form the Al_5MnFe compound (iron is usually present in aluminium and its alloys as a harmful impurity and reduces the corrosion resistance of the alloy). The formation of Al_5MnFe compounds inside aluminium cells does not allow halogens to destroy these cells and increases the strength of these cells compared to cells containing Al_6Mn compounds. Manganese atoms in aluminium alloys neutralise iron atoms, which leads to strengthening of the alloys.

2) As shown in [19], in alloys, any increase in the number of bonds with chromium atoms increased the corrosion resistance in seawater. For example, this occurs when the number of chromium atoms in the alloy was increased. Trivalent chromium atoms could be incorporated into both the cubic and rhombic subsystems of the aluminium cell lattice to form various intermetallic compounds such as $Al_{13}Cr$ (Figure 3, Supplementary Material). Also, atoms of chromium and manganese can simultaneously be in the aluminium cell, forming the compound $Al_{12}CrMn$, but given the small concentrations of chromium and manganese in the alloy AMg2, AMg3 the number of cells containing this compound is insignificant.

Taking into account the above, it can be stated that in seawater, aluminium cells containing chromium or manganese atoms, or chromium and manganese atoms simultaneously, do not corrode.

3) The embedded of titanium creates intermetallic compounds in the alloy structure that do not interact with halogen ions. This reduces the grain structure, which decreases structural corrosion.

4) Implantation of zinc into AMg alloys leads to the disappearance of anisotropy of mechanical properties in tensile strength of samples. Zinc atoms as well as magnesium atoms are divalent and at

interaction of zinc with magnesium in aluminium cells instead of Mg_2Al_4 structure the compound $MgZnAl_4$ is formed. At a mass fraction of not more than 0.5 mass % zinc has an anticorrosive effect on aluminium and its alloys [8].

5) Iron is always contained as a harmful impurity in aluminium alloys - free iron always impairs corrosion resistance [3, 19].

The percentage of aluminium cells containing each of the listed atoms was calculated. The number of cells containing a certain type of atoms of alloying elements, it was calculated knowing the density of the alloys under consideration, the spatial structure of the alloy cells, and the mass fraction of each of the alloying elements in each of the alloys. The results of calculations were shown in Table 4.

Table 4. Chemical composition of aluminium alloys AMg2, AMg3.

	% of protected cells						
	Mn	Cr	Ti	Cu	Zn	Fe	Total percentage of protected cells
AMn (1,5 mass %)	10%	0%	-	-	-	-	+10
AMg2, (Mg 2.6 mass %, Cr 0.05 mass %, Mn 0.6 mass %, Zn 0.15 mass %, Ti 0.15 mass %, Cu 0.15 mass %)	+4,1	+0,36	+1.18	+0.89	+0,86	-3.36	+4.03
AMg3, (Mg 3.8 mass %, Cr 0.05 mass %, Mn mass 0.6 %, Zn 0.2 mass %, Ti 0.1 mass %, Cu 0.1 mass %)	+4.08	+0.36	+0.75	+0.6	+1.14	-3.34	+3.59

First, the maximum number of structural cells was calculated in which the atoms of these alloying elements can be located (at the rate of one alloying element atom per one structural cell). It was calculated for each alloying element, taking into account its mass fraction in alloys. The plus sign (+) in the cell of Table 4 before the figure shows that this result increases the degree of protection of the alloy from corrosion. The minus sign (-) before the figure in the cell of the table shows that this result reduces the degree of protection from corrosion. The results of calculation of the total number of protected from corrosion cells (taking into account the positive and negative influence of alloying elements) of aluminium in AMg2 and AMg3 alloys correlate with the results of our experiment on comparative corrosion of AMg2 and AMg3 alloys in seawater. The more protected from corrosion structural cells, the lower the corrosion rate of the alloy. The calculation showed that in the alloy AMg2 (Table 4) the total number of cells protected from corrosion is 11% higher than in the alloy AMg3 (Table 4). We believe that the corrosion rate of alloys is directly related to the number of corrosions protected cells of the alloy. The difference in the number of protected from cell corrosion is equal to the difference in the corrosion rate of alloys. In the case of the considered alloys AMg2 and AMg3, the theoretically calculated difference in the corrosion rate of alloys in ΔV_{teor} was equal to 11%. This result was close to the result obtained by us in the experiment on comparative corrosion of alloys AMg2 and AMg3. Experimentally determined corrosion rate in seawater in alloy AMg2 was16.8% less than in alloy AMg3 (ΔV_{exp}= 16.8%).

Some difference between the result of this model and the experimental result is due to the different number of pure aluminium cells in AMg2 and AMg3 alloys. According to the average statistical model of cell calculation (Figure 2) in the alloy AMg2 the number of pure aluminium cells is twice as much as in the alloy AMg3. In the alloy AMg3, half of the cells contain pure aluminium and the other half contains the compound Mg_2Al_4. The PM3 calculation showed that the corrosion mechanism in seawater for both types of cells is the same, but the rate of interaction with halogen ions is different. For practical use of this model of corrosion rate calculation it is necessary to use a correction factor:

$$\Delta V_{exp} = \Delta V_{teor} + K, \quad (4)$$

where K= 5.8% correction factor - for investigated alloys AMg2 and AMg3 of the given composition.

The value of K depends on the percentage of aluminium cells containing Mg_2Al_4 group. The greater the percentage, the greater the value of K, and the greater the corrosion rate of the studied alloy AMg. The

corrosion rate of aluminium cells containing Mg_2Al_4 in seawater is higher than the corrosion rate of pure aluminium cells.

In the AMg3 alloy the number of cells containing Mg_2Al_4 group is 50% of the total number of cells. In alloy AMg2 number of cells with group Mg_2Al_4 is 25% less. In the case of the studied alloys AMg2 and AMg3 correction factor K = 5.8% is due to 25% difference in the number of cells containing the group Mg_2Al_4. Then for AMg alloys containing any number of cells (from AMg0.2 to AMg3.5) the correction factor K was calculated by the formula.

$$K= 0.232 * \Delta N, \quad (5)$$

where, ΔN is the difference between the percentage of cells containing Mg_2Al_4 in the alloy AMg2 and the percentage of cells with Mg_2Al_4 in the studied AMg alloy. The alloy AMg_2 contains 25% of cells with Mg_2Al_4 group. For analysed AMg alloys with a percentage of cells with Mg_2Al_4 group less than 25%, the correction factor is applied with a minus sign.

It is possible to calculate the change in the corrosion rate of known AMg alloys with a fairly good accuracy when changing the percentage of alloying elements, using the calculation model that takes into account the average percentage of alloy cells protected from corrosion. The model is not intended for calculation of corrosion resistance of AMg alloys with magnesium content in the alloy of 4 and more %of the mass fraction. This limitation on the use of the model is due to the fact that starting from 4% of magnesium content the solid alpha solution of AMg alloy is oversaturated with magnesium) [20].

For example, it was calculated the change in corrosion rate of the modified alloy AMg2+Mn (0.2 mass %) (Mg - 2.6 mass %, Cr -0.05 mass %, Mn - 0.8 mass %, Zn -mass 0.15 mass %, Ti -0.15 mass %, Cu - mass 0.15%, Fe -mass 0.5%). Since the percentage of cells containing the Mg_2Al_4 group has not changed the correction factor is not used. In this alloy the mass fraction of manganese is increased by 0.2 mass % in comparison with the standard alloy AMg2 (Mg - 2.6 mass%, Cr -0.05 mass %, Mn - 0.6 mass %, Zn - 0.15 mass %, Ti - 0.15 mass %, Cu - 0.15 mass %). It is known that if the mass fraction of Mn is less than 1 mass %, the brittleness of aluminium alloys does not increase. In this way increasing the mass fraction of manganese in the alloy AMg2 up to 0.8 mass % should increase the strength of the alloy and corrosion resistance, without increasing brittleness. The change in the number of corrosion-protected cells of alloy AMg2 was calculated when the mass fraction of manganese increases by 0.2 mass %. The percentage of corrosion-protected cells of AMg2 alloy increased to 5.04% of the total number of cells of the alloy. Increasing the number of corrosion-protected cells should reduce the corrosion rate by 14% compared to the standard alloy AMg2.

Further it was calculated the change in corrosion rate of modified alloy AMg2+ Cr 0.55%, (Mg - 2.6 mass %, Cr - 0.6 mass %, Mn- 0.6 mass %, Zn- 0.15 mass %,Ti - 0.15 mass %, Cu- 0.15 mass %, Fe - 0.5 mass %). Since the percentage of cells containing Mg_2Al_4 group did not change the correction factor is not used. In the studied alloy AMg2 the chromium content is increased to 0.6 mass %. It is known that there are no technical problems in melting aluminium alloy if the mass fraction of chromium does not exceed 0.7 mass % [21]. When the mass fraction of chromium is 0.6 mass % in AMg2 alloy, the percentage of cells protected by chromium will increase to 4.32 mass %, of the total number of cells. The total number of protected cells at increasing the mass fraction of chromium to 0.6 mass % in the alloy AMg2 increased to 8%. At the same time, the corrosion rate of AMg2 alloy decreased by 34% compared to the standard AMg2 alloy with chromium content of 0.05 mass %.

Furthermore, it was calculated the modified alloy AMg2 in which the mass fractions of manganese and chromium were increased simultaneously AMg2 + Cr 0.55 mass % +Mn0.2 mass % (Mg - 2.6 mass %, Cr - 0.6 mass %, Mn - 0.8 mass %, Zn - 0.15 mass %, Ti - 0.15 mass %, Cu - 0.15 mass %, Fe - 0.5 mass %). Since the percentage of cells containing Mg_2Al_4 group has not changed the correction factor is not used. In this modification of AMg2 alloy, the percentage of protected cells reached 13.4 %, which reduced the corrosion rate by 54.9 % compared to the standard AMg2 alloy (Table 2).

Taking into account the results of the article [17], it was assumed that if cells without magnesium atoms are completely oxidized in the AMg2 alloy, these completely oxidized cells will stop to interact with halogen ions from seawater. The corrosion resistance of the treated AMg2 alloy will increase significantly. It is necessary to oxidize 75% of the alloy cells on the surface of the products.

AMg2 samples were placed in a 5% iodine solution in ethyl alcohol for 72 hours to test the hypothesis shown above. The corrosion resistance of untreated AMg2 samples and AMg2 samples exposed to ozone for

6 hours at a temperature of 190 °C. was studied. Ozone was generated by ultraviolet radiation from atmospheric oxygen. The experimental method is described in detail in the article [19]. The choice of a temperature of 190 °C during sample processing was chosen due to the fact that the source [13] shows that the physico-chemical properties of AMg alloys deteriorate sharply when these alloys are heated above a temperature of 210 °C. This phenomenon was caused by a change in the internal structure of the cells containing a magnesium atom, as the beta phase of Al_3Mg_2 is formed [14].

The surfaces of the untreated AMg2 sample after 72 hours in the iodine solution and the sample pretreated for 6 hours of ozone treatment with AMg2 after 72 hours in the iodine solution are shown in Figure 4.

a) b)

Fig.4. Photographs of the surface of samples exposed to alcohol solution of iodine for 72 hours: a) an untreated AMg2 sample; b) a sample treated with ozone for 6 hours.

Significant surface damage is recorded on the surface of the untreated AMg2 sample (Figure 4, a). Only a small pitting corrosion was observed on the surface of the ozone-treated AMg2 sample (Figure 4, b). If the untreated AMg2 alloy sample lost 5.74% of its mass in 72 hours, then the sample subjected to ozone treatment lost 4.23% of its mass within 6 hours. The experiment showed a significant increase in the corrosion resistance by 26% of the surface of the AMg2 alloy treated with ozone for 6 hours.

Thus, the surface treatment of AMg2 alloy products with ozone at a temperature of 190 ° C can be recommended in order to increase corrosion resistance in seawater.

5. Conclusions

1) The analysis showed that the corrosion resistance of AMg2, AMg3 alloys depends on the percentage of aluminium cells containing manganese, chromium, titanium, zinc, copper, iron and magnesium atoms. The combined effect of these elements increases or decreases the corrosion resistance of AMg alloys in seawater. In seawater destruction of structural cells in pure aluminium and in cells of AMg alloys containing Mg_2Al_4 compound occurs by the same mechanism, but at different rates. There is a detachment by the negative halogen ion of the central aluminium or magnesium atom located on the outer edge of the alloy cells. Aluminium cells containing the compound Mg_2Al_4 are destroyed faster than pure aluminium cells.

2) The developed model of calculation of change in corrosion resistance of AMg2 and AMg3 alloys showed results close to those obtained in the experiment.

3) It is recommended to use AMg2 alloys with increased manganese and chromium content in marine atmospheres:

a) In the modified alloy AMg2 (Mg - 2.6 mass %, Cr - 0.05 mass %, Mn - 0.8 mass %, Zn - 0.15 mass %, Ti - 0.15 mass %, Fe - 0.5 mass %) the amount of manganese has been increased by 0.2 mass % compared to the standard alloy AMg2. The corrosion rate in this modification of AMg2 alloy have been reduced by 14 % compared standard AMg2 alloy with manganese content of 0.6 mass %;

b) In the modified alloy AMg2 (Mg - 2.6 mass %, Cr - 0.6 mass %, Mn - 0.6 mass %, Zn - 0.15 mass %, Ti - 0.15 mass %, Cu - 0.15mass %, Fe - 0.5mass %) the amount of chromium has been increased by 14 times compared to the standard alloy AMg2. The corrosion rate in this modification of AMg2 alloy have been reduced by 34% compared to the standard AMg2 alloy with chromium content of 0.05 mass %;

c) In the modified alloy AMg2 (Mg - 2.6 mass%, Cr - 0.6 mass%, Mn - 0.8 mass%, Zn - 0.15 mass %, Ti - 0.15 mass%, Cu - 0.15 mass%, Fe - 0.5 mass%) the amount of chromium has been increased by 14 times in comparison with the standard alloy AMg2 and the amount of manganese have been increased by 0.2 mass% compared to the standard alloy AMg2. The corrosion rate in this modification of AMg2 alloy have been reduced by 54.9% compared to the standard AMg2 alloy with chromium content of 0.05 mass% and manganese content of 0.6 mass%.

d) Additional oxidation of the AMg2 alloy surface with ozone significantly reduces the rate of corrosion by 26% in seawater.

Conflict of interest statement

The authors declare that they have no conflict of interest in relation to this research, whether financial, personal, authorship or otherwise, that could affect the research and its results presented in this paper.

CRediT author statement

Guchenko S.A.: investigation, writing - original draft; **Seldyugaev O.B.:** conceptualization, writing - review & editing; **Fomin V.N.:** investigation, formal analysis; **Afanasyev D.A.:** visualization, writing - review & editing.
The final manuscript was read and approved by all authors.

Acknowledgements

The authors are grateful to Tuleuov S.D. for assistance in preparing the article.

References

1 Polmear J.I. (1996) Recent developments in light alloys. *J. Mat. Transactions, JIM,* 37, 1, 12–31. https://doi.org/10.2320/matertrans1989.37.12

2 Zhu Q., Abdob M.F., Talamantes-Silva J., Sellars C.M., Linkens D.A., Beynon J.H. (2003) Hybrid modelling of aluminium-magnesium alloys during thermomechanical processing in terms of physically-based, neuro-fuzzy and finite element models. *J. Acta Materialia.* 51, 17, 5051 – 5062. https://doi.org/10.1016/S1359-6454(03)00353-7

3 Zhang L., Lin D.-Y., Wang H., Car R., Weinan E. (2019) Active learning of uniformly accurate interatomic potentials for materials simulation. *Phys. Rev. Mater.,* 3, I.2, 023804(9) https://doi.org/10.1103/PhysRevMaterials.3.023804

4 Erkmen J., Hamamci B., Aydin A. (2024). Examining the corrosion behavior of 6061-T6 al alloy inside seawater with decorative gold- and silver-color coating. *Gazi University J. of Science***,** 37, 2, 953 – 967. https://doi.org/10.35378/ gujs.1219180

5 Lim M.L.C., Kelly R.G., Scully J.R. (2015) Overview of intergranular corrosion mechanism, phenomenological observations, and modeling of AA5083. *J. Mat. Science.,* 72, .2, 198-220. https://doi.org/10.5006/1818

6 Lim J., Jeong G., Seo K., Lim J., Park S., Ju W., Janani G., Lee D., Kim J., Han M., Kim T., Park S., Cho H., Sim U. (2022) Controlled optimization of Mg and Zn in Al alloys for improved corrosion resistance via uniform corrosion. *J. Mat. Adv.,* 3. 4813 – 4823. https://doi.org/10.1039/D1MA01220G

7 Verissimo N.C., Freitas E.S., Cheung N., Garcia A., Osóri W.R. (2017) The effects of Zn segregation and microstructure length scale on the corrosion behavior of a directionally solidified Mg-25 wt.%Zn alloy. *J. of Alloys and Compounds,* 723, 649 – 660. http://dx.doi.org/10.1016/j.jallcom.2017.06.199

8 Kim Y., Park J., An B., Lee Y., Yang Ch., Kim J. (2018) Investigation of zirconium effect on the corrosion resistance of aluminum alloy using electrochemical methods and numerical simulation in an acidified synthetic sea salt solution. *J. Mat.,* 11, I.10, 982. https://doi.o1rg/10.3390/ma11101982

9 Wolverton C. (2001) Crystal structure and stability of complex precipitate phases in Al-Cu-Mg-(Si) an Al-Zn-Mg alloys. *J. Acta Materialia,* 49, 16, 3129 – 3142. https://doi.org/10.1016/S1359-6454(01)00229-4

10 Stewaet J.P. (1989) Optimization of parameters for semiempirical methods 2. 1989. *Applications J. Computational Chemistry*, 10(2), 221-264. https://doi.org/10.1002/jcc.540100209

11 Bokiya G.B. (1971) *Crystallochemistry*, Institute of Radio Engineering and Electronics. USSR Academy of Sciences, Moscow. Available at: https://cat.libnvkz.ru/CGI/irbis64r_14/cgiirbis_64.exe?LNG=&Z21ID=&I21DBN [in Russian]

12 Kvasov F.I., Fridlyander I.N. (1982) *Industrial aluminium alloys: reference book,* Metallurgiya, Moscow. Available at: https://i.twirpx.link/file/1686114/ [in Russian]

13 Shepelevich V.G. (2007) Structure of rapidly solidified foils of AMg6 alloy. *Bulletin of P.O. Sukhoi State Technical University*, 28, 12 – 16. Available at: http://elib.gstu.by/handle/220612/9923 [in Russian]

14 Golovkin P.A. (2022) About the factor of quantitative content of intermetallic phases in the nature of destruction of AMg6 alloy open forgings. *Technol. Light Alloys*, 2, 5 – 19. Available at: https://doi.org/10.24412/0321-4664-2022-2-15-19

15 GOST 4784-2019. Aluminium and wrought aluminium alloys. Grades (State Standard 4784-2019). Publishing House of Standards, Moscow. Available at: https://files.stroyinf.ru/Data2/1/4293728/4293728395.pdf?ysclid=m2sxpac9co349327183

16 Kolachev B.A., Livanov V.A., Elagin V.I. (1972) Metallurgy and heat treatment of non-ferrous metals and alloys. Metallurgy, Moscow. Available at: https://techlibrary.ru/b2/2s1p1m1a1y1f1c_2i.2h._2m1m1a11j1o [in Russian]

17 Berdibekov A.T., Khalenov O.S., Zinoviev L.A., Laurynas V.Ch., Gruzin, V.V., Dolya, A.V. (2023) Reason of corrosion of aluminium products in seawater. *Eurasian phys. tech. j.*, 20, 3(45), 20–26. https://doi.org/10.31489/2023No3/20-26

18 Sinyavskiy V.S., Valkov V.D., Budov G.M. (1979) Corrosion and protection of aluminium alloys. Metallurgiya, Moscow. Available at: https://echemistry.ru/literatura/korroziya/korroziya-i-zashhita-alyuminievyh-splavov.html

19 Baikenov M.I., Seldyugaev O., Guchenko S.A., Afanasyev D.A. (2024) Reason of pitting corrosion of martensitic steel in seawater. *Eurasian phys. tech. j.*, 21, 1(47), 38–48. https://doi.org/10.31489/2024No1/38-48

20 Song Ch.-R., Dong B.-X., Zhang S.-Y., Yang H.-Y., Liu L., Kang J., Meng J., Luo Ch.-J., Wang Ch.-G., Cao K., Qiao J., Shu Sh.-L., Zhu M., Qiu F., Jiang Q.-Ch. (2024) Recent progress of Al–Mg alloys: Forming and preparation process, microstructure manipulation and application. *J. of Materials Research and Technology*, 31, 3255 - 3286. https://doi.org/10.1016/j.jmrt.2024.07.051

21 Shakhnazarov T.A., Takhtarova Yu.A. (2008) Russian patent. Method of alloying with chrome. Available at: https://patenton.ru/patent/RU2324753C2?ysclid=m4gwqsw68m972534492

AUTHORS' INFORMATION

Guchenko, Sergei A. – Master (Sci.), Junior Research Fellow, E.A. Buketov Karaganda University, Karaganda, Kazakhstan; ORCID iD: 0000-0002-9954-5478; guchen@mail.ru

Seldyugaev, Oleg B. – Candidate of chemical sciences, Junior Research Fellow, E.A. Buketov Karaganda University, Karaganda, Kazakhstan; ORCID iD: 0009-0004-9729-1015; oleg.seldyugaev@gmail.com

Fomin, Vitaly N. – Candidate of chemical sciences, Scientific direction of the Laboratory of engineering profile "Physic-chemical methods of research", E.A. Buketov Karaganda University, Karaganda, Kazakhstan; ORCID iD: 0000-0002-2182-2885; vitfomin@mail.ru

Afanasyev, Dmitriy A. – PhD, Professor, E.A. Buketov Karaganda University, Karaganda, Kazakhstan; ORCID iD: 0000-0002-0437-5315; a.d.afanasyev2@gmail.com

EURASIAN PHYSICAL TECHNICAL JOURNAL

2025, Volume 22, No. 2 (52)

https://doi.org/10.31489/2025N2/109-120

Received: 20/01/2025 Revised: 24/05/2025 Accepted: 23/06/2025 Published online: 30/06/2025

Research Article

UDC 53.043

INVESTIGATION OF THE STRESS-STRAIN STATE DURING NEW COMBINED DEFORMATION TECHNOLOGY

Volokitina I.E.*, Panin E.A., Volokitin A.V., Fedorova, T.D., Latypova, M.A., Makhmutov B.B.

Karaganda Industrial University, Temirtau, Kazakhstan
*Corresponding author: irinka.vav@mail.ru

Abstract. *This paper presents the results of finite element modeling of a novel technology of combined deformation by radial-shear broaching and traditional drawing. Using DEFORM program, the parameters of stress-strain state and deformation forces were studied. A range of models with varying initial diameters of the workpiece, single and total compressions, and different temperatures of heating the workpiece were considered. It was revealed that the optimal conditions occurred at 30-25-20 scheme at a temperature of 900°C. However, this scheme can be recommended when the strength of the deforming equipment is sufficient. In other cases, it is necessary to select a scheme that allows for deformation without exceeding the limiting loads.*

Keywords: drawing, modelling, bar, steel, stress-strain state.

1. Introduction

The manufacture of high-quality carbon steel bars is a complex undertaking requiring a synthesis of traditional and contemporary metalworking methodologies. Conventional techniques, with their proven track record and years of application, ensure stability and predictability of outcomes. Nevertheless, their capacity to attain the highest quality and dimensional accuracy is constrained. Furthermore, these methods frequently incur substantial production costs, often due to considerable energy consumption and protracted processing cycles. Furthermore, traditional methods such as hot rolling frequently result in heterogeneity of the metal structure and an increased level of internal stresses, which have a detrimental effect on the properties of the finished product. For instance, during the rolling process, significant fluctuations in thickness and geometric parameters occur, necessitating subsequent additional processing, which increases the cost.

However, modern technologies, particularly those involving severe plastic deformation (SPD) [1-5] and progressive deformation methods such as radial-shear rolling (RSR) or hydrostatic extrusion, offer novel solutions to this challenge. Nevertheless, it should be noted that these modern methods also have their limitations, including the high cost of equipment and the complexity of mastering the technology, which can render them economically unprofitable for some enterprises [6-8].

The optimal approach to be adopted is the creation of flexible, modular technological processes that combine the advantages of both traditional and modern methods [9-11]. This approach enables the adaptation of the production process to the specific requirements of the customer, the utilization of the most effective methods at each stage of production, and the minimization of costs. It is imperative to acknowledge the role of heat treatment, a critical component in the production of carbon steel bars, in significantly extending the duration of the technological cycle and escalating costs. Consequently, it is imperative to minimize the

number and duration of thermal operations. Optimal process design, therefore, entails the use of pressure treatment methods in a more efficient manner, thereby reducing the necessity for additional heat treatment. For instance, the selection of the most appropriate deformation mode and tool can result in the attainment of the desired mechanical properties without the necessity for additional annealing or quenching.

The proposed innovative technology for deforming carbon steel rods is based on a combination of radial-shear broaching (RSB) and traditional drawing [12, 13]. The fundamental distinction between the two methodologies lies in the cessation of the roll drive during the RSB process. This configuration is designed to prevent the conflict between the two deformation methods that would otherwise be impossible to avoid in a traditional configuration. The cessation of drive during the RSB phase facilitates a seamless transition to the drawing phase, thereby enabling the effective integration of the merits of both methodologies. RSB ensures rough processing and preforming of the rod, while drawing ensures high dimensional accuracy and excellent surface quality. This technological integration enables the optimization of energy consumption, enhancement of productivity, and reduction of production costs, while ensuring the manufacture of bars that exhibit superior mechanical characteristics and exceptional surface quality.

The complexity of the processes involved in designing and optimizing plastic deformation using a complex loading scheme necessitates the implementation of multiscale analysis and numerical modelling support. A plethora of models of plasticizing stresses are employed in computer modelling. Some of these models are based on empirical equations, such as the Sabbat model, while others are based on physical principles and phenomena occurring in a deformable material. The DEFORM software package is utilized for the analysis of diverse metalworking and heat treatment processes. With the help of DEFORM it is possible:

- To test the developed process not experimentally, in real production, but virtually on a computer;
- To conduct a numerical experiment and, based on its results, make changes to the parameters of the technological process;
- To predict the nature of metal shaping during pressure treatment. This significantly reduces the cost of experimental research;
- To study the processes of metal deformation during different types of tool movement. It is possible to vary the friction conditions, the models of the medium and the rheological properties of the material;
- To evaluate the process for defects (formation of cracks, creases, non-filling of the stamp, etc.). The results include a force graph, stress, strain, and temperature distribution fields.

The utilization of modelling in DEFORM has been demonstrated to facilitate a reduction in the production time of structures and components, enhance their quality, and mitigate costs that may emerge during the production process.

The novelty of this work lies in the study of the stress-strain state of a carbon steel bar deformed by a novel combined technology in the DEFORM program. The key feature of this work is a comprehensive study of energy-force parameters at the theoretical level using FEM modeling. The data obtained will form the basis at the design stage of the experimental installation, which will avoid possible equipment breakdowns from overloads.

2. Materials and Methods

In order to analyze the stress-strain state in the DEFORM program, a number of models of the radial-shear broaching process with subsequent drawing were constructed. In these models, both geometric and technological parameters were varied with the objective of determining the most optimal process conditions. Geometric parameters, such as the initial diameter of the workpiece and the absolute compression at each of the two passes, were varied. Among the technological parameters, the initial temperature of the workpiece was varied. As a result, the following models were built:

- the workpiece with a diameter of 30 mm was compressed sequentially to 27 mm, then to 23 mm.;
- the workpiece with a diameter of 30 mm was compressed successively to 25 mm, then to 20 mm.;
- the workpiece with a diameter of 20 mm was compressed successively to 18 mm, then to 16 mm.

Each of these models was considered at three temperatures: 20°C, 500 °C and 900°C.

The material of the blank was steel 10. The following friction coefficients were set: at the contact of the workpiece with the rolls of the RSR mill – 0.4; at the contact of the workpiece with the fiber – 0.1. The rolls of the RSP mill were disconnected from the drive and rotated from friction upon contact with the workpiece. The compression in the rolls and in the fiber were set to be similar, i.e., for example, in the model 30-27-23, on the first pass, the gap between the rolls and the diameter of the drawing die were equal to 27 mm.

The mesh of finite elements on the workpiece was constructed using tetragonal elements. Their distribution on the workpiece was carried out according to two distribution criteria:

- using the Size Ratio coefficient equal to 6, which grinds the volume of elements in the loaded zones by 6 times compared to the rest of the zones;
- using two zones of local condensation of elements – "Mesh Window" with a coefficient of 0.1, located in two deformation zones – in the rolls and in the drawing tool. These windows additionally thicken the mesh by a factor of 10.

All this led to the fact that in both deformation zones, the average face length of the final element was 0.18 mm approximately.

3. Results and discussion

In the course of the study of the strain state, the parameter "equivalent strain" was considered, which is a cumulative parameter reflecting the accumulation of all types of deformation. As illustrated in Fig. 1, a comprehensive overview of the equivalent strain of all models is provided. As the results for all nine models are presented on a single scale of ε = 0-4, it can be observed that the strain patterns in the horizontal direction are consistent across all models.

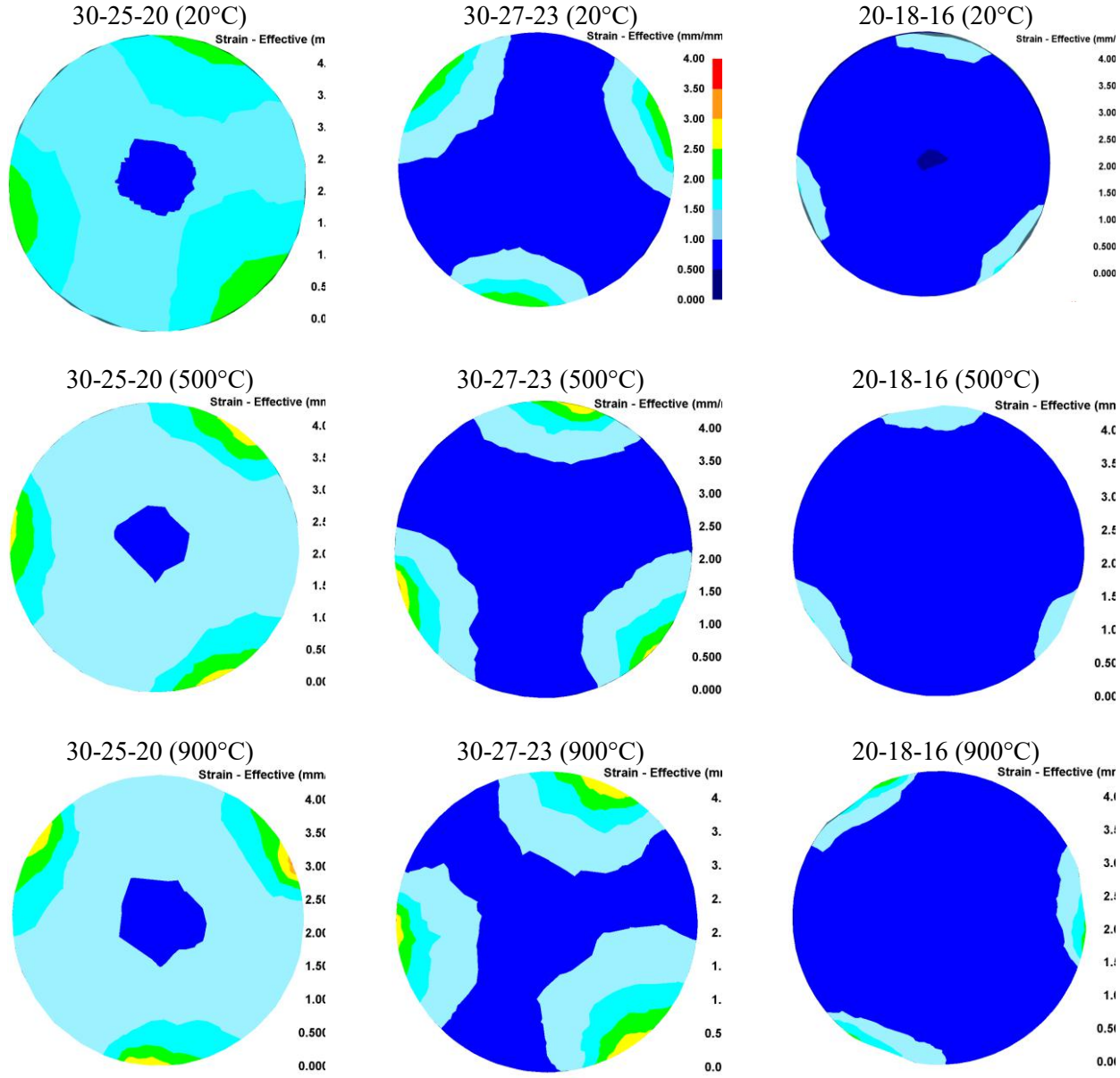

Fig. 1. Distribution of equivalent strain over the workpiece section

Furthermore, it is evident that models 30-25-20 exhibit the maximum metal processing over the entire cross-section at all temperatures considered. This phenomenon can be attributed to the highest values of single compression and total compression (10 mm versus 7 mm and 4 mm). A comparable outcome was achieved in a study of conventional zirconium RSR [14]. In the 30-27-23 model, the processing effect is slightly lower, but it is still at a fairly high level in the areas of contact with the rolling rolls. The lowest effect is observed in models 20-18-16. In this model, the level of processing in the surface layers is comparable to the level of elaboration of the central zone in model 30-25-20.

It is evident from the presented patterns of vertical strain that the initial temperature of the workpiece exerts a significant influence on the distribution of strain, both in terms of its extent and its nature. In this instance, the predominant effect of elevated strain is discernible solely in the surface areas of the workpiece. In areas of direct contact with rolling rolls, an increase in temperature leads to an enhancement in the metal's malleability, resulting in a gradual increase in strain. To quantify the strain state, the obtained values of equivalent strain in the surface zones and in the center were summarized in the resulting diagram in Fig. 2.

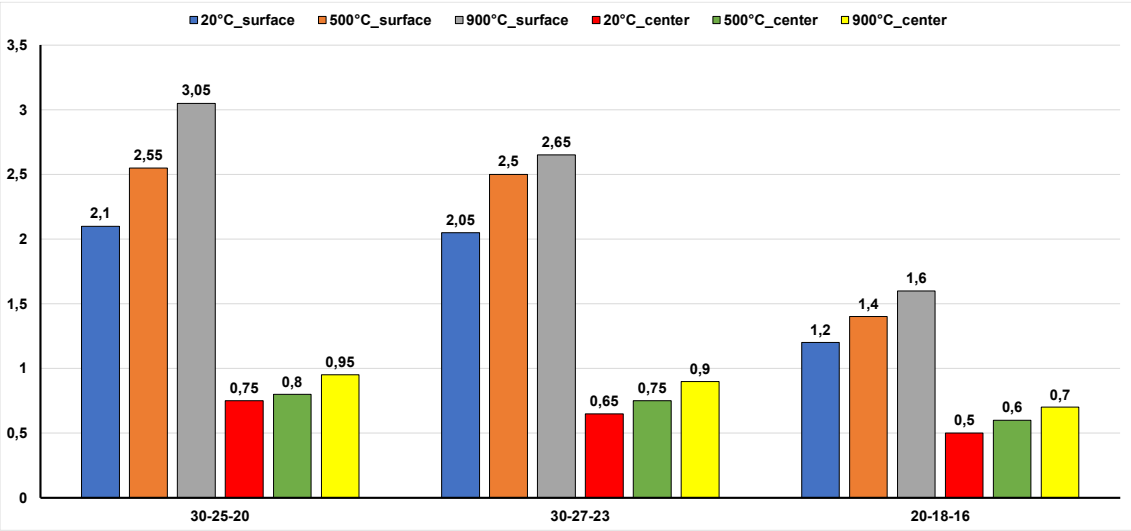

Fig. 2. Numerical values of equivalent strain

As illustrated in the diagram, the maximum strain values exceeding 3 are observed at maximum compression in the 30-25-20 model at an elevated temperature of 900°C. Concurrently, a decline in temperature to ambient levels results in a reduction in the degree of processing in the surface areas by approximately 25-30% across all models. Furthermore, a comparison of the values at constant temperatures reveals a heightened sensitivity to the degree of compression. To illustrate this point, we may consider the strain level in model 30-25-20 as the baseline. A decrease in the total compression level by 3 mm (model 30-27-23) results in a 15% decrease in deformation at 900°C. However, this difference diminishes to 3% as the temperature is reduced, thereby reducing the ductility of the metal in the areas of contact with the rolls. A further decrease in the total compression level by 3 mm (model 20-18-16) results in a 48% difference in strain values at 900°C, while with a decrease in temperature, this difference decreases to 42%. Consequently, it can be deduced that the extent of equivalent strain in the process under investigation is more dependent on the total compression applied. While the influence of temperature is also observed, its effect is significantly less pronounced.

It is evident that analogous dependencies of the strain amount on the total compression and temperature are sustained for the central layers of the workpiece. However, the location of the rolling rolls in the space in the form of a RSR mill leads to the fact that at the broaching stage, strain develops only in the surface zones, and the central region receives an increase in strain only at the drawing stages. Consequently, an uneven gradient structure emerges in the cross-section of the workpiece, exhibiting a disparity in equivalent strain ranging from 200% to 300%. It is also noteworthy that the central zone of the workpiece demonstrates minimal processing across all cases, with strain levels ranging from $\varepsilon = 0.5 - 0.7$ at room temperature, and reaching $\varepsilon = 0.7 - 0.95$ at elevated temperatures of 900°C.

In order to study the stress state, there are a number of recommended parameters that must be selected, with the consideration of the strain pattern being of particular importance. For instance, within the ECAP process, the study of the equivalent stress is adequate due to the utilization of an all-encompassing compression scheme. In the studied combined process of radial-shear broaching with drawing, there are both compression zones from the action of deforming tools and stretching zones from the action of a pulling force applied to the front end of the workpiece. Consequently, the most appropriate approach would be to analyze the average hydrostatic pressure, which accounts for the direction of the applied stresses. As illustrated in Fig. 3, the images depict the average hydrostatic pressure within the workpiece section situated within the deformation zone of the rolling rolls. A comparison of the obtained patterns of average hydrostatic pressure as a function of total compression (in the horizontal direction) reveals a direct proportional relationship.

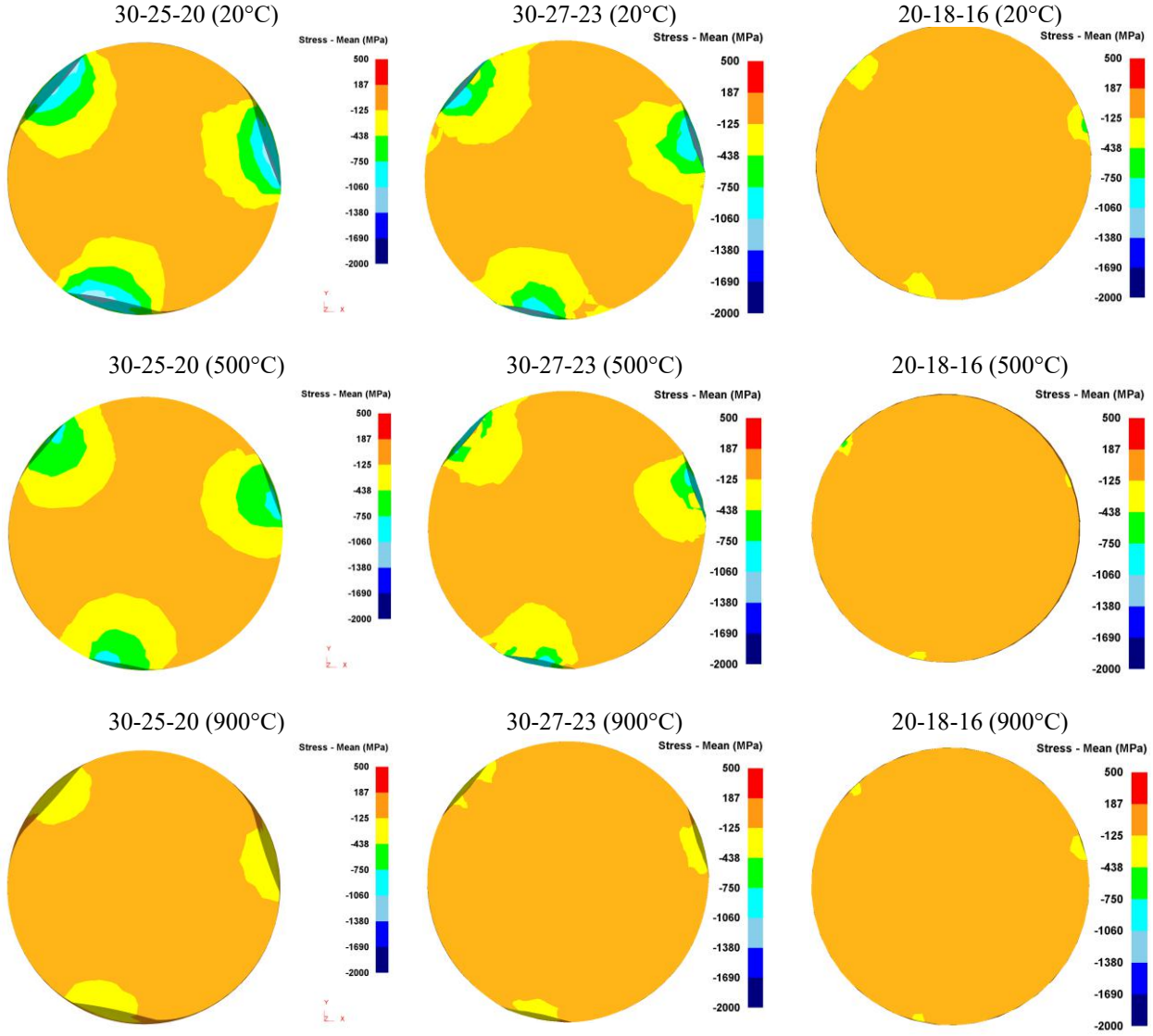

Fig. 3. Distribution of the average hydrostatic pressure over the workpiece cross section in the deformation zone of the rolling rolls

The highest levels of compressive stresses are observed in models 30-25-20, where the compression value is maximum. With a decrease in total compression, compressive stresses decrease, and a decrease in the length of direct impressions from contact with the rolls is also clearly visible. In addition, an inverse proportional relationship is evident when comparing the patterns of average hydrostatic pressure as a function of temperature (in the vertical direction). The highest level of compressive stresses is observed in models where the workpiece temperature is 20°C. As the temperature increases, the level of compressive stresses decreases, as well as the extent of the deformation zones. In order to quantify the stress state, the

values of the average hydrostatic pressure on the surface and in the deformation zone of the rolling rolls were summarized in the resulting diagram in Fig. 4.

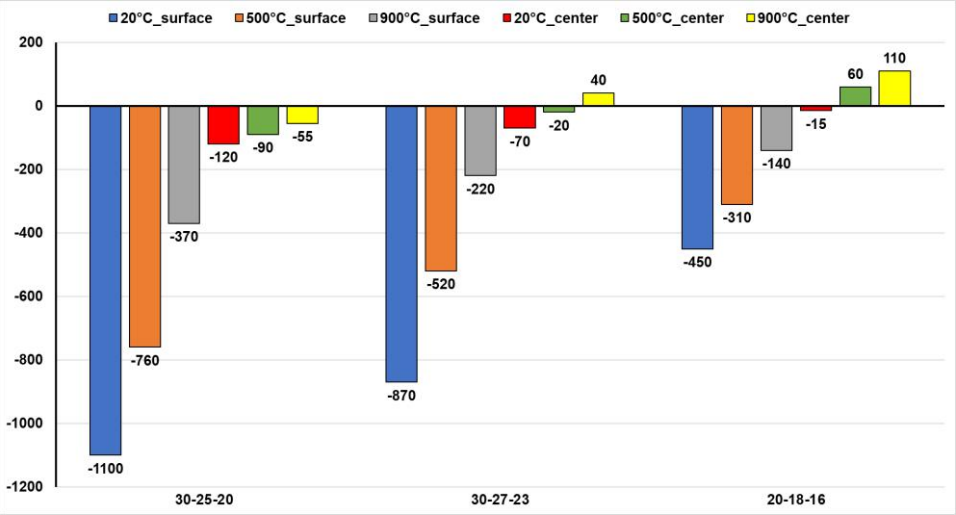

Fig. 4. Numerical values of the average hydrostatic pressure in the deformation zone of rolling rolls

As illustrated in the diagram, the maximum values of the average hydrostatic pressure above 1 GPa are attained at maximum compression in the 30-25-20 model at a temperature of 20°C. An increase in temperature to 900°C leads to a decrease in the level of average hydrostatic pressure in the surface zones by approximately threefold. A parallel comparison of the values at constant temperatures reveals a high degree of correlation with the extent of compression. For instance, when the total compression level is reduced by 3 mm (model 30-27-23), the pressure level decreases by approximately 20% at 20°C. However, as the temperature rises, this difference increases to 40%, resulting in enhanced ductility of the metal in the areas of contact with the rolls. A further decrease in the total compression level by 3 mm (model 20-18-16) results in an increase in the strain values at 20°C of almost 60%, with an increase in temperature causing an enhancement of this difference to 65%.

In considering the pressure within the central layers of the workpiece, it is important to note their comparatively low level in relation to the surface layers. Concurrently, under certain conditions (at an elevated temperature of 900°C), tensile stresses reaching up to 100 MPa begin to act within this zone. This heterogeneous stress state gives rise to a gradient of properties across the workpiece cross-section. Consequently, it can be deduced that the mean hydrostatic pressure during the process under scrutiny is found to be considerably influenced by both the total compression and the temperature of the workpiece.

In the analysis of deformation forces, the force values on each passage for each deforming tool (rolls and lugs) were taken into consideration. The resultant force graphs for the 30-25-20 model are presented in Fig. 5. The graphs for rolls are shown in red, and for drawing dies in green. A close examination of the graphs reveals that the most significant exertions take place during the drawing stages. Concurrently, the level of effort exerted during the initial pass invariably surpasses that of the subsequent pass, which is concomitant with a diminution in the length of the deformation zone within the drawing die. This reduction in length is attributable to a general decrease in the workpiece diameter. The influence of the heating temperature on the nature of the graphs is also clearly noticeable. At a temperature of 20°C, all graphs exhibit an even horizontal appearance. However, when the workpiece is heated to 500°C during the initial stage of radial-shear broaching, the graph exhibits an upward trend, indicating the workpiece's cooling and a reduction in the ductility of the material. Conversely, at the subsequent stage (the initial stage of drawing), the temperature has already decreased to a sufficient extent, resulting in the force graph acquiring a horizontal appearance. However, when the workpiece is heated to 900°C, the force graphs at the first stage of radial shear broaching, the first stage of drawing, and the second stage of radial-shear broaching have an increasing appearance, indicating a prolonged cooling process for the workpiece.

A quantitative analysis of the forces reveals that the maximum level of 209 kN is attained at the initial stage of drawing in the model at 20°C, with a subsequent decline to 130 kN at the subsequent stage. With an increase in temperature to 500°C, a force of approximately 182 kN is observed at the first stage of drawing, and at the second stage of drawing, the force is around 112 kN. When the workpiece is heated to 900°C at

the first stage of drawing, a force of about 170 kN is exerted at the end of the stage, and at the second stage of drawing, the force is about 124 kN.

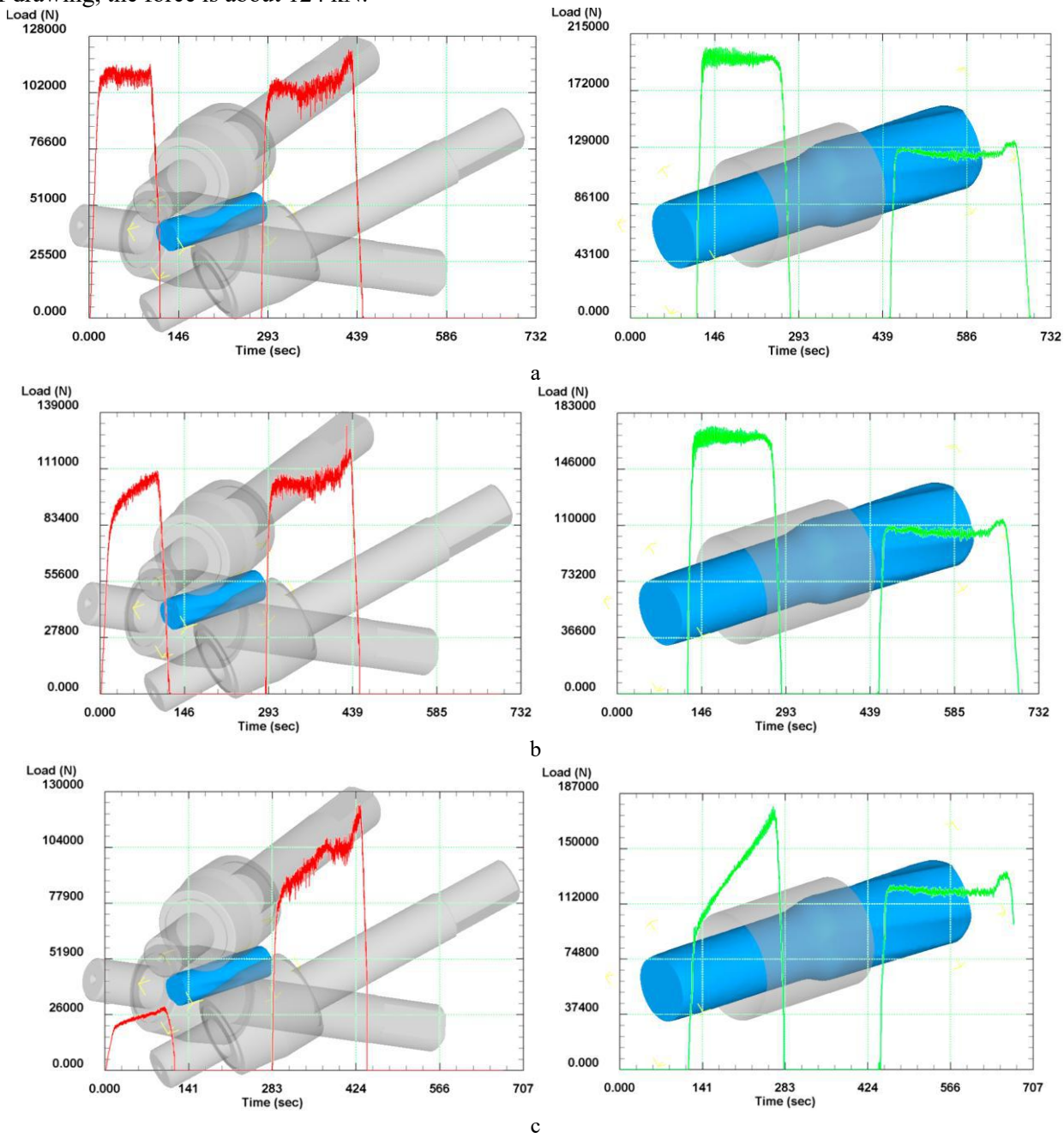

Fig. 5. Force graphs for the 30-25-20 model: a – at 20°C; b - at 500°C; c - at 900°C

Notwithstanding the elevated heating temperature, a greater degree of force was documented at the second stage of the drawing process. The underlying reason for this phenomenon becomes evident when analyzing the force graphs of radial shear stretching. At 20°C, the initial stage of radial shear broaching yielded a force of 108 kN, while the subsequent stage resulted in an approximate force of 117 kN. It is noteworthy that the force graphs at both stages exhibited a horizontal trajectory, indicating the absence of a cooling factor for the workpiece. At 500°C, the graph at the first stage of radial shear broaching has an inclined appearance due to the reduction in ductility of the material resulting from the cooling of the workpiece, with a force of 108 kN being reached at the end of the stage. At the second stage of radial shear broaching, the force is approximately 117 kN, and the force graph at this stage has a horizontal appearance. At 900°C in the initial stage of radial shear broaching, the force reduces to 28 kN by the conclusion of the

stage. Concurrently, the augmentation in exertion at this stage is less pronounced in comparison to the preceding instance, signifying a diminished cooling intensity of the more heated workpiece. In the subsequent stage of radial shear broaching, the force curve exhibits an upward trend, reaching a maximum of 105 kN before leveling off, suggesting the termination of the pronounced cooling process. Subsequently, a force jump of up to 128 kN, a hallmark of the RSR scheme, occurs, denoting the output of the workpiece from the rolls [14]. Fig.6 shows the force graphs for the 30-27-23 model.

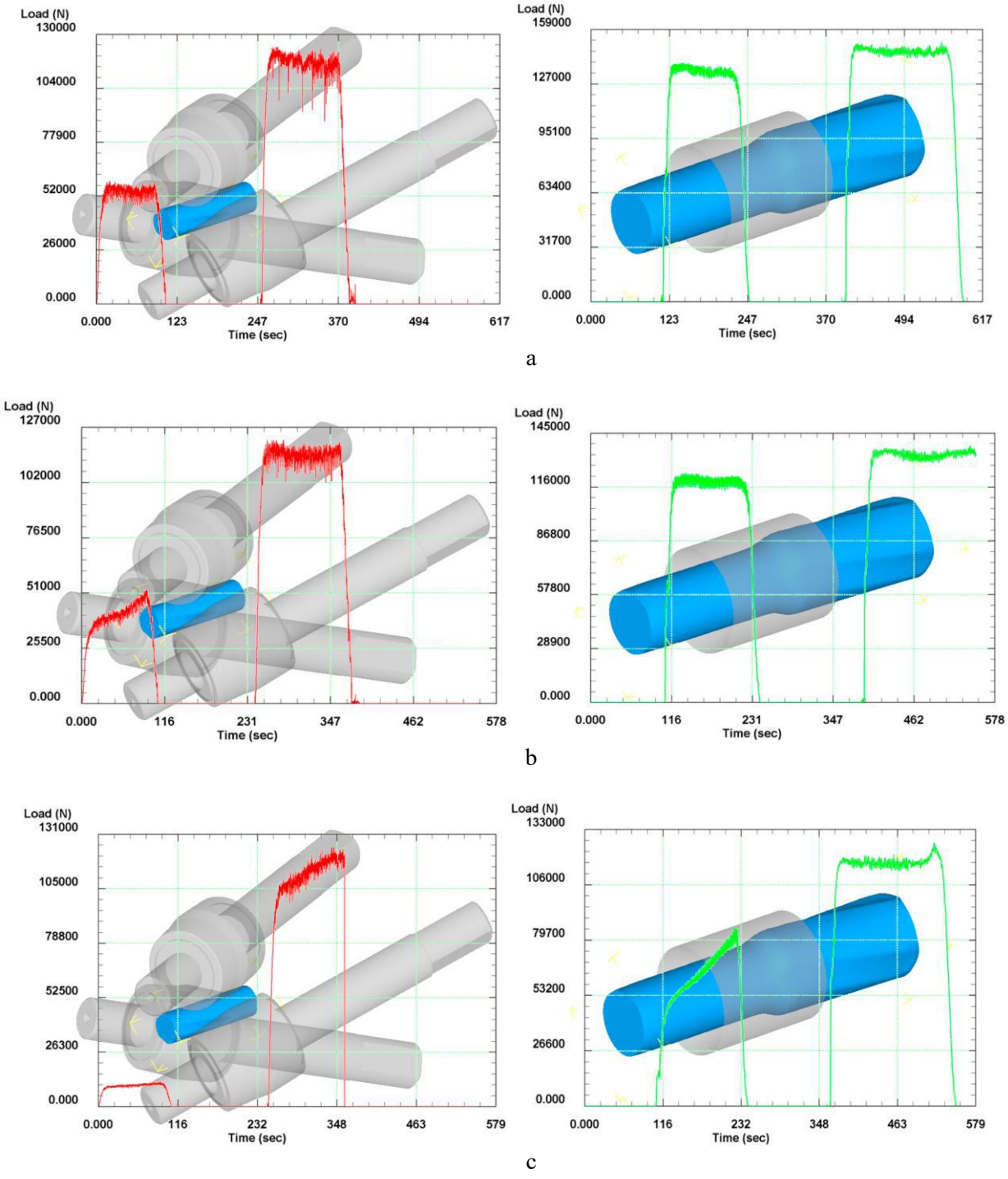

Fig. 6. Force graphs for the 30-27-23 model: a – at 20°C; b - at 500°C; c - at 900°C

In this model, it is necessary to take into account the unevenness of the compression: in the initial stages, the compression is 3 mm, whereas in the subsequent stages, it is 4 mm. Consequently, the drawing forces of the second stage at all temperatures exceed the drawing forces of the first stage. This phenomenon is also the underlying cause of the increased force difference observed during the stages of radial shear broaching. As observed in the 30-25-20 model, the maximum effort is also encountered during the drawing stages. At 20°C, a force of 130 kN is generated during the initial stage of drawing, while the subsequent stage generates approximately 150 kN. The force graphs at both stages exhibit a horizontal trajectory, owing to the absence of cooling of the workpiece. Drawing graphs at a temperature of 500°C demonstrate a similar appearance, with the cooling process concluding at the initial stage of radial shear broaching. At 500°C, the graphs for the first stage of drawing show a force of 118 kN, and for the second stage, the force is approximately 140 kN. At 900°C, the nature of the graphs is similar to the previously considered 30-25-20 model – at the first stage of drawing, the graph has an oblique appearance, as the workpiece cools intensively, which ends at the second stage of radial shear broaching. The second stage of drawing is distinguished by the absence of cooling, resulting in a horizontal graph. At 900°C, a force of 80 kN is generated during the initial stage of drawing, while at the subsequent stage, the force increases to approximately 128 kN.

In the initial phase of radial-shear broaching at 20°C, a force of 53 kN is generated. At the subsequent stage, the force increases to approximately 125 kN. The force graph at both stages exhibits a horizontal trajectory. At 500°C, the graph at the first stage of radial shear broaching has an inclined appearance, reaching 50 kN at the end of the stage. At the second stage of radial shear broaching, the force is approximately 120 kN, and the force graph at this stage has a horizontal appearance. At 900°C in the initial stage of radial shear broaching, the force reaches a mere 10.5 kN at the conclusion of the stage. Concurrently, the augmentation in force at this stage is found to be negligible, in contrast to the 30-25-20 model, which can be attributed to a diminution in the cooling intensity due to a reduction in the value of a single compression from 5 mm to 3 mm. The force graph of the second stage of radial shear broaching also exhibits an upward trend, which becomes horizontal at approximately 120 kN, suggesting the termination of the intensive cooling process. The absence of a force jump in this model can be attributed to the disparity in single and total compression of the same workpiece with a diameter of 30 mm.

As demonstrated in Fig. 7, the force graphs for the 20-18-16 model are presented. In contradistinction to the preceding model (30-27-23), it is imperative to consider the uniformity of compression in this model. At both stages, the uniformity of compression is 2 mm; however, the diameter of the initial blank is reduced to 20 mm. Consequently, a decrease in the length of the deformation focus is observed at all deformation zones, resulting in a substantial reduction in effort when compared to blank models with a diameter of 30 mm. Notably, this model exhibits an opposite effect, where maximum forces are attained at all temperatures during the second stage of radial-shear broaching. Concurrently, the magnitude of the force at the initial stage of radial-shear broaching is found to be negligible, with a maximum recorded force of 6.5 kN.

At 20°C, a force of 64 kN is generated during the initial stage of drawing, while at the subsequent stage, the force reduces to approximately 50 kN. The force graphs for both stages exhibit a horizontal trajectory, a consequence of the inadequate cooling of the workpiece. Drawing graphs at a temperature of 500°C demonstrate a similar appearance – here, cooling ceases at the initial stage of radial shear broaching. At 500°C, a force of 56 kN is generated during the initial stage of drawing, and in the subsequent stage, the force is approximately 42 kN. At 900°C, the nature of the graphs is similar to that of the previously considered models 30-25-20 and 30-27-23. At the first stage of drawing, the graph has an oblique appearance due to intensive cooling of the workpiece. Conversely, the second stage of drawing is distinguished by the absence of cooling, resulting in a horizontal graph. At 900°C, a force of 46 kN is generated during the initial stage of drawing, while at the subsequent stage, the force reduces to approximately 40 kN.

At the initial stage of radial-shear broaching at 20°C, a force of 6.5 kN is generated, while at the subsequent stage, the force increases to approximately 62 kN. Notably, the force graphs at both stages exhibit a horizontal orientation. At 500°C, the graph at the first stage of radial shear broaching has an inclined appearance, reaching 5 kN at the end of the stage. At the second stage of radial shear broaching, the force is approximately 55 kN, and the force graph at this stage has a horizontal appearance. At 900°C, the force at the end of the first stage of radial shear broaching is only 1.5 kN. In the subsequent stage of radial shear broaching, the force increases to approximately 47 kN. It is evident that the absence of a force jump in this model is attributable to the reduced diameter of the initial workpiece.

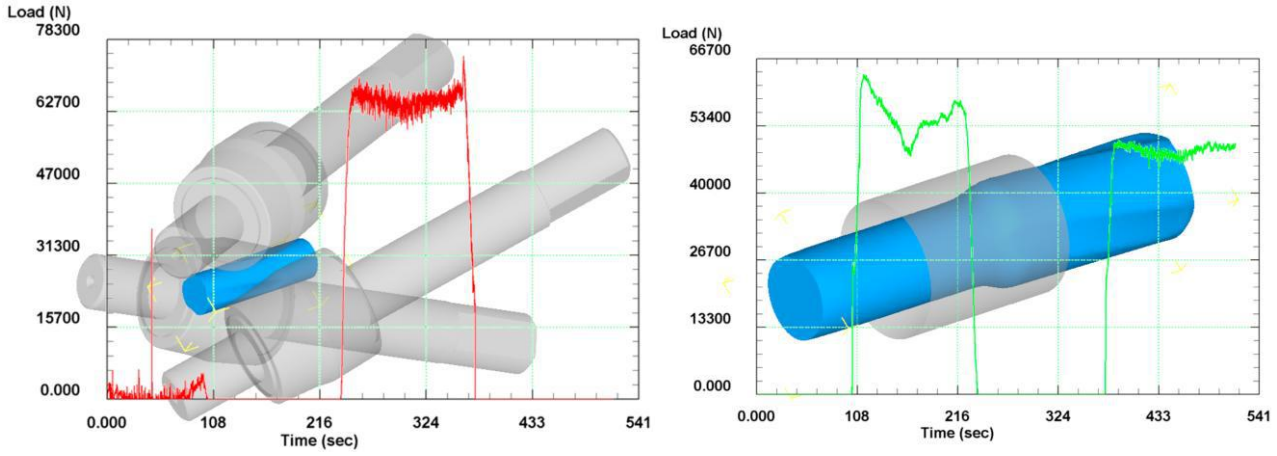

a)

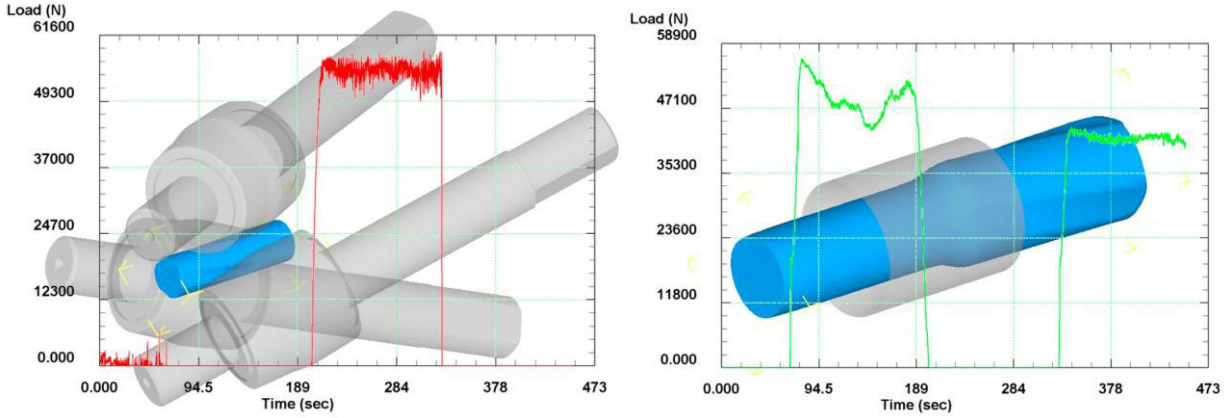

b)

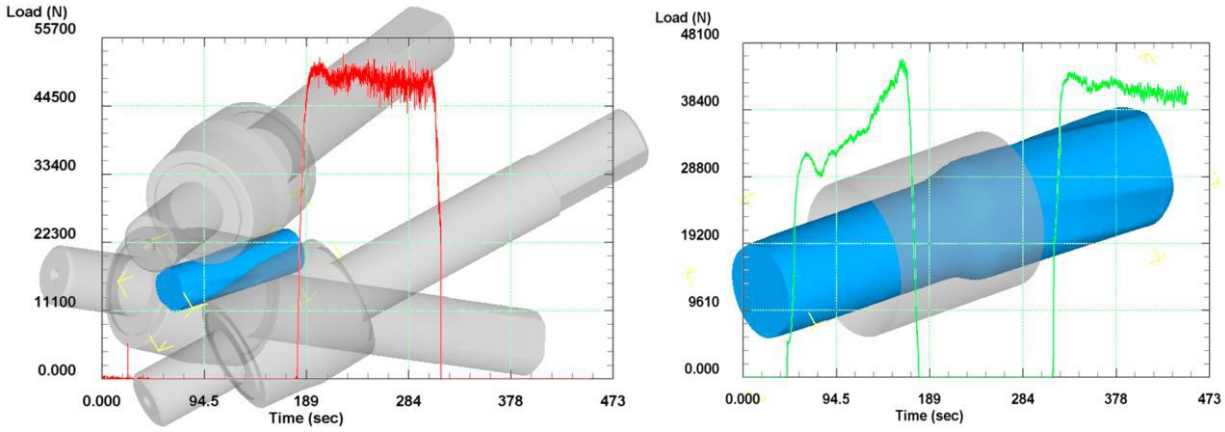

c)

Fig. 7. Force graphs for the 20-18-16 model: a – at 20°C; b - at 500°C; c - at 900°C

4. Conclusion

The paper employed finite element modelling of the radial-shear broaching process, followed by drawing in the Deform program, to study the stress-strain state and energy-strength parameters. A range of models with varying initial diameters of the workpiece, single and total compressions, and different temperatures of heating the workpiece were considered. The study revealed that the optimal processing of the metal occurred under the 30-25-20 scheme at a temperature of 900°C, with the 30-27-23 scheme demonstrating comparable efficacy. Concurrently, it is imperative to acknowledge the substantial reduction in compressive stresses that occurs at elevated temperatures. The selection of the deformation scheme is

paramount, and the values of the deformation forces must be given due consideration, as they provide a comprehensive representation of the loads occurring at all stages of the process. It is noteworthy that a considerable degree of effort is required for models with a blank of 30 mm. However, when the strength of the deforming equipment is sufficient, the 30-25-20 scheme can be recommended. In cases where this is not the case, it is necessary to select a scheme that allows for deformation without exceeding the limiting loads.

Conflict of interest statement

The authors declare that they have no conflict of interest in relation to this research, whether financial, personal, authorship or otherwise, that could affect the research and its results presented in this paper.

CRediT author statement

Conceptualization, I.V.; Methodology, E.P. and A.V.; Software, A.V.; Validation, T.F., M.L and I.V.; Formal Analysis, I.V. and A.V.; Investigation, E.P. and B.M.; Resources, B.M.; Data Curation, I.V. and M.L.; Writing – Original Draft Preparation, I.V. and E.P; Writing – Review & Editing, I.V.; Visualization, E.P.; Supervision, A.V. and M.L. The final manuscript was read and approved by all authors.

Funding

This research has been/was/is funded by the Science Committee of the Ministry of Science and Higher Education of the Republic of Kazakhstan (Grant No. AP19678974).

References

1 Surzhikov A.P., Lysenko E.N., Malyshev A.V., Petrova A., Ghyngazov S.A., Aimukhanov A.K. (2020) Phase transformations in ferrites during radiation-thermal sintering. *Eurasian phys. tech. j.*, 17, 1, 144-153. https://doi.org/10.31489/2020No1/26-34

2 Nurumgaliyev A., Zhuniskaliyev T., Shevko V., Yerekeyeva G. (2024) Modeling and development of technology for smelting a complex alloy (ligature) Fe-Si-Mn-Al from manganese-containing briquettes and high-ash coals. *Scientific Reports*, 14, 1, 7456. https://doi.org/10.1038/s41598-024-57529-6

3 Issagulov A.Z., Kim V.A. Kvon S.S., Kulikov V.Y., Tussupova A.U. (2014) Production of technical silicon and silicon carbide from rice-husk. *Metalurgija*, 53(4), 685–688. Available at: https://hrcak.srce.hr/122222

4 Sapargaliyeva B., Agabekova A., Syrlybekkyzy S., Kolesnikov A., Ulyeva G., Yerzhanov A., Kozlov P. (2023) Study of changes in microstructure and metal interface Cu/Al during bimetallic construction wire straining. *Case Studies in Construction Materials*, 18, e02162. https://doi.org/10.1016/j.cscm.2023.e02162

5 Kovalev P.V., Popova S.D., Issagulov A.Z., Kulikov V.Y., Kvon S.S. (2017) Investigation of the effect of high strength strips steel modification with rare-earth metal (REM). *Metalurgija*, 56(3-4), 393–395. Available at: https://hrcak.srce.hr/180992

6 Naseri R. (2017) An experimental investigation of casing effect on mechanical properties of billet in ECAP process. *Intern. Journal of Advanced Manufacturing Technology*, 90, 3203–3216. https://doi.org/10.1007/s00170-016-9658-1

7 Denissova A., Kuatbay Y., Liseitsev Y. (2023) Effect of thermomechanical processing of building stainless wire to increase its durability. *Case Studies in Construction Materials*, 19, e02346. https://doi.org/10.1016/j.cscm.2023.e02346

8 Kawasaki M., Ahn B., Lee H.J., Zhilyaev A.P., Langdon T.G. (2015) Using high-pressure torsion to process an aluminum–magnesium nanocomposite through diffusion bonding. *J. Mater. Res.*, 31, 88-99. https://doi.org/10.1557/jmr.2015.257

9 Panichkin A., Wieleba W. Kenzhegulov A., Uskenbayeva A.M, Kvyatkovskii S., Kasenova B. (2023) Effect of thermal treatment of chromium iron melts on the structure and properties of castings. *Materials Research Express*, 10(8), 086502. https://doi.org/10.1088/2053-1591/acead7

10 Albert M., Schilling K. (2015) The line coating robot – An automated mobile system for high precision powder coating. *Proceeding of the 2nd IFAC Conference on Embedded Systems. Computer Intelligence and Telematics*, 28, 10, 58-62. https://doi.org/10.1016/j.ifacol.2015.08.108

11 Volokitin A.V., Panin E.A., Latypova M.A., Kassymov S.S. (2022) Microstructure evolution of steel-aluminum wire during deformation by "equal-channel angular pressing-drawing" method. *Eurasian phys. tech. j.*, 19, 1, 73-77. https://doi.org/10.31489/2022No1/73-77

12 Volokitina I., Volokitin A., Makhmutov B. (2024) Formation of Symmetric Gradient Microstructure in Carbon Steel Bars. *Symmetry*, 16(8), 997. https://doi.org/10.3390/sym16080997

13 Volokitina I., Volokitin A., Panin E. (2024) Gradient microstructure formation in carbon steel bars. *Journal of Materials Research and Technology*, 31, 2985–2993. https://doi.org/10.1016/j.jmrt.2024.07.038

14 Arbuz A., Kawalek A., Ozhmegov K., Dyja H., Panin E., Lepsibayev A., Sultanbekov S., Shamenova R. (2020) Using of Radial-Shear Rolling to Improve the Structure and Radiation Resistance of Zirconium-Based Alloys. *Materials*, 13, 19, 4306. https://doi.org/10.3390/ma13194306

AUTHORS' INFORMATION

Volokitina, Irina Evgenievna – PhD, Professor, Department of Metallurgy and Materials Science, Karaganda Industrial University, Temirtau, Kazakhstan; Scopus Author ID: 55902810800, ORCID: 0000-0002-2190-5672; irinka.vav@mail.ru

Panin, Evgeny Alexandrovich – PhD, Professor, Department of Metal forming, Karaganda Industrial University, Temirtau, Kazakhstan; Scopus Author ID: 55903153300, ORCID: 0000-0001-6830-0630; cooper802@mail.ru

Volokitin, Andrei Valeryevich – PhD, Associate Professor, Department of Metal forming, Karaganda Industrial University, Temirtau, Kazakhstan; Scopus Author ID: 56524247500, ORCID: 0000-0002-0886-3578; dyusha.vav@mail.ru

Fedorova, Tatiana Dmitrievna – Master, Department of Metallurgy and Materials Science, Karaganda Industrial University, Temirtau, Kazakhstan; Scopus Author ID: 57222628232; ORCID: 0009-0005-6117-1297, tanyusik88@bk.ru

Latypova, Marina Alexandrovna – Master, Accounting and audit, Karaganda Industrial University, Temirtau, Kazakhstan, Scopus Author ID: 57219097120, ORCID: 0000-0003-4340-6134; marinapray@mail.ru

Makhmutov, Bolat Bizhanovich – Candidat of Technical Sciences, Vice-Rector for Research and International Co-operation, Karaganda Industrial University, Temirtau, Kazakhstan; Scopus Author ID: 57356852600, ORCID: 0009-0001-8978-8097; bb.makhmut@tttu.edu.kz

EURASIAN PHYSICAL TECHNICAL JOURNAL

2025, Volume 22, No. 2 (52)

https://doi.org/10.31489/2025N2/121-132

Received: 25/03/2025 Revised: 19/05/2025 Accepted: 23/06/2025 Published online: 30/06/2025

Research Article

UDC: 537.632; 520.66; 519.876.5

THERMAL INFRARED OBJECT DETECTION WITH YOLO MODELS

Turmaganbet U.[1], Zhexebay D.[1], Turlykozhayeva D.[1]*, Skabylov A.[1], Akhtanov S.[2], Temesheva S.[1], Masalim P.[1], Tao M.[3]

[1]al-Farabi Kazakh National University, Almaty, Kazakhstan
[2]Unmanned Aerial Vehicle Laboratory, Scientific Research Institute of Experimental and Theoretical Physics, Almaty, Kazakhstan
[3]School of Electronics and Information, Northwestern Polytechnical University, Xian, China
*Corresponding author: dana.turlykozhayeva@kaznu.edu.kz

Abstract. *Object detection is a fundamental task in computer vision and remote sensing, aimed at recognizing and categorizing different types of objects within images. Unmanned aerial vehicle - based thermal infrared remote sensing provides crucial multi-scenario images and videos, serving as key data sources in public applications. However, object detection in these images remains challenging due to complex scene information, lower resolution compared to visible-spectrum videos, and a shortage of publicly available labeled datasets and trained models. This article introduces a Unmanned aerial vehicle - based thermal infrared object detection framework for analyzing images and videos in public applications and evaluates the performance of YOLOv8n/v8s, YOLOv11n/v11s, and YOLOv12n/v12s models in extracting features from ground-based thermal infrared images and videos captured by Forward-Looking Infrared cameras, as well as from unmanned aerial vehicle - recorded thermal infrared videos taken from various angles. The YOLOv8n/v8s, YOLOv11n/v11s, and the latest YOLOv12n/v12s models were deployed on a Raspberry Pi 5 using the OpenVINO framework. The successful deployment of these models, including the most recent version, demonstrates their feasibility for unmanned aerial vehicle-based thermal infrared object detection. The results show that YOLOv8 and YOLOv11 achieved high accuracy and recall rates of 93% and 92%, respectively, while the YOLOv12 model demonstrated good precision but comparatively lower performance in accuracy and recall, suggesting the possibility for further improvement.*

Keywords: object detection, YOLO models, Unmanned aerial vehicle, Forward-Looking Infrared cameras, thermal infrared images, Raspberry Pi 5.

1. Introduction

Object detection is a key task in computer vision, primarily focused on classifying and locating specific objects within an image. Remote sensing images, captured by various sensors on different platforms, often contain multiple objects at various scales, making them a rich source for object detection. Remote sensing has been applied to spaceborne, aerial, and ground-based platforms [1, 2]. Ground remote sensing systems, which use platforms such as high towers, vehicles, and ships, provide valuable optically labeled datasets. However, there are fewer thermal infrared (TIR) datasets available for detecting multiple objects at ground level. Unmanned aerial vehicle (UAV) platforms, on the other hand, can capture high-resolution thermal images and videos, compensating for the lack of high-resolution thermal data from satellites due to sensor limitations. With the rapid development of UAVs, the demand for efficient and effective detection algorithms is growing. UAV-based TIR images are now used in precision agriculture (PA), which helps

optimize farming practices by detecting variations in soil and crops. However, UAV TIR platforms generate large volumes of unlabeled data, creating challenges for the development of transfer techniques, algorithms, and detection applications based on ground-labeled data [1-9]. Unlike optical sensors, TIR sensors can capture images in both day and night conditions. As TIR technology continues to improve, it has found widespread use in applications like body temperature detection, traffic monitoring, and public health and safety, receiving significant attention. Despite this, object detection on UAV TIR images and videos remains relatively underdeveloped. Previous studies have focused on pedestrian detection using TIR images in ground settings [3], as well as the detection of ships [4], vehicles [5], thermal bridges in buildings [6], and electrical equipment [7]. For instance, in [8] authors compared the accuracy and performance time of various surveillance systems for detecting human presence using thermal imagery. In [9] authors developed a method for detecting vehicles with TIR images, which was successfully applied to traffic flow monitoring. They demonstrated that thermal image-based object detection could be effectively used in road traffic surveillance [9].

In general, object detection and UAV technologies are growing fields with diverse applications, not only in computer vision and deep learning but also in areas such as COVID-19 prevention and control, search and rescue operations, and Advanced Driver Assistance Systems (ADAS) using thermal imaging [10]. Despite these advances, object detection from UAV TIR images and videos continues to face numerous challenges, including complex backgrounds, low resolution, long imaging distances, and the presence of multiple scenes and objects [11-13].

Recently, YOLO-based object detection in thermal infrared imagery has gained significant traction, offering enhanced accuracy and efficiency in diverse real-world applications. In [11], the authors proposed enhancing search and rescue (SAR) missions using YOLOv8 for human detection in thermal imagery, achieving high precision with YOLOv8n at 90%. To expand object detection beyond the visible spectrum, in [12] authors proposed a TIR detection framework using YOLO models for Forward-Looking Infrared (FLIR) cameras. In [13], the authors propose an improved Mask-RCNN algorithm for UAV TIR video stream target detection, enhancing efficiency and reducing storage, but with potential limitations in complex environments and varying target sizes. In [14], the authors introduced ALSS-YOLO, a lightweight detector for TIR aerial images, achieving state-of-the-art wildlife detection performance on the BIRDSAI and ISODTIR UAV datasets. The above-mentioned articles [9-15] demonstrate relatively good efficiency in object detection, but there is potential to further improve metrics such as precision, accuracy, and recall.

This article presents an object detection framework based on thermal infrared (TIR) imaging using unmanned aerial vehicles (UAVs) for public applications. It evaluates the performance of the latest YOLOv12 models alongside YOLOv8n/v8s and YOLOv11n/11s. These models were tested on ground-based TIR images and videos captured by FLIR cameras under both bright and dark conditions, prior to being applied to UAV-captured TIR videos from various angles. The YOLOv8n/v8s, YOLOv11n/11s, and the latest YOLOv12n/v12s models were successfully deployed on a Raspberry Pi 5 using the OpenVINO (Open Visual Inference and Neural Network Optimization) framework, demonstrating their feasibility for UAV-based TIR object detection. We believe that the proposed integrated approach has strong potential to enhance real-time object detection performance in public applications.

2. Background

2.1 YOLO models

The YOLO architecture [16-18] consists of three core components: the backbone, the neck, and the head. The backbone is responsible for extracting features from the input image, while the neck and head process these features to generate predictions for bounding boxes, object classes, and confidence scores. The loss function integrates squared errors for bounding box coordinates, square-rooted differences for width and height, and classification errors, with weighted coefficients to emphasize both localization precision and object detection accuracy. Table 1 presents the structures of the YOLO models.

YOLOv8 focuses on a lightweight architecture with CSPNet, anchor-free design, and balanced performance between speed and accuracy. YOLOv11 improves upon YOLOv8 by introducing C3k2 blocks and spatial attention (C2PSA), enhancing computational efficiency and detection precision. YOLOv12 further refines the architecture with R-ELAN backbones, FlashAttention-driven area attention, and 7×7 separable convolutions, achieving higher accuracy, especially for small or occluded objects, while

maintaining real-time speeds. Each version builds on its predecessor to optimize object detection for diverse scenarios [19-21].

Table 1. Comparison of YOLOv8/11/12 structure

YOLO model	Backbone	Neck	Activation	Loss	Models
YOLOv8	CSPNet+CBS+C2f	FPN+PAN+SPPF	SiLU	Anchor-free approach	YOLOv8n/s/m/l/x
YOLOv11	CSPNet+C3k2	FPN+PAN+SPPF+C2PSA	LeakyReLU	Bounding Box,Class	YOLOv11n/s/m/l/x
YOLOv12	CSPNet+R-ELAN	FPN+PAN+Area Attention	LeakyReLU	Bounding Box,Class	YOLOv12n/s/m/l/x

2.2 Evaluation metrics

In this study, the performance of the YOLO models for object detection training and validation was assessed using precision, recall, accuracy, and FPS (Frames Per Second).

Precision measures the proportion of true positive samples out of all the predicted positive samples, while recall measures the proportion of true positive samples out of all the actual positive samples [22-24]. The calculations for precision and recall are provided in Eqs. (1) and (2):

$$precision = \frac{TP}{TP+FP}, \quad (1)$$

$$recall = \frac{TP}{TP+FN}, \quad (2)$$

TP (True Positive) refers to the number of persons that are correctly identified as persons, while FP (False Positive) indicates the number of instances where non-person objects are incorrectly classified as persons. FN (False Negative) represents the number of persons that are incorrectly classified as non-person objects.

Accuracy is a common performance metric in machine learning and object detection tasks, which measures how many predictions the model got right (both positive and negative) compared to all predictions made [25-28]. It is calculated using the formula:

$$accuracy = \frac{TP+TN}{TP+TN+FP+FN}, \quad (3)$$

While accuracy provides a general sense of model performance, it can be misleading when there is a class imbalance. In such cases, other metrics like precision and recall are often used alongside accuracy to gain a more comprehensive understanding of the model's performance.

FPS is a performance metric used to measure how quickly a model can process and analyze video frames or images. In the context of object detection, FPS indicates how many frames the model can process in one second, giving an idea of the speed or real-time capability of the detection system. A higher FPS value means the model is able to process more frames per second, which is crucial for real-time applications such as video surveillance, autonomous vehicles, or drones. The ability to maintain high FPS while accurately detecting objects ensures that the system can operate effectively in dynamic environments where fast responses are necessary. In object detection tasks, balancing FPS with accuracy is important, as a model that runs too slowly might not be practical in real-time applications, even if it achieves high accuracy [29].

2.3 TIR image dataset

The FLIR Thermal Starter Dataset (FLIR, 2019) was used, which includes four object classes: person, car, bicycle, and dog. It contains both annotated thermal images and non-annotated optical images for training and validating object detection neural networks. The dataset comprises 10,288 annotated thermal infrared (TIR) images, featuring 28,151 persons and 46,692 cars, as well as 4,224 video-annotated TIR

images, with 21,965 persons and 14,013 cars. These images were captured on streets and highways in Santa Barbara, California, USA, between November and May, under mostly clear sky conditions, both during the day and at night. The images were taken with either a FLIR Tau2 camera (13 mm f/1.0, 45° horizontal field of view (HFOV) and 37° vertical field of view (VFOV)) or a Boson camera. While TIR images typically have lower spatial resolution, smaller signal-to-noise ratios (SNR), and fewer texture features compared to conventional optical images, they offer the advantage of being captured both day and night. In contrast, optical images can only be collected during the day unless artificial lighting is available. To take advantage of both all-day thermal infrared imaging and the features of optical images, it was assumed that the shape features learned by YOLO models from optical datasets [30] for detecting persons and cars would also apply to TIR images. This assumption provides a solid foundation for using pre-trained models to detect objects in thermal infrared images, offering a reasonable starting point for effective detection in this type of imagery [31-33].

2.4. Performance of YOLOv8/v11/v12

The Raspberry Pi 5 is a high-performance single-board computer designed for real-time processing. Equipped with a 64-bit Broadcom BCM2712 processor (Cortex-A76, up to 2.4 GHz) and a VideoCore VII GPU (800 MHz), it offers substantial improvements over its predecessors. With options for 4 GB or 8 GB LPDDR4X-4267 RAM, it efficiently manages multitasking and large datasets. The PCIe 2.0 interface facilitates external accelerator integration, boosting data processing capabilities. Despite requiring 5A and 5V of power, the Raspberry Pi 5 remains compact and efficient for various applications [34-37].

To deploy YOLOv8, YOLOv11 and YOLOv12 on the Raspberry Pi 5, the trained models were converted to an OpenVINO-compatible format. Using OpenVINO's Model Optimizer, the best.pt file was converted into an Intermediate Representation (IR) model, optimizing it for more efficient execution on resource-constrained devices. OpenVINO is an Intel toolkit that optimizes deep learning models for CPUs, GPUs, FPGAs, and VPUs. It converts models from frameworks such as TensorFlow and PyTorch into IR format using the Model Optimizer, and the Inference Engine ensures efficient execution. When integrated with the Raspberry Pi 5, OpenVINO improves inference efficiency, reducing computational overhead and enabling real-time processing through its BCM2712 processor and VideoCore VII GPU.

After converting the model to the OpenVINO format, the best_yolov8s_openvino_model was deployed on the Raspberry Pi 5. Test images stored in./test/images, along with their corresponding YOLO-format annotations in./test/labels, were used for evaluation. A Python script running on the Raspberry Pi 5 handles the complete object detection process: it loads and preprocesses images, performs inference using the YOLO model via OpenVINO, and compares the predicted bounding boxes with ground truth annotations. This workflow enables a detailed assessment of the model's accuracy and performance in real-time object detection on resource-constrained hardware.

For each test image, the following steps are performed: the image is loaded into memory, processed through the YOLO model to obtain predicted object coordinates, and compared with the ground truth annotations. Bounding boxes are visualized, with predictions shown in green and actual annotations in red, providing a clear indication of detection accuracy. The inference time for each image is recorded to evaluate real-time performance. Finally, the processed images, with bounding boxes, are saved in the./results directory for further analysis. This methodology ensures a thorough evaluation of both detection accuracy and processing efficiency.

3. Results and discussions

3.1 Confusion matrix and accuracy

In Figure 1, an example of thermal reflections is shown, with thermal reflections placed in a box. To accurately identify the specific area of an object in a thermal image, it is crucial to detect and differentiate the thermal reflections. Figure 1 demonstrates that the detection capabilities of the YOLOv8, YOLOv11 and YOLOv12 models are suitable for use in a range of public applications and conditions. Figure 2 shows the confusion matrix (a, c) and accuracy curves (b, d) of the YOLOv8n/s models. The x-axis represents the true class labels of the samples, while the y-axis indicates the predicted results.

In Figure 2, YOLOv8n (a) correctly identifies 213 people with 23 background instances misclassified as people and 6 people as background, while YOLOv8s (c) detects 212 people correctly, misclassifying 23 background instances as people and 7 people as background. The accuracy curves in (b) and (d) illustrate the

training process over 100 epochs, showing a sharp initial improvement followed by a gradual stabilization around 92%.

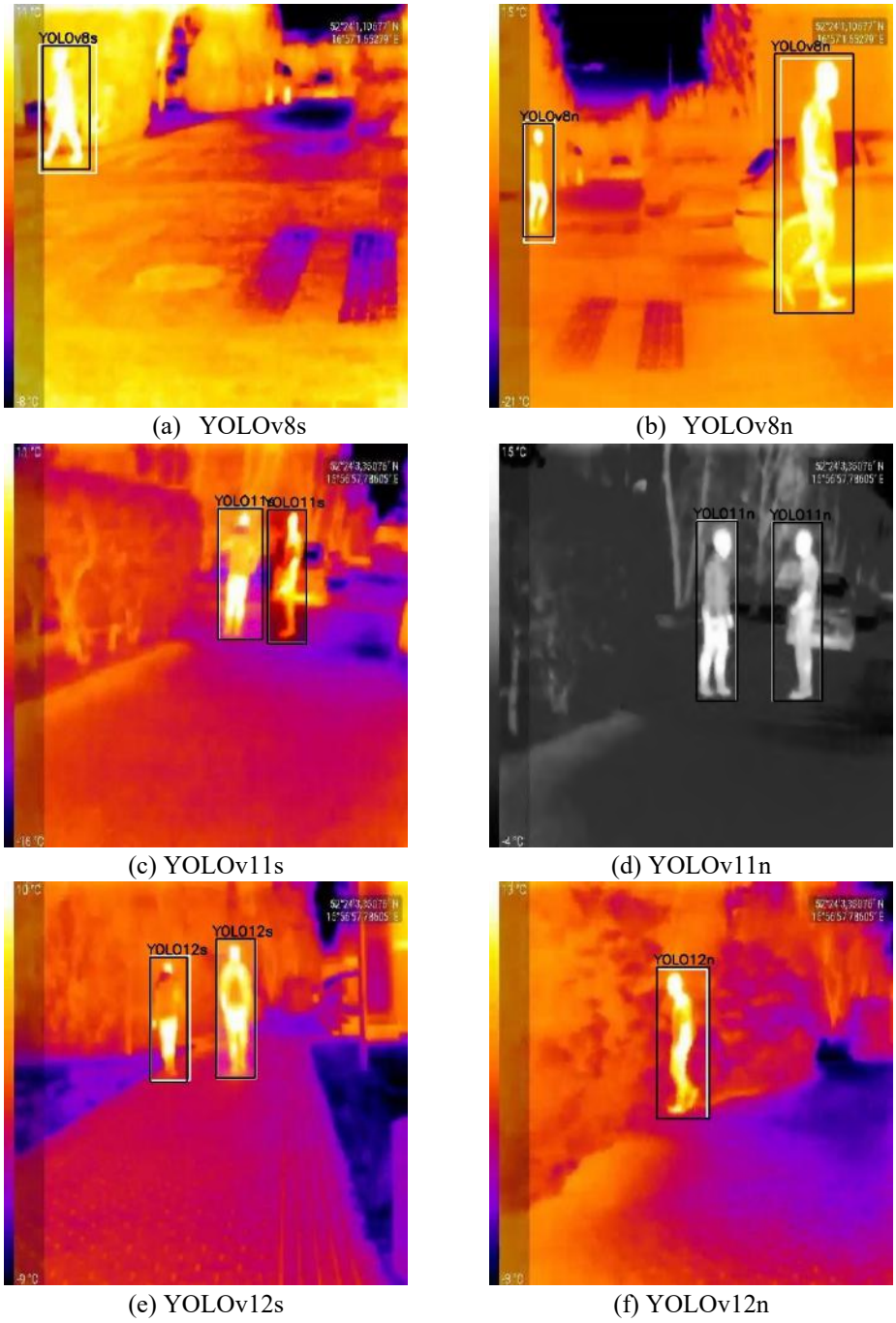

(a) YOLOv8s (b) YOLOv8n

(c) YOLOv11s (d) YOLOv11n

(e) YOLOv12s (f) YOLOv12n

Fig.1. Thermal images with thermal reflections.

Figure 3 presents the results of the confusion matrix (a, c) and accuracy curves (b, d) of the YOLOv11n and YOLOv11s models. In Figure 3, YOLOv11n (a) accurately identifies 211 people, misclassifying 30 as background and 8 background instances as people, resulting in zero correctly classified background instances, while YOLOv11s (c) also detects 211 people correctly, misclassifying 21 as background and 8 background instances as people, again leading to no correctly identified background instances. The accuracy curves in (b) and (d) illustrate the training progression over 100 epochs, showing a steep initial gain before gradually stabilizing around 93%.

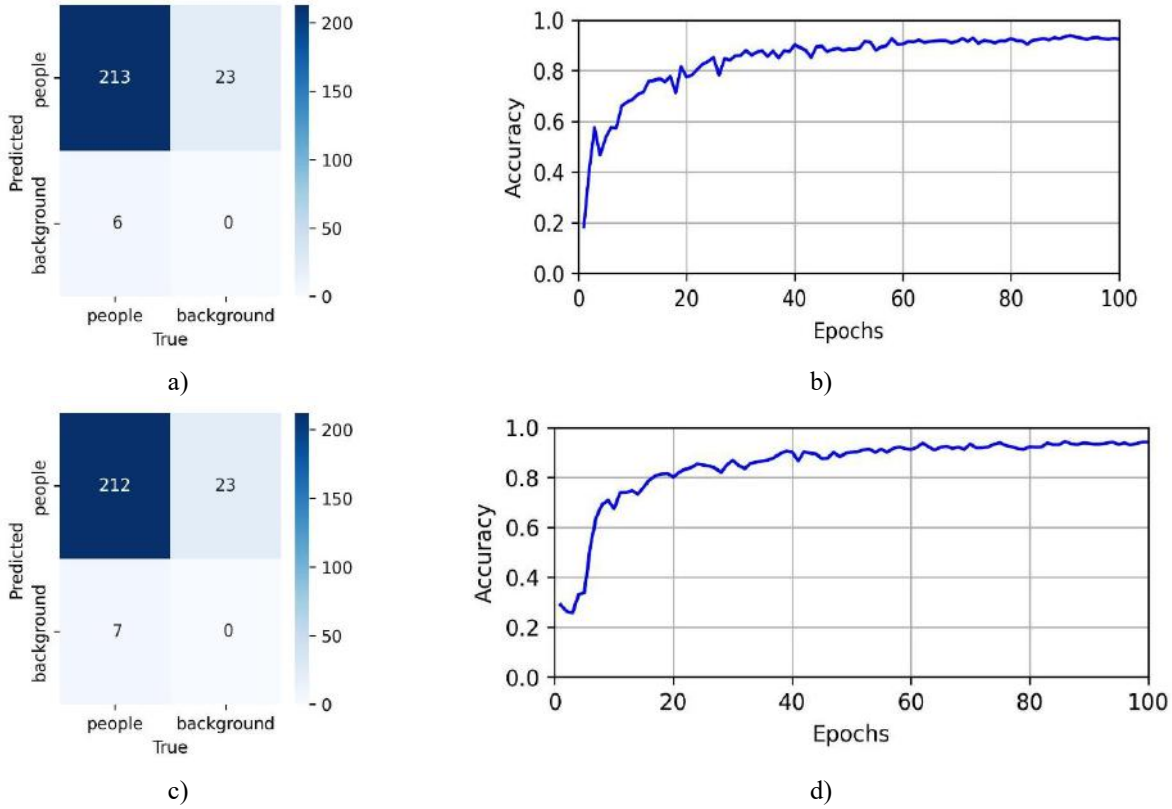

Fig. 2. (a, c) – YOLOv8n/s confusion matrix; (b, d) – Accuracy curve

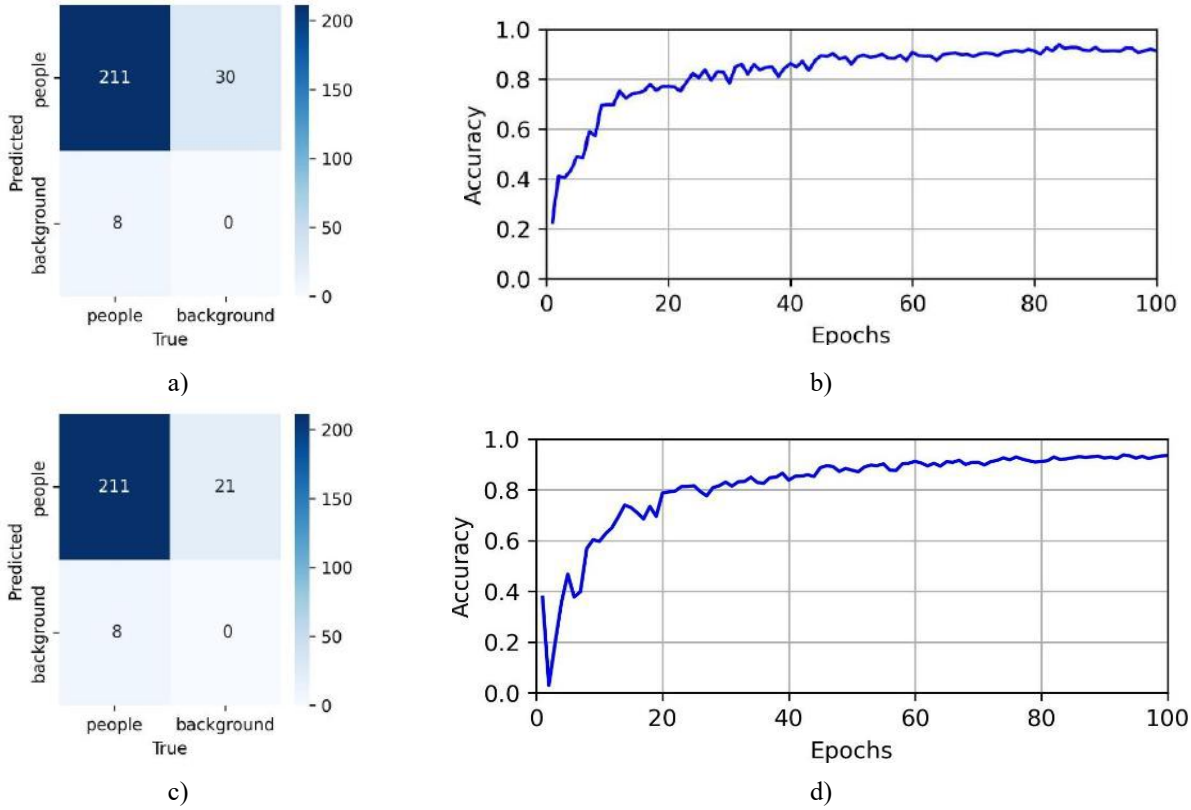

Fig.3. (a,c) – YOLOv11n/s confusion matrix; (b,d) – Accuracy curve

Figure 4 presents the results of the confusion matrix (a, c) and accuracy curves (b, d) of the YOLOv12n and YOLOv12s models.

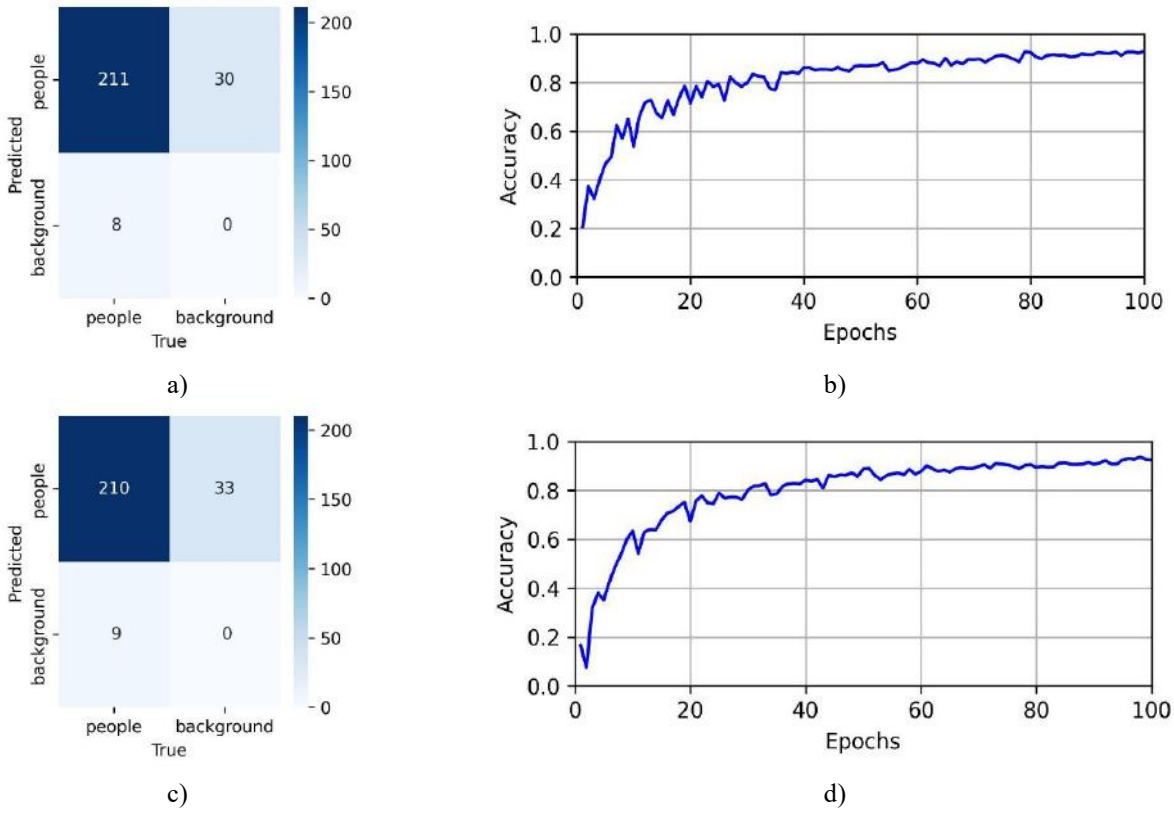

Fig.4. (a,c) – YOLOv12n/s confusion matrix; (b,d) – Accuracy curve

In Figure 4, YOLOv12n (a) correctly identifies 211 people, misclassifying 30 as background and 8 background instances as people, while YOLOv12s (c) detects 210 people, misclassifying 33 as background and 9 background instances as people, with both models failing to correctly classify any background instances. The accuracy curves in (b) and (d) depict the training process over 100 epochs, showing an abrupt initial gain before gradually stabilizing around 90%.

3.2 Recall and precision

In Figure 5, the precision and recall values demonstrate the performance of YOLOv8n/s, YOLOv11n/s, and YOLOv12n/s over 100 training epochs. All models show rapid improvements in the first 20 epochs, followed by stabilization beyond epoch 50.

YOLOv8n/s begins with a Precision of approximately 0.60 and Recall around 0.55. By epoch 20, these rise to about 0.88 and 0.85, respectively, and eventually stabilize at around 0.95 (Precision) and 0.92 (Recall). YOLOv11n/s starts similarly with Precision near 0.58 and Recall at 0.50 but shows slightly more fluctuation during training. After minor instability around epoch 25, it reaches a stable Precision of about 0.94 and Recall of 0.91-0.92. YOLOv12n/s outperforms both, starting stronger with Precision around 0.62 and Recall at 0.58. It surpasses 0.90 in both metrics by epoch 20 and stabilizes after epoch 50 with Precision near 0.97 and Recall around 0.95. Its training curves are smoother and more stable, indicating better learning dynamics and generalization.

3.3 Accuracy and FPS comparison

Figure 6 (a, b) presents the comparative analysis of object detection accuracy and FPS for the YOLOv8n/s, YOLOv11n/s, and YOLOv12n/s models. According to Figure 6 (a), YOLOv8n and YOLOv8s achieve the highest accuracy, both nearing 0.88, indicating strong performance, while YOLOv11s also performs well at a similar level, suggesting optimizations in this version. YOLOv11n follows with slightly

lower accuracy, remaining above 0.84, while YOLOv12n is close behind. YOLOv12s records the lowest accuracy, approaching 0.82. According to Figure 6 (b), YOLOv11n achieves the highest FPS, exceeding 11, followed by YOLOv8n, which reaches approximately 10 FPS.

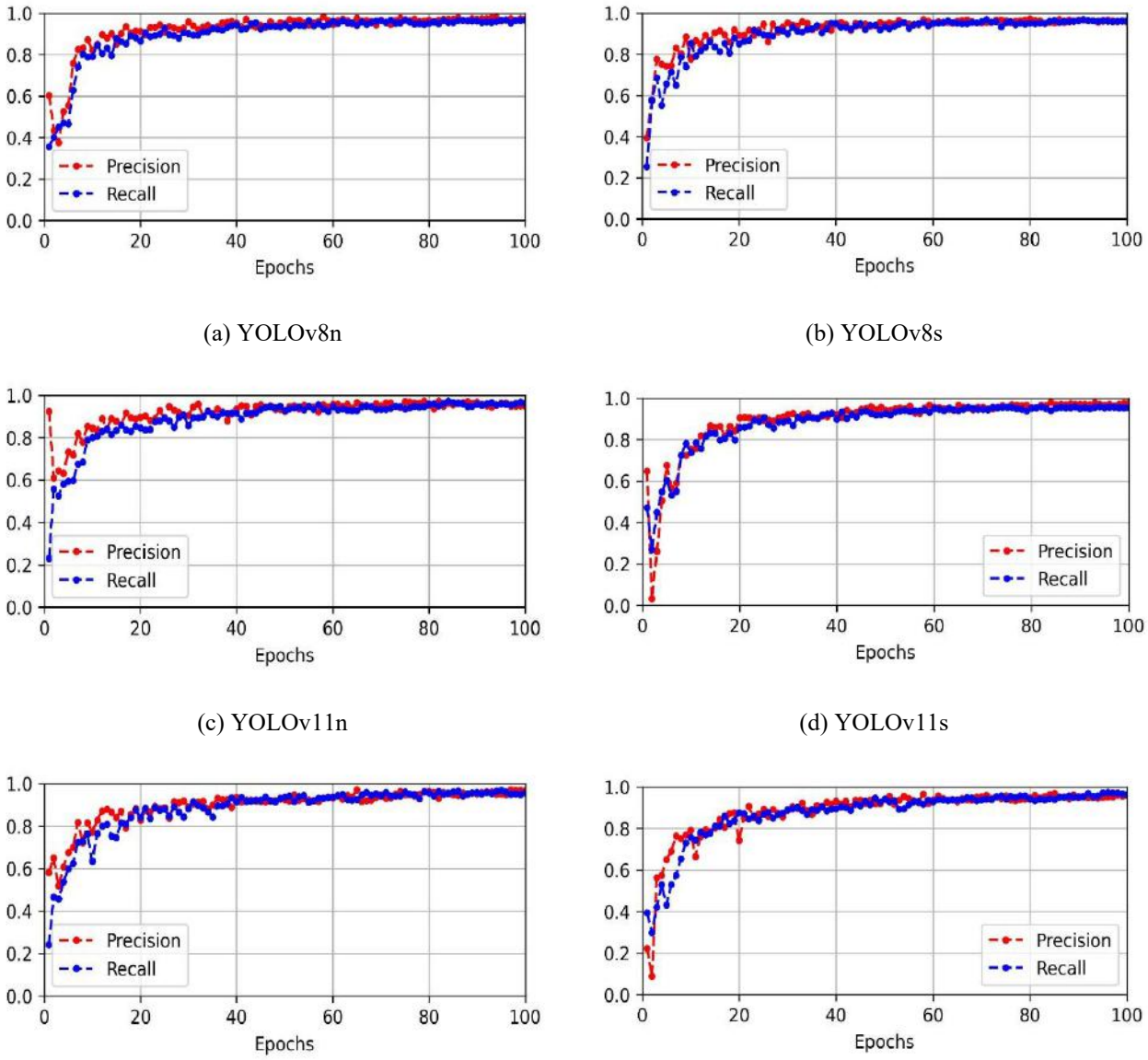

(a) YOLOv8n (b) YOLOv8s

(c) YOLOv11n (d) YOLOv11s

(e) YOLOv12n (f) YOLOv12s

Fig.5. Precision and recall results of YOLO models.

YOLOv12n performs moderately, achieving approximately 7 FPS. YOLOv8s and YOLOv11s show lower performance, with FPS values around 5 and 4, respectively. YOLOv12s has the lowest FPS, measuring slightly above 2 FPS. Figure 7 provides a comparison of the efficiency of YOLOv8n/s, YOLOv11n/s and YOLOv12n/s models, showcasing their performance in terms of accuracy and processing speed.

Figure 7 demonstrates that YOLOv8n, YOLOv11n and YOLOv12n achieve the highest FPS and accuracy compared to the other evaluated models. Meanwhile, YOLOv8s and YOLOv11s exhibit slightly lower FPS but maintain competitive accuracy, balancing speed and precision in object detection, while YOLOv12s demonstrates the least efficiency.

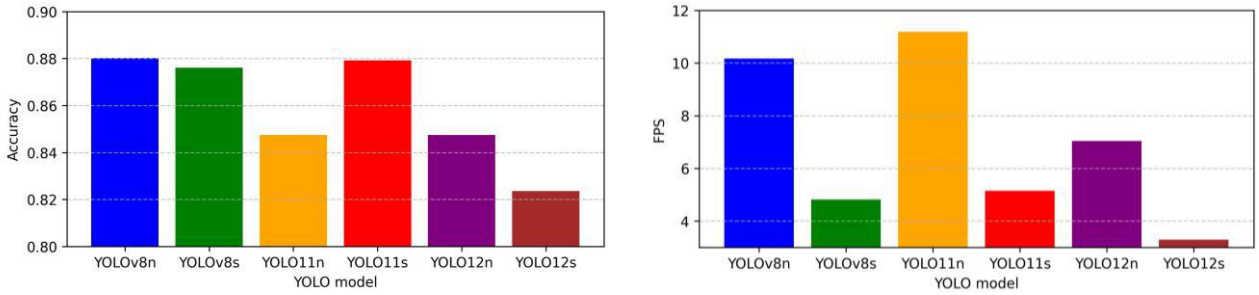

(a) (b)

Fig. 6. Accuracy and FPS comparison of YOLO models

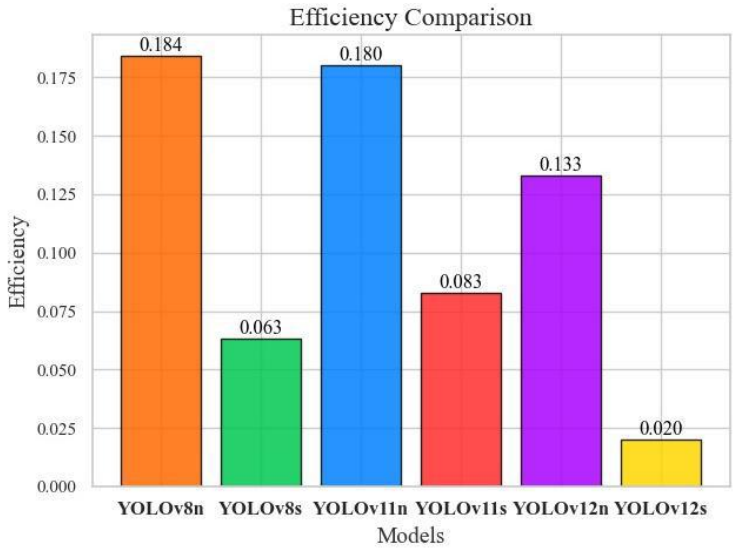

Fig.7. Efficiency Comparison of YOLOv8/11/12 models

4. Conclusion

In summary, this study assessed the performance of YOLOv8n/v8s, YOLOv11n/v11s, and YOLOv12n/v12s models for human detection in thermal infrared (TIR) UAV-captured imagery across various public applications. The results demonstrate that the YOLOv8n/v8s and YOLOv11n/v11s models offer notable improvements in detection accuracy (92% and 93%, respectively) and computational efficiency compared to YOLOv12n/v12s. YOLOv11n achieved the fastest detection speed at 11.50 frames per second, while YOLOv12s had the smallest model size. Additionally, the YOLOv11 models achieved the highest recall at 93% and strong precision of 92%. Their successful deployment on a Raspberry Pi 5 using the OpenVINO framework confirmed their feasibility for real-time object detection in thermal infrared imagery captured by UAVs.

The use of FLIR thermal infrared cameras provides a significant advantage by capturing high-quality imagery in both day and night conditions, allowing for effective object detection even in low-light and obscured scenarios. The ability to capture images from different angles further enhances detection performance, providing a broader view of the scene and improving object localization and identification in real-world applications. Future work will focus on integrating YOLO models with FPGA hardware and advanced thermal infrared imaging in UAV systems, enabling ultra-efficient, real-time object detection for public safety and monitoring applications. Additionally, we plan to utilize improved FLIR cameras with enhanced resolution and sensitivity to further boost detection accuracy and reliability during both day and night captures.

Conflict of interest statement

We want to make it clear that we have absolutely no conflicts of interest that could sway the finding or conclusions presented here. Financially, personally, or in terms of authorship, there's nothing that could interfere with the integrity of our work. It's important to us that our research is seen as unbiased and credible.

CRediT author statement

Turmaganbet U.K.: Conceptualization, Supervision, Zhexebay D.M.: Data Curation, Writing-Original Draft, Turlykozhayeva D.A.: Writing-Review&Editing, Skabylov A.A.: Data Curation, Writing-Original Draft, Akhtanov S.N.: Data Curation, Writing-Original Draft, Temesheva S.A.: Writing-Review&Editing, Masalim P.S.: Writing-Review&Editing, Tao M.: Writing-Review&Editing. The final manuscript was read and approved by all authors.

Funding

The research was funded by the Ministry of Science and Higher Education of Republic of Kazakhstan, grant AP19674715.

Acknowledgements

We would like to express our sincerest gratitude to the Research Institute of Experimental and Theoretical Physics of the al-Farabi Kazakh National University for supporting this work by providing computing resources of the Department of Physics and Technology for this study.

References

1 Ren X., Sun M., Zhang X., Liu L., Zhou H., Ren X. (2022) An improved mask-RCNN algorithm for UAV TIR video stream target detection. *International Journal of Applied Earth Observation and Geoinformation*, *106*, 102660. https://doi.org/10.1016/j.jag.2021.102660

2 Laghari A. A., Jumani A.K., Laghari R.A., Li H., Karim S., Khan A.A. (2024) Unmanned aerial vehicles advances in object detection and communication security review. *Cognitive Robotics*, https://doi.org/10.1016/j.cogr.2024.07.002

3 Mesvan N. (2021) Cnn-based human detection for uavs in search and rescue. *arXiv preprint arXiv:2110.01930*. https://doi.org/10.48550/arXiv.2110.01930

4 Jiang C., Ren H., Ye X., Zhu J., Zeng H., Nan Y., . Huo H. (2022) Object detection from UAV thermal infrared images and videos using YOLO models. *International Journal of Applied Earth Observation and Geoinformation*, *112*, 102912. https://doi.org/10.1016/j.jag.2022.102912

5 Haider A., Shaukat F., Mir J. (2021) Human detection in aerial thermal imaging using a fully convolutional regression network. *Infrared Physics & Technology*, *116*, 103796. https://doi.org/10.1016/j.infrared.2021.103796

6 Murthy J. S., Siddesh G.M., Lai W.C., Parameshachari B.D., Patil S.N., Hemalatha K.L. (2022) ObjectDetect: A Real-Time Object Detection Framework for Advanced Driver Assistant Systems Using YOLOv5. *Wireless Communications and Mobile Computing*, 2022(1), 9444360. https://doi.org/10.1155/2022/9444360

7 Yeom S. (2024) Thermal image tracking for search and rescue missions with a drone. *Drones,* 8(2), 53. https://doi.org/10.3390/drones8020053

8 Rizk M., Bayad I. (2025) Bringing Intelligence to SAR Missions: A Comprehensive Dataset and Evaluation of YOLO for Human Detection in TIR Images. *IEEE Access*. https://doi.org/ 10.1109/ACCESS.2025.3529484

9 Song Z., Yan Y., Cao Y., Jin S., Qi F., Li Z., Lu G. (2025) An infrared dataset for partially occluded person detection in complex environment for search and rescue. *Scientific Data,* 12(1), 300. https://doi.org/10.1038/s41597-025-04600-0

10 Dinh H.T., Kim E.T. (2025) A Lightweight Network Based on YOLOv8 for Improving Detection Performance and the Speed of Thermal Image Processing. *Electronics*, 14(4), 783. https://doi.org/10.3390/electronics14040783

11 Abbas Y., Al Mudawi N., Alabdullah B., Sadiq T., Algarni A., Rahman H., Jalal A. (2024) Unmanned aerial vehicles for human detection and recognition using neural-network model. *Frontiers in Neurorobotics*, 18, 1443678. https://doi.org/10.3389/fnbot.2024.1443678

12 Shao Z., Cheng G., Ma J., Wang Z., Wang J., Li D. (2021) Real-time and accurate UAV pedestrian detection for social distancing monitoring in COVID-19 pandemic. *IEEE Trans. Multimed.*, 1–16. https://doi.org/ 10.1109/TMM.2021.3075566

13 Shin D.-J., Kim J.-J. (2022) A deep learning framework performance evaluation to use YOLO in nvidia jetson platform. *Appl. Sci.*, 12 (8), 3734. https://doi.org/10.3390/app12083734

14 Jiang C., Ren H., Ye X., Zhu J., Zeng H., Nan Y., Huo H. (2022) Object detection from UAV thermal infrared images and videos using YOLO models. *International Journal of Applied Earth Observation and Geoinformation*, 112, 102912. https://doi.org/10.1016/j.jag.2022.102912

15 Zeng, S., Yang W., Jiao Y., Geng L., Chen X. (2024) SCA-YOLO: A new small object detection model for UAV images. *The Visual Computer*, 40(3), 1787-1803. https://doi.org/10.1007/s00371-023-02886-y

16 Kumar S., Yadav D., Gupta H., Verma O.P., Ansari I.A., Ahn C.W. (2021) A novel YOLOv3 algorithm-based deep learning approach for waste segregation: Towards smart waste management. *Electron,* 10, 1–20. https://doi.org/10.3390/electronics10010014

17 Li Z., Namiki A., Suzuki S., Wang Q., Zhang T., Wang W. (2022) Application of low-altitude UAV remote sensing image object detection based on improved YOLOv5. *Applied Sciences*, 12(16), 8314. https://doi.org/10.3390/app12168314

18 Liu P., Wang Q., Zhang H., Mi J., Liu Y. (2023) A lightweight object detection algorithm for remote sensing images based on attention mechanism and YOLOv5s. *Remote Sensing*, 15(9), 2429. https://doi.org/10.3390/rs15092429

19 Rasheed A.F., Zarkoosh M. (2025) Optimized YOLOv8 for multi-scale object detection. *Journal of Real-Time Image Processing,* 22(1), 6. https://doi.org/10.1007/s11554-024-01582-x

20 Rasheed A.F., Zarkoosh M. (2024) YOLOv11 Optimization for Efficient Resource Utilization. arXiv preprint arXiv:2412.14790. https://doi.org/10.48550/arXiv.2412.14790

21 Khanam R., Hussain M. (2024) Yolov11: An overview of the key architectural enhancements. arXiv preprint arXiv:2410.17725. https://doi.org/10.48550/arXiv.2410.17725

22 Jegham N., Koh C.Y., Abdelatti M., Hendawi A. (2024) Evaluating the evolution of yolo (you only look once) models: A comprehensive benchmark study of yolo11 and its predecessors. arXiv preprint arXiv:2411.00201. https://doi.org/10.48550/arXiv.2411.00201

23 Ussipov N., Akhtanov S., Turlykozhayeva D., Temesheva S., Akhmetali A., Zaidyn M., Tang X. (2024) MEGA: Maximum-Entropy Genetic Algorithm for Router Nodes Placement in Wireless Mesh Networks. *Sensors*, *24*(20), 6735. https://doi.org/10.3390/s24206735

24 Ussipov N., Akhtanov S., Zhanabaev Z., Turlykozhayeva D., Karibayev B., Namazbayev T., . Tang X. (2024) Automatic modulation classification for MIMO system based on the mutual information feature extraction. *IEEE Access*. 10.1109/ACCESS.2024.3400448

25 Andrushchenko M., Selivanova K., Avrunin O., Palii D., Tymchyk S., Turlykozhayeva D. (2024) Hand movement disorders tracking by smartphone based on computer vision methods. *Informatyka, Automatyka, Pomiary W Gospodarce I Ochronie Środowiska, 14: 5–10.* http://doi.org/10.35784/iapgos.6126

26 Turlykozhayeva, D., Temesheva, S., Ussipov, N., Bolysbay, A., Akhmetali, A., Akhtanov, S., & Tang, X. (2024, October). Experimental Performance Comparison of Proactive Routing Protocols in Wireless Mesh Network Using Raspberry Pi 4. In *Telecom* (Vol. 5, No. 4, pp. 1008-1020). MDPI. https://doi.org/10.3390/telecom5040051

27 Turlykozhayeva D.A., Akhtanov S. N., Baigaliyeva A.N., Temesheva S. A., Zhexebay D. M., Zaidyn M., Skabylov A.A. (2024) Evaluating Routing Algorithms Across Different Wireless Mesh Network Topologies Using Ns-3 Simulator. *Eurasian Physical Technical Journal*, *21*(2). https://doi.org/10.31489/2024No2/70-82

28 Turlykozhayeva D.A., Akhtanov S.N., Zhanabaev Z.Z., Ussipov N.M., Akhmetali A. (2025) A routing algorithm for wireless mesh network based on information entropy theory. *IET Communications*, *19*(1), e70011. https://doi.org/10.1049/cmu2.70011

29 Turlykozhayeva D., Waldemar W., Akhmetali A., Ussipov N., Temesheva S., Akhtanov S. (2024) Single Gateway Placement in Wireless Mesh Networks. *Physical Sciences and Technology*, *11*(1-2). https://doi.org/10.26577/phst2024v11i1a5

30 Turlykozhayeva D., Akhtanov S., Zhexebay D., Ussipov N., Baigaliyeva A., Wójcik W., Boranbayeva N. (2024) Evaluating machine learning-based routing algorithms on various wireless network topologies. Photonics Applications in Astronomy, Communications, Industry, and High Energy Physics Experiments, 13400, 236-245. https://doi.org/10.1117/12.3058676

31 Ibraimov M. K., Tynymbayev S. T., Skabylov A.A., Kozhagulov Y., Zhexebay D.M. (2022) Development and design of an FPGA-based encoder for NPN. *Cogent Engineering*, *9*(1), 2008847. https://doi.org/10.1080/23311916.2021.2008847

32 Zhexebay D., Skabylov A., Ibraimov M., Khokhlov S., Agishev A., Kudaibergenova G., Agishev A. (2025) Deep Learning for Early Earthquake Detection: Application of Convolutional Neural Networks for P-Wave Detection. *Applied Sciences*, *15*(7), 3864. https://doi.org/10.3390/app15073864

33 Ussipov N., Zhanabaev Z., Almat A., Zaidyn M., Turlykozhayeva D., Akniyazova A., Namazbayev T. (2024) Classification of Gravitational Waves from Black Hole-Neutron Star Mergers with Machine Learning. *Journal of Astronomy and Space Sciences,* 41(3), 149-158. https://doi.org/10.5140/JASS.2024.41.3.149

34 Akhmetali A., Namazbayev T., Subebekova G., Zaidyn M., Akniyazova A., Ashimov Y., Ussipov N. (2024) Classification of Variable Star Light Curves with Convolutional Neural Network. *Galaxies,* 12(6), 75.

AUTHORS' INFORMATION

Turmaganbet, Ulpan - PhD student, Department of Physics and Technology, al-Farabi Kazakh National University, Almaty, Kazakhstan; ORCID iD: 0009-0002-3782-425X ; uturmaganbet@gmail.com

Zhexebaym, Dauren – PhD, Researcher, Lecturer, Department of Physics and Technology, al-Farabi Kazakh National University, Almaty,Kazakhstan, ORCID iD: 0009-0008-1884-4662 ; zhexebay.dauren@kaznu.edu.kz

Turlykozhayeva, Dana - PhD, Researcher, Lecturer, Department of Physics and Technology, al-Farabi Kazakh National University, Almaty, Kazakhstan, ORCID iD: 0000-0002-7326-9196 ; turlykozhayeva.dana@kaznu.edu,kz

Skabylov, Alisher – PhD, Researcher, Lecturer, Department of Physics and Technology, al-Farabi Kazakh National University, Almaty, Kazakhstan, ORCID iD: 0000-0002-5196-8252 ; skabylov.alisher@kaznu.edu.kz

Akhtanov, Sayat - PhD, Researcher, Senior Lecturer, Unmanned Aerial Vehicle Laboratory, Scientific Research Institute of Experimental and Theoretical Physics, Almaty, Kazakhstan, ORCID iD:0000-0002-9705-8000; akhtanov.sayat@kaznu.edu.kz

Temesheva, Symbat - PhD student, Department of Physics and Technology, al-Farabi Kazakh National University, Almaty, Kazakhstan; ORCID iD: 0009-0000-2795-9586 ; symbat.temesheva@gmail.com

Masalim, Perizat – Master student, Department of Physics and Technology, al-Farabi Kazakh National University, Almaty, Kazakhstan, masalimperizat@gmail.com

Tao, Mingliang - PhD, Researcher, Professor, School of Electronics and Information, Northwestern Polytechnical University, Xian, China, ORCID iD: 0000-0002-0329-7124 ; mltao@nwpu.edu.cn

EURASIAN PHYSICAL TECHNICAL JOURNAL

2025, Volume 22, No.2 (52)

https://doi.org/10.31489/2025N2/133-146

Received: 05/09/2024 Revised: 24/03/2025 Accepted: 11/04/2025 Published online: 30/06/2025

Original Research Article

UDC 523.44

SPECTROPHOTOMETRIC STUDIES OF ASTEROIDS I: REFLECTANCE SPECTRA

AimanovaG.K. [1*], Serebryanskiy A.V. [1], Shcherbina M.P. [2,3], Krugov M.A.[1]

[1] Fesenkov Astrophysical Institute, Almaty, Kazakhstan
[2] Institute of Astronomy of the Russian Academy of Sciences, Moscow, Russia
[3] Sternberg Astronomical Institute, Moscow State University, Moscow, Russia
*Corresponding author: gauhar@fai.kz

Abstract. *The paper presents the results of the analysis of the reflectivity spectra of asteroids based on observations obtained on 2024-02-22, 2023-11-03, 2023-11-04 and 2023-11-21 at the Assy-Turgen Observatory (77°.87114 E, 43°.225527 N, 2658 meters above sea level, international observatory code 217) using a long-slit spectrograph based on volume-phase holographic gratings (VPHG) installed at the prime focus of the AZT-20 telescope with an aperture of 1.5 meters. The observations were carried out in the low-resolution mode (R=600) in the range of 3500-7500Å using a grating of 360 lines per mm, a dispersion of 4.25Å per pixel, in the first binning in the EMCCD mode with a gain of 5 and an exposure time of 10 seconds, the slit width of 9 arc seconds. The spectrum of asteroids was measured using the differential method: by comparing the fluxes from the object and a standard star. Solar analog stars (G-class stars) were used as standards. Processing and calculation of reflectance spectra, alongside the determination of taxonomic classification according to the Tholen and SMASSII systems, based on spectral morphology and selected spectral characteristics, were conducted for a sample of 19 asteroids, primarily consisting of Main Belt members (14). A comparison was made with the spectra of asteroids based on INASAN observations in 2013–2017 and the reflectivity spectra of asteroids obtained from Gaia (DR 3) observations, and their taxonomic types were determined without taking into account the albedo of the asteroids.*

Keywords: spectrophotometry, asteroids; reflectance spectra; Gaia DR3

1. Introduction

Asteroids are the least altered relics of the primordial matter of the Solar System. The study of the physical and chemical composition of these bodies is necessary for solving cosmogonic problems: analysis of the type of minerals that make up the surface of asteroids allows us to assess the plausibility of various models of the formation of the Solar System. In addition, asteroids are considered as possible sources of extraterrestrial natural resources (Board S. S. et al., 2010) [1].

The presence of fragmented material on the surface of asteroids allows us to determine their shape, structure, particle parameters, and also makes it possible to study their chemical and mineral composition. Traditional methods of studying these bodies are photometry, spectrophotometry, and polarimetry, which are independent and complement each other. Photometry and polarimetry are most effective in studying the physical parameters of solid celestial bodies, while spectrophotometry allows us to carry out a qualitative, and sometimes quantitative, assessment of the composition of the substance of these bodies. Spectrophotometry allows us to obtain a reflectivity spectrum of the entire visible hemisphere of a sufficiently distant celestial body, observed as a point-source object.

.

The spectral range of optical transparency of the Earth's atmosphere is approximately between 350 and 1000 nm. In this range, the asteroid only reflects solar radiation, so such a characteristic as "reflection spectrum" is used, which is the measured spectrum of the object divided by the average spectrum of the Sun. Spectral and geochemical studies of meteorites, which are most likely fragments of asteroids, show that the features of the reflection spectra in the range of ~200–2500 nm characterize their chemistry and mineralogy. That is, the asteroid's reflection spectrum (normalized to flux at wavelength of 550 nm) mainly characterizes the composition of the asteroid's matter. Bodies are categorized into several classes based upon the predominant substances within their composition.

2. Characteristics for the classification of the asteroids under study

C-type asteroids are important objects for studying the evolution of the Solar System and potential targets for future resource mining missions. Their composition allows us to study the early stages of planet formation and the possible presence of water. Research by Binzel (2019) [2] highlights the key role of these asteroids in understanding the evolution of the Solar System due to their pristine chemical composition. DeMeo and Carry (2014) [3] note the importance of spectral analysis for understanding the distribution of carbonaceous materials in the asteroid belt, showing that such asteroids may contain significant reserves of water in the form of hydrated minerals. Clark et al. (2002) [4] investigated the space weathering processes affecting the spectral properties of these objects and found that long-term exposure to the solar wind and micrometeoroid bombardment alters their surface properties, reducing reflectivity and changing spectral lines. Examples of this asteroid class include 51 Nemausa, 70 Panopaea, 107 Camilla, 144 Vibilia, 163 Erigone, 345 Tercidina, and 481 Emita.

M-class asteroids have been studied rather poorly and are classified as a separate class because their spectra in the 0.3-2.5 μm range do not have noticeable absorption bands, and their reflectivity increases with wavelength similar to the spectra of iron meteorites and enstatite chondrites with a high content of free metal (Lupishko et al., 2000) [5]. According to Tholen's spectral classification the (97) Klotho and (55) Pandora belongs to the metal-rich M-class asteroids, but radar observations do not confirm a notable content of iron-nickel composites in the composition of its surface (Shepard et al., 2005) [6]. It should be noted that asteroids of this type can vary significantly in their composition, ranging from metal-rich to metal-poor, and include various groups of minerals. In particular, Hardersen et al. (2011) [7] found diagnostic absorption bands of pyroxenes, olivines, phyllosilicates and hydroxides in the near infrared (NIR: ca. 0.75–2.50 μm) spectrum of 60% of Tholen class M/X asteroids. These data highlight the spectral and mineralogical diversity in the M-class asteroid population. Possible meteoritic analogues include mesosiderites, CB/CH chondrites and silicate-containing nickel-iron meteorites. Asteroids lacking characteristic spectral signatures are related to meteoritic analogues such as nickel-iron meteorites, enstatite chondrites and stony-iron meteorites.

S-type asteroids are silicate asteroids, which make up about 17% of all discovered asteroids. The concentration of celestial bodies in this class decreases with distance from the Sun. Asteroids of this class are moderately bright, with a slightly reddish color. Spectrophotometry indicates olivine, pyroxenes, and Fe-Ni metal (Lupishko et al., 2000) [5] as the main components of the S-type asteroids. Given that the majority of S-type asteroids exhibit an olivine-metal composition with a comparatively limited amount of pyroxene, it is postulated that contemporary S-type asteroids, such as (482) Petrina, are remnants of larger S-type asteroids that underwent fragmentation. These ancestral asteroids are theorized to have originated in the proximity of the core-mantle boundary within their respective parent bodies.

P-type asteroids are objects with a fairly low albedo of 0.02 to 0.07 and a flat reddish spectrum without noticeable absorption lines. Such properties are characteristic of carbon- or organic-enriched matter silicates that have not undergone significant changes since their formation (De Pater, Imke et al., 2001) [8], (Ehrenfreund et al., 2004) [9]. They are, for example, part of interplanetary dust, which probably filled the near-solar protoplanetary disk even before the formation of the planets. Based on this similarity, it can be assumed that P-asteroids are the most ancient, little-changed bodies in the Main Belt (McSween Jr. and Harry Y., 1999) [10]. Such asteroids may be rich in carbon and silicates, possibly mixed with water ice. According to the Malkhe classification, this class of asteroids includes (65) Cybele, (447) Valentine and (160) Una.

B-type asteroids are a relatively rare class of asteroids that belong to the carbonaceous asteroids and are predominantly found in the outer part of the Main Belt. They are generally similar to C-type asteroids, but are distinguished by an almost complete absence of absorption at wavelengths below 0.5 μm and have a slightly bluish color. Spectroscopic studies have suggested that the main components of the surface are anhydrous silicates, hydrated clay minerals, organic polymers, magnesites, and sulfides. Most asteroids that have signs of cometary activity belong to this class, for example, according to the SMASSII classification, asteroids (88) Thisbe and (47) Aglaja belong to this class.

X-type asteroids are a class of asteroids that cannot be classified into any of the other classes. Typically, such objects are assigned to M, E, or P classes after albedo analysis.

3. Statement of the research objective

It is known that the reflectivity spectra of asteroids observed with different detectors and at different epochs often show significant differences, mainly in the slope of the spectrum from blue to red wavelengths.

Reflectivity spectra of asteroids observed with different detectors and at various periods of time often show significant differences. This issue is the subject of an extensive analysis of the diversity of reflectivity spectra obtained at different epochs for moderately large and bright Main Belt asteroids. Mostly, such differences concern the slope of the spectrum from “blue” to “red” wavelengths. Sometimes such differences are considered to be a consequence of surface inhomogeneity, but this interpretation is often speculative.

The differences in the reflectivity spectra obtained may be related to the spectral variability of the asteroids and their heterogeneous composition, and to the fact that the comparison spectrum is not the spectrum of an ideal solar analogue. Research conducted over decades shows that there are essentially three physical processes that play a major role in the evolution of the asteroid population and affect the change in the reflectivity spectrum. The first is collisional evolution, which gradually affects the size distribution of Main Belt asteroids and their surfaces. When objects collide, the outer layers of the surfaces can be destroyed and fragmented, the inner layers of the asteroid can be exposed, changing the visible chemical composition of its surface. In addition, collisions can lead to an exchange of matter between the asteroid and the object it collided with. If the impactor and target asteroid initially belonged to different spectral classes and had different mineralogical compositions, then their collision leads to a mixing of materials. This makes it difficult to determine their spectral class, since the surface begins to show signs of different minerals characteristic of both parent bodies. The second is space weathering, which occurs due to cosmic rays, solar wind and collisions with micrometeoroids on the asteroid surface. Over decades, space weathering gradually changes the reflectance spectra of asteroids. The surface of the asteroid darkens and becomes reddish. This change is associated with processes that change the spectral characteristics of the surface, such as the formation of thin metallic films and a change in the size of regolith particles. The most important effects were found for the class of asteroids belonging to the S-class. This class includes objects considered to be the parent bodies of the most common class of meteorites - ordinary chondrites. The third is that a simple cycle of thermal expansion and contraction of the material constituting the outer layer of the surface regolith, due to the rotation of the asteroid, leads to a progressive evolution of the structural and thermal properties of the regolith.

Observations and analyses of reflectance spectra are essential for elucidating the principal physical mechanisms governing asteroid evolution and spectral alterations. Notably, there has been an increasing discovery of asteroids exhibiting sublimation-dust and dust activity triggered by diverse physical factors in recent years. This paper presents the findings of spectrophotometric observations conducted on several Main Belt primitive asteroids, aimed at detecting potential indications of sublimation-dust activity induced by elevated subsolar temperatures and solar eruptive events. This endeavor necessitates a comparative analysis of reflectance spectra derived from various sources and observational epochs. As an illustration, Busarev et al. (2019) posit that spectral signatures of sublimation activity are discernible in (51) Nemausa and (65) Cybele.

.

In the present study, one of the primary objectives is the selection of the most optimal stars—solar analogues—for accurate computation of asteroid reflectance spectra. The most common methodology for obtaining normalized asteroid reflectance spectra involves using a single solar analogue for each observed object, which is observed on the same night as the target. In contrast, this work employs a method of averaging the spectra of several top-quality solar analogues (described in detail in Section 3), which enhances the accuracy and reliability of the resulting spectra and prevents loss of observational data due to a poor choice of solar analogue. By comparing these results with data from other observatories, one can objectively assess the applicability and advantages of this approach based on the quality of the reflectance spectra.

4. Observations

To analyze the reflectivity spectra of individual Main Belt asteroids, data were obtained from three sources: observations conducted at different times at the Fesenkov Astrophysical Institute (FAI), the Institute of Astronomy of the Russian Academy of Sciences (INASAN), and the Gaia DR3 Mission of the European Space Agency (ESA).

The observations FAI were carried out in 2023 at the Assy-Turgen Observatory using a long-slit spectrograph based on volume-phase holographic gratings (VPHG) installed at the prime focus of the AZT-20 telescope with an aperture of 1.5 meters and a relative focal length of 5.72 meters (f=1:3.8). The focal lengths of the collimator and the spectrograph camera are 130 mm and 85 mm, respectively. The spectrograph is equipped with an iXon Ultra 888 EMCCD with a size of 1024 × 1024 pixels, and the pixel size is 13 microns, which gives an image scale of 0″.717 per pixel.

The observations were carried out in the low-resolution mode (R=600) using a grating of 360 lines per mm, a dispersion of 4.25 Å per pixel, in the first binning in the EMCCD mode with a gain of 5 and an exposure time of 10 seconds, the slit width of 9 arc seconds. To calibrate the wavelengths, the spectra of a standard source - a He-Ne-Ar lamp - were taken. The spectrum of the asteroids was obtained using the differential method - by comparing the fluxes from the object and a standard star. Solar analogues stars (class G stars) were used as standards.

Table 1 presents the designation of asteroid, date and time of observation, exposure time and air mass. Data format: 1 - Date and time in YYMMDD, 2 - Universal Time in hhmmss, 3 and 4 - right ascension and declination at the time of observation in the J2000, 5 - distance from the observer to the object (in AU), 6 - distance from the Sun to the object (in AU), 7 - solar elongation (in °), 8 - phase angle of the object (in °), 9 - predicted stellar magnitude, 10 - air mass, 11 - exposure time. Columns 3-9 are given according to the Minor Planet Center at the time of observations. The last row of the table contains information on the EMCCD mode used during observations.

INASAN reflectivity spectra were obtained at the Peak Terskol observatory (3150 meters above sea level) using a 2-meter telescope manufactured by Carl Zeiss Jena GmbH, with a prism CCD spectrometer (WI CCD 1240×1150). Low-resolution spectra (R≈100) were used in INASAN observations, which nevertheless allowed determining the spectral classes of asteroids and identifying large features of the reflectivity spectra (wide absorption bands). Data processing was performed using DECH software (DECH20T and DECH95 packages).

The GAIA mission of the European Space Agency has been regularly observing Solar System objects since the beginning of its operations in August 2014. The third Gaia data release (DR3) includes for the first time the mean reflectance spectra of a selected sample of 60,518 such objects, mostly asteroids, observed between 5 August 2014 and 28 May 2017. Each reflectance spectrum was obtained from measurements taken with the “blue” and “red” photometers operating in the wavelength ranges 330–680 nm and 640–1050 nm, respectively (Gaia Collaboration: L. Galluccio et al., 2023) [12]. The Gaia DR3 database presents the mean reflectance spectrum for each asteroid, calculated for 16 points representing integrated reflectivity.

5. Research methodology

The main research method is the meticulously carried out observations and analysis of the spectra of solar radiation reflected by the object and the spectra of solar-type stars. Data processing was performed using standard procedures, using the Image Reduction and Analysis Facility (IRAF) package. The spectra of asteroids and the standard source were processed using an identical technique, taking into account the effect of air mass changes during observations.

Observational and instrumental difficulties in observing asteroids in the range below 5000Å make this wavelength range poorly studied compared to the visible and near infrared range. In particular, the choice of the solar analog star used to obtain the asteroid reflectivity spectrum is a major challenge (Noem et al., 2016) [13], (Cellino et al., 2020) [14], (de León et al., 2010) [15].

Not all solar analogues present in catalogues are truly identical to the Sun. This effect is particularly important in the blue part of the spectrum, where solar analogues often show significant differences with respect to each other and to the solar spectrum (Raḿırez et al., 2012) [16]. Furthermore, the suitability of many used solar analogues is usually assessed only in the visible wavelength range, while some of these objects show spectra that are quite different from the Sun's spectrum at wavelengths below 5500Å. The stars HD 28099 (Hyades 64) and HD 186427 (16 Cyg B) are well-studied solar analogues that have spectra very similar to the Sun's spectrum in the wavelength range between 3600Å and 5500Å.

In Tinaut-Ruano et al. (2023) [17], the authors assessed the suitability of the solar analogues selected for the near-ultraviolet reflectivity study of asteroids included in the Gaia DR3 release. They found that the solar analogues selected for Gaia DR3 to calculate the asteroid reflectivity spectra have a systematically redder spectral tilt at wavelengths shorter than 5500Å than Hyades 64.

For the analysis of asteroid reflectivity spectra, it is important to select comparison stars whose spectral type is as close as possible to the Sun's. Additional criteria are availability of the star for observations on a given night, as well as its sufficient brightness to obtain a spectrum with a high signal-to-noise ratio. To minimize possible errors when using the spectra of Sun-like stars to obtain reflectivity spectra, the spectra of several best (in terms of the quality of the obtained spectra and proximity to the Sun’s spectral type) Sun-like stars observed on the night of observations were averaged, as was done by Farnham et al. (2000) [18] and Tedesco et al. (1982) [19]. Four stars were selected from a total of 12 observed stars. An analysis was performed of the extinction-corrected and 0.55 μm flux-normalized spectra of all standard spectra observed on that night. Figure 1 shows the normalized spectra of the standard stars selected for analysis - HD 34411 (G1.5IV), HD 13043 (G2V), HD 219018 (G5V). Then, the average spectrum of the best solar-like stars for the given night was compiled, which is shown in the figure as the “average spectrum”.

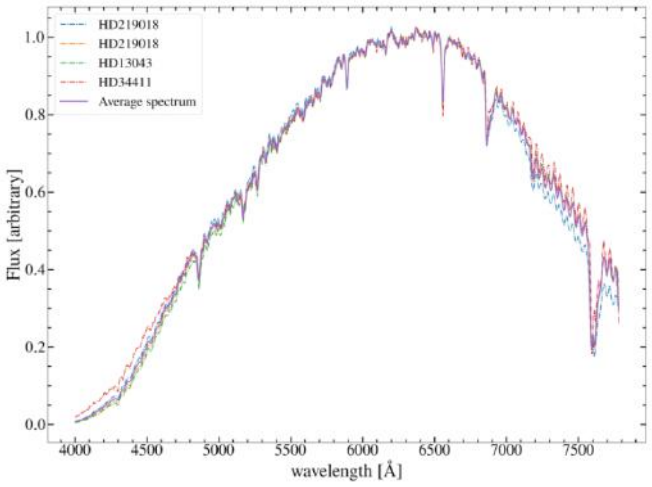

Fig.1. - Normalized spectra of standard stars - HD 34411 (G1.5IV), HD 13043 (G2V), HD 219018 (G5V)

.

The resulting reflectivity spectra of asteroids were obtained by dividing the asteroid spectrum by the spectrum of a standard star, in our case by the same averaged spectrum of several standard stars. This procedure introduces additional noise into the final result due to the presence of noise in the spectra of solar analog stars.

Our experience with satellite reflectance spectra has shown that the Butterworth filter (Serebryanskiy et al., (2022)) [20] is effective for smoothing the reflectance spectra. The Butterworth filter is implemented in the *scipy* package (Virtanen et al., 2020) [21] using the *signal.butter* method, which uses the order of the filter and cutoff frequency in Nyquist frequency units as parameters. In our case, the filter's order is chosen to be 3, and the cutoff frequency is 0.086, which corresponds to smoothing the spectrum in a window of 50Å wide with a spectral resolution of about 4Å. Testing with different cutoff frequency values showed that this is the optimal value and the smoothing result, when choosing this parameter in a reasonable range, does not change the final conclusions. The smoothing process itself is carried out by the *signal.fultfilt* method of the *scipy* package. Measurement errors in the reflection spectra were determined through averaging multiple spectra to account for fluctuations in observational conditions, rather than solely relying on the formal errors of the spectra or the signal-to-noise ratio. The final error, incorporating the smoothing procedure, is within 10% of the reflection value. Notably, a substantial increase in error below a 4000Å wavelength range imposes limitations on the analyzed spectral range.

6. Results and discussion

A comparative analysis of the reflectance spectra obtained at FAI in 2023 was carried out with the spectra obtained at INASAN in 2013-2017 and with the reflectance spectra from the GAIA DR3 database. Figure 2 shows the reflectivity spectra of asteroids (51) Nemausa, (70) Panopaea, (107) Camilla, 144 Vibilia, 163 Erigone, 345 Tercidina, 481 Emita, which according to the classification of Tholen D.J. (1989) [22] belong to class C, as well as asteroids (366) Vincentina, (381) Myrrha, (407) Arachne, which belong to subclass Ch (SMASSII classification). The results obtained align broadly with those from independent sources. Reflectance spectra of (51) Nemausa, (366) Vincentina, (407) Arachne, (481) Emita, and (107) Camilla demonstrate qualitative correspondence to the INASAN spectra, exhibiting a variation in the gradient within the blue region, and deviate from the GAIA spectra. The observed spectral discrepancy in the 0.4-0.6 nm range may indicate a subtle manifestation of sublimation activity.

Figure 3 shows the reflectivity spectra of the asteroids (97) Klotho and (55) Pandora, according to the classification of Tholen. Whilst for the asteroid (97) Klotho we obtained a fairly good agreement with the INASAN and GAIA DR3 data during the comparative analysis, the spectrum of (55) Pandora does not agree with either the INASAN or GAIA data. At the same time, the INASAN and GAIA DR3 data agree well in the spectral region of 5000-9500Å. According to the spectral classification of Tholen, the asteroid (55) Pandora belongs to class M, but according to the SMASS classification it belongs to class X. Rather, it corresponds to the spectral classification of SMASS (class X), showing stronger absorption in the region below 0.5 μm.

Asteroid (482) Petrina (Fig.4) belongs to the Tholen class S and has growth in the long-wavelength region and, according to Shcherbina et al. (2019) [23], corresponds to high-temperature mineralogy. According to FAI data, the reflectivity spectrum also increases in the long-wavelength region and is closer to the GAIA DR3 data. This asteroid has a high albedo (0.24), which indirectly confirms its belonging to the S class.

Fig.5 shows the reflectivity spectra of class P asteroids - (65) Cybele, (447) Valentine and (160) Una. The reflectivity spectrum of the asteroid (65) Cybele shows agreement with the GAIA DR3 spectrum obtained for this class and has discrepancies with the spectrum obtained by INASAN in 2017 (Fig.5). However, the peculiarity of the reflectivity spectrum obtained at the Peak Terskol observatory, namely the maximum reflectivity in a fairly wide range of 0.4 to 0.7 μm, changing in intensity in the range of 0.4 to 0.5 μm, was explained in Busarev et al. (2019) [11] by the presence of weak sublimation activity of the asteroid. The sharp change in the shape of the reflectivity spectrum in the short-wave region according to FAI data for (160) Una and the slight increase in the reflectivity spectrum according to INASAN data remain questionable and require additional observations of this asteroid.

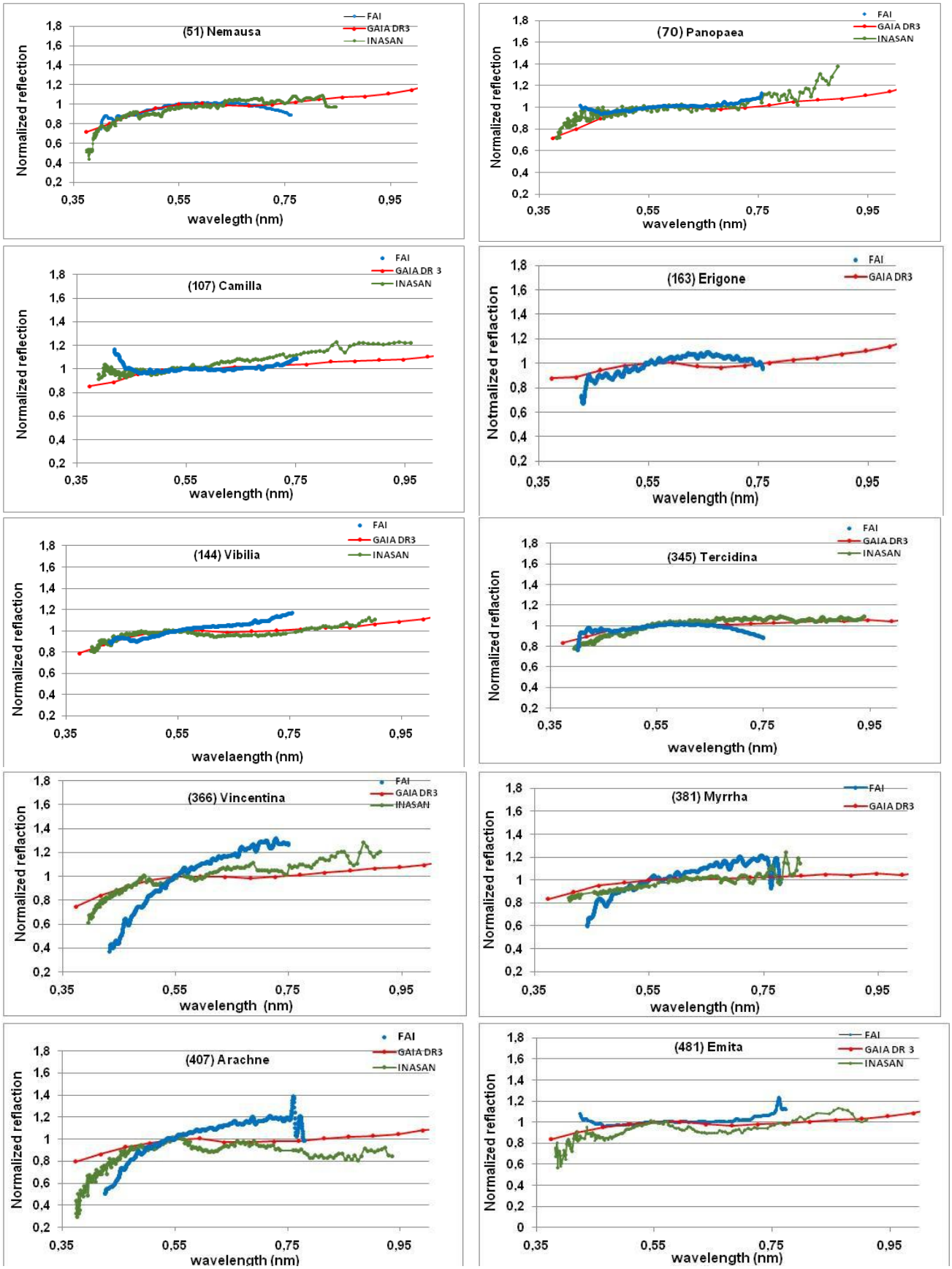

Fig.2. Reflectivity spectra of class C and subclass Ch asteroids

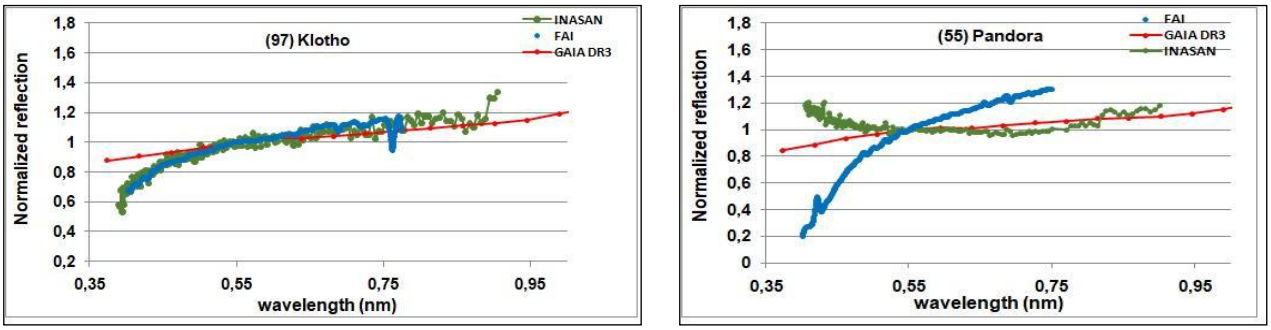

Fig. 3. Reflectivity spectra of asteroids (97) Klotho and (55) Pandora of class M

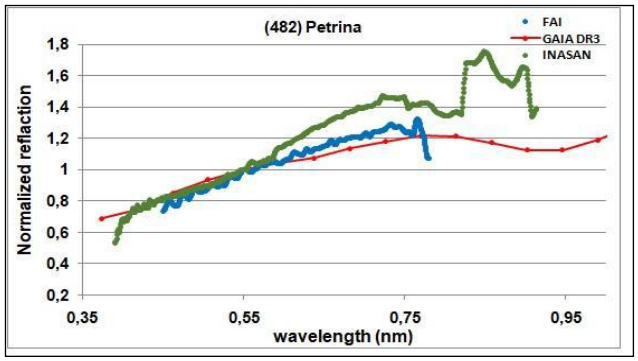

Fig.4. Reflectivity spectrum of the S-type asteroid (482) Petrina

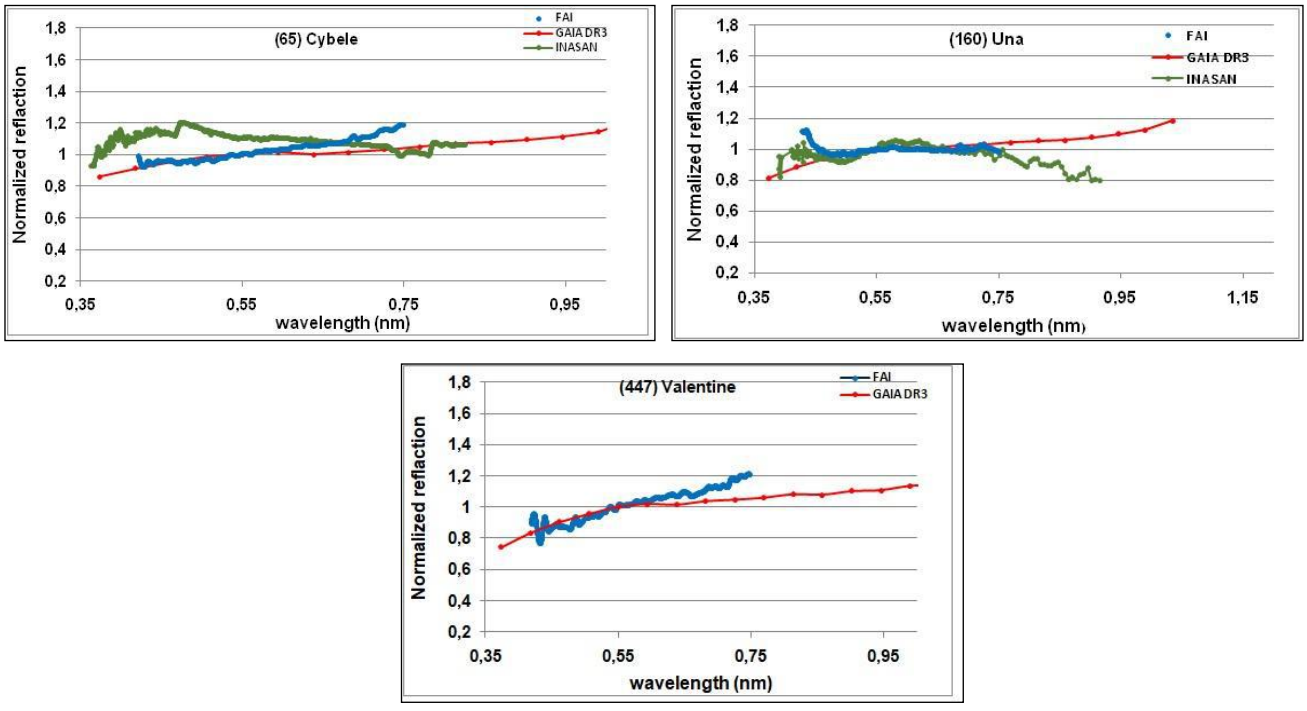

Fig.5. Reflectivity spectra of asteroids (65) Cybele, (447) Valentine and (160) Una

Fig.6 shows the reflectivity spectra of asteroids (88) Thisbe и (47) Aglaja. (88) Thisbe is a Main Belt asteroid of SMASSII class B, Tholen class CF, and Malkhe class C, indicating that it likely contains hydrogen, nitrogen, ammonia, and iron. (47) Aglaja is Tholen class C and has a

carbonaceous composition. The SMASSII classification system rates it as a rare B-class asteroid associated with the presence of magnetite, which gives the asteroid a blue color. The reflectivity spectrum of asteroid (47) Aglaja shows good agreement with the GAIA DR3 spectrum and the spectrum obtained by INASAN in 2017. The reflectivity spectrum of asteroid (88) Thisbe has discrepancies with the spectrum obtained by INASAN in 2017 and the spectrum of the GAIA DR3 database. We suspect the presence of sublimation activity. To clarify the observed variations in the short wavelength region of asteroid (88) Thisbe's reflectance spectrum, additional observations at different heliocentric distances, including around perihelion, are required. The spectral classification derived from our measurements is consistent with that reported by previous studies. Consequently, asteroid (88) Thisbe should be considered a promising candidate for activity and included in future observation programs.

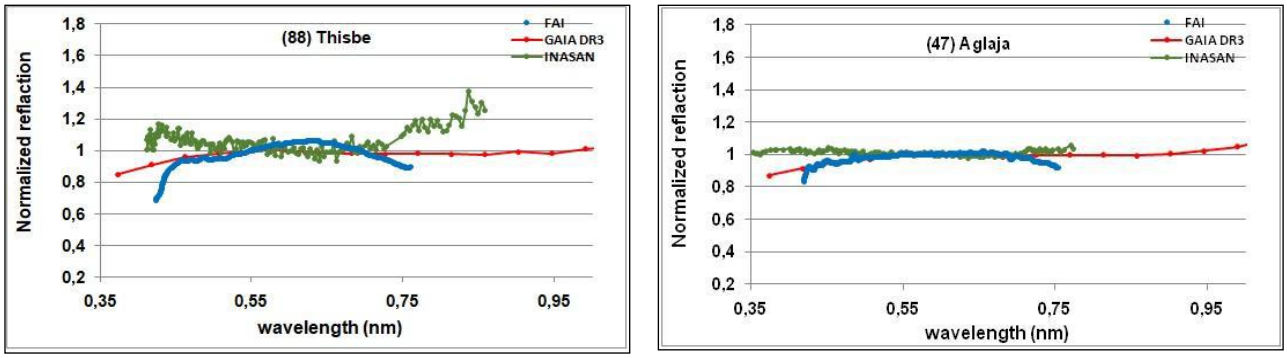

Fig.6. Reflectivity spectra of asteroids (88) Thisbe and (47) Aglaja

Fig.7 shows the reflectivity spectra of (718) Erida, which, according to SMASSII, belongs to class X, i.e. to asteroids that remain poorly classified. A more precise determination of the asteroid class requires additional albedo analysis and comparison with classes C, S and M.

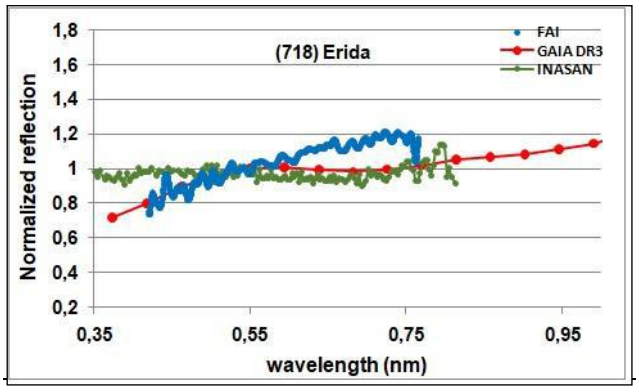

Fig.7. Reflectivity spectra of asteroids (718)

7. Conclusions

Spectral processing and reflectance spectra calculations were performed for 19 Main Belt asteroids, followed by taxonomic classification according to Tholen and SMASSII based on spectral morphology and characteristic features. Reflectance spectra were derived from data collected at the Fesenkov Astrophysical Institute (FAI), the Institute of Astronomy of the Russian Academy of Sciences (INASAN), and the Gaia DR3 Mission of the European Space Agency (ESA). To mitigate potential inaccuracies in reflectance spectra resulting from the use of solar-analog stars, multiple high-quality solar-analog star spectra, closely matching

.

the Sun's spectral class and obtained during the observation period, were averaged. Furthermore, to minimize noise in the reflectance spectra, multiple spectra were averaged to account for observational variations.

This approach delivers high-quality reflectance spectra comparable to those obtained using a single standard star analogue. Moreover, it minimizes the risk of unwanted spectral distortions—spurious features in the asteroid's reflectance spectrum caused by employing an improperly matched solar analogue that significantly differs from the Sun.

The study's findings indicate that the reflection spectra of asteroids (51) Nemausa, (366) Vincentina, (407) Arachne, (481) Emita, and (107) Camilla exhibit qualitative correspondence with the INASAN spectra. This correspondence is characterized by a variation in gradient within the blue spectral region, and these spectra are notably divergent from the GAIA spectra. It is posited that the spectral disparity observed within the 0.4-0.6 nm range may signify a subtle expression of sublimation activity.

The discrepancy observed between the FAI and INASAN data regarding the reflectivity spectrum of asteroid (160) Una, specifically the sharp alteration in the short-wave region and the marginal increase, respectively, warrants further investigation and additional observational data for confirmation.

The reflectivity spectrum of asteroid (718) Erida, which belongs to the SMASSII class X and was obtained by FAI, does not permit the precise classification of the asteroid. Furthermore, evidence confirms the potential sublimation activity of asteroids (51) Nemausa and (65) Cybele.

To ascertain the taxonomic classification of individual asteroids from spectra acquired by FAI, supplementary investigations will be conducted employing the "template" methodology delineated in the study by Savelov et al. (2022) [24], alongside the utilization of visual albedo, a parameter indicative of the chemical and mineralogical attributes of the asteroids' surface material.

Conflict of interest statement.
The authors declare that they have no conflict of interest in relation to this research, whether financial, personal, authorship or otherwise, that could affect the research and its results presented in this paper

CRediTauthor statement
Aimanova G.K. and Serebryanskiy A.V.: Conceptualization, Methodology, Investigation, Data Curation, Writing Original Draft; Shcherbina M.P.: Methodology, Resources, Validation; Krugov M.A.: Investigation, Resources.
The final manuscript was read and approved by all authors.

Funding

This research has been funded by Program No. BR20381077 of the Aerospace Committee of the Ministry of Digital Development, Innovations and Aerospace Industry of the Republic of Kazakhstan.

The observations at the "Peak Terskol" Observatory were conducted as part of the state assignment of the Institute of Astronomy of the Russian Academy of Sciences, code FFWN-2024-0010, approved by the Ministry of Education and Science of Russia, using the Large-Scale Research Facility "Zeiss-2000 Telescope" of the Core Shared Research Facilities "Terskol Observatory" of INASAN.

Acknowledgements

We thank the FAI observers for their efficient work.

References

1 Board S.S. (2010) Defending Planet Earth: Near-Earth Object Surveys and Hazard Mitigation Strategies. National Academies Press, 152. https://doi.org/10.17226/12842

2 Binzel R.P. (2019) Small bodies looming large in planetary science. *Nature Astronomy*, 3(4), 282-283. https://doi.org/10.1038/s41550-019-0747-6

3 DeMeo F.E., Carry B. (2014) Solar System evolution from compositional mapping of the asteroid belt. *Nature, 505,* 629-634. https://doi.org/10.48550/arXiv.1408.2787

4 Clark B.E., Hapke B., Pieters C., Britt D. (2002) Asteroid Space Weathering and Regolith Evolution. *Asteroids III*, 585-599. Available at: https://www.researchgate.net/publication/253857329_Asteroid_Space_Weathering_and_Regolith_Evolution

5 Lupishko D., Karazin V.N. (2000) Physical properties of asteroids. *Astronomical School's Repor., 1(2).* 63-77. https://doi.org/10.18372/2411-6602.01.2063

6 Shepard M.K. (2005) A Long-Term Radar Survey of M-Class Asteroids. *Bulletin of the American Astronomical Society, 37.* 628. Available at: https://ui.adsabs.harvard.edu/abs/2005DPS....37.0707S/abstract

7 Hardersen P.S., Cloutis E.A., Reddy V., Mothe-Diniz T., Emery J.P. (2011). The M-/X-asteroid menagerie: Results of an NIR spectral survey of 45 main-belt asteroids. *Meteoritics & Planetary Science, 46(12)*. 1910-1938. https://doi.org/10.1111/j.1945-5100.2011.01304.x

8 De Pater, Imke; Lissauer, Jack Jonathan (2001). Planetary sciences. Cambridge University Press. 528. Available at: https://books.google.kz/books?id=RaJdy3_VINQC&printsec=frontcover&hl=ru&source=gbs_ge_summary_r&cad=0#v=onepage&q&f=false

9 Ehrenfreund P., Irvine W.M., Owen T., Becker L., Jen Blank, Brucato J.R., Colangeli L., Derenne S., Dutrey A., Despois D., Lazcano A., Robert F. (2004). *Astrobiology: Future Perspectives.* Springer Science & Business. 159. Available at: https://www.amazon.ae/Astrobiology-Future-Perspectives-P-Ehrenfreund/dp/1402023049

10 McSween Jr, Harry Y. (1999). *Meteorites and their Parent Planets*. Cambridge University Press. 324. Available at: https://www.amazon.com/Meteorites-Parent-Planets-Harry-McSween/dp/0521587514

11 Busarev V.V., Shcherbina M.P., Barabanov S.I., Irsmambetova T.R., Kokhirova G.I., Khamroev U.Kh., Khamitov I.M., Bikmaev I.F., Gumerov R.I., Irtuganov E.N. & Mel'nikov S.S. (2019) Confirmation of the Sublimation Activity of the Primitive Main-Belt Asteroids 779 Nina, 704 Interamnia, and 145 Adeona, as well as its Probable Spectral Signs on 51 Nemausa and 65 Cybele. *Solar System Research*, 53. 261-277. https://doi.org/10.1134/S0038094619040014

12 Gaia Collaboration: L. Galluccio, et al. (2023) Gaia Data Release 3: Reflectance spectra of Solar System small bodies. *A&A*, 674 (A35), 29. https://doi.org/10.1051/0004-6361/202243791]

13 Pinilla-Alonso, Noem, de Le´on, J., Walsh, K. J., Campins, H., Lorenzi, V., Delbo, M., DeMeo, F., Licandro, J., Landsman, Z., Lucas, M. P., Al´ı-Lagoa, V., Burt, B. (2016) Portrait of the Polana-Eulalia Family Complex: Surface homogeneity revealed from Near-Infrared Spectroscopy. *Icarus, 274:231-248.* https://doi.org/10.1016/j.icarus.2016.03.022

14 Cellino A., Ph. Bendjoya, M. Delbo, L. Galluccio, J. Gayon-Markt, P. Tanga, and E. F. Tedesco (2020) Ground-based visible spectroscopy of asteroids to support the development of an unsupervised Gaia asteroid taxonomy. *A&A,* 642. A80. https://doi.org/10.1051/0004-6361/202038246

15 de León, J. Licandro, M. Serra-Ricart, N. Pinilla-Alonso, H. Campins (2010) Observations, compositional, and physical characterization of near-Earth and Mars-crosser asteroids from a spectroscopic survey. *A&A,* 517. A23. https://doi.org/10.1051/0004-6361/200913852

16 Ramırez I, R. Michel, R. Sefako, M. Tucci Maia, W. J. Schuster, F. van Wyk, J. Melendez, L. Casagrande, and B. V. Castilho (2012). The UBV(RI) Colors of the Sun. *The Astrophysical Journal, 752, 5, 13.* https://doi.org/10.1088/0004-637X/752/1/5

17 Tedesco E.F., Tholen D.J., Zellner B. (1982) The eight-color asteroid survey - Standard stars. *AJ,* 87(11). 1585-1592. Available at: https://adsabs.harvard.edu/full/1982AJ.....87.1585T

18 Farnham T. L., Schleicher D. G., A'Hearn M. F. (2000) The HB Narrowband Comet Filters: Standard Stars and Calibrations. *Icarus, 147(1),* 180-204. https://doi.org/10.1006/icar.2000.6420

19 Tinaut-Ruano F., E. Tatsumi, P. Tanga, J. de León, M. Delbo, F. De Angeli, D. Morate , J. Licandro, and L. Galluccio (2023). Asteroids' reflectance from Gaia DR3: Artificial reddening at near-UV wavelengths. *A&A*, 669, L14. https://doi.org/10.1051/0004-6361/202245134]

20 Serebryanskiy A.V., Omarov Ch.T., Aimanova G.K., Krugov M.A., Akniyazov Ch.B. (2022). Spectral Observations of Geostationary Satellites. *Eurasian Physical Technical Journal, 19(2).* 93-100. https://doi.org/10.31489/2022No2/93-100

21 Virtanen P., Ralf Gommers, Travis E. Oliphant, Matt Haberland, Tyler Reddy, David Cournapeau, Evgeni Burovski, Pearu Peterson, Warren Weckesser, Jonathan Bright, Stéfan J. van der Walt, Matthew Brett, Joshua Wilson, K. Jarrod Millman, Nikolay Mayorov, etc., and SciPy 1.0 Contributors. (2020) SciPy 1.0: Fundamental Algorithms for Scientific Computing in Python. *Nature Methods, 17(3),* 261-272. https://doi.org/10.1038/s41592-019-0686-2

22 Tholen D.J. Asteroid taxonomic classifications. (1989) IN: Asteroids II; Proceedings of the Conference, Tucson, AZ, Mar. 8-11, 1988 (A90-27001 10-91). Tucson, AZ, University of Arizona Press, 1139-1150. Available at: https://ui.adsabs.harvard.edu/abs/1989aste.conf.1139T/abstract

23 Shcherbina M.P., Busarev V.V., Barabanov S.I. (2019) Spectrophotometric Studies of Near-Earth and Main-Belt Asteroids. *Moscow University Physics Bulletin, 74(6).* 675–678. Available at: https://link.springer.com/article/10.3103/ S0027134919060237

.

24 Savelova A.A., Busarev, V.V., Shcherbina, M.P., Barabanov, S.I. (2022) Using "templates" of spectral types of asteroids to enhance the mineralogy of these bodies and detect the signs of sublimation-pyretic and solar activity. *INASAN Science Reports*, 7, 143-148. http://dx.doi.org/10.51194/INASAN.2022.7.2.008 [in Russian]

AUTHORS' INFORMATION

Serebryanskiy, Alexander Vladimirovich — PhD, Head of Observational Astrophysics Department, Fesenkov Astrophysical Institute, Almaty, Kazakhstan; https://orcid.org/0000-0002-4313-7416; serebryanskiy@fai.kz

Aimanova, Gauhar Kopbaevna — Candidate of Physical and Mathematical Sciences, Chief Researcher, Fesenkov Astrophysical Institute, Almaty, Kazakhstan; https://orcid.org/0000-0002-3869-8913; gauhar@fai.kz

Shcherbina, Marina P. — Candidate of Physical and Mathematical Sciences, Researcher, Institute of Astronomy of the Russian Academy of Sciences; Sternberg Astronomical Institute, Moscow State University, Moscow, Russia; Scopus Author ID: 57210443798 57; https://orcid.org/0000-0002-8455-2034; mpshcherbina@inasan.ru

Krugov, Maxim A. — Master, Engineer, Fesenkov Astrophysical Institute, Almaty, Kazakhstan; https://orcid.org/0000-0002-2788-2176; krugov@fai.kz

Appendix

Table1. Logs of observations

Date (y m d)	UT (h m s)	R.A. (h m s)	Decl. (° ‘ “)	Delta (AU)	R (AU)	Elong (°)	Ph (°)	$V^{(m)}$	Airmass	Exp Time (s)
1	2	3	4	5	6	7	8	9	10	11
47 Aglaja										
2023 11 03	151112	22 03 42.0	-13 22 29	2.067	2.549	107.7	21.8	12.9	1.907	120
2023 11 03	151316	22 03 42.0	-13 22 28	2.067	2.549	107.7	21.8	12.9	1.903	120
51 Nemausa										
2023 11 03	161256	22 54 59.7	-08 20 26	1.863	2.524	121.2	19.7	12.1	1.709	120
2023 11 03	161502	22 54 59.7	-08 20 27	1.863	2.524	121.2	19.7	12.1	1.715	120
55 Pandora										
2023 11 03	180255	23 31 11.7	-03 04 40	1.585	2.362	131.4	18.3	11.7	1.835	120
2023 11 03	180501	23 31 11.7	-03 04 40	1.585	2.362	131.4	18.3	11.7	1.849	120
65 Cybele										
2023 11 04	190303	04 20 35.2	+16 43 57	2.893	3.816	155.2	6.3	12.6	1.167	120
2023 11 04	190508	04 20 35.1	+16 43 57	2.893	3.816	155.2	6.3	12.6	1.165	120
70 Panopaea										
2023 11 04	192008	04 18 18.0	+24 39 53	1.811	2.740	154.6	8.9	12.3	1.077	240
2023 11 04	192412	04 18 17.9	+24 39 53	1.811	2.740	154.6	8.9	12.3	1.074	240
88 Thisbe										
2023 11 03	163654	23 17 42.7	+03 39 03	1.710	2.474	130.6	17.7	11.4	1.365	120
2023 11 03	163900	23 17 42.7	+03 39 03	1.710	2.474	130.6	17.7	11.4	1.369	120
97 Klotho										
2023 11 03	182443	23 33 56.5	-12 48 14	1.437	2.188	127.6	21.0	11.4	2.637	120
2023 11 03	182646	23 33 56.5	-12 48 14	1.437	2.188	127.6	21.0	11.4	2.667	120
107 Camilla										
2023 11 03	134138	21 08 37.4	-12 22 51	3.444	3.671	95.3	15.6	13.5	1.784	10
2023 11 03	134155	21 08 37.5	-12 22 51	3.444	3.671	95.3	15.6	13.5	1.784	10
2023 11 03	134226	21 08 37.5	-12 22 51	3.444	3.671	95.3	15.6	13.5	1.785	60
2023 11 03	134332	21 08 37.5	-12 22 51	3.444	3.671	95.3	15.6	13.5	1.787	60
2023 11 04	142703	21 09 08.6	-12 23 07	3.459	3.671	94.4	15.6	13.5	1.923	240
2023 11 04	143109	21 09 08.7	-12 23 07	3.459	3.671	94.4	15.6	13.5	1.924	240
144 Vibilia										
2023-11-04	171606	03 40 24.6	+15 28 22	1.144	2.117	164.7	7.1	10.6	1.331	120
2023-11-04	171812	03 40 24.5	+15 28 22	1.144	2.117	164.7	7.1	10.6	1.324	120
160 Una										
2023-11-04	194708	05 23 25.3	+28 03 24	1.711	2.549	139.6	14.6	13.1	1.097	240
2023-11-04	195158	05 23 25.2	+28 03 24	1.711	2.549	139.7	14.6	13.1	1.090	240

.

Continuation of the Table 1.

1	2	3	4	5	6	7	8	9	10	11
163 Erigone										
2023-11-03	153139	22 15 17.9	-12 26 30	1.857	2.393	110.6	22.8	14.1	1.887	120
2023-11-03	153343	22 15 17.9	-12 26 30	1.857	2.393	110.6	22.8	14.1	1.895	120
345 Tercidina										
2023 11 03	184719	00 30 23.9	+06 21 15	1.341	2.248	148.6	13.3	12.3	1.468	120
2023 11 03	184923	00 30 23.9	+06 21 14	1.341	2.248	148.6	13.3	12.3	1.476	120
366 Vincentina										
2023 11 03	155150	22 33 43.9	-07 04 42	2.411	2.992	116.8	17.2	13.9	1.661	120
2023 11 03	155356	22 33 43.9	-07 04 421	2.411	2.992	116.8	17.2	13.9	1.667	120
381 Myrrha										
2023 11 03	174225	23 24 42.2	-17 57 06	2.552	3.202	123.0	15.1	13.8	2.715	120
2023 11 03	174429	23 24 42.1	-17 57 06	2.552	3.202	123.0	15.1	13.8	2.741	120
407 Arachne										
2023 11 21	162505	05 54 52.6	+30 29 09	1.627	2.526	149.1	11.6	13.0	1.640	240
2023 11 21	162913	05 54 52.4	+30 29 09	1.627	2.526	149.1	11.6	13.0	1.613	240
447 Valentine										
2023 11 03	165015	02 35 55.0	+11 13 12	1.862	2.853	176.1	1.3	12.9	1.291	120
2023 11 03	165221	02 35 55.9	+11 13 12	1.862	2.853	176.1	1.3	12.9	1.287	
481 Emita										
2023 11 03	184257	04 04 38.4	+16 48 19	1.358	2.308	158.0	9.3	11.9	1.173	120
2023 11 03	184502	04 04 38.3	+16 48 19	1.358	2.308	158.0	9.3	11.9	1.170	120
482 Petrina										
2023 11 03	144726	21 57 53.3	-08 33 51	2.458	2.921	108.0	18.9	14.2	1.652	120
2023 11 03	144931	21 57 53.3	-08 33 51	2.458	2.921	108.0	18.9	14.2	1.656	
718 Erida										
2023 11 03	171341	23 24 44.0	-09 30 56	2.837	3.527	127.3	12.9	15.5	1.885	240
2023 11 03	171747	23 24 44.0	-09 30 56	2.837	3.527	127.3	12.9	15.5	1.906	240
TEMP = - 60 (matrix cooling temperature); READTIME = 1.0E-06 (Pixel readout time); GAIN=5 (signal gain factor)										

EURASIAN PHYSICAL TECHNICAL JOURNAL

2025, Volume 22, No.2 (52)

https://doi.org/10.31489/2025N2/147-154

Received: 30/11/20254 Revised: 21/04/2025 Accepted: 25/06/2025 Published online: 30/06/2025

Original Research Article

UDC 539.124; 539.12...162

DEMONSTRATING NONLINEAR OSCILLATIONS OF CHARGED PARTICLE BY THE HOMOTOPY PERTURBATION METHOD

Al-Garalleh B.F.[1], Akour A.N.[2*], Jaradat E.K.[1], Jaradat O.K.[3]

[1] Department of Physics, Mutah University, Al-Karak, Jordan
[2] Department of Basic Scientific Sciences, Al-Huson College, Al-Balqa Applied University, Salt, Jordan
[3] Department of Physics, Mutah University, Al-Karak, Jordan.
*Corresponding author: abd-akour@bau.edu.jo

Abstract. *This document describes explicitly the nonlinear equation handling the oscillation of charged particles affected by electrical field using the Homotopy Perturbation Method. This method success to construct a significant approximate solution. Our analysis has resulted in the development of an initial set of four equations that govern the oscillatory of charged particles. Following this, we have visually depicted these equations and satisfied a deep clear interpretations vision of the investigated outcomes. Our analysis has resulted in the development of an initial set of four equations that govern the oscillatory of charged particles. Following this, we have visually depicted these equations and satisfied a deep clear interpretations vision of the investigated outcomes.*

Keywords: Charged particle oscillation; Nonlinear harmonic equation, Homotopy Perturbation Method.

1. Introduction

The aim of this study is to provide an explicit interpretation and describe the behavior of a charged body moved under influence of electrical forces that expressed as in real natural physical system by equation(1) [1]. This actual serious harmonic equation is commonly used in physics to describe the motion of a charged body under the influence of electrical forces between it and its neighbored charges. Such equations are used in physics to understand the motion and dynamics of systems affected by electrical forces, aiding in the comprehension of real natural phenomena, and predicting the behavior of objects in such contexts:

$$\ddot{x}(t) + \frac{kqQ}{m}\left(\frac{1}{2R^3}x(t) + \frac{9}{16R^5}x(t)^3 + \cdots\right) = 0 \qquad (1)$$

where $x(t), \ddot{x}(t)$the displacement and time dependent acceleration of a particular body from its equilibrium position over time, the kqQ/R^2term represents the electrical force between two charged bodies, where: k is the Coulomb's constant. And the last two terms introduced as a primary and secondary terms components of the electrical forces between the two bodies respectively.

The second term$\frac{kqQ}{m}\frac{1}{2R^3}x(t)$: the linear restoring force (attractive force), similar as Hooke's law.

The third term $\frac{kqQ}{m}\frac{9}{16R^5}x(t)^3$: the nonlinear correction to the restoring force

.

The Homotopy perturbation (HP) method is one of the most significant methods that considered as a universal method for solving non-linear partial differential equations (DF) of various kinds. It investigates the analytic solution by an infinite series which using a phony parameter p. Furthermore, HPM does not require any small parameter in the equation as that of other iteration methods but it has a parameter p∈[0,1] (a small parameter) so it catches a significant advantage. Otherwise, it is the first time used to solve our interested problem in our known, that provide a new look on this problem and test other method on competing to provide accurate solution. This method shows a great efficiency in providing accurate solutions to partial DF in some physical systems [2]. Biazar and Ghazvini [3] studied the efficient valid condition for convergence of the HP method, and provide a test of this condition for the three well-known problems of Burgers' equation [2], the 4th variable coefficients parabolic, and Schrödinger partial DF [3]. Researchers found that the analytical approximation to the solutions is reliable and confirms the power and ability of the HP method as an easy device for computing the solution of partial DF. The examination of convergence conditions for DF, integral equations, integrodifferential equations, and their systems operating the HP method, is also developed [4]. The (HP) Transform Method is used to solve the nonlinear RLC circuit equation [5]. This paper proposes three third-order, sixth-order, and seventh-order iterative methods, respectively, to solve nonlinear equations using the modified HP technique attached with the equations of the system [6]. It also provides approximate and exact solutions to the nonlinear Burger's equation by means of (HP) method [7]. The (HP) method predicts an approximate analytical description for the nonlinear Schrödinger equation with a harmonic oscillator. Accordingly, the nonlinear Schrödinger equation was presented in one and two dimensions to demonstrate the effects of the harmonic oscillator on the behavior of the wave function [8]. Laplace–Adomian decomposition method (LDM) is hold for describing charge oscillation and it provides a good sense.

This study is unique since it's the first for providing a particular description and solution for nonlinear serious harmonic charged oscillation using the significant HP method. Also, it instructs typical model procedure to demonstrate a real serious nonlinear harmonic oscillation of charges. Otherwise it provides us with regular mathematical variables as control switch buttons to recognize and understand the change in physical properties of the wave motion such amplitude and frequency variance. Finally this method significantly shortens a lot of mathematical computation, calculation and provides a high degree of accuracy and efficiency. This paper is settled as follows: section 2 provides the Basic idea for HP method, section 3 demonstrates result and analysis, section 4 declares the conclusion.

2. Basic Idea of HP Method

Here we work to clarify the basic idea of HP Method. So let us suppose the following differential equation.

$$A(u) - f(r) = 0, \qquad r \in \Omega \tag{2}$$

The boundary conditions.

$$B\left(u, \frac{\partial u}{\partial r}\right) = 0, \qquad r \in \Gamma \tag{3}$$

(A) is a general calculus operator, *(B)* is a parametric operator, (Ω) is a domain bound, and *(f(r))* is a well-known analytic function. The linear part and the non-linear part can be obtained by decomposing the operator (A) into two parts, become eq (2):

$$L(u) + N(u) - f(r) = 0 \tag{4}$$

where *L(u)* linear and *N(u)* non-linear. If a nonlinear equation does not contain (slight parameter), we can assume an artificial parameter in eq (2) [4].

$$L(u) + p\big(N(u)\big) - f(r) = 0 \tag{5}$$

where p∈[0,1] is an artificial parameter, Equation (4) can be indicated as a series of power p [9].

$$u = u_0 + pu_1 + p^2u_2 + p^3u_3 + \cdots \tag{6}$$

When p→1 in eq (5) then the approximate solution is obtained as eq (4). The adjustment parameter is quiet.

3. Result and Analysis

The equation

$$\ddot{x}(t) + \frac{kqQ}{m}\left(\frac{1}{2R^3}x(t) + \frac{9}{16R^5}x(t)^3 + \cdots\right) = 0$$

The initial conditions

$$x(0) = 1\ , \quad x(0)' = 0$$

$$\ddot{x}(t) + \left(\frac{kqQ}{2mR^3}x(t) + \frac{9kqQ}{16mR^5}x(t)^3\right) = 0$$

But $\frac{\mathrm{kqQ}}{2\mathrm{mR}^2} = \text{constant}$ and $\frac{9\mathrm{kqQ}}{16\mathrm{mR}^2} = \text{constant}$, so we can assume.

$$\frac{kqQ}{2mR^3} = C$$

And

$$\frac{9kqQ}{16mR^5} = D$$

To become the equation

$$\ddot{x}(t) + C\,x(t) + D\,x(t)^3 = 0 \tag{7}$$

But

$$f(x) = 0$$

And

$$L(u) = \ddot{x}(t) + Cx(t) \qquad N(u) = D\,x(t)^3$$

We are now using the Homotopy perturbation method, with initial condition. Using eq (5) we construct (HPM) shown below.

$$H(x,p) = (1-p)(\ddot{x} + Cx) + p(\ddot{x} + Cx + Dx^3) = 0$$

Become

$$\ddot{x} + Cx = pDx^3 \tag{8}$$

But

$$x = x_0 + px_1 + p^2x_2 + \cdots \tag{9}$$

where

$$x(t) = \lim_{p\to 1} x = x_0 + x_1 + x_2 + \cdots \tag{10}$$

Substituting eq (8) in eq (9), we get

$$\frac{\partial^2}{\partial t^2}(x_0 + px_1 + p^2x_2 + \cdots) + C(x_0 + px_1 + p^2x_2 = p(D(v_0 + pv_1 + p^2v_2 + \cdots)^3) \tag{11}$$

But

$$\begin{aligned}(v_0 + pv_1 + p^2v_2 + \cdots)^3 &= p^{12}\,v_4^3 + 3\,p^{11}\,v_3\,v_4^2 + 3\,p^{10}\,v_2\,v_4^2 + 3\,p^{10}\,v_3^2\,v_4 + p^9\,v_3^3 \\ &+ 3\,p^9\,v_1\,v_4^2 + 6\,p^9\,v_2\,v_3\,v_4 + 3\,p^8\,v_2\,v_3^2 + 3\,p^8\,v_0\,v_4^2 \\ &+ 3\,p^8\,v_2^2\,v_4 + 6\,p^8\,v_1\,v_3\,v_4 + 3\,p^7\,v_1\,v_3^2 + 3\,p^7\,v_2^2\,v_3 \\ &+ 6\,p^7\,v_1\,v_2\,v_4 + 6\,p^7\,v_0\,v_3\,v_4 + p^6\,v_2^3 + 3\,p^6\,v_0\,v_3^2 \\ &+ 6\,p^6\,v_1\,v_2\,v_3 + 3\,p^6\,v_1^2\,v_4 + 6\,p^6\,v_0\,v_2\,v_4 + 3\,p^5\,v_1\,v_2^2 \\ &+ 3\,p^5\,v_1^2\,v_3 + 6\,p^5\,v_0\,v_2\,v_3 + 6\,p^5\,v_0\,v_1\,v_4 + 3\,p^4\,v_0\,v_2^2 \\ &+ 3\,p^4\,v_1^2\,v_2 + 6\,p^4\,v_0\,v_1\,v_3 + 3\,p^4\,v_0^2\,v_4 + p^3\,v_1^3 \\ &+ 6\,p^3\,v_0\,v_1\,v_2 + 3\,p^3\,v_0^2\,v_3 + 3\,p^2\,v_0\,v_1^2 + 3\,p^2\,v_0^2\,v_2 \\ &+ 3\,p\,v_0^2\,v_1 + v_0^3\end{aligned}$$

We compare both sides of the equation with equal the power of p, we have.

.

$$p^0: \frac{\partial^2 x_0}{\partial t^2} + C\, x_0 = 0 \tag{12}$$

$$p^1: \frac{\partial^2 x_1}{\partial t^2} + C\, x_1 = -D\, x_0^3 \tag{13}$$

$$p^2: \frac{\partial^2 x_2}{\partial t^2} + C\, x_2 = 3D\, x_0^2\, x_1 \tag{14}$$

$$p^3: \frac{\partial^2 x_3}{\partial t^2} + Cx_3 = -D(3\, x_0^2\, x_2 + 3\, x_0\, x_1^2) \tag{15}$$

Now, we involve Laplace Transform ***(LT).*** *LT* reformulate differential equations into more resolvable forms, and overcoming complexity of especially with obtaining initial conditions. By transferring derivatives to a frequency domain, solutions could be demonstrated by standard algebraic treatment which are generally straightforward and easier to solve. Once the algebraic equation is solved, the inverse *LT* is used to recover the original time-dependent solution.

Solve the prior differential equations (1,10,11) using the *LT* to equations from [12-15]. Solve equation 12 using *LT.*

$$\frac{\partial^2 x_1}{\partial t^2} + C\, x_1 = 0 \tag{16}$$

$$x_0(t) = A\cos\left(t\sqrt{C}\right) + B\sin\left(t\sqrt{C}\right) \tag{17}$$

$$but\ x_0(0) = 1\ , A = 1$$
$$and\ x_0(0)' = 0\ , \qquad B = 0$$

$$x_0 = \cos(t\sqrt{C}) \tag{18}$$

Solve equation 13 using *LT.*

$$\frac{\partial^2 x_1}{\partial t^2} + C\, x_1 = -D\, x_0^3 = -D\, \cos^3\left(t\sqrt{Z}\right) \tag{19}$$

$$x_1(t) = D\mathcal{L}^{-1}\left[\frac{1}{s^2 + C}\mathcal{L}\left[\cos^3\left(t\sqrt{Z}\right)\right]\right] \tag{20}$$

$$x_1 = \frac{D}{32C}(\mathrm{Cos}(\sqrt{C}t) + \mathrm{Cos}(3\sqrt{C}t) - 12\sqrt{C}t\mathrm{Sin}(5\sqrt{C}t)) \tag{21}$$

Solve equation 14 using *LT.*

$$\frac{\partial^2 x_2}{\partial t^2} + C\, x_2 = 3D\, x_0^2\, x_1 \tag{22}$$

$$x_2(t) = -\frac{3D^2}{32\, C}\mathcal{L}^{-1}\left[\frac{1}{s^2 + C}\mathcal{L}\left[\ \mathrm{Cos}\left(\sqrt{C}t\right)^3 + cos\left(t\sqrt{C}\right)^2\mathrm{Cos}(3\sqrt{C}t)\right.\right.$$
$$\left.\left. - 12\sqrt{C}tcos\left(t\sqrt{C}\right)^2\mathrm{Sin}(3\sqrt{C}t)\right]\right] \tag{23}$$

$$x_2(t) = -\frac{3D^2}{32\, C}\mathcal{L}^{-1}\left[\frac{1}{s^2 + C}\left(\left(24\, C\, s\frac{(21C^2 + 6s^2 + s^4)}{(C + s^2)^2(9C + s^2)^2}\right) + \frac{s(7C + s^2)}{(C + s^2)(9C + s^2)}\right.\right.$$
$$\left.\left. + \frac{1}{4}s\left(\frac{2}{9C + s^2} + \frac{1}{25C + s^2} + \frac{1}{C + s^2}\right)\right)\right] \tag{24}$$

$$x_2 = \frac{D^2}{1024\, C^2}\left[-72\, t^2\, C\cos\left(t\sqrt{C}\right) + 96\, t\sqrt{C}\sin\left(t\sqrt{C}\right) - 36\, t\sqrt{C}\sin\left(3t\sqrt{C}\right)\right.$$
$$\left. + 23\cos\left(t\sqrt{C}\right) - 24\cos\left(3t\sqrt{C}\right) - \cos\left(5t\sqrt{C}\right)\right] \tag{25}$$

Solve equation 15 using *LT*.

$$\frac{\partial^2 x_3}{\partial t^2} + Cx_3 = -3D(\, x_0^2\, x_2 + \, x_0\, x_1^2) \tag{26}$$

$$\begin{aligned}
x_3(t) = -\frac{D^3}{C^3}\Bigg[& \frac{69}{32768}\left(12t\sqrt{C}\sin\left(t\sqrt{C}\right) + \cos\left(t\sqrt{C}\right) - \cos\left(3t\sqrt{C}\right)\right) \\
& - \frac{3}{4096}\left(12\, t\sin\left(t\sqrt{C}\right) + 7\cos\left(t\sqrt{C}\right) - 6\cos\left(t\sqrt{C}\right) - \cos\left(5t\sqrt{C}\right)\right) \\
& + \frac{1}{65536}\left(11\cos\left(t\sqrt{C}\right) - 6\cos\left(5t\sqrt{C}\right) - 4\cos\left(5t\sqrt{C}\right) - \cos\left(7t\sqrt{C}\right)\right) \\
& + \frac{9}{4096}\left(-8t^2 C\cos\left(t\sqrt{C}\right) + 8t\sqrt{C}\sin\left(t\sqrt{C}\right) - 4t\sqrt{C}\sin\left(3t\sqrt{C}\right)\right. \\
& \left. + 3\cos\left(t\sqrt{C}\right) - 3\cos\left(3t\sqrt{C}\right)\right) \\
& - \frac{27}{32768}\left(32\, t^3\, C^{\frac{3}{2}}\sin\left(t\sqrt{C}\right) + 48\, t^2\, C\cos\left(t\sqrt{C}\right) - 8t^2 C\cos\left(3t\sqrt{C}\right)\right. \\
& - 48\, t\sqrt{C}\sin\left(t\sqrt{C}\right) + 12t\sqrt{C}\sin\left(3t\sqrt{C}\right) - 7\cos\left(t\sqrt{C}\right) \\
& \left. + 7\cos\left(3t\sqrt{C}\right)\right) \\
& - \frac{3}{32768}\left(-72\, t^2 C\cos\left(t\sqrt{C}\right) + 72t\sqrt{C}\sin\left(t\sqrt{C}\right) - 72t\sqrt{C}\sin\left(3t\sqrt{C}\right)\right. \\
& - 12\, t\sqrt{C}\sin\left(5t\sqrt{C}\right) + 59\cos\left(t\sqrt{C}\right) - 54\cos\left(3t\sqrt{C}\right) - 5\cos\left(5t\sqrt{C}\right)\Big) \\
& + \frac{1}{16384}\left(-32\, t^3\, C^{\frac{3}{2}}\sin\left(t\sqrt{C}\right) - 48\, t^2 C\cos\left(t\sqrt{C}\right)\right. \\
& - 24\, t^2 C\cos\left(3t\sqrt{C}\right) \\
& + 48t\sqrt{C}\sin\left(t\sqrt{C}\right) + 36t\sqrt{C}\sin\left(3t\sqrt{C}\right) - 21\cos\left(t\sqrt{C}\right) \\
& \left. + 21\cos\left(3t\sqrt{C}\right)\right) \\
& - \frac{1}{16384}\left(72t^2\, C\cos\left(t\sqrt{C}\right) - 72t\sqrt{C}\sin\left(t\sqrt{C}\right) - 12t\sqrt{C}\sin\left(5t\sqrt{C}\right)\right. \\
& \left. + 5\cos\left(t\sqrt{C}\right) - 5\cos\left(5t\sqrt{C}\right)\right) \\
& - \frac{1}{16384}\left(36\, t\sqrt{C}\sin\left(t\sqrt{C}\right) + \cos\left(t\sqrt{C}\right) - \cos\left(5t\sqrt{C}\right)\right) \\
& + \frac{9}{16384}\left((-8)t^2 C\cos\left(t\sqrt{C}\right)\right. \\
& \left. + 8t\sqrt{C}\sin\left(t\sqrt{C}\right) - 4t\sqrt{C}\sin\left(3t\sqrt{C}\right) + 3\cos\left(t\sqrt{C}\right) - 3\cos\left(3t\sqrt{C}\right)\right) \\
& + \frac{3}{32768}\left(12t\sqrt{C}\sin\left(t\sqrt{C}\right) + \cos\left(t\sqrt{C}\right) - \cos\left(3t\sqrt{C}\right)\right) \\
& + \frac{1}{65536}\left(48t\sqrt{C}\sin\left(t\sqrt{C}\right) + 3\cos\left(t\sqrt{C}\right) - 2\cos\left(5t\sqrt{C}\right)\right. \\
& \left. - \cos\left(7t\sqrt{C}\right)\right)\Bigg]
\end{aligned} \tag{27}$$

We solve the equation using Equation $x(t) = \lim_{p\to 1} x = x_0 + x_1 + \cdots$

.

$$
\begin{aligned}
x(t) = \cos\left(t\sqrt{C}\right) &- \frac{D}{32C}\left(12t\sqrt{C}\sin\left(t\sqrt{C}\right) + \cos\left(t\sqrt{C}\right) - \cos\left(3t\sqrt{C}\right)\right) \\
&+ \frac{D^2}{1024\,C^2}\left[-72\,t^2\,C\cos\left(t\sqrt{C}\right) + 96\,t\,\sqrt{C}\sin\left(t\sqrt{C}\right)\right. \\
&- 36\,t\,\sqrt{C}\sin\left(3t\sqrt{C}\right) + 23\cos\left(t\sqrt{C}\right) - 24\cos\left(3t\sqrt{C}\right) - \cos\left(5t\sqrt{C}\right)\Big] \\
&- \frac{D^3}{C^3}\left[\frac{69}{32768}\left(12t\sqrt{C}\sin\left(t\sqrt{C}\right) + \cos\left(t\sqrt{C}\right) - \cos\left(3t\sqrt{C}\right)\right)\right. \\
&- \frac{3}{4096}\left(12\,t\sin\left(t\sqrt{C}\right) + 7\cos\left(t\sqrt{C}\right) - 6\cos\left(t\sqrt{C}\right) - \cos\left(5t\sqrt{C}\right)\right) \\
&+ \frac{1}{65536}\left(11\cos\left(t\sqrt{C}\right) - 6\cos\left(5t\sqrt{C}\right) - 4\cos\left(5t\sqrt{C}\right) - \cos\left(7t\sqrt{C}\right)\right) \\
&+ \frac{9}{4096}\left(-8t^2C\cos\left(t\sqrt{C}\right) + 8t\sqrt{C}\sin\left(t\sqrt{C}\right) - 4t\sqrt{C}\sin\left(3t\sqrt{C}\right)\right. \\
&+ 3\cos\left(t\sqrt{C}\right) - 3\cos\left(3t\sqrt{C}\right)\Big) \\
&- \frac{27}{32768}\Big(32\,t^3\,C^{\frac{3}{2}}\sin\left(t\sqrt{C}\right) + 48\,t^2\,C\cos\left(t\sqrt{C}\right) - 8t^2C\cos\left(3t\sqrt{C}\right) \\
&- 48\,t\sqrt{C}\sin\left(t\sqrt{C}\right) + 12t\sqrt{C}\sin\left(3t\sqrt{C}\right) - 7\cos\left(t\sqrt{C}\right) \\
&+ 7\cos\left(3t\sqrt{C}\right)\Big) \\
&- \frac{3}{32768}\left(-72\,t^2C\cos\left(t\sqrt{C}\right) + 72t\sqrt{C}\sin\left(t\sqrt{C}\right) - 72t\sqrt{C}\sin\left(3t\sqrt{C}\right)\right. \\
&- 12\,t\sqrt{C}\sin\left(5t\sqrt{C}\right) + 59\cos\left(t\sqrt{C}\right) - 54\cos\left(3t\sqrt{C}\right) - 5\cos\left(5t\sqrt{C}\right)\Big) \\
&+ \frac{1}{16384}\Big(-32\,t^3\,C^{\frac{3}{2}}\sin\left(t\sqrt{C}\right) - 48\,t^2C\cos\left(t\sqrt{C}\right) \\
&- 24\,t^2C\cos\left(3t\sqrt{C}\right) \\
&+ 48t\sqrt{C}\sin\left(t\sqrt{C}\right) + 36t\sqrt{C}\sin\left(3t\sqrt{C}\right) - 21\cos\left(t\sqrt{C}\right) \\
&+ 21\cos\left(3t\sqrt{C}\right)\Big) \\
&- \frac{1}{16384}\left(72t^2\,C\cos\left(t\sqrt{C}\right) - 72t\sqrt{C}\sin\left(t\sqrt{C}\right) - 12t\sqrt{C}\sin\left(5t\sqrt{C}\right)\right. \\
&+ 5\cos\left(t\sqrt{C}\right) - 5\cos\left(5t\sqrt{C}\right)\Big) \\
&- \frac{1}{16384}\left(36\,t\sqrt{C}\sin\left(t\sqrt{C}\right) + \cos\left(t\sqrt{C}\right) - \cos\left(5t\sqrt{C}\right)\right) \\
&+ \frac{9}{16384}\Big((-8)t^2C\cos\left(t\sqrt{C}\right) \\
&+ 8t\sqrt{C}\sin\left(t\sqrt{C}\right) - 4t\sqrt{C}\sin\left(3t\sqrt{C}\right) + 3\cos\left(t\sqrt{C}\right) - 3\cos\left(3t\sqrt{C}\right)\Big) \\
&+ \frac{3}{32768}\left(12t\sqrt{C}\sin\left(t\sqrt{C}\right) + \cos\left(t\sqrt{C}\right) - \cos\left(3t\sqrt{C}\right)\right) \\
&+ \frac{1}{65536}\left(48t\sqrt{C}\sin\left(t\sqrt{C}\right) + 3\cos\left(t\sqrt{C}\right) - 2\cos\left(5t\sqrt{C}\right)\right. \\
&- \cos\left(7t\sqrt{C}\right)\Big)\Big] \qquad .
\end{aligned}
\tag{28}
$$

Significantly, these partition solutions agree completely one hundred percent with those provides using LDM [11]. The four particular solutions are demonstrated in figure 1. The figure shows a convergence of four mathematical functions. Each curve corresponds to a distinct equation, and their interactions weave a intricate tapestry. By varying the "t" variable from 0 to 10, the graph unveils the dynamic behavior of these equations. The contours of the curves, their points of intersection, and the overarching patterns offer valuable insights into the functions' behaviors and interconnections. However, the first portion of solution x_0; shows a behavior of simple harmonic motion where the amplitude, wave length and periodic time all are constant. Otherwise, this state presents the stability of atom, where no nonlinear term (physically no additional external field) appears.

The second part of solution x1, shows growing in the wave amplitude as the time increase. Also, it shows a slight decrease in periodic time.

The third part of solution x_2, also shows growing in the wave amplitude and a recognizable decrease in periodic time as the time increase.

The effect of the fourth part of solution is very small and doesn't provide a recognizable contribution on the general solution.

Lastly, all nonlinear parts of solutions (x_1, x_2 and x_3) show differ from the linear x_0 solution with about ($\pi/2$) phase shift.

On the other hand, figure 2, demonstrates the total solution where the four partition solutions construct to investigate the charge oscillation as a function of time.

The chart illustrates a intricate physical system or phenomenon, showcasing prominent characteristics such as oscillations with fluctuations in both amplitude and frequency. These oscillations hint at the system's periodic behavior. The intricacy of the graph implies the possible involvement of multiple interacting components or forces within the system. The variations in amplitude and frequency of the oscillations may suggest a non-linear or chaotic nature of the system.

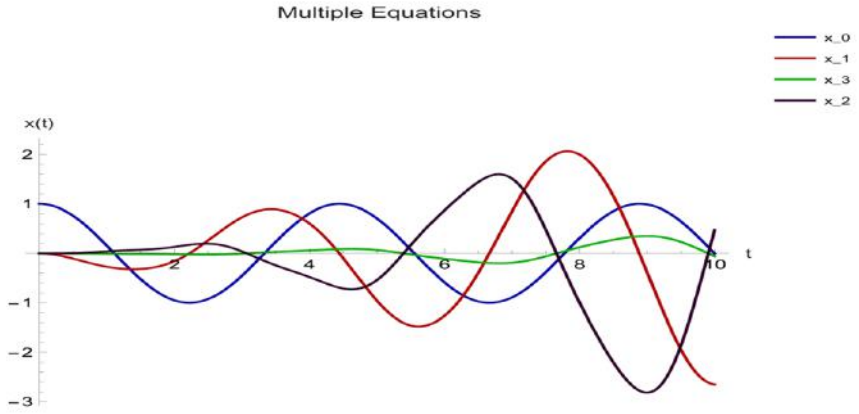

Fig. 1. The relation between the partition solutions as a function of time.

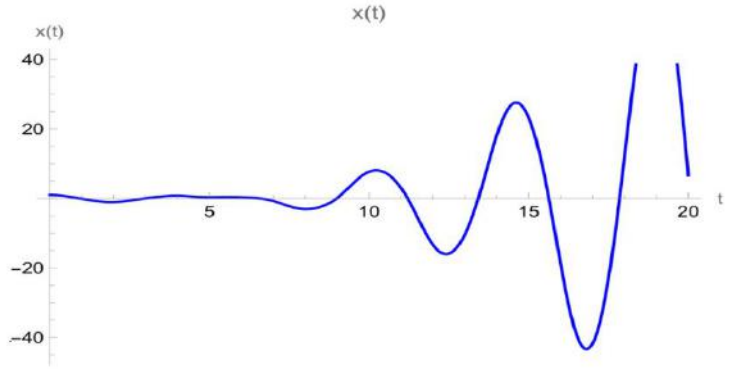

Fig.2. The total solution x(t) as a function of time.

4. Conclusion

We encountered intricacies and demonstrating explicitly the non-linear harmonic oscillation for charged particles affected by electrical field. The HP method is utilized to involve initially the initial four boundaries before progressing to ascertain the comprehensive solution. The HP method with a significant accuracy investigate physical properties of the wave function and demonstrate regular mathematical variables as control switch buttons to recognize and understand the change in physical properties of the wave motion such amplitude and frequency variance. This complex dynamic model which expresses a nonlinear oscillator where the restoring force is not purely linear but involving a cubic term, is demonstrating analytically and graphically. The presence of the linear term displays the predatory in the motion while the cubic term provides the system's stiffness changes with displacement. Otherwise, the result provides an identical partition solutions comparing to those provide by LDM. The outcomes proved to be noteworthy, as illustrated by the conclusive graphs and sufficient solution.

.

Conflict of interest statement

The authors declare that they have no conflict of interest in relation to this research, whether financial, personal, authorship or otherwise, that could affect the research and its results presented in this paper.

CRediT author statement

Bashar and Emad: Conceptualization, Data Curation, Writing Original Draft; Bashar and Omar: Methodology, Investigation; Abdulrahman and Emad.: Writing Review & Editing, Supervision.
The final manuscript was read and approved by all authors.

References

1 Griffiths D. J. (2023) *Introduction to Electrodynamics (5th ed.)*. Cambridge: Cambridge University Press. https://doi.org/10.1017/9781009397735

2 Abdulrahman N. Akour, Emad K. Jaradat , Omar K. Jaradat (2023) Describing Bateman-Burgers' equation in one and two dimensions using Homotopy perturbation method. *Journal of Interdisciplinary Mathematics,* 26 (2), 271-283. https://doi.org/10.47974/JIM-147

3 Biazar, J. and Ghazvini, H. (2009). Convergence of the Homotopy Perturbation Method for Partial Differential Equations. *Nonlinear Analysis: Real World Applications*.10, 2633-2640. https://doi.org/10.1016/j.nonrwa.2008.07.002

4 Chakraverty S., Rani Mahato N., Karunakar P., Dilleswar Rao T. (2019) *Advanced Numerical and Semi-Analytical Methods for Differential Equations*. John Wiley & Sons. Available at: https://onlinelibrary.wiley.com/doi/book/10.1002/9781119423461

5 Reem G. Thunibat, Emad K. Jaradat, Jamil M. Khalifeh (2021) Solution of Non-Linear RLC Circuit Equation Using the Homotopy Perturbation Transform Method. *Jordan Journal of Physics,* 14(1), 89-100. Available at: https://journals.yu.edu.jo/jjp/JJPIssues/Vol14No1pdf2021/9.html

6 Srinivasarao Thota, Shanmugasundaram P. (2022) On new sixth and seventh order iterative methods for solving non-linear equations using homotopy perturbation technique. *BMC research notes*, 15(1), 267. https://doi.org/10.1186/s13104-022-06154-5

7 Ravendra S., Dinesh K. M. , Yogendra K.R. (2020) A mathematical model to solve the nonlinear Burger's equation by Homotopy perturbation method. *Mathematics in Engineering, Science and Aerospace*, 11(1), 115-125. Available at: https://nonlinearstudies.com/index.php/mesa/article/view/2153

8 Emad K. Jaradat, Omar Alomari, Mohmmad Abudayah, A. M. Al-Faqih (2018) An approximate analytical solution of the nonlinear Schrödinger equation with harmonic oscillator using homotopy perturbation method and Laplace-Adomian decomposition method. *Advances in Mathematical Physics,* 2018(1): 6765021, 1-11. https://doi.org/10.1155/2018/6765021

9 He J. (2003) New Interpretation of Homotopy Perturbation Method. *International Journal of Modern Physics B*, 20(18): 2561–2568. https://doi.org/10.1142/S0217979206034819

10 Srinivasarao Thota, Shanmugasundaram P. (2022) On new sixth and seventh order iterative methods for solving non-linear equations using homotopy perturbation technique. *BMC research notes*, 15(1) : 267, 1-15. https://doi.org/10.1186/s13104-022-06154-5

11 Alomari O., Garalleh B.F., Jaradat E. K., Omidi Koma B. (2024) Solving the nonlinear charged particle oscillation equation using the Laplace–Adomian decomposition method. *Advances in Mathematical Physics*, 2024, 6066821. https://doi.org/10.1155/2024/6066821

AUTHORS' INFORMATION

al-Garalleh, Bashar F. - Master, Researcher, Department of Physics, Mutah University, al-Karak, Jordan; Scopus Author ID: 59397246500; ORCID ID: 0009-0003-0489-0100; bashar.qa11@gmail.com

Akour, Abdulrahman N. – Ph.D., Associated Professor, Department of Basic Scientific Sciences, al-Huson College, Al-Balqa Applied University, Jordan; Scopus Author ID: 57197845143; ORCID ID: 0000-0002-9026-4098; abd-akour@bau.edu.jo

Jaradat, Emad K. - Ph.D., Full Professor, Department of Physics, al Imam Mohammad Ibn Saud Islamic University, Riyadh, Saudi Arabia; Scopus Author ID: 55173947600; ORCID ID: 0000-0001-5335-7060; ekyjaradat@imamu.edu.sa

Jaradat, Omar K. - Ph.D., Full Professor, Department of Mathematics, Mutah University, al-Karak, Jordan; Scopus Author ID: 24066935400; ORCID ID: 0009-0006-7404-7129; jaradat@mutah.edu.jo

EURASIAN PHYSICAL TECHNICAL JOURNAL

2025, Volume 22, No.2 (52)

https://doi.org/10.31489/2025N2/155-162

Received: 25/01/2025 Revised: 23/04/2025 Accepted: 20/06/2025 Published online: 30/06/2025

Original Research Article

UDC 53.01

STUDY OF BRIGHTNESS VARIATIONS OF IRAS 07080+0605 FROM THE ASAS SN DATA

Khokhlov A.A., Agishev A.T., Vaidman N.L., Agishev A.T.*

al-Farabi Kazakh National University, Almaty, Kazakhstan.
*Corresponding author: agishev.aldiyar@kaznu.kz

Abstract. *This paper presents the findings of an analysis of the light curve of the star IRAS07080+0605, a member of the FS CMa class. The analysis was conducted using data from the ASAS-SN survey, collected between 2014 and 2025. The year-by-year analysis of the ASAS-SN time series in the g filter reveals that the system's period changes over time, and the shape of the phase curve varies during individual intervals. The asymmetry observed in the phase curves suggests potential orbital changes, possibly related to the system's dynamics, including variations in the separation between the components. Additionally, we describe changes in the luminosity amplitude of IRAS07080+0605, which may reflect alterations in the star's physical state, such as pulsations in its outer layers or interactions with its environment.*

Keywords: binary systems, light curves, FS CMa, catalog ASAS SN

1. Introduction

The FS CMa-type objects that exhibit the B[e] phenomenon were first distinguished as a distinct evolutionary group in [1]. The B[e] phenomenon is characterized by the presence of both allowed (Balmer lines, Fe II, and others, and forbidden ([Ca II], [O I], and others) emission lines in the spectra of stars with surface temperatures ranging from ~10000 to ~30000 K (formerly classified as B-type stars) and a significant excess of IR emission relative to the expected stellar emission, attributable to the presence of circumstellar dust. The most probable scenario for the formation of FS CMa objects [1], according to the confirmed existing data [2] as well as the results of analyses, is the evolution of a close double system in which there is a strong mass transfer between the components of the double system, leading to the loss of some of this mass into the circumstellar space and the formation of a dust shell or disc.

Recent studies have made significant progress in the research of FS CMa-type stars. Through detailed and comprehensive analyses of long time series of observations, new properties of this group of stars have been discovered, including rapid spectral variations [3] and the presence of lithium lines in the stellar spectrum [1, 4]. Furthermore, orbital periods have been determined for a number of objects in this group [4, 5], the physical characteristics of the system components have been described [6], and key physical parameters of the stars have been determined [6]. These studies have revealed a wide range of luminosities among these objects, suggesting the existence of numerous such systems both in our galaxy and in others. The observed strong IR excesses indicate that FS CMa group objects represent a previously unrecognized source of dust in the galaxy. These objects have not previously been considered dust producers, and a reassessment of Galactic dust production is necessary.

Considerable attention has been devoted to the study of hot stars surrounded by circumstellar material, particularly in binary systems and during late evolutionary phases such as the post-AGB stage. These investigations have revealed a broad diversity in photometric and spectroscopic behavior, strongly influenced by dynamic interactions within the system and the structure of the surrounding envelope. For instance, [7] Zharikov et al. (2025) analyzed the FS CMa-type candidate IRAS 17449+2320, identifying a complex circumstellar environment affected by a variable magnetic field and orbital modulation, suggesting strong binary interaction and non-uniform envelope morphology. Similarly, [8] Ikonnikova et al. (2025) examined the post-AGB star IRAS 21546+4721, reporting cyclic photometric variability and spectroscopic changes indicative of pulsations and variable extinction from circumstellar dust. On a broader scale, [9] Kwok (2025) provided an in-depth theoretical review of chemical synthesis in stellar envelopes, emphasizing how mass-loss and outflow processes contribute to the development of molecular complexity in the circumstellar medium. These studies further demonstrate the importance of long-term photometric monitoring for identifying instability mechanisms and interpreting the evolutionary status of stars with extended envelopes.

This work is devoted to the study of the star IRAS 07080+0605 (a northern hemisphere object), which has one of the strongest IR excesses among objects with the B[e] phenomenon. This object was first identified as an emission star in [10], in a survey of stars with emission lines.

There are conflicting opinions on the conclusions about the nature of the object. In [11,12], the object IRAS 07080+0605 is considered to be a pre-main-sequence star. However, in a recent paper [13], it was concluded that the object IRAS 07080+0605 satisfies the observational and physical criteria for the FS CMa and a suggestion that it could be an analog of Red Rectangle at an early evolutionary stage.

There are also a number of works on the study of the variation of the light of this object, but the values of the period are different. In [12], the authors discovered multiple periods through the analysis of the periodogram of the ASAS-SN survey data, with a particular focus on the most reliable ones: 72.1, 248.8, and 203.1 days. A similar period of 246.7 days was determined in [11] using ASAS-3 survey data [14].A recent study [13] on an individual study of the object IRAS 07080+0605 also suggested a period of ~190 days, but it was noted that this period was not revealed in the 2014 and 2019 seasons. The period value was derived from data from the ASAS-SN survey from the 2014 to 2019 seasons only. In this paper, the authors noted that the ASAS-SN survey data [15] was used to find the period because it has less error compared to the ASAS-3 survey data. However, the photometric survey data for the most recent observing period (up to 2025) from the ASAS-SN survey, when stacked with the above periods from both [13] and [11,12], show a very large dispersion around the mean sinusoidal curves (see the Analysis Results section). Therefore, one can conclude that the light curve behavior is ambiguous.

The primary objective of this study is to analyze the light curve of the object IRAS 07080+0605. This analysis builds upon the findings of previous studies, including those presented in [13], which covered the period up to 2019. In this work, we utilize the most extensive and comprehensive set of observational data on the object's luminosity available to date.

Study is based on the data from the All-Sky Automated Survey for Supernovae (ASAS-SN), a photometric monitoring project launched in 2013. The ASAS-SN program began regular accumulation of high-quality optical photometry in mid-2014. From this period onward, the data series provides sufficient temporal coverage, uniform cadence, and photometric accuracy to allow robust analysis of long-term brightness variations. For this reason, our analysis covers the time range from 2014 to 2025, encompassing the full available span of precise ASAS-SN photometric observations.

2. Observational data and methods for analyzing the star's luminosity

ASAS-SN photometric data were used in this paper. The ASAS-SN survey data cover the period from half of 2014 to 2025. The survey data from 2018 were observed in the g filter and were converted to the Johnson-Cousins system filter V using formula 1, according to the work of [16]. The mean value of (B-V) = 0.12 was taken from [13]. The rationale for the choice of ASAS-SN survey data is due to the fact that the ASAS-3 data are strongly inferior to the ASAS-SN data. The light curve derived from ASAS-3 data (see Figure 5 in [13]) exhibits significant noise and errors, likely caused by larger uncertainties in brightness measurements.

$$V = g' - 0.54(B - V) + 0.07$$

The Lomb-Scargle Periodogram method [16] is used to analyse time series in this paper. The Lomb-Scargle method is particularly useful for analysing non-uniformly distributed time series, where traditional methods of frequency analysis, such as the discrete Fourier transform, are inapplicable due to the need for uniform data sampling. This makes it an indispensable tool for working with astronomical observations, which are often characterised by irregularity. The algorithm implemented on the website [17] was deployed to search for the period.

3. Results

The ASAS-SN survey data in the g filter were selected for analysis to ensure the optimal homogeneity in timeliness of the observations, as evidenced by the reduced number of areas lacking observations in this band when compared to those in band V (see Figure 1, upper panel). The long-term trend was subtracted for this band (see Figure 1, bottom panel). The trend removal procedure entailed the following steps:

– For each observation season, the mean JD values and the brightness value were calculated;

– Subsequently, coefficients were calculated from these mean points, as well as spline values for each real JD value.

– The difference between the lightness value and the spline was determined, resulting in a series with a subtracted trend.

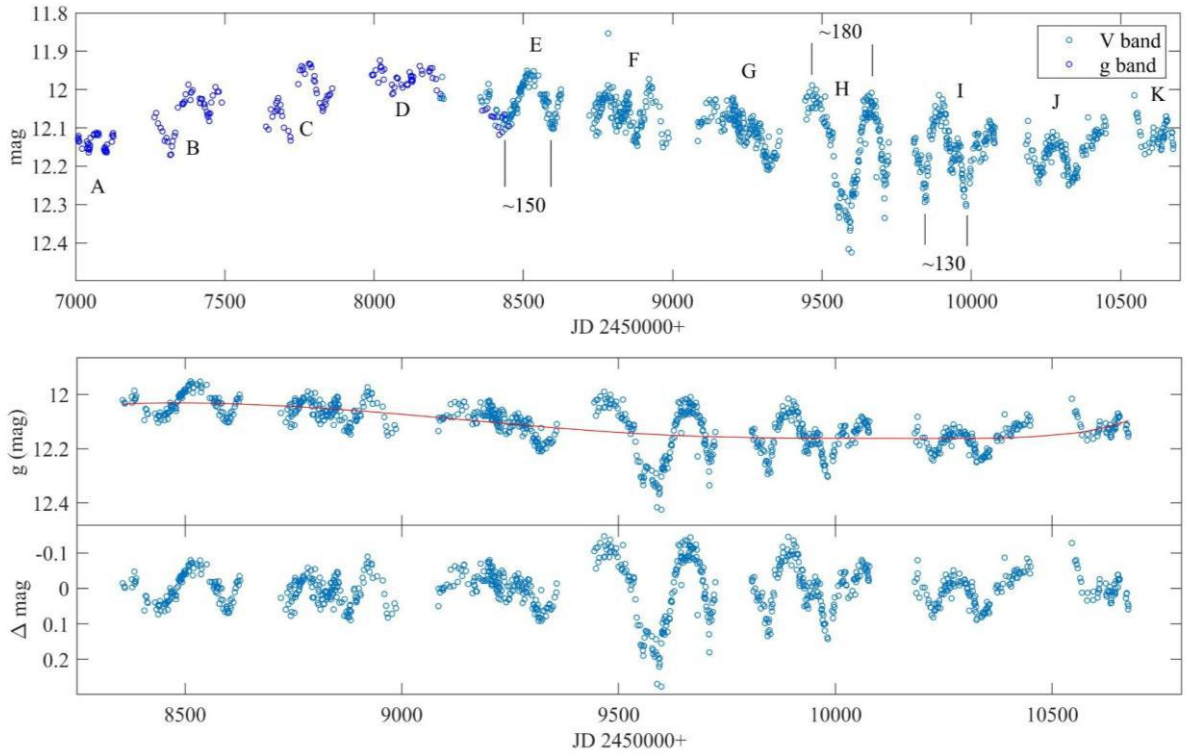

Fig. 1. Light curve of the IRAS 07080+0605 system from the ASAS SN data. The upper panel shows brightness variations IRAS 07080+0605 in 2014–2025 from the ASAS SN data. The middle panel shows the light curve with the actual data (open circles) and the running average (red line) used to determine the brightness trend. The bottom panel shows a detrended g-band brightness with respect to the running average

As demonstrated in Figure 2 (bottom panel), the Fourier power spectrum indicates a peak at approximately 125 days. The phase curve, convolved with this period, displays a substantial spread of approximately 0.2 magnitude.

The ASAS-SN survey data in the g filter were analyzed using the previously proposed periods of approximately 72, 190, 203, and 250 days. The results of this analysis indicated that none of these periods produced consistent phase curves, instead resulting in significant scatter.

However, when constructing phase curves for individual intervals, as indicated by the letters in the upper panel of Figure 1, different periods were observed. These periods (cycles) were found to be similar in both shape and amplitude. Despite this, the intervals exhibit clear periodicity. For instance, the light curves

.

of interval H show a periodicity of approximately 180 days, as illustrated by the phase curve in Figure 3, which displays a clear minimum and maximum.

Therefore, a range of potential values for the period (cycle) is observed. The determination of the precise nature of these values is challenging, as evidenced by the dispersion in the phase light curves. In spite of this, the periods defined on a wide data sample may vary from season to season (time domains of observations without significant gaps) and practically vary within a particular season. For instance, the time domain 'H', as illustrated in the top panel of Figure 1, shows a difference between maximum peaks of ~180 days and minimum peaks of ~120 days. The LS method periodogram calculation, which indicates the largest power spectrum, is achieved through convolution with a period value of 171.9 days.

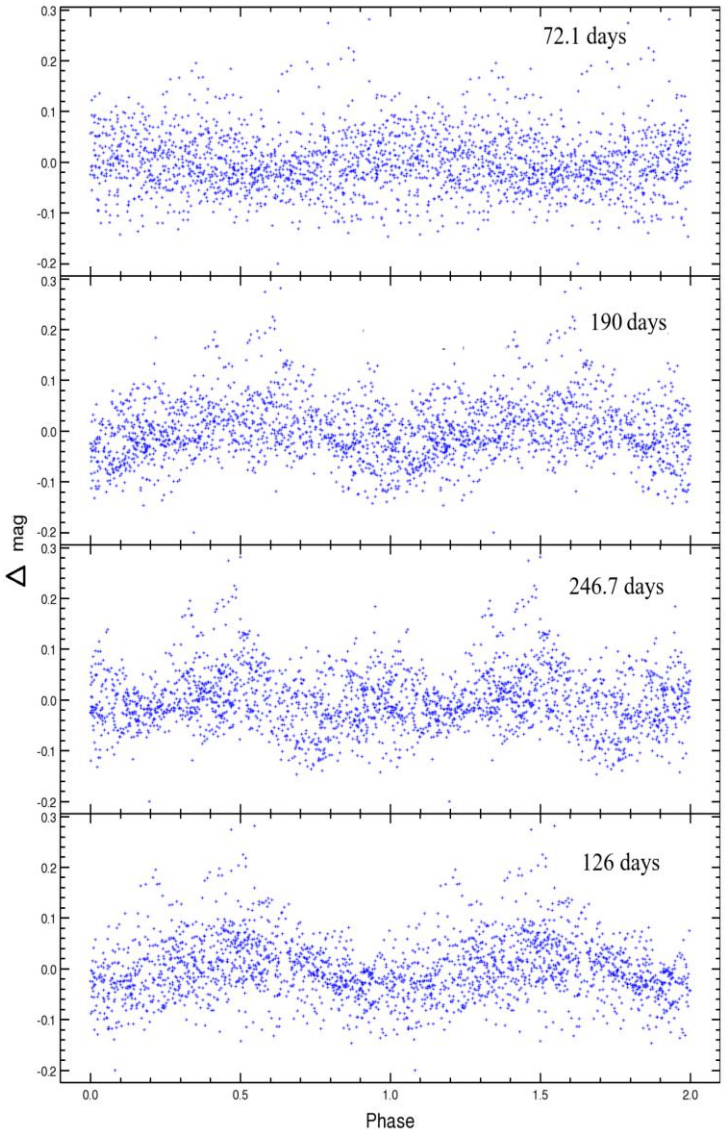

Fig. 2. The curves are convolved with the indicated periods based on the entire data sample between 2014 and 2025 in bands V and g from the survey data.

The behavior described above may suggest the presence of a quasi-periodic process with variable amplitude occurring in the dust disk, or alternatively, it may indicate a possible change in orbit, which may be related to the dynamics of the system, including changes in the separation between objects. In order to investigate the temporal changes in the stellar magnitude of the object, data containing corrected stellar magnitudes and their associated errors were analyzed.

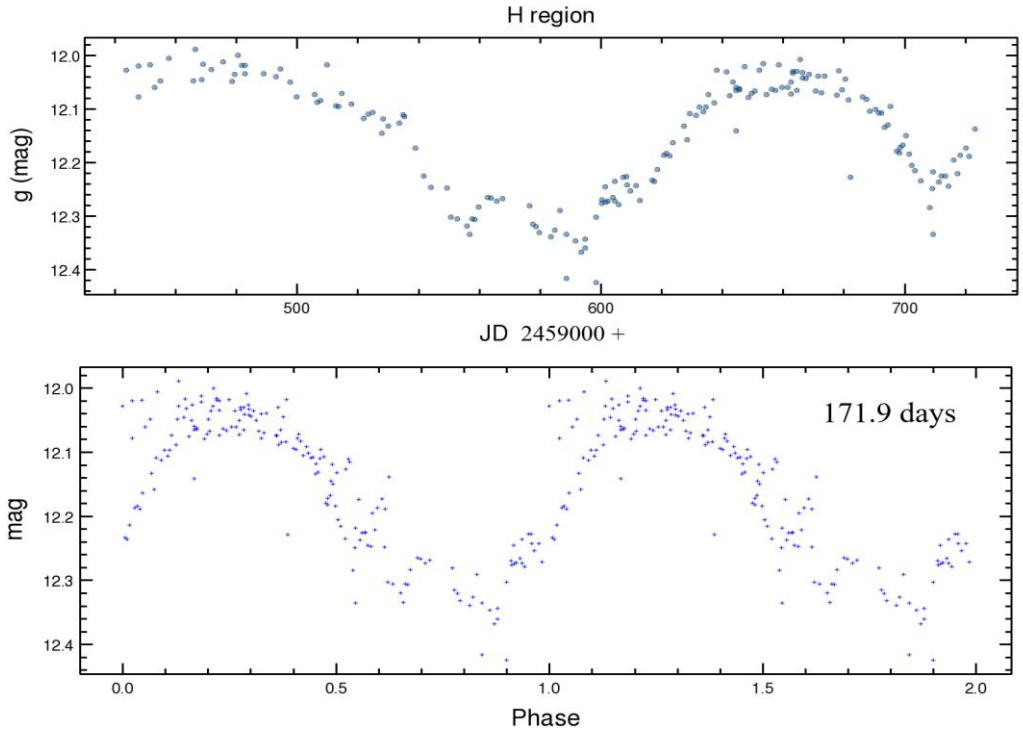

Fig. 3. Light curve in the g filter (upper panel) and the corresponding phase curve convolved with a period of 171.9 days.

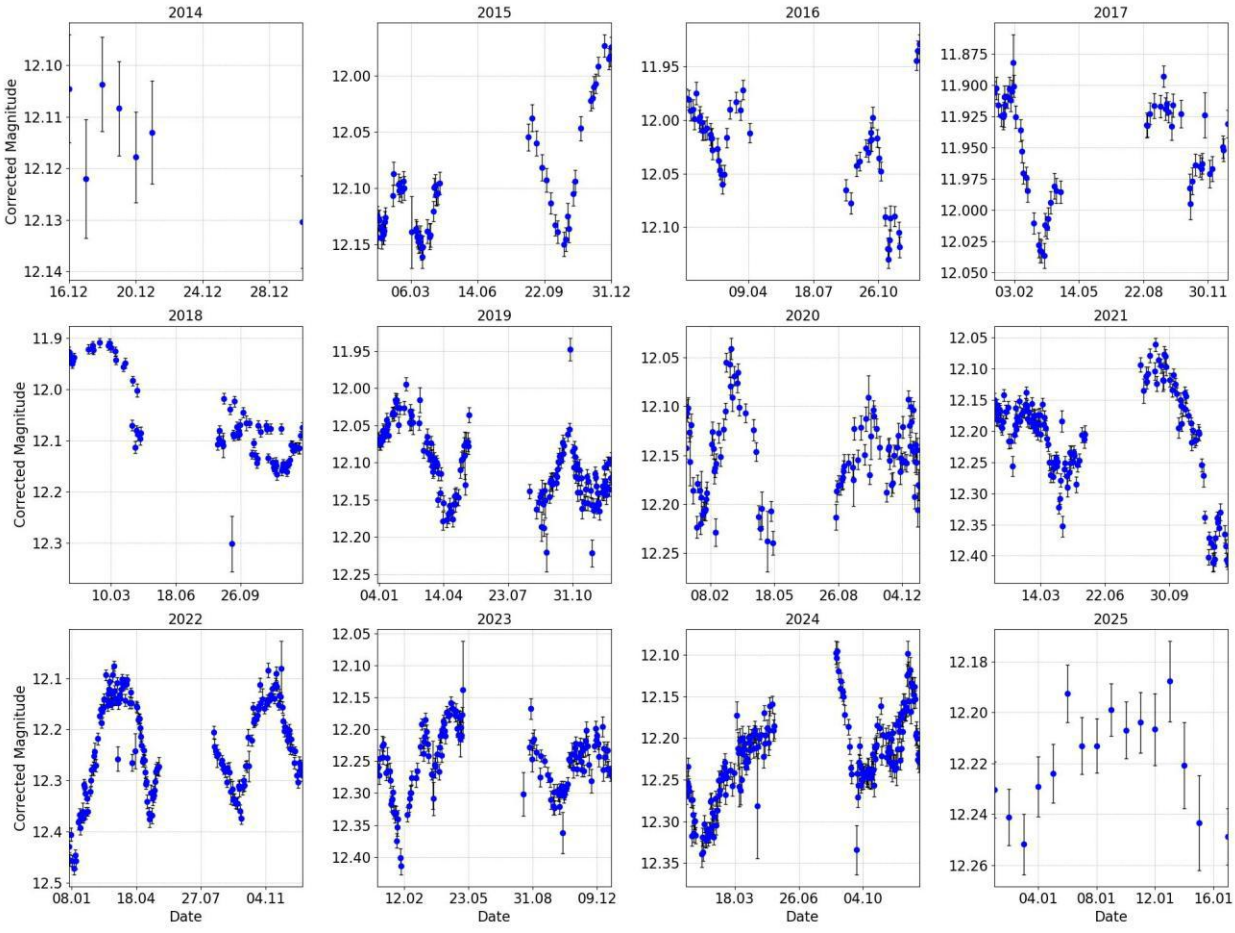

Fig. 4. Changes in the stellar magnitude of the object from 2014 to 2025.

The initial processing included the exclusion of anomalous points. Then, for each year and half-year, the mean signal amplitudes were calculated based on the difference between the minimum and maximum values of the correlated magnitude for the specified time interval. In order to obtain a visualization of temporal changes, the dependence of the mean corrected stellar magnitudes on time was plotted, with the errors of the data considering. The data were grouped by years and visualized in a separate subgraph for each year, thus allowing general trends in the object brightness variations to be identified and possible long-period variations to be estimated. Special attention was paid to the exclusion of incorrect data and anomalies, as well as to the respect of scales in order to facilitate the comparison of plots between years.

A more detailed analysis of changes in the object luminosity amplitude by season was conducted, whereby the average amplitudes for each half-year were calculated. To this end, the data were divided into time intervals depending on the season, and the amplitude values were calculated as the difference between the maximum and minimum mean luminosity values in each half-year. Furthermore, for each amplitude, the error was estimated on the basis of the statistical properties of the sample.

The visualization process involved the utilization of smoothed curves, which were obtained through the implementation of spline interpolation. This methodological approach facilitated the construction of a smooth plot, which depicted the trend of amplitude change over time. This trend revealed long-period variations. Moreover, the original measured values were plotted alongside their respective errors. This methodological approach was adopted to emphasize the validity of the calculations.

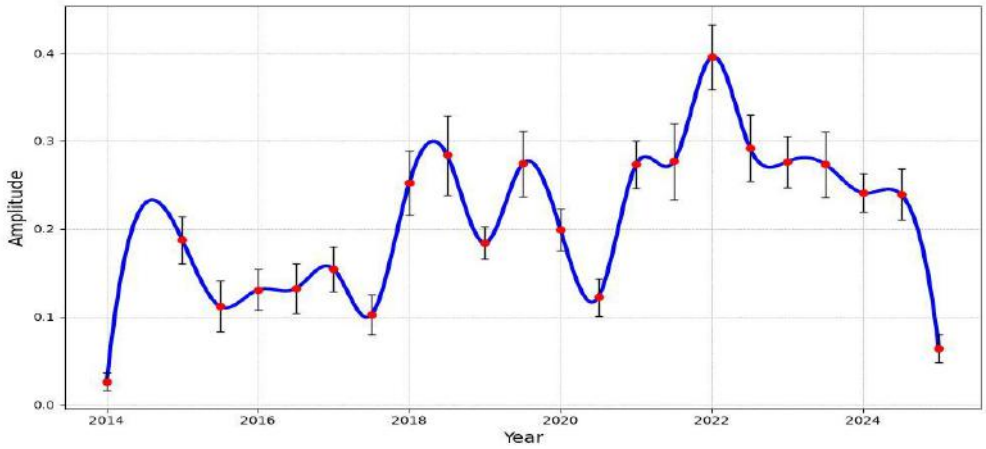

Fig. 5. Long-period changes in the amplitude of stellar magnitude.

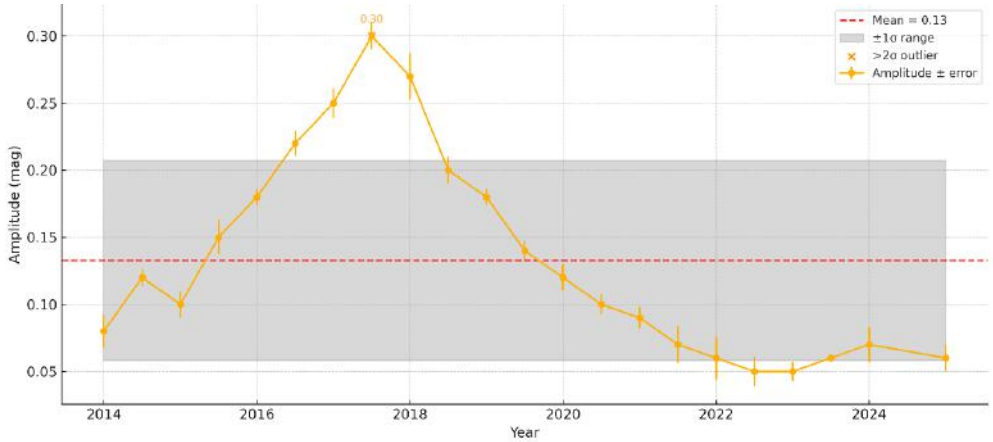

Fig. 6. Estimated amplitude of brightness variations of IRAS 07080+0605 between 2014 and 2025 based on ASAS-SN data. The red dashed line indicates the mean amplitude (~0.13 mag), and the shaded gray area represents the ±1σ confidence interval. Orange points mark outliers exceeding 2σ from the mean, which may reflect significant physical variability in the system, such as changes in pulsation activity or circumstellar dust properties. Error bars correspond to the standard photometric uncertainty for each data point.

The graph illustrates variations in the luminosity amplitude of a star believed to be in the post-AGB transition stage. These fluctuations may reflect changes in the star's physical state, such as pulsations of the outer layers or interactions with the surrounding environment. Periods of increased amplitude may be attributable to enhanced pulsations or changes in the composition and temperature of the star's atmosphere. Smoothed long-period trends may indicate global processes, such as changes in the envelope mass or the gradual decay of the star's activity during this stage of evolution.

4. Conclusion

This paper presents an analysis of time series separated by years, revealing that the period of the system changes over time and the shape of the phase curve undergoes changes at individual intervals. In particular, the appearance of asymmetries in the phase curves indicates possible orbital changes that may be related to the dynamics of the system, including changes in the separation between objects. In the late stages of evolution, such as the transition to post-AGB, a significant amount of mass can be lost through stellar wind, affecting the orbital parameters, including the system momentum, momentum and orbital eccentricity.

The presence of instabilities in the data may result from mass-loss processes and stellar pulsations, as well as the effects of dynamical interactions within the system. During specific time intervals, an uneven distribution of the data is observed, which could indicate the influence of additional factors, such as surrounding matter or complex interactions between the star and its companion.

Furthermore, the role of the circumstellar environment in shaping the photometric behavior of IRAS 07080+0605 should be emphasized. The presence of a non-uniform dust disk and extended envelope likely contributes to the observed light curve asymmetries and amplitude variations. Variable extinction, scattering, and potential interactions with a companion star may account for both short-term irregularities and long-term trends. These effects highlight the need for complementary studies to fully understand the dynamical structure of the system.

The detected photometric instabilities are most likely driven by a combination of stellar pulsations and dynamic interactions within the system. These mechanisms, typical for evolved stars in the post-AGB phase, contribute to both variability in brightness and changes in phase curve morphology. Identifying and disentangling these contributions remains a crucial objective for future studies.

Additionally, the paper describes amplitude variations that may reflect changes in the physical state of the star, such as pulsations of the outer layers or interaction with the environment. In this context, an increase in amplitude may correlate with the lengthening of local periods within cycles. The smallest dispersion of light curve values from the full ASAS SN dataset from 2014 to 2025 minus the long-term trend is obtained by convolution with a period of 126 days.

Conflict of interest statement

The authors declare that they have no conflict of interest in relation to this research, whether financial, personal, authorship or otherwise, that could affect the research and its results presented in this paper.

CRediT author statement

Khokhlov A.A.: Conceptualization, Methodology, Supervision; **Agishev A.T.:** Investigation, Data curation, Writing - Review & Editing, Project administration; **Vaidman N.L.:** Formal analysis, Software, Visualization, Writing - Original Draft; **Agishev A.T.:** Validation, Resources. The final manuscript was read and approved by all authors.

Funding

This research was funded by the Committee on Science of the Ministry of Science and Higher Education of the Republic of Kazakhstan (grant AP19175392 of the Ministry of Education and Science of the Republic of Kazakhstan).

References

1 Miroshnichenko A.S. (2007) Toward understanding the B [e] phenomenon. I. Definition of the galactic FS CMa stars. *Astrophysical Journal*, 667(1), 497-504. https://doi.org/10.1086/520798

2 Miroshnichenko A.S., Zharikov S.V., Danford S., Manset N., Korčáková D., Kříček R., Šlechta M., Omarov Ch.T., Kusakin A.V., Kuratov K.S., Grankin K.N. (2015) Toward Understanding the B[e] Phenomenon. V. Nature and

.

Spectral Variations of the MWC 728 Binary System. *Astrophysical Journal*, 809(2). 129. https://doi.org/10.1088/0004-637X/809/2/129

3 Khokhlov S.A., Miroshnichenko A.S., Mennickent R., Cabezas M., Reichart D.E., Ivarsen K.M., Haislip J.B., Nysewander M.C., LaCluyze A.P. (2017) Fundamental parameters and spectral variations of HD85567. *Astronomical Society of the Pacific Conference Series,* 508, 377. https://doi.org/10.3847/1538-4357/835/1/53

4 Nodyarov A. S., Miroshnichenko A. S., Khokhlov S. A., Zharikov S. V., Manset N., Klochkova V. G., Grankin K. N., Arkharov A. A., Efimova N., Klimanov S., Larionov V. M., Rudy R. J., Puetter R. C., Perry R. B., Reva I. V., Omarov C. T., Kokumbaeva R. I. (2022) Toward Understanding the B[e] Phenomenon. IX. Nature and Binarity of MWC645. *Astrophysical Journal,* 936, 129. https://doi.org/10.3847/1538-4357/ac87a1

5 Khokhlov S. A., Miroshnichenko, A. S., Zharikov, S. V., Manset, N., Arkharov, A. A., Efimova, N., Klimanov, S., Larionov, V. M., Kusakin, A. V., Kokumbaeva, R. I., Omarov, Ch. T., Kuratov, K. S. (2018) Toward Understanding the B[e] Phenomenon. VII. AS 386, a Single-lined Binary with a Candidate Black Hole Component. *Astrophysical Journal*, 856(2), 13. https://doi.org/10.3847/1538-4357/aab49d

6 Miroshnichenko A.S., Zharikov S.V., Manset N., Khokhlov S.A., Nodyarov A.S., Klochkova V.G., Danford S., Kuratova A.K., Mennickent R., Chojnowski D.S., Raj A. and Bisht D. (2023) Recent Progress in Finding Binary Systems with the B[e] Phenomenon. *Galaxies*, 11(1) https://doi.org/10.3390/galaxies11010036

7 Zharikov S., Miroshnichenko A., Reva I., Kokumbaeva R., Omarov C., Danford S., Aarnio A., Manset N., Raj A., Chojnowski S. D., Daglen J. (2025) IRAS 17449+2320: A Possible Binary System with the B[e] Phenomenon and a Strong Magnetic Field. *Galaxies*, 13(2), 32. https://doi.org/10.3390/galaxies13020032

8 Ikonnikova N., Burlak M., Dodin A. (2025) The Photometric Variability and Spectrum of the Hot Post-AGB Star IRAS 21546+4721. *Galaxies*, 13(2), 31. https://doi.org/10.3390/galaxies13020031

9 Kwok S. (2025) Chemical Synthesis in the Circumstellar Environment. *Galaxies*, 13(2), 36. https://doi.org/10.3390/galaxies13020036

10 Kohoutek L., Wehmeyer R. (1999) Catalogue of H-alpha emission stars in the Northern Milky Way. *Astronomy and Astrophysics*, 134, 255. https://doi.org/10.1051/aas:1999101

11 Arias María L., Cidale Lydia S., Kraus Michaela, Torres Andrea F., Aidelman Yael, Zorec Juan, Granada Anahí (2018) Near-infrared Spectra of a Sample of Galactic Unclassified B[e] Stars. *Publications of the Astronomical Society of the Pacific*, 130 (993), https://doi.org/10.1088/1538-3873/aadf23

12 Condori C.A.H., Borges Fernandes M., Kraus M., Panoglou D., Guerrero C.A. (2019) The study of unclassified B[e] stars and candidates in the Galaxy and Magellanic Clouds. *Monthly Notices of the Royal Astronomical Society*, 488(1), 1090-1110. https://doi.org/10.1093/mnras/stz1540

13 Khokhlov S., Miroshnichenko A., Zharikov S., Grankin K., Zakhozhay O., Manset N., Arkharov A., Efimova N., Klimanov S., Larionov V., Khokhlov A., Kusakin A., Omarov C., Kokumbaeva R., Reva I., Agishev A. (2022) Toward Understanding the B[e] Phenomenon. VIII. Nature and Variability of IRAS 07080+0605. *Astrophysical Journal*, 932. https://doi.org/10.3847/1538-4357/ac6de0

14 Pojmanski G. (2002) The all Sky Automated Survey. Catalog of Variable Stars. I. 0 h - 6 h Quarter of the Southern Hemisphere. *Acta Astronomica*, 52, 397-427. https://doi.org/10.48550/arXiv.astro-ph/0210283

15 Kochanek C.S., Shappee B. J., Stanek K. Z., Holoien T.W.-S., Thompson Todd A., Prieto J. L., Dong Subo, Shields J.V., Will D., Britt C., Perzanowski D., Pojmański G. (2017) The All-Sky Automated Survey for Supernovae (ASAS-SN) Light Curve Server v1.0. *Publications of the Astronomical Society of the Pacific*, 129(980), 104502. https://doi.org/10.1088/1538-3873/aa80d9

16 Fukugita M., Ichikawa T., Gunn J.E., Doi M., Shimasaku K., Schneider D.P. (1996) The Sloan Digital Sky Survey Photometric System. *Astronomical Journal,* 111, 1748. https://doi.org/10.1086/117915

17 Scargle J.D. (1982) Studies in astronomical time series analysis. II-Statistical aspects of spectral analysis of unevenly spaced data. *Astrophysical Journal*, 263, 835-853. https://doi.org/10.1086/160554

AUTHORS' INFORMATION

Khokhlov, Azamat - PhD, Al-Farabi Kazakh National University, Almaty, Kazakhstan, Scopus: 57945306100, ORCID: 0000-0001-6987-9058, kh.azamat92@gmail.com

Agishev, Almansur, PhD student, Al-Farabi Kazakh National University, Almaty, Kazakhstan, ORCID: 0009-0004-8989-238X, agishev_almansur2@live.kaznu.kz

Vaidman, Nadezhda, MSc, Al-Farabi Kazakh National University, Almaty, Kazakhstan, Scopus: 58554640500, ORCID: 0000-0002-7449-0108, nva1dmann@gmail.com

Agishev, Aldiyar, PhD, Al-Farabi Kazakh National University, Almaty, Kazakhstan, Scopus: 57201661110, ORCID: 0000-0001-9788-7485, agishev.aldiyar@kaznu.kz

SUMMARIES	ТҮСІНІКТЕМЕЛЕР	АННОТАЦИИ

Ибраев Н.Х., Меньшова Е.П.

Плазмондық нанобөлшектер болған кезде ішкі ауыр атомның синглетті оттегі генерациясына әсері

Күміс нанобөлшектерінің плазмондық өрісінде синглетті оттегінің генерациясына ауыр атомның әсері зерттелді. Сенсибилизаторлар ретінде поливинилбутираль қабыршақтарындағы родамин 123 және дибромродамин 123 бояғыштары қолданылды. Бояғыш қабыршақтары кварцты төсеніш бетінде синтезделген күміс аралшық қабыршақтарға спин-коутинг әдісімен жағылды. Алынған нәтижелер бояғыш молекуласында бром атомының болуы синглетті оттегі өндірісінің тиімділігін арттыратынын көрсетті. Есептелген Штерн-Вольмер константалары Ag нанобөлшектері болған кезде дибромродамин 123 бояғыш молекулаларының триплетті күйлерінің молекулярлық оттегімен сөндірілуінің күшеюін көрсетеді.

Кілт сөздері: :ауыр атомның әсері, интеркомбинациялық конверсия, синглетті оттегі, наноплазмоника, фотосенсибилизатор.

Ибраев Н.Х., Меньшова Е.П.

Эффект внутреннего тяжелого атома на генерации синглетного кислорода в присутствии плазмонных наночастиц

Исследован эффект тяжёлого атома на генерацию синглетного кислорода в плазмонном поле наночастиц серебра. В качестве сенсибилизаторов использованы красители родамин 123 и дибромродамин 123 в плёнках поливинилбутираля. Плёнки красителей были нанесены методом спин-коутинга на островковые плёнки серебра, синтезированные на поверхности кварцевых подложек. Полученные результаты показали, что присутствие атома брома в молекуле красителя увеличивает эффективность производства синглетного кислорода. Вычисленные константы Штерна-Фольмера демонстрируют усиление тушения молекулярным кислородом триплетных состояний молекул красителя дибромродамин 123 в присутствии наночастиц Ag.

Ключевые слова: эффект тяжёлого атома, интеркомбинационная конверсия, синглетный кислород, наноплазмоника, фотосенсибилизатор.

Кучеренко М.Г., Русинов А.П.

Полимерлі қабаттағы O_2 молекулаларының кеңістіктік таралуы мен диффузиялық ағынын көпимпульсті люминесценттік детектірлеу

Берілген жұмыста көпимпульсті белсендіру жағдайында боялған полимерлі үлгідегі тотығу фотореакцияларының кинетикасы зерттелді. Реакция барысында жұмсалатын оттегінің атмосферадан қабат-қабат диффузиялық толықтырылуы ескерілді. Зерттеу барысында оттегі молекулаларының антраценнің иммобилизацияланған молекулаларымен байланысу үдерісі тіркелді. Бұл молекулалар фотосенсибилизатор ретінде органикалық бояғыш (эритрозин) қосылған, оттегі өткізетін поливинилбутираль негізіндегі полимерлі қабықшада орналастырылған. Оттегіге тәуелді фотохимиялық реакциялардың кинетикасын және полимерлі қабаттың көпимпульсті лазерлік әсері кезінде люминесценттік дабылдың қалыптасуын сипаттайтын математикалық модель ұсынылды. Бұл модель белсендіру импульстары арасындағы үзілістерде оттегінің диффузиялық түрде қалпына келуін ескереді. Эксперименттік және есептелген люминесценция дабылдарының салыстырмалы талдауы негізінде полимерлі қабықшадағы фотосенсибилизатор мен тотығатын реагенттің кеңістіктік біртексіз сипатына баға берілді.

Кілт сөздері: синглеттік оттегі, химиялық тұзақтар, баяу флуоресценцияның сөнуі, сенсибилизацияланған активтеу.

Кучеренко М.Г., Русинов А.П.

Многоимпульсное люминесцентное детектирование пространственного распределения реагентов и диффузионного потока молекул O_2 в полимерный слой.

Исследована кинетика окислительных фотореакций в окрашенной полимерной пленке при многократной импульсной активации системы с учетом послойного диффузионного восполнения из атмосферы концентрации расходуемого в реакции кислорода. Регистрировался процесс химического связывания молекул кислорода с иммобилизованными молекулами антрацена в кислородопроницаемой полимерной пленке поливинилбутираля, содержащей, в качестве фотосенсибилизатора, молекулы органического красителя (эритрозин). Предложена математическая модель, описывающая кинетику кислородозависящих фотореакций в пленке и формирование сигналов люминесцентного отклика при ее многоимпульсной лазерной активации с учетом диффузионного восполнения молекул кислорода в промежутках между активирующими импульсами. На основе сравнительного анализа экспериментальных и расчетных сигналов люминесценции проведена оценка характера неоднородного пространственного распределения фотосенсибилизатора и окисляемого реагента в полимерной пленке.

Ключевые слова: Синглетный кислород, химические ловушки, тушение замедленной флуоресценции, сенсибилизированная активация.

Шарапов И., Омарова Г., Садыкова А., Селиверстова Е.

Ag/TiO_2 және Ag/SiO_2 нанобөлшектерінің қасиеттері және олардың жартылай өткізгіш нанокомпозиттің фотокаталитикалық қасиеттеріне әсері

TiO_2 немесе SiO_2 қабығымен қапталған күміс нанобөлшектерінің оптикалық қасиеттері мен электр өрісінің таралуы зерттелді. Плазмонды нанобөлшектердің айналасындағы қабықтың болуы олардың жұтылу жолағының максимумының батохромдық ығысуына әкелетіні көрсетілді. Плазмонды нанобөлшектердің айналасындағы электр өрісінің максималды кернеулігі радиалды түрде шоғырланып, негізінен зерттелген нанобөлшектердің бетінде орналасады. Кванттық тиімділік, яғни сәулеленген фотондардың жұтылған фотондарға қатынасы, Ag/TiO_2 нанобөлшектері үшін Ag/SiO_2-мен салыстырғанда 50%-ға жоғары. Ag/TiO_2 және Ag/SiO_2 ядро/қабық нанобөлшектері болған жағдайда TiO_2/rGO нанокомпозитінің фотокаталитикалық белсенділігі тиісінше 2,7 және 1,7 есеге артады. Бақыланған өзгерістер TiO_2/rGO заряд тасымалдау қасиеттерінің жақсаруымен және нанобөлшектерден жартылай өткізгішке ыстық электрондардың инжекциясымен байланысты.

Кілт сөздері: плазмон, нанобөлшектер, оптикалық қасиеттер, фотокатализ, нанокомпозиттер.

Шарапов И., Омарова Г., Садыкова А., Селиверстова Е.

Свойства наночастиц Ag/TiO_2 и Ag/SiO_2 и их влияние на фотокаталитические свойства полупроводникового нанокомпозита

Изучены оптические свойства и распределение напряженности электрического поля вокруг наночастиц серебра с оболочкой из TiO_2 или SiO_2. Показано, что наличие оболочки вокруг плазмонной наночастицы приводит к батохромному сдвигу максимума её полосы поглощения. Максимальная напряженность электрического поля вокруг плазмонных наночастиц сконцентрирована радиально и преимущественно на поверхности исследуемых наночастиц. Оценка квантовой эффективности, которая в физическом смысле представляет отношение числа излученных фотонов к числу поглощенных фотонов для наночастиц Ag/TiO_2 почти на 50% больше, чем для Ag/SiO_2. В присутствии наночастиц ядро/оболочка состава Ag/TiO_2 и Ag/SiO_2 фотокаталитическая активность нанокомпозита TiO_2/rGO увеличивается в 2,7 и 1,7 раза, соответственно. Наблюдаемые изменения связаны как с улучшением зарядо-транспортных свойств TiO_2/rGO, так и возможной инжецией горячих электронов от наночастиц в полупроводник.

Ключевые слова: плазмон, наночастицы, оптические свойства, фотокатализ, нанокомпозиты.

Ахат Р., Амангелды Н., Баратова А.А., Ануар А., Райымбеков Е., Ерғалиұлы Ғ.

^{13}C және ^{19}F ядроларымен ^{15}N бөлшектерінің серпімді шашырауын феноменологиялық, жартылай микроскопиялық және CRC-талдау арқылы жан-жақты зерттеу

Бұл зерттеуде ^{15}N+ ^{13}C реакциясы үшін E_{lab} = 30.0, 32.0 және 45.0 МэВ ал ^{15}N + ^{19}F жүйесі үшін E_{lab} = 23.0, 26.0 и 29.0 МэВ сәуле энергияларында алынған бұрыштық таралуларды кешенді талдау жүргізілді. Зерттеу оптикалық модельді, еселік фолдинг моделін және реакция арналарының байналысқан әдісін (CRC) қолдану арқылы жүзеге асырылды. Жұмыстың басты мақсаты феноменологиялық және жартылай микроскопиялық тәсілдер арқылы оптикалық потенциалдың оңтайлы параметрлерін анықтау болды. Нәтижесінде екі ядролық жүйе үшін потенциал параметрлері мен олардың энергияға тәуелділігі есептеліп шығарылды. Теориялық модельдер тәжірибелік бұрыштық таралуларды дәл сиппаттай алды. Артқы бұрыштардағы шашырауды талдау кезінде CRC әдісімен алынған нәтижелер тәжірибе мәліметтерімен өте жақсы сәйкес келді. Сондай-ақ $^{15}N \rightarrow {}^{13}C + d$ және $^{19}F \rightarrow {}^{15}N + \alpha$ конфигурациялары үшін түрлі энергиялардағы ^{15}N иондарының спектроскопиялық амплитудалары есептелді. Алынған нәтижелер бұрын жарияланған деректермен салыстырылып, осы зерттеудің дәлдігі мен үйлесімділігін бағалауға мүмкіндік берді.

Кілт сөздері: серпімді шашырау, оптикалық модель, екілік фолдинг модель, серпімді тасымал, спектроскопиялық амплитуда.

Ахат Р., Амангелды Н., Баратова А.А., Ануар А., Райымбеков Е., Ерғалиұлы Ғ.

Комплексный феноменологический, полумикроскопический и CRC анализ упругого рассеяния ^{15}N на ядрах ^{13}C и ^{19}F

В настоящем исследовании угловые распределения, полученные при энергиях пучка E_{lab} = 30.0, 32.0 и 45.0 МэВ для реакции ^{15}N + ^{13}C и E_{lab} = 23.0, 26.0 и 29.0 МэВ для системы ^{15}N + ^{19}F, были проанализированы с использованием оптической модели, модели двойного фолдинга и метода сопряжённых каналов (CRC). Основной целью работы было определение оптимального оптического потенциала путём феноменологического и полумикроскопического анализа. В результате детальных расчётов были получены приемлемые параметры потенциалов и их зависимость от энергии для обеих ядерных систем. Отмечено, что теоретические модели хорошо воспроизводят экспериментальные угловые распределения. При анализе рассеяния на больших углах

метод CRC показал высокое соответствие с экспериментальными данными. В результате анализа были извлечены спектроскопические амплитуды для конфигураций $^{15}N \rightarrow {}^{13}C + d$ и $^{19}F \rightarrow {}^{15}N + \alpha$ при различных энергиях падающих ионов ^{15}N. Полученные значения спектроскопических амплитуд были сопоставлены с ранее опубликованными данными, что позволило оценить согласованность и точность настоящего исследования.

Ключевые слова: упругое рассеяние, оптическая модель, модель двойного фолдинга, упругий перенос, спектроскопическая амплитуда

Rohmawati L., Ferdianto S.P., Ma'arif M.S., Ardiansyah F.F., Muadhif F.I., Setyarsih W., Supardi Z.A.I., Darminto D.

Ананас қабығының экстрактынан алынған ZnO нанобөлшектерін Cu элементімен легирленген және табиғи бояғыштың модификацияланған ерітіндісі арқылы бояғышпен сенсибилизацияланған күн элементтерінің тиімділігін арттыру

Бояғышпен сенсибилизацияланған күн элементтерінің тұрақтылығы мен тиімділігі үшін фотоанодтар мен бояғыш ерітінділері шешуші рөл атқарады. Осы зерттеуде фотоанод ретінде ананас қабығының экстрактынан биоредукция арқылы «жасыл синтез» әдісімен алынған Cu элементімен легирленген ZnO үлгісі қолданылды. Сонымен қатар, мацерация әдісімен дайындалған бояғыш ерітіндісі тұт ағашының жемісі мен моринга жапырақтарының экстракттарынан алынды. Сенсибилизацияланған күн элементтерінде қолдану үшін 1%, 3%, 5% және 10% Cu концентрацияларымен легирленген ZnO фотоанодтары ITO шыны бетіне шөгіріліп, бір тәулік бойы бояғыш ерітіндісіне малынды. Кейін бұл үлгілердің электрөткізгіштігі мен күн элементінің тиімділігі бағаланды. Фотоанодтағы Cu легирлеу концентрациясының артуы сенсибилизацияланған күн элементтерінің өнімділігіне әсер ететіні анықталды. Нәтижесінде, 5% Cu легирленген ZnO фотоаноды 12 мс электрон өмір сүру уақытымен 1,67% ең жоғары тиімділікті көрсетті, бұл Cu легирленбеген немесе 1%, 3% және 10% концентрацияларымен легирленген үлгілермен салыстырғанда жоғары көрсеткіш. Осылайша, табиғи материалдардан алынған бояғыш ерітінділері мен Cu элементімен легирленген ZnO нанобөлшектері бояғышпен сенсибилизацияланған күн элементтері үшін болашақта қолдануға тиімді материалдар ретінде дамытылуы мүмкін.

Кілт сөздері: бояғышпен сенсибилизацияланған күн элементтері, ZnO нанобөлшектері, Cu легирлеу, бояғыш ерітіндісі, жасыл синтез.

Rohmawati L., Ferdianto S.P., Ma'arif M.S., Ardiansyah F.F., Muadhif F.I., Setyarsih W., Supardi Z.A.I., Darminto D.

Повышение эффективности сенсибилизированных красителем солнечных элементов с использованием легирования Cu из экстракта кожуры ананаса наночастицами ZnO с помощью модифицированного раствора натурального красителя.

Фотоаноды и растворы красителей незаменимы для стабильности и эффективности работы сенсибилизированных красителем солнечных элементов. В этом исследовании фотоанод использует образец ZnO, легированный Cu, изготовленный с использованием метода зеленого синтеза с биовосстановлением из экстракта кожуры ананаса. Между тем, с использованием метода мацерации раствор красителя изготавливается из экстракта плодов шелковицы и листьев моринги. Для применения в сенсибилизированных красителем солнечных элементах фотоаноды ZnO, легированные 1%, 3%, 5% и 10% Cu, были истощены на стекле ITO и погружены в раствор красителя на один день. Затем результаты были проверены на электропроводность и производительность в сенсибилизированных красителем солнечных элементах. Добавление концентрации легирования Cu к фотоаноду ZnO может повлиять на производительность сенсибилизированного красителем солнечного элемента. В этой работе образец ZnO, легированный 5% Cu в качестве фотоанода, показал самую высокую эффективность в 1,67% со временем жизни электронов 12 мс по сравнению с фотоанодом без легирования Cu или с легированием Cu при концентрациях 1%, 3% и 10%. Таким образом, легированные Cu наночастицы ZnO и растворы красителей из природных материалов могут быть дополнительно разработаны для приложений сенсибилизированных красителем солнечных элементов. Ключевые слова: сенсибилизированные красителем солнечные элементы, наночастицы ZnO, легирование Cu, раствор красителя, зеленый синтез.

Дуйсенбаева М. С., Шрагер Э. Р., Сакипова С.Е., Нусупбеков Б. Р.

Органикалық қалдықтардан құнды компоненттерді тиімді алу үшін электро-гидро-импульсті өңдеудің оңтайлы энергетикалық параметрлерін зерттеу

Мақалада қалдықтарды, атап айтқанда, тамақ өнеркәсібінің жаңартылатын биоқалдықтарын қайта өңдеуге қатысты өзекті мәселені шешудің кейбір аспектілері қарастырылады. Әртүрлі органикалық қалдықтарды өңдеу мен кәдеге жаратудың заманауи технологияларын әзірлеу және енгізу қазба энергия көздеріне тәуелділікті азайтуға, көміртегі бейтараптығына қол жеткізуге және экологиялық қауіпсіздікті сақтауға мүмкіндік береді. Зерттеу нысаны сүйек массасы түріндегі агроөнеркәсіптік кешеннің органикалық қалдықтары болып табылады.

Электро-гидроимпульсті өңдеуді қолдана отырып, құнды компонентті тиімді алу мүмкіндіктері эксперименттік түрде зерттелді. Электр-гидроимпульстік қондырғының принципиалды сұлбасы мен әртүрлі өңдеу режимдерінде сынау әдістемесі сипатталған. Өңдеу уақытын қысқарта отырып, органикалық шикізаттан құнды компоненттерді алу дәрежесін арттыруға мүмкіндік беретін электротехникалық параметрлердің оңтайлы мәндері анықталды.
Кілт сөздері: электро-гидроимпульстік қондырғы, ұшқындық разряд, өңдеу, органикалық қалдықтар, сүйек массасы, құнды компоненттер

Дуйсенбаева М. С., Шрагер Э. Р., Сакипова С.Е., Нусупбеков Б. Р.
Исследование оптимальных энергетических параметров электро-гидроимпульсной обработки для эффективного извлечения ценных компонентов из органических отходов.
В статье рассматриваются некоторые аспекты решения актуальной проблемы, связанной с переработкой отходов, в частности, возобновляемых биоотходов пищевой промышленности. Разработка и внедрение современных технологий обработке и утилизации различных органических отходов позволит снизить зависимость от ископаемых источников энергии, достичь углеродной нейтральности и сохранить экологическую безопасность. Объектом исследования является органические отходы агропромышленного комплекса в виде костной массы. Экспериментально исследованы возможности эффективного извлечения ценного компонента с применением электро-гидроимпульсной обработки. Приведено описание принципиальной схемы электро-гидроимпульсной установки и методики проведения испытаний при разных режимах обработки. Определены оптимальные значения электротехнических параметров, позволяющие увеличить степень экстрагирования ценных компонентов из органического сырья с одновременным сокращением времени обработки.
Ключевые слова: электро-гидроимпульсная установка, искровой разряд, обработка, органические отходы, костная масса, ценные компоненты.

Аскарова А.С., Болегенова С.А., Оспанова Ш.С., Максутханова А.М., Болегенова К.А., Байдуллаева Г.Е.
Биоотын тамшыларының бүрку және жануының жылуфизикалық динамикасын зерттеу.
Мақалада тікелей бүрку қозғалтқышының жану камерасында биоотын (биодизель) тамшыларының бүрку және турбулентті жануы кезінде жүзеге асырылатын жылуфизикалық процестерді 3D компьютерлік модельдеу зерттеу ұсынылған. Осы мақсатта күрделі турбулентті әсерлесуші ағынды есептеуге арналған математикалық, кеңістіктік және сандық қосалқы модельдерді қамтитын кешенді компьютерлік модель әзірленді. Әзірленген модельді пайдалана отырып, жану камерасындағы температура мен қысымның өзгеруінің әсерін ескере отырып, биодизельдің әсерлесуші отын-ауа қоспасының жылулық және аэродинамикалық қасиеттерін зерттеу үшін 3D есептеу эксперименттері жүргізілді. Зерттеу нәтижелері биодизельді жағу кезіндегі температуралық және зиянды қалдықтардың концентрациялық сипаттамаларымен әсерлесуші ағынның 3D визуализациясын алуға мүмкіндік берді. Модельдеу кезінде алынған сандық мәліметтер дәстүрлі дизельдік отынның нәтижелерімен салыстырылды.
Кілт сөздері: биоэнергетика, биоотын, бүрку, кешенді модель, аккумуляторлық отын жүйесі, 3D визуализация, зиянды қалдықтар.

Аскарова А.С., Болегенова С.А., Оспанова Ш.С., Максутханова А.М., Болегенова К.А., Байдуллаева Г.Е.
Исследование теплофизической динамики при распылении и горении капель биотоплива.
В статье представлено исследование 3D компьютерного моделирования теплофизических процессов, происходящих при распылении и турбулентном горении капель биотоплива (биодизеля) в камере сгорания двигателя с непосредственным впрыском. Для этого была разработана комплексная компьютерная модель, включающая математическую, пространственную и численную подмодели для расчета сложного турбулентного реагирующего течения. С использованием разработанной модели были проведены 3D вычислительные эксперименты по исследованию тепловых и аэродинамических свойств реагирующей топливно-воздушной смеси биодизеля с учетом влияния изменения температуры и давления в камере сгорания. Результаты исследований позволили получить 3D визуализацию реагирующего течения с температурными и концентрационными характеристиками вредных выбросов при сжигании биодизеля. Полученные в ходе моделирования численные данные сравнивались с результатами для традиционного дизельного топлива.
Ключевые слова: биоэнергетика, биотопливо, распыление, комплексная модель, аккумуляторная топливная система, 3D визуализация, вредные выбросы.

Супрун Т.Т.
Жылуэнергетикалық жабдықтағы тасымалдау процестерін бағалауға жергілікті тәсілді қолдануды жалпылау
Жұмыс беттерінің және жылутасымалдағышты жеткізу жүйесінің жылу тиімділігін арттыру шараларын әзірлеу үшін сыртқы (артқан турбуленттілік) және ішкі (ажырау) турбуленттік әсерлердің күрделі өзара әрекеттесу

жағдайындағы тасымалдау процестерін кешенді зерттеу нәтижелерін талдау қажет. Бұл құбылыстар жылуэнергетикалық жабдыққа тән. Зерттеудің мақсаты - жұмыс ортасының сипаттамалық аймақтарында жылуфизикалық параметрлерді жергілікті бақылауға негізделген жылуэнергетикалық жабдықтағы тасымалдау процестерін бағалау әдістерін әзірлеу болып табылады. Зерттеу нысаны ретінде энергетикалық, химиялық және электрондық жабдықтардың жылуалмасу беттері мен жылутасымалдағышты жеткізу жүйелері алынды. Зерттеу әдістері ретінде түрлі табиғаттағы турбуленттік құбылыстар мен жылу, импульс және масса тасымалдау процестерін физикалық модельдеу, термоанемометриялық және электрокалориметриялық өлшеу әдістері, сондай-ақ жылу мен масса ұқсастықтар әдістері қолданылды. Мақалада түрлі мақсаттағы жылуэнергетикалық жабдықтың ағындық бөлігінде артқан турбуленттіліктің, жергілікті тұйық ажыраулардың және бейстационарлық ағындардың тасымалдау процестеріне әсерін бағалау мысалдары арқылы жергілікті тәсілді қолданудың жалпылауы қарастырылған. Сонымен қатар өсімдік қалдықтарының фрагменттерін кептіру технологиясына арналған жылутасымалдағышты жеткізу жүйесін әзірлеу барысында жергілікті тәсілді қолдану талданды. Алынған нәтижелер жұмыс беттерінің жылу тиімділігін арттыру бойынша шаралар әзірлеудің негізі болып табылады.

Кілт сөздері: жергілікті жылуфизикалық параметрлер, жергілікті аэродинамикалық сипаттамалар, жылуалмасу беттері, жылутасымалдағышты жеткізу жүйесі.

Супрун Т.Т.

Обобщение применения локального подхода к оценке процессов переноса в теплоэнергетическом оборудовании

Для разработки мер по повышению тепловой эффективности рабочих поверхностей и системы подачи теплоносителя необходимо рассмотреть и проанализировать результаты комплексных исследований процессов переноса в сложных условиях взаимодействия внешних (повышенная турбулентность) и внутренних (отрыв) турбулентных эффектов, характерных для теплоэнергетического оборудования. Целью работы является разработка методов оценки процессов переноса в таком оборудовании на основе локального контроля теплофизических параметров в характерных зонах рабочей среды. Объектом исследования являются теплообменные поверхности энергетического, химического и электронного оборудования, а также систем подачи теплоносителя. Методом исследования является физическое моделирование турбулентных явлений различной природы и процессов переноса тепла, импульса и массы с использованием термоанемометрических, электрокалориметрических методов, а также методов аналогии тепла и массы. В статье рассмотрено обобщение применения локального подхода на примерах оценки влияния повышенной турбулентности, местных замкнутых отрывов и нестационарных течений на процессы переноса в проточной части теплоэнергетического оборудования различного назначения. Также рассмотрен локальный подход к разработке эффективной системы подачи теплоносителя для технологии досушивания фрагментов растительных отходов. Полученные результаты являются основой для разработки мероприятий по повышению тепловой эффективности рабочих поверхностей.

Ключевые слова: локальные теплофизические параметры, локальные аэродинамические характеристики, поверхности теплообмена, система подачи теплоносителя.

Шаймерденова К.М., Тлеубергенова А.Ж., Танашева Н.К., Дюсембаева А.Н., Миньков Л.Л., Бахтыбекова А.Р.

Құрамалы қалақшалары бар жел энергетикалық қондырғының аэродинамикалық сипаттамаларын арттыру: аэродинамика мен қысым таралуының сандық және эксперименттік талдау.

Жел энергетикалық қондырғылардың тиімділігін арттыру жаңартылатын энергия көздеріне сұраныстың өсуі жағдайында өзекті міндет болып табылады. Бұл жұмыста қозғалмайтын профильдер мен айналмалы цилиндрлерді біріктіретін, екі құрамалы қалақшалармен жабдықталған, жел энергетикалық қондырғының аэродинамикалық сипаттамалары зерттелді. Зерттеу нысаны – ағын бағытын оңтайландыруға және көтеру күшін ұлғайтуға арналған қондырғы моделі. Әдіснама Ansys Fluent пакетіндегі сандық моделдеуді және зертханалық жағдайларда эксперименттік сынақтарды қамтиды. Негізгі нәтижелер ауа ағынының жылдамдығы 3-тен 12 м/с-қа дейін артқан кезде тарту күші 0,5 Н-дан 3,85 Н-қа дейін артатынын көрсетеді. Тарту коэффициенті Рейнольдс санының өсуімен 1,45-тен 1,05-ке дейін азаяды, бұл турбуленттік режимге көшу кезінде аэродинамикалық сипаттамалардың жақсарғанын дәлелдейді. Қалақшалардың бетіндегі ең аз және ең жоғары қысымды салыстырмалы талдау айналу жылдамдығының өсуі мен қысым айырымының артуы арасындағы күшті корреляцияны анықтады: p_{max} шамамен 0,4 Па-дан 0,7 Па-ға дейін, ал p_{min} – 0,15 Па-дан 0,4 Па-ға дейін өседі. Сандық және эксперименттік деректерді салыстыру 5%-дан аспайтын айырмашылықты көрсетті, бұл модельдің дұрыстығын және әдістеменің дұрыстығын растайды. Қорытындылар құрамалы қалақшаларды қолдану жел энергетикалық қондырғылардың аэродинамикалық тиімділігін дәстүрлі конструкциялармен салыстырғанда 8-10%-ға арттыруға мүмкіндік беретінін көрсетеді. Бұл жақсару жел энергетикасының неғұрлым тиімді және орнықты жүйелерін, әсіресе жел әлеуеті төмен және орташа өңірлерде құруға ықпал етуі мүмкін.

Кілт сөздері: жел энергетикалық қондырғы, құрамалы қалақшалар, қысымның таралуы, аэродинамикалық сипаттамалар, сандық модельдеу.

Шаймерденова К.М., Тлеубергенова А.Ж., Танашева Н.К., Дюсембаева А.Н., Миньков Л.Л., Бахтыбекова А.Р.

Повышение аэродинамических характеристик ветроэнергетической установки с комбинированными лопастями: числовой и экспериментальный анализ аэродинамики и распределения давления

Повышение эффективности ветроэнергетических установок является актуальной задачей в условиях растущего спроса на возобновляемые источники энергии. В данной работе исследуются аэродинамические характеристики ветроэнергетической установки, оснащённой двумя комбинированными лопастями, сочетающими неподвижные профили и вращающиеся цилиндры. Объект исследования - модель установки, предназначенная для оптимизации направления потока и увеличения подъёмной силы. Методология включает численное моделирование в пакете Ansys Fluent и экспериментальные испытания в лабораторных условиях. Основные результаты показывают, что при увеличении скорости воздушного потока с 3 до 12 м/с тяга возрастает с 0,5 Н до 3,85 Н. Коэффициент тяги уменьшается с 1,45 до 1,05 с ростом числа Рейнольдса, что свидетельствует об улучшении аэродинамических характеристик при переходе к турбулентному режиму. Сравнительный анализ минимального и максимального давлений на поверхности лопастей выявил сильную корреляцию между ростом скорости вращения и увеличением перепада давлений: p_{max} возрастает приблизительно с 0,4 Па до 0,7 Па, а p_{min} — с 0,15 Па до 0,4 Па. Сопоставление численных и экспериментальных данных показало расхождение не более 5 %, что подтверждает достоверность модели и корректность методики. Выводы указывают, что применение комбинированных лопастей позволяет повысить аэродинамическую эффективность ветроэнергетических установок на 8–10 % по сравнению с традиционными конструкциями. Это улучшение может способствовать созданию более эффективных и устойчивых систем ветроэнергетики, особенно в регионах с низким и средним ветровым потенциалом.

Ключевые слова: ветроэнергетическая установка, комбинированные лопасти, распределение давления, аэродинамические характеристики, численное моделирование.

Кенбай А.А., Ережеп Д.Е., Алдияров А.У.

Көмірсутек материалдарының ИҚ Фурье-спектроскопиясы үшін төмен температуралық ұяшықты әзірлеу.

Бұл жұмыста көмірсутекті материалдардың төмен температурада және атмосфералық қысымда FTIR спектроскопия технологиясы көрсетілген. Бұл құрылғы әртүрлі заттардың оптикалық қасиеттерін 77 – 300 К температура диапазонында вакуумсыз зерттеуге және бұл салада зерттеулер жеткіліксіз болғандықтан жаңа іргелі мәліметтер алуға мүмкіндік береді. Сипатталған жаңа әдістер мен әдістемелер FTIR спектрометрімен, диффузиялық шағылыстыру қондырғысымен және екі Дьюар ыдысымен жұмыс істейді, криогендік капиллярлық жүйеде сұйық азотпен салқындату және ИҚ-белсенді емес ортаны құру үшін газды азотпен үрлеу. Бұл жаңа әдістемені теориялық ақпарат ретінде білім беру саласымен қатар әртүрлі энергетикалық және инфрақұрылымдық салалар үшін пайдалы принципті жаңа деректерді алудың құнды әдісіне айналдырады.

Кілт сөздер: FTIR спектроскопиясы, төмен температура, ұяшық, криогенді капиллярлық жүйе, көмірсутекті материалдар.

Кенбай А.А., Ережеп Д.Е., Алдияров А.У.

Разработка низкотемпературной ячейки для ИК Фурье-спектроскопии углеводородных материалов.

В данной работе представлена технология ИК-Фурье спектроскопии углеводородных материалов при низких температурах и атмосферном давлении. Это устройство позволяет изучать оптические свойства различных веществ в диапазоне температур 77 – 300 К без необходимости использования вакуума и получать новые фундаментальные данные, поскольку исследований в этой области недостаточно. Описаны новые методики и методы работы с ИК-Фурье спектрометром, приставкой диффузного отражения и двумя сосудами Дьюара, использующими для охлаждения жидким азотом внутри криогенной капиллярной системы и продувки газообразным азотом для создания ИК-неактивной среды. Это делает новую методику ценным методом получения принципиально новых данных, полезных для различных сфер энергетики и инфраструктуры, а также для области образования в качестве теоретической информации.

Ключевые слова: ИК Фурье-спектроскопия, низкая температура, ячейка, криогенная капиллярная система, углеводородные материалы.

Гученко С.А., Сельдюгаев О.Б., Фомин В.Н., Афанасьев Д.А.

Магналийдің коррозияға тізімділігін болжау.

Ұсынылған жұмыста теңіз суындағы магнийдің (AMg қорытпалары – алюминий-магний қорытпасы) беріктігі мен коррозия жылдамдығына әсер ететін факторлар зерттелді. Қанықпаған альфа-қатты ерітінділерде алюминий құрылымындағы магнийдің негізгі түрі алюминий ұяшықтарындағы орторомбты ішкі жүйесінің

бөлігі болып табылатын Mg_2Al_4 электрондық қосылысы болып табылатыны көрсетілген. Есептеу көрсеткендей, алюминий ұяшықтарында орторомбты ішкі жүйе ретінде Mg_2Al_4 тобы неғұрлым көп болса, соғұрлым бұл қорытпалардың беріктігі жоғары болады. РМ3 әдісі құрамында Mg_2Al_4 тобы бар алюминий ұяшықтары мен таза алюминий ұяшықтарының галоген иондарымен жойылу механизмін анықтау үшін қолданылды. Ұяшықтардың екі түрінің де жойылуы бірдей сценарий бойынша, теңіз суымен шектесетін ұяшықтарының жоғарғы жағындағы орталық атомның галоген иондары арқылы ажырауы арқылы жүреді. Теңіз суында құрамында Mg_2Al_4 тобы бар алюминий элементтерінің коррозия жылдамдығы таза алюминий элементтерінің коррозия жылдамдығынан жоғары екені дәлелденді. Теңіз суындағы магнийдің төмен массалық үлесі (3,5% қоса алғанда магний) бар магнийдің коррозия жылдамдығының өзгеруін есептеуге мүмкіндік беретін математикалық модель әзірленді. Модель негізгі легирлеуші элементтердің (Mg, Cr, Mn, Zn, Ti, Cu) массалық үлесінің коррозия жылдамдығына әсерінің өзгеруін есепке алуға мүмкіндік береді. Алюминий қорытпасының үш нұсқасы үшін теңіз суындағы коррозия жылдамдығының өзгеруі осы модель арқылы есептелді. Алюминий-магний қорытпасының бұл нұсқаларына легірлеуші элементтердің Cr және Mn мөлшерінің жоғарылауымен 2,6 масса% құрайтын магний кіреді.
Кілт сөздер: коррозия, алюминий-магний қорытпасы, магний, алюминий, текше ішкі жүйе, галогендер, кванттық химиялық есептеулер.

Гученко С.А., Сельдюгаев О.Б., Фомин В.Н., Афанасьев Д.А.
Прогнозирование коррозиционной стойкости магналиев.
В представленной работе рассмотрены факторы, влияющие на прочность и скорость коррозии в морской воде магналиев (сплавов АМг - алюминиево-магниевый сплав). Показано, что в ненасыщенных твердых альфа растворах основной формой магния в структуре алюминия является электронное соединение Mg_2Al_4 , входящее в ромбическую подсистему ячеек алюминия. Расчет показал, что чем больше ячеек алюминия содержат в качестве ромбической подсистемы группу Mg_2Al_4, тем выше прочность данных сплавов. Методом РМ3 определен механизм разрушения ионами галогенов ячеек чистого алюминия и ячеек алюминия содержащих группу Mg_2Al_4. Разрушение обоих типов ячеек происходит по одинаковому сценарию, через отрыв ионами галогенов центрального атома в верхней грани ячеек, граничащих с морской водой. Показано, что в морской воде скорость коррозии ячеек алюминия содержащих группу Mg_2Al_4 больше, чем скорость коррозии ячеек чистого алюминия. Разработана математическая модель, позволяющая рассчитать изменение скорости коррозии магналиев с низкой массовой долей магния (до 3,5 % магния включительно) в морской воде. Модель позволяет учитывать изменение влияния массовой доли основных легирующих элементов (Mg, Cr, Mn, Zn, Ti, Cu) на скорость коррозии. Изменение скорости коррозии в морской воде трех вариантов сплава алюминия рассчитано с использованием данной модели. Эти варианты алюминиево-магниевых сплавов включают содержание магния 2,6 массовых % с повышенным содержанием легирующих элементов Cr и Mn.
Ключевые слова: Коррозия, алюминиево-магниевый сплав, магналий, алюминий, кубическая подсистема, галогены, квантово-химические расчеты.

Волокитина И.Е., Панин Е.А., Волокитин А.В., Федорова Т.Д., Латыпова М.А., Махмутов Б.Б.
Жаңа біріктірілген технологиямен деформациялау кезіндегі шыбықтың кернеулі-деформациялық күйін зерттеу
Бұл жұмыста радиалды-ығысу тарту мен дәстүрлі созудың біріктірілген деформациялау технологиясын ақырлы элементтер әдісі арқылы модельдеу нәтижелері келтірілген. DEFORM бағдарламасы көмегімен кернеулі-деформациялық күй параметрлері мен деформация күштері зерттелді. Әр түрлі бастапқы диаметрдегі дайындамалармен, бір реттік және толық қысумен, сондай-ақ әртүрлі қыздыру температураларымен бірнеше модельдер қарастырылды. Зерттеу нәтижелері бойынша, 900°С температурада 30–25–20 сұлбасы оңтайлы жағдайлармен сипатталады. Алайда, бұл сұлба деформациялаушы жабдықтың жеткілікті беріктігі жағдайында ғана ұсынылады. Басқа жағдайларда шекті жүктемелерден аспайтын деформацияны қамтамасыз ететін сұлбаларды таңдау қажет.
Кілт сөздері: созу, модельдеу, шыбық, болат, кернеулі-деформациялық күй.

Волокитина И.Е., Панин Е.А., Волокитин А.В., Федорова Т.Д., Латыпова М.А., Махмутов Б.Б.
Исследование напряженно-деформированного состояния прутка при деформировании новой совмещенной технологии
В данной работе представлены результаты конечно-элементного моделирования новой технологии комбинированного деформирования радиально-сдвиговой протяжки и традиционного волочения. С помощью программы DEFORM исследованы параметры напряженно-деформированного состояния и силы деформирования. Рассматривался ряд моделей с различными начальными диаметрами заготовки, однократным и полным обжатием, различными температурами нагрева заготовки. Выявлено, что оптимальные условия имеет схема 30-25-20 при температуре 900°С. Однако данная схема может быть рекомендована при достаточной прочности деформирующего оборудования. В остальных случаях

необходимо выбирать схему, обеспечивающую деформацию без превышения предельных нагрузок.
Ключевые слова: волочение, моделирование, пруток, сталь, напряженно-деформированное состояние.

Турмаганбет У., Жексебай Д., Турлыкожаева Д., Скабылов А., Ахтанов С. Темешева С., Масалим П., Тао М.
Термиялық инфрақызыл нысандарды YOLO модельдері арқылы анықтау.

Объектілерді анықтау - компьютерлік көру және қашықтан зондтаудағы негізгі міндет, ол кескіндердегі объектілердің әртүрлі түрлерін тануға және санаттарға бөлуге бағытталған. Ұшқышсыз әуе аппаратурасының термиялық инфрақызыл қашықтан зондтауы қоғамдық қолданбаларда негізгі деректер көзі ретінде қызмет ететін маңызды көп сценарийлі кескіндер мен бейнелерді қамтамасыз етеді. Дегенмен, бұл кескіндердегі нысандарды анықтау күрделі көрініс ақпаратына, көрінетін спектрлік бейнемен салыстырғанда төмен ажыратымдылыққа және жалпыға қолжетімді таңбаланған деректер жиыны мен оқытылған үлгілердің болмауына байланысты қиын болып қала береді. Бұл құжат жалпыға қолжетімді қолданбаларда кескін және бейне талдауы үшін ұшқышсыз негізделген нысанды анықтау құрылымын ұсынады және YOLOv8n/v8s, YOLOv11n/v11s және YOLOv12n/v12s үлгілерінің жер үсті жылу инфрақызыл кескіндерінен мүмкіндіктерді алудағы өнімділігін бағалайды және сонымен қатар тікелей камералардан түсірілген бейнелер мен бейнелерді, әртүрлі бұрыштардан түсірілген инфрақызыл бейнелер. YOLOv8n/v8s, YOLOv11n/v11s және соңғы YOLOv12n/v12s үлгілері Raspberry Pi 5 жүйесінде OpenVINO құрылымы арқылы орналастырылған. Бұл модельдерді сәтті орналастыру, соның ішінде соңғы нұсқасы, олардың ұшқышсыз термиялық инфрақызыл нысандарды анықтауға жарамдылығын көрсетеді. Нәтижелер YOLOv8 және YOLOv11 жоғары дәлдік пен сәйкесінше 93% және 92% еске түсіру көрсеткіштеріне қол жеткізгенін көрсетеді, ал YOLOv12 моделі жақсы дәлдікті көрсетті, бірақ салыстырмалы түрде төмен дәлдік пен еске түсіру жылдамдығы, әрі қарай жетілдіруге мүмкіндік береді.
Кілт сөздері: Объектілерді анықтау, YOLO үлгілері, ұшқышсыз ұшу аппараттары, алға қарай бағытталған инфрақызыл камералар, термиялық инфрақызыл кескіндер, Raspberry Pi 5.

Турмаганбет У., Жексебай Д., Турлыкожаева Д., Скабылов А., Ахтанов С. Темешева С., Масалим П., Тао М.
Тепловое инфракрасное обнаружение объектов с помощью моделей YOLO.

Обнаружение объектов является фундаментальной задачей в компьютерном зрении и дистанционном зондировании, направленной на распознавание и категоризацию различных типов объектов на изображениях. Беспилотное летательное аппаратное тепловое инфракрасное дистанционное зондирование обеспечивает важные многосценарные изображения и видео, выступая в качестве ключевых источников данных в общественных приложениях. Однако обнаружение объектов на этих изображениях остается сложной задачей из-за сложной информации о сцене, более низкого разрешения по сравнению с видео в видимом спектре и нехватки общедоступных маркированных наборов данных и обученных моделей. В этой статье представлена структура обнаружения объектов на основе беспилотных летательных аппаратов для анализа изображений и видео в общественных приложениях и оценивается производительность моделей YOLOv8n/v8s, YOLOv11n/v11s и YOLOv12n/v12s при извлечении признаков из наземных тепловых инфракрасных изображений и видео, снятых камерами переднего обзора, а также из записанных беспилотными летательными аппаратами тепловых инфракрасных видео, снятых с разных ракурсов. Модели YOLOv8n/v8s, YOLOv11n/v11s и новейшая модель YOLOv12n/v12s были развернуты на Raspberry Pi 5 с использованием фреймворка OpenVINO. Успешное развертывание этих моделей, включая самую последнюю версию, демонстрирует их пригодность для обнаружения тепловых инфракрасных объектов на основе беспилотных летательных аппаратов. Результаты показывают, что YOLOv8 и YOLOv11 достигли высокой точности и показателей полноты 93% и 92% соответственно, в то время как модель YOLOv12 продемонстрировала хорошую точность, но сравнительно более низкие показатели точности и полноты, что предполагает возможность дальнейшего улучшения.
Ключевые слова: обнаружение объектов, модели YOLO, беспилотные летательные аппараты, инфракрасные камеры переднего обзора, тепловые инфракрасные изображения, Raspberry Pi 5.

Айманова Г.К., Серебрянский А.В., Щербина М.П., Кругов М.А.
I астероидтардың спектрофотометриялық зерттеуі: шағылу спектрі

2024 жылғы 22 ақпан, 2023 жылғы 3 қараша, 4 қараша және 21 қарашада Ассы-Түрген обсерваториясында (шығ. бойлығы 77°.87114, солт. ендігі 43°.225527, теңіз деңгейінен биіктігі 2658 м, Халықаралық обсерваториялар коды — 217) жүргізілген бақылаулар негізінде астероидтардың шағылу спектрлерін талдау нәтижелері келтірілген. Бақылаулар апертурасы 1,5 метрлік AZT-20 телескопының негізгі фокусына орнатылған көлемдік-фазалық голографиялық торлар (VPHG) негізіндегі ұзын саңылаулы спектрографты пайдалана отырып жүргізілді. Бақылаулар төменгі спектрлік ажыратымдылық режимінде (R=600), 3500–7500 Å толқын ұзындықтары диапазонында, әр миллиметрде 360 сызықты торды, пиксельге 4.25 Å дисперсияны қолдана отырып, бірінші биннингте EMCCD режимінде, күшейту коэффициенті 5 және экспозиция уақыты 10 секунд, саңылау ені 9 доғалық секунд болған жағдайда жүзеге асырылды. Астероид спектрлерін өлшеу

дифференциалдық әдіспен - объект пен стандартты жұлдыз арасындағы жарық ағындарын салыстыру арқылы жүргізілді. Стандарт ретінде Күн тектес-жұлдыздар (G спектрлік класы) пайдаланылды. Шағылу спектрлерін өңдеу мен есептеу, сондай-ақ спектрлік морфология мен таңдап алынған спектрлік сипаттамалар негізінде Tholen және SMASSII жүйелері бойынша таксономиялық жіктеу жүргізілді. Бұл жұмыс негізінен Басты белбеу мүшелері (14) болып табылатын 19 астероидтан тұратын таңдама үшін орындалды. Талдау нәтижелері 2013–2017 жылдары ИНАСАН жүргізген бақылаулар негізіндегі астероидтар спектрлерімен және Gaia (DR3) миссиясы арқылы алынған шағылу спектрлерімен салыстырылды, және альбедо көрсеткіштерін ескерусіз таксономиялық типтері анықталды.

Кілт сөздер: спектрофотометрия, астероидтар, шағылу спектрі, Gaia DR3.

Айманова Г.К., Серебрянский А.В., Щербина М.П., Кругов М.А.

Спектрофотометрические исследования астероидов I: спектры отражения

Приведены результаты анализа спектров отражения астероидов по наблюдениям, проведенным 2024-02-22, 2023-11-03, 2023-11-04 и 2023-11-21 в обсерватории Ассы-Тургень (77°.87114 в.д., 43°.225527 с.ш., высота 2658 метров над уровнем моря, код международной обсерватории 217) с использованием спектрографа с длинной щелью на основе объемно-фазовых голографических решеток (VPHG), установленного в главном фокусе телескопа AZT-20 с апертурой 1.5 метра. Наблюдения проводились в режиме низкого разрешения (R=600) в диапазоне 3500-7500Å с использованием решетки 360 линий на мм, дисперсией 4.25Å на пиксель, в первом биннинге в режиме работы EMCCD с коэффициентом усиления 5 и временем экспозиции 10 секунд, ширина щели 9 угловых секунд. Измерение спектра астероидов проводилось дифференциальным методом: сравнением световых потоков от объекта и стандартной звезды. В качестве стандартов использовались звезды - солнечные аналоги (звезды класса G). Обработка и расчет спектров отражения, а также определение таксономической классификации по системам Tholen и SMASSII на основе спектральной морфологии и избранных спектральных характеристик были проведены для выборки из 19 астероидов, в основном состоящей из членов Главного пояса (14). Проведено сравнение со спектрами астероидов по наблюдениям ИНАСАН в 2013–2017 гг. и спектрами отражения астероидов, полученными по наблюдениям Gaia (DR 3), а также определены их таксономические типы без учета альбедо астероидов.

Ключевые слова: спектрофотометрия, астероиды, спектр отражения, Gaia DR3.

al-Garalleh B.F., Akour A.N., Jaradat E.K., Jaradat O.K.

Гомотопиялық ұйытқу әдісімен зарядталған бөлшектердің сызықсыз тербелістері.

Бұл мақалада электр өрісінің әсерінен зарядталған бөлшектердің тербелісін сипаттайтын сызықсыз теңдеудің қарапайым сипаттамасы берілген. Сипаттау үшін гомотопиялық ұйытқу әдісі қолданылды. Бұл әдіс мағыналы жуықталған шешімді алуға мүмкіндік береді. Талдау нәтижесінде зарядталған бөлшектердің тербелісін сипаттайтын төрт теңдеуден тұратын бастапқы жүйе әзірленді. Бұл теңдеулер визуализацияланып, алынған нәтижелерге жан-жақты түсіндірме берілген.

Кілт сөздері: зарядталған бөлшектердің тербелісі, сызықсыз гармоникалық теңдеу, гомотопиялық ұйытқу әдісі.

al-Garalleh B.F., Akour A.N., Jaradat E.K., Jaradat O.K.

Нелинейные колебания заряженных частиц методом гомотопического возмущения.

В данной статье представлено упрощенное описание нелинейного уравнения, описывающее колебания заряженных частиц под воздействием электрического поля с использованием гомотопического возмущения. Этот метод позволяет получить значимое приближённое решение. В результате анализа была разработана начальная система из четырех уравнений, описывающих колебания заряженных частиц. Эти уравнения были визуализированы, а также представлено всестороннее объяснение полученных результатов.

Ключевые слова: колебания заряженных частиц, нелинейное гармоническое уравнение, метод гомотопического возмущения.

Хохлов А.А., Агишев А.Т., Вайдман Н.Л., Агишев А.Т.

ASAS-SN деректері бойынша IRAS 07080+0605 жұлдызының жарықтығының вариацияларын зерттеу

Берілген жұмыста FS CMa тобына жататын IRAS 07080+0605 жұлдызының жарықтылық қисығының ASAS-SN шолуы деректері негізінде (2014–2025 жж. аралығы) талдау нәтижелері ұсынылады. ASAS-SN шолуының *g*-фильтріндегі жылдар бойынша бөлінген уақыттық қатарларын зерттеу барысында жүйенің периоды уақыт өте өзгеретіні және фазалық қисықтың пішіні жекелеген интервалдарда өзгеріске ұшырайтыны анықталды. Атап айтқанда, фазалық қисықтарда асимметриялардың пайда болуы орбитаның өзгеруін көрсетуі мүмкін, бұл жүйенің динамикасымен, соның ішінде объектілер арасындағы ара-қашықтықтың (сепарацияның) өзгеруімен байланысты болуы ықтимал. Сонымен қатар, IRAS07080+0605 жұлдызының жарық амплитудасының өзгерістері сипатталып, олар жұлдыздың физикалық күйінің өзгерістерін, мысалы, сыртқы қабаттардың пульсациясын немесе қоршаған ортамен өзара әрекеттесуінің салдарынан болу мүмкіндігі көрсетілді.

Кілт сөздері: қос жұлдызды жүйелер, жарықтылық қисықтары, FS CMa, ASAS-SN каталогы.

Хохлов А.А., Агишев А.Т., Вайдман Н.Л., Агишев А.Т.

Исследование вариаций блеска IRAS 07080+0605 по данным ASAS SN

В данной работе представлены результаты анализа кривой блеска звезды IRAS07080+0605, относящейся к классу FS CMa, с использованием данных обзора ASAS SN в период с 2014 по 2025 года. В данной работе анализируя временные ряды обзора ASAS SN в фильтре g, разделенные по годам, выявлено, что период системы изменяется с течением времени, а форма фазовой кривой претерпевает изменения на отдельных интервалах. В частности, появление асимметрий в фазовых кривых указывает на возможное изменение орбиты, которые могут быть связаны с динамикой системы, включая изменение сепарации между объектами. Дополнительно описаны изменения амплитуды блеска звезды IRAS07080+0605, которые могут отражать изменения физического состояния звезды, такие как пульсации внешних слоёв или взаимодействие с окружающей средой.

Ключевые слова: двойные системы, кривые блеска, FS CMa, каталог ASAS SN.